11-4-2019 10:30 AM

Investigations of the High Pressure Effects on Structural Properties and CO2 Adsorption Performance of MOFs using Vibrational Spectroscopy

Shan Jiang, *The University of Western Ontario*

Supervisor: Huang, Yining, *The University of Western Ontario*
Joint Supervisor: Song, Yang, *The University of Western Ontario*
A thesis submitted in partial fulfillment of the requirements for the Doctor of Philosophy degree in Chemistry
© Shan Jiang 2019

Recommended Citation

Abstract

The pre- and post-combustion carbon dioxide capture has drawn much attention in the past few decades owing to the increasing concentration of CO_2 in the atmosphere. Among all the potential solid adsorbents for CO_2 capture, metal-organic frameworks (MOFs) are a promising class of materials due to their large surface areas, high tunability and their high selectivity for gas adsorption applications. It has been widely demonstrated that the application of high external pressure in gigapascal level can substantially tune the structure, pore size and opening of porous material. Consequently, the structural, as well as gas adsorption properties of these materials, can be modified and optimized. In this thesis, we focused on the high-pressure studies of 6 types of MOFs with various topologies, structures and properties. *In situ* vibrational spectroscopies and are synchrotron X-ray diffraction used as preliminary methods for characterizing the structural and gas adsorption properties of MOFs under high pressure. In PbSDB and CdSDB, strongly contrasting guest-host interactions in terms of the pressure-regulated CO_2 adsorption sites have been observed. SIFSIX-3-Zn features ultra-micro pore and one-dimensional channel was then studied. The framework fluorine and hydrogen atoms were found to play important roles in interacting with CO_2 under high pressure, and ultimately formed a new CO_2 binding site. ZIF-8 and UiO-66 are two noble MOFs that possess enormous cages and are anticipated to have great potential in accommodating CO_2 under high pressure. However, it was severely limited by the phase change of the free CO_2 at 0.6 GPa under room temperature. With the aid of temperature (i.e., 30-100 °C), the CO_2 storage capacity in ZIF-8 and UiO-66 was significantly improved. $ZnAtzOx(H_2O)$ is constructed by zinc-3-amino-1,2,4-triazolate sheets that are linked into the third dimension by oxalate pillars, creating ultra-micro pores with different sizes along three directions. The high pressure studies on the framework itself, CO_2 loaded, D_2O loaded, as well as CO_2-D_2O co-loaded $ZnAtzOx(H_2O)$ have shown excellent structural stability of the framework and better CO_2-framework affinity under high pressure even in the presence of water (i.e., D_2O). Overall, it is hoped that the information our study provides is insightful for designing and modifying MOFs and porous material for CO_2 adsorption, and provides guidance for optimizing the CO_2 capture and storage conditions.

Keywords

Metal-organic frameworks, high pressure, diamond anvil cell, vibrational spectroscopy, infrared spectroscopy, Raman spectroscopy, framework stability, reversibility, pressure-induced phase transition, CO_2 storage, CO_2 binding site, guest-host interaction, amorphization, synergetic effect of high pressure and high temperature.

Summary for Lay Audience

Metal-organic frameworks (MOFs), are a class of crystalline materials constructed by bridging metal-containing units with organic linkers to create open rigid frameworks with permanent porosity. Due to their high thermal stability, enormous surface area, finely tunable chemical functionality, MOFs are believed to have great potential in CO_2 capture and storage. Compared to the conventional CO_2 absorption methods, using MOFs as solid adsorbent has the advantages of being less corrosiveness and more energy efficient. It is well known that temperature, pressure and volume are three basic macroscopic parameters to describe a thermodynamic system. Among these parameters, pressure spans over 60 orders of magnitude in the universe, from 10-32 in intergalactic space to 1032 Pascal in the center of neutron star. Under such a broad range of pressure, materials could exhibit various structures as well as novel properties, especially under high pressure. When applying pressure to materials, the general effect is to reduce the volume and thus shorten then inter-/intra-molecular distances. As a result, lots of interesting phenomena and novel materials can be generated under high pressure, including phase transitions, chemical reaction, novel bondings and new properties. Previous studies have demonstrated a wide variety of pressure behavior of MOFs, including unusual elastic responses, phase transitions, chemical reactions and high-pressure guest insertion. In terms of CO_2 storage, it has been reported that high pressure can efficiently tune the channel size and shape, pore volume and surface area in MOFs. Consequently, these pressure-induced modifications on the framework will affect the adsorption capacity, selectivity, and thus better adsorption performance. In this thesis, our studies on six MOFs featuring distinctive structures and topologies are performed under high pressure and other conditions (i.e. the presence of water, high temperature). All these MOFs have shown extraordinary stability and a well-enhanced CO_2 adsorption performance under high pressure. The structural changes, enhanced guest-host interactions, as well as improved CO_2 adsorption capacity are characterized by vibration spectroscopy, which allows the understanding of local structures, chemical bonding, and thus the nature of guest-host interactions. It is anticipated that our findings would inspire the design of new MOF structures to address practical applications in the future.

Co-Authorship Statement

This thesis contains contents from previously publication authored by Shan Jiang and co-authored or edited by others mentioned below. Prof. Yining Huang and Prof. Yang Song are the corresponding authors on the presented paper and are responsible for the supervision of Shan Jiang over the course of her Ph.D. study. Both of them played a major role in the editing and revision of the materials presented in all chapters of this thesis.

Chapter 3 is from the publication authored by Shan Jiang, Yue Hu, Shoushun Chen, Prof. Yining Huang and Prof. Yang Song (Chem. Eur. J. 2018, 24, 19280-19288). Dr. Shoushun Chen (Prof. Yining Huang's group, the Department of Chemistry) is credited for the synthesis of the samples. Shan Jiang is responsible for the post-synthesis sample preparation, data collection of the synchrotron XRD patterns at APS, vibrational spectroscopy spectra in Prof. Song's lab, and data analysis.

In *Chapter 4 and 6*, Shan Jiang is responsible for all sample synthesis, post-synthesis preparation, data collections and analysis. The sample preparation was done in Prof. Yining Huang's lab; the *in situ* high-pressure IR and Raman measurements were performed in Prof. Song's lab.

In *Chapter 5*, a highly customized High-temperature and High-pressure FTIR system was built for data acquisition. Prof. Yang Song and Dr. Jiwen Guan (Prof. Yang Song's group, the Department of Physics and Astronomy) are credit for the system development, testing and calibration. Shan Jiang is responsible for system assembly, sample preparation and data collection. The data analysis is done by Shan Jiang, with the inspiration from Prof. Yining Huang and Dr. Jiwen Guan.

I am aware of the University of Western Ontario Policy on Authorship, and I certify that I have properly acknowledged the contribution of other researchers to this thesis.

Acknowledgements

First and foremost, I would like to thank my two advisors Prof. Yining Huang and Prof. Yang Song for their constant teachings, inspiring advice, instructions and their key role in supporting my research. Without their exceptional supervision and patient guidance, my Ph.D. study would not have been possible. I am sincerely grateful to study and work under their supervision. Their strong work ethos and dedication in research will continuously encourage me for the rest of my life.

I would also like to extend thanks to Prof. T. K. Sham, Prof. Yining Huang, Prof. Yang Song, Prof. François Lagugné-Labarthet and Dr. Paul D. Boyle for their excellent graduate courses. I would like to thank the members of my examination committee, Prof. Mark S. Workentin, Prof. T. K. Sham, for taking the time to conduct my thesis examination.

Also, I would like to give my appreciation to Jan Mathers, Sandra Zakaria Holtslag, and Susan England in First-Year Chemistry Lab, the undergraduate laboratory manager Dr. Chris Levy. I spent a lot of time working with them, and it was the best work experience I ever had. I would like to acknowledge all my collaborators and beamline scientists at APS, Dr. Changyong Park, Dr. Dmitry Popov, and Dr. Zou Finfrock for their help and technical support, which have been much needed for the fulfillment of my studies.

I would also like to thank all my past and present colleagues in both Prof. Huang and Prof. Song's groups: Dr. Yue Hu, Dr. Jiwen Guan, Dr. Pan Wang, Ms. Fengping Xiao, Dr. Bryan Lucier, Dr. Yue Zhang, Dr. Shoushun Chen, Ms. Yuanjun Lu, Mr. Zitong Wang, Mr. Vinicius Martins, Mr. Kyungseop Lee, Ms. Xinkai Xie, Prof. Ying Guo, Prof. Mansheng Chen, Prof. Jinghui Lyu, Ms. Yingxian Li, Mr. Bowei Wu, Ms. Xuzhao Zhao, Ms. Sandamini Ulpanhewa Vidanalage; all the undergrad students I work with: Miss Cici Yang, Mr. Ryan Ho and Mr. Zexi Wu. It has been a privilege to work with all of them. I would also like to extend my gratitude to my good friends at Western: Dr. Nazhen Liu, Dr. Jun Li, Dr. Zhiqiang Wang, Ms. Chaochao Chen, Ms. Mengnan Guo, Dr. Dan Guo, Ms. Mi Li, and Mr. Hanqing Zhao. It is you who took my loneliness away and made my graduate study colorful and joyful. Five years company makes them my lifetime friends.

Finally, I would like to give my special thanks to my beloved family for their unconditional support, understanding and encouragement during the five years of my graduate study.

Table of Contents

List of Tables

List of Figures

List of Abbreviations

ANL   Argonne National Laboratory

APS   Advanced Photon Source

BDC   1,4-benzenedicarboxylate

BET   Brunauer-Emmett-Teller

BS   beam splitter

BTC   benzene-1,3,5-tricarboxylate

CCD   charge coupled device

CCS   carbon capture and storage

DAC   diamond anvil cell

DMF   *N,N*-dimethylformamide

DOBDC   2,5-dioxido-1,4-benzenedicarboxylate

GCMC   Grand Canonical Monte Carlo

GPa   gigapascal

HKUST   Hong Kong University of Science and Technology

HP   high pressure

HT   high temperature

HUM   hybrid ultramicroporous material

IR   infrared

IRMOF   isoreticular metal-organic framework

MIL   Matériaux de l'Institut Lavoisier

MOF	metal-organic framework
NLC	negative linear compressibility
NMR	nuclear magnetic resonance
PTM	pressure transmitting medium
PXRD	powder X-ray diffraction
RT	room temperature
SCXRD	single crystal X-ray diffraction
SDB	4,4′-sulfonyldibenzoic acid
SSNMR	solid-state nuclear magnetic resonance
UiO	Universitetet i Oslo
XRD	X-ray diffraction
ZAG	zinc alkyl gate
ZIF	zeolitic imidazolate framework
ZnAtzOx	zinc-aminotriazolato-oxalate
1D	one-dimensional
3D	three-dimensional

Chapter 1

1 Introduction

1.1 Metal-Organic Frameworks

For a little over two decades, the study of the family of materials known as metal-organic frameworks (MOFs) has rapidly expanded. First having been termed in 2005,[1] the phrase MOF now refers to tens of thousands of crystalline materials made up of metal ions or clusters, which are bridged together using organic linkers.[2-3] One of the most commonly explored applications for MOFs is gas adsorption,[2-6] due to the high surface areas and gas loading capacities that are attainable. This makes MOFs promising candidates for gas purification, separation, storage and catalysis applications. Other applications for MOFs include optics, drug delivery and chemical detection, etc.[7]

The key distinguishing feature between MOFs and other porous solids, such as zeolites and activated carbon, is their degree of tunability and flexibility. Using different combinations of metal centers and linkers allows for MOFs to be altered to adsorb specific molecules with an ideal interaction strength. Isoreticular MOFs, possessing the same underlying topology, can be synthesized and functionalized using different organic linkers, as was first done with the MOF-5 family,[8-9] two examples of MOF-5 and UiO-66[10] are illustrated in Figure 1.1. The size and volume of the unit cell, and the porosity and density of the material are all key elements in gas adsorption that can be fine-tuned in MOF development through changes to the reactants and chemical conditions. Similarly, by replacing the metal ions comprising the nodes of MOF structures, an isostructural series of MOFs can have their adsorption properties tuned even further. This strategy was employed to great effect in the HKUST-1[11-15] and M-MOF-74[16-17] series of MOFs. Many MOFs are also renowned for their high surface areas, with materials such as NU-110[18] and DUT-60[19] having Brunauer-Emmett-Teller surface areas of 7000 $m^2 \cdot g^{-1}$ or greater.
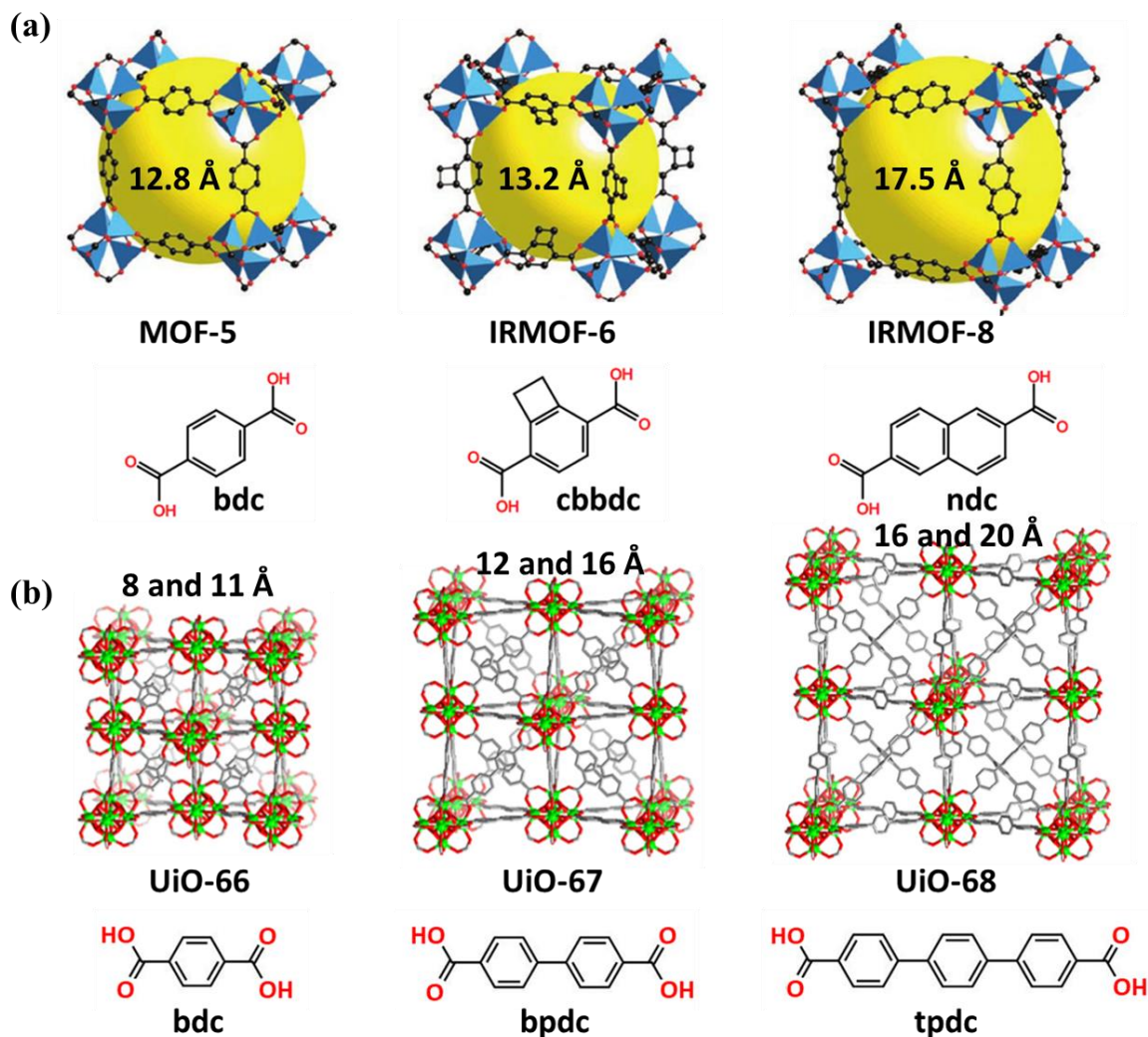
Figure 1.1 Isoreticular expansion of (a) MOF-5,[9] and (b) UiO-66.[10] Each panel shows the ligands of the frameworks, and a scaled comparison of the smallest, medium, and largest structures of the MOF skeleton.

Though the exact quantity of known MOF structures is a question without a perfect answer, it numbers in at least the tens of thousands,[20] though only a handful are currently available commercially. HKUST-1 (named for the Hong Kong University of Science and Technology),[21] MIL-53 (named as the Matériaux de l'Institut Lavoisier)[22] and ZIF-8 (a zeolitic imidazolate framework)[23] are among the first MOFs to become widely available, all of which are known for their adsorption of hydrogen and other gases. In addition to commercially available MOFs, there are currently an array of techniques of varying complexity which can be used to synthesize such structures, including solvothermal,

microwave-assisted, electrochemical and mechanochemical.[24-27] There is ongoing research in MOF design and in understanding the factors which control gas adsorption performance, which is expected to lead to an increase in practical and commercially available MOFs in the coming years.

Much of the recent research into MOFs has focused on exploring their viability as adsorbents for various greenhouse gases, primarily carbon dioxide.[4, 28] This could lead to the usage of MOFs as a part of carbon capture and storage (CCS) technologies, and assist in the stabilization of atmospheric CO_2 concentrations.[29-31] Over half of anthropogenic CO_2 is contained within flue gases emitted from immobile point sources,[30, 32] which includes sources involved in energy production, heating and other industrial activities. Post-combustion CO_2 capture is the most widely explored CCS strategy, and would involve the extraction of CO_2 gas directly from such flue gas streams. Upon isolation of the CO_2 or other greenhouse gases from the stream, these gases could then be transported and sequestered into a long-term storage location.[33-34]

The primary advantage of a CCS strategy is the ability to implement the technology on existing combustion sources without the need for costly new facilities or extensive modifications. The challenges lie in being able to isolate CO_2 or other gases from flue gas at low concentrations, minimizing the energy usage of the separation and regeneration process, and accounting for the presence of impurities such as SO_2, NOx or water which can interfere with the materials used.[28] The design of advanced materials is therefore essential to implementing CCS on a wide scale.

CCS technology has been approached from multiple angles: cryogenic distillation, membrane purification, absorption using liquids, and adsorption using solids.[33] The most success thus far has been achieved using chemisorbent alkanolamine aqueous solutions, such as monoethanol amine, which act as the current benchmark for CCS materials.[35-36] However, drawbacks relating to equipment corrosion, high energy consumption and solvent loss[37-39] have pushed research into other materials, including traditional sorbents such as zeolites and activated carbons, as well as the previously discussed MOFs.

Given the high porosity and surface area of MOFs, they represent less hazardous and more energy efficient solid adsorbent materials for post-combustion CCS. The high tunability of MOFs means that their properties can be easily adjusted to promote energy efficient CO_2 adsorption at flue gas concentrations. This would eventually lead to the design of MOFs that are robust enough to withstand the continued use in CCS. For example, Mg-MOF-74[40] and HKUST-1[41] are well-studied MOFs that have already demonstrated high CO_2 uptake capacities and strong host-guest interactions with CO_2. Such strong interactions between CO_2 and these frameworks are due to the presence of open metal sites within the structure. These sites produce a strong adsorptive interaction selectively promoting the adsorption of polar molecules such as CO_2. Besides open metal sites, other aspects of a given MOF, such as pore dimensions and the functional groups, also have strong effects on the adsorption behavior of the material. Table 1.1 highlights the physical proprieties, CO_2 adsorption sites and performance of some popular MOFs.

The ideal solid sorbent material would possess high CO_2 uptake, strong selectivity against N_2 and other gases, low regeneration energy requirements and high mechanical, chemical and thermal stability. The wide variety of MOF structures in existence necessitates the detailed study of individual frameworks and their performance in these areas. This will promote the rational understanding of these frameworks and their adsorption behaviors, and lead to more efficient and more well-designed MOFs in the future.

Table 1.1 A summary of physical properties and CO₂ adsorption properties of selected metal-organic frameworks

Compound	Metal	Linkers	Coordination types	Space group	Adsorption sites	Pore geometry or sizes	BET (m²/g)	CO₂ capacity (wt%)	Pressure (bar)	Temp (K)	Ref
NU-100	Cu	LH_6^a	Cu-O	Fm$\bar{3}$m	Open metal site	13 Å, 15 Å, 27 Å^h	6143	69.8	40	298	42
MOF-177	Zn	BTB^b	Zn-O	P6$_3$	Phenyl rings	10.6-12.7 Å	5400	3.6	1	298	40
Mg-MOF-74	Mg	DOBDC^c	Mg-O	R$\bar{3}$	Open metal site	11 Å^h	1174	27.5	1	298	43
Co-MOF-74	Co	DOBDC	Co-O	R$\bar{3}$	Open metal site	11 Å^h	957	24.9	1	298	43
Ni-MOF-74	Ni	DOBDC	Ni-O	R$\bar{3}$	Open metal site	11 Å^h	936	23.9	1	298	43
Zn-MOF-74	Zn	DOBDC	Zn-O	R$\bar{3}$	Open metal site	11 Å^h	774	19.8	1	296	43
MIL-53(Al)	Al	BDC^d	Al-O	C2/c (lt), Imcm (ht)	Bridging -OH	7.6×19.5 Å (lt) 12.8×16.7 Å (ht)	1300	10.6	1	298	44
NH₂-MIL-53(Al)	Al	NH₂-BDC	Al-O	C2/c (lt), Imcm (ht)	Amines	7.5 Å(lt) 12 Å(ht)	960	12	1	298	44
MIL-53(Cr)	Cr	BDC	Cr-O	C2/c (lt), Imcm (ht)	Bridging-OH	7.85 Å(lt) 13.04 Å(ht)	1500	8.5	1	304	45
MIL-101(Cr)	Cr	BDC	Cr-O	Fd$\bar{3}$m	Open metal site	29-34 Å	2674	4.2	1	319	46

Table 1.1 Continued

Compound	Metal	Linkers	Coordination types	Space group	Adsorption sites	Pore geometry or sizes	BET (m²/g)	CO₂ capacity (wt%)	Pressure (bar)	Temp (K)	Ref
MIL-47	V	BDC	V-O	Pnam	Framework O or H	10.5×11.0 Å	600	8.1	1	298	43
ZIF-8	Zn	2mIM[e]	Zn-N	I$\bar{4}$3m	Imidazole rings	11.6 Å[h]	1700	4.3	1	298	43
UiO-66	Zr	BDC	Zr-O	Fm$\bar{3}$m	Bridging-OH	8 Å, 11 Å[h]	1340	24.3	18	303	47
SIFSIX-3-Zn	Zn	SiF$_6^{2-}$, pyrazine	Zn-F, Zn-N	P4/mmm	Si-F	3.84 Å	250	11.5	1	298	48
HKUST-1	Cu	BTC[f]	Cu-O	Fm$\bar{3}$m	Open metal site	10 Å 14 Å[h]	1400	19.8	1	293	49
ZnAtzOx(H₂O)	Zn	3-AT[g], oxalate	Zn-O, Zn-N	P2₁/c	Amines	3.5×4.0 Å	308	20.7	1.1	293	50

[a] **LH$_6$** = 1,3,5-tris[(1,3-carboxylic acid-5-(4-(ethynyl)phenyl))ethynyl]-Benzene

[b] BTB = benzene-1,3,5-tribenzoate

[c] DOBDC = 2,5-dioxido-1,4-benzenedicarboxylate

[d] BDC = 1,4-benzenedicarboxylate

[e] 2mIM = 2-methylimidazole

[f] BTC = 1,3,5-benzenetricarboxylate

[g] 3-AT = 3-amino-1,2,4-triazolate

[h] cage diameter

1.2 High-pressure Sciences

1.2.1 High-pressure phenomena

It is well-established that the equilibrium of a thermodynamic system is controlled by pressure, temperature and volume. Of all these variables, pressure spans around 50 orders of magnitude, with the lowest measurable pressure being 10^{-26} GPa in the intergalactic voids and the highest calculatable pressure being 10^{25} GPa in the center of a neutron star.[51-52] Such a vast scale of pressure opens up an unexplored expanse bearing huge potential for discovery. When pressure is applied to materials, the immediate response is to shorten the inter-molecular and intra-molecular distances, which further induces a contraction of the total volume and an increase in internal energy,[53] as described by Equation 1.1.[54]

$$P = -\frac{\partial E}{\partial V} \qquad\qquad \text{Equation 1.1}$$

As a result, due to the tendency of a system to recover its free energy minimum, a series of unusual behaviors and novel phenomena of the materials become accessible, including phase transformations, ionization, condensation, polymerization, amorphization, dissociation, and in the most extreme cases, atomization and metallization,[55-56] as illustrated in Figure 1.2, representative examples of each high-pressure phenomena are highlighted.[55]
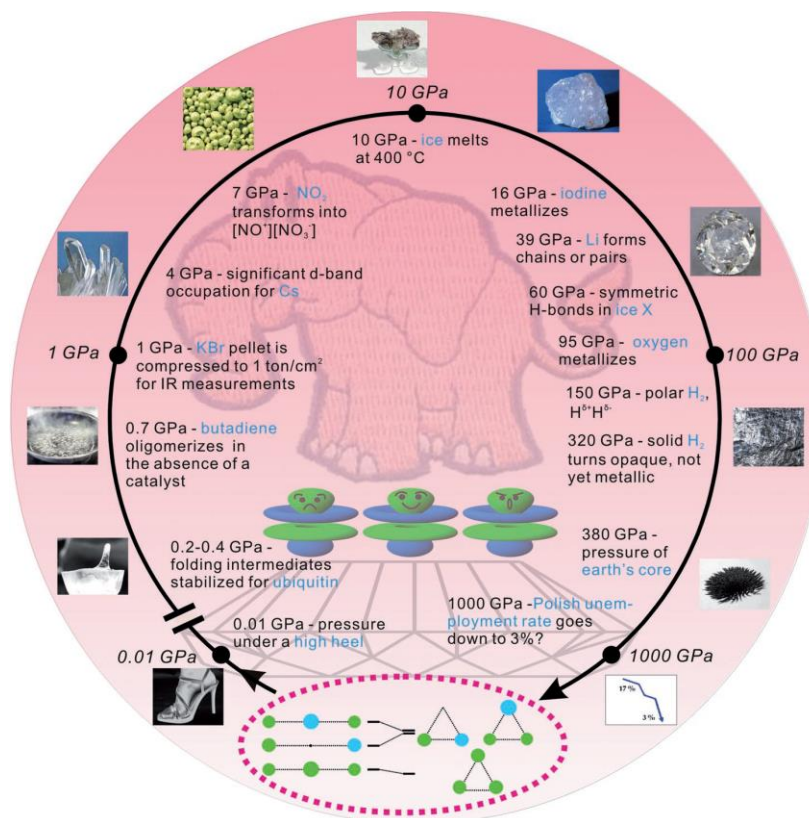
Figure 1.2 Examples of various high-pressure phenomena.[55]

1.2.2 Chemistry at high pressure

It is well-known that most chemical reactions involve the participation of electronically excited states.[57] With the assist of high pressure, the gap between the ground and excited states could be significantly reduced and thus facilitates these reactions to take place.[58-59] Assuming other factors remain constant, the relation between equilibrium constant K of a chemical reaction and pressure is of a positive correlation, as described by Equation 1.2,[57] where ΔV^0 is the difference of the molar volumes in the standard state between the products and the reactants.

$$\left(\frac{\partial RTlnK}{\partial P}\right)_T = -\Delta V^0 \qquad \text{Equation 1.2}$$

Moreover, pressure can also work as a physical means to activate chemical reactions in a way that could not otherwise be achievable through conventional chemical pathways.[58, 60-62] This is, for instance, the case for the laboratory-grown diamonds, where high pressure

and high temperature are required (i.e. 5 GPa and 1500 °C) to transform the layer structured graphite to the isotropic 3D structured diamond. Furthermore, high-pressure has been demonstrated as a promising tool for tuning the pore shape and size, cage opening, internal surface area, as well as local geometry in porous materials,[19, 63-104] which could further lead to considerable improvements in structural and adsorptive performances for various applications, such as caffeine encapsulation,[105] guest inclusion,[106-114] pressure sensor,[64-65] CO_2[115-118] or gas storage,[119] and energy absorber.[70, 120] The details will be discussed in the following sessions.

1.2.3 High pressure studies on MOFs

As one of the prerequisites for utilizing MOFs for CO_2 capture and adsorption, the frameworks must be chemically and mechanically stable to retain its framework structure and porosity, in order to meet the application standards. When applying external pressure to MOFs, even marginal modifications on the structural features could potentially result in significant impacts on their performance for CO_2 adsorption. Compared to intensive studies on structural and adsorption performance of MOFs under low temperatures or near ambient pressure,[5] there are still so many aspects in MOFs under high pressure in the gigapascal level yet to explore. Therefore, it is of particular interest to fully unveil the pressure responses and adsorption properties of MOFs, as well as the connection between structure and performance. Since high pressure studies on MOFs started to emerge in 2009, researches have examined the behavior of a number of MOFs under pressure. These high-pressure phenomena can be roughly divided into the following four categories.

1.2.3.1 Phase transitions

In the past decade, researchers have found that some MOFs exhibit phase transformation upon applying high external pressure. The most common phase transitions observed under high pressures is the crystalline to amorphous transformation. Researches have shown that the conditions for amorphization in different MOFs may vary, depending on framework flexibility,[22, 68, 78, 84, 115-116, 120] pressurization methods,[71, 111] presence of the guest molecules and so forth.[74, 111] It has been widely accepted that the pressure transmitting medium (PTM) plays an important role in regulating the phase transitions, where the same MOF could have

completely opposite responses to external pressures with and without the presence of PTM. For example, by loading different PTMs to α-Mg$_3$-(HCOO)$_6$, the framework has shown strongly contrasting structural behaviors and stabilities in each compression-decompression cycle.[69] The activated α-Mg$_3$-(HCOO)$_6$ is found to undergo an irreversible crystalline-to-crystalline phase transition above 2 GPa, whereas the DMF and benzene loaded frameworks show no obvious signs of amorphization, with pressure-induced modifications on these two systems being completely reversible.[69] This similar PTM-regulated phase transition is also observed in other MOFs as well, such as ZIF-8,[111] MIL-47(V),[78] Co$_2$(4,4'-bipyridine)$_3$(NO$_3$)$_4$,[76] Sc$_2$BDC$_3$[112] (as shown in Figure 1.3) and, etc.
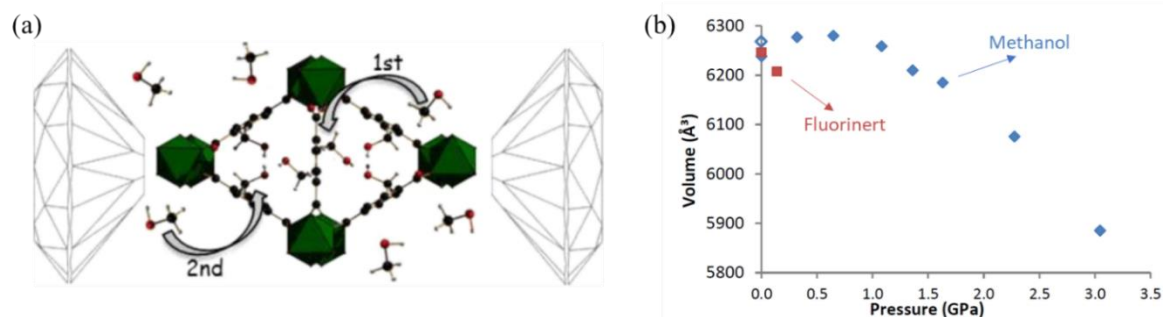
Figure 1.3 (a) Pressure-regulated methanol insertion in Sc$_2$BDC$_3$. (b) Unit cell volume of Sc$_2$BDC$_3$ in methanol (blue squares) and Fluorinert (red squares) as a function of pressure. [112]

1.2.3.2 Unusual pressure responses

Besides the phase transformations, MOFs also exhibit a wide range of mechanical behaviors in response to external pressures.[19, 85, 94, 99-100, 104] In the past few years, intensive researches and efforts have been put into developing and customizing characterization systems that allow the measurements of mechanical properties in MOFs, such as bulk modulus,[66, 120] Young's moduli and stiffness,[70] crystal morphology as a function of pressure,[66, 70, 120] through high-pressure crystallography,[63, 65, 87, 111, 121-123] nanoindentation,[63, 71, 124] and *in situ* SEM nano-compression,[66, 70, 120] respectively. Recent studies on mechanical properties of MOFs have shown that some frameworks with special topologies are substantially more flexible than others because the combination of flexibility

and rigidity allows the component to rotate or reorient more easily at the flexible sites upon compression.[125]

One of the most intriguing mechanical responses of MOFs is negative linear compressibility (NLC), in which the material expands along one direction when compressed uniformly. It is considered "unusual" because our intuition is that materials should shrink evenly throughout the entire structure when hydrostatic pressure is applied.[126] The NLC is favored by frameworks with the special "wine rack" or honeycomb-like topology, including $Ag_3[Co(CN)]_6$ (silver(I) hexacyanocobaltate(III)),[81] $[NH_4][M(HCOO)_3]$ (M = Mn^{2+}, Fe^{2+}, Ni^{2+}),[127-129] $Zn[Au(CN)_2]_2$,[80] and MIL-53,[22, 68, 84, 100] etc. Such peculiar structural arrangements allow the frameworks to expand along a certain direction while contract along the other two in response to added pressure, as demonstrated in Figure 1.4.
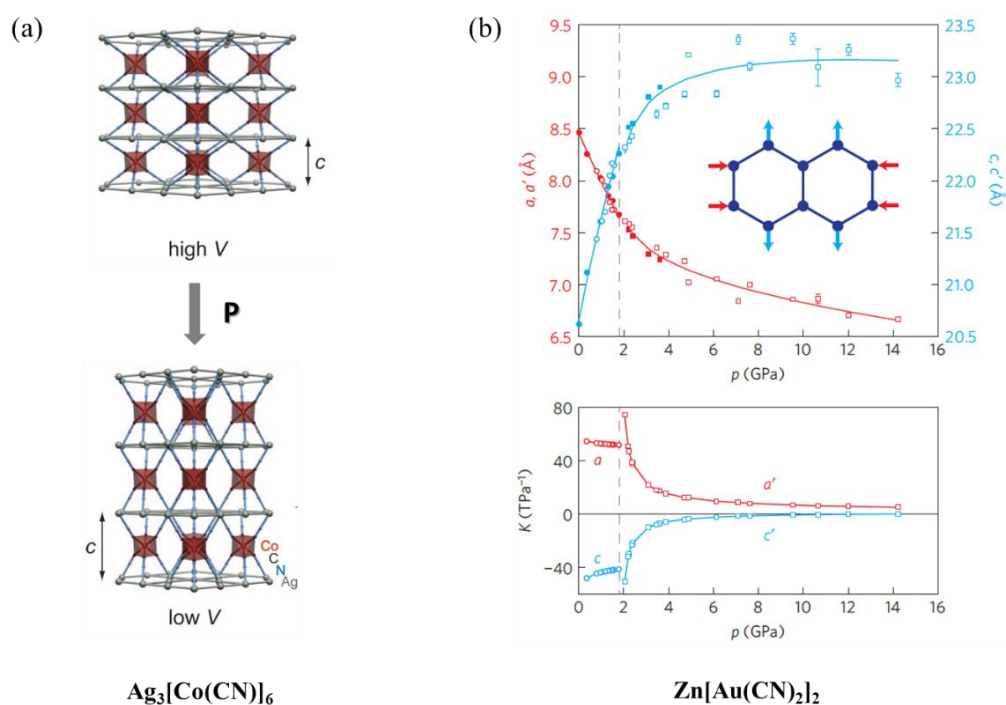
Figure 1.4 (a) Compression mechanism in Ag$_3$[Co(CN)$_6$],[81] the framework expands along *c* axis in response to an increase in pressure. (b) Evolution of unit cell parameters during hydrostatic compression of zinc dicyanoaurate[80]: a (red), c (blue), single-crystal X-ray diffraction (filled markers), powder X-ray diffraction (open markers), ambient phase (circles) and high-pressure phase (squares).

Two prototype examples of the NLC in MOFs are MIL-53 family and zinc alkyl gate (ZAG) family.[64, 68] In these MOFs, MIL-53(Al) and its derivative NH_2-MIL-53(Al) exhibit an expansion along *b* axis accompanied by a shrinkage in both *a* axis and the unit cell volume, up to 2 GPa and 3 GPa respectively.[100] Likewise, for the isoreticular ZAG-4 and ZAG-6, the frameworks expand in *b* direction while contracting along *a* and *c* axes are observed in the pressure regions of 0-3 GPa and 0-6.9 GPa.[64-65] Although these observations are similar, the mechanisms of their negative linear compressibility are somehow much different. Serra-Crespo *et al.* vividly described the root of the NLC in the MIL-53 family as a combination of the M(OH) chains acting as hinges while the rigid BDC ligands (i.e. 1,4-benzenedicarboxylate) acting as struts.[68] The relation between variables in the a and b lattice parameters is imposed by the stiffness of these BDC linkers in this wine-rack framework: when *a* decreases, *b* increases.[68] Whereas in ZAG-4 and ZAG-6, the coiling of the alkyl chains at high pressures is responsible for the expansion and contraction along different directions, as shown in Figure 1.5.[64] The NLC phenomenon in MOFs might potentially lead to a variety of applications, such as the development of artificial muscles, and amplification of piezoelectric response for sensors.[64, 125-126]
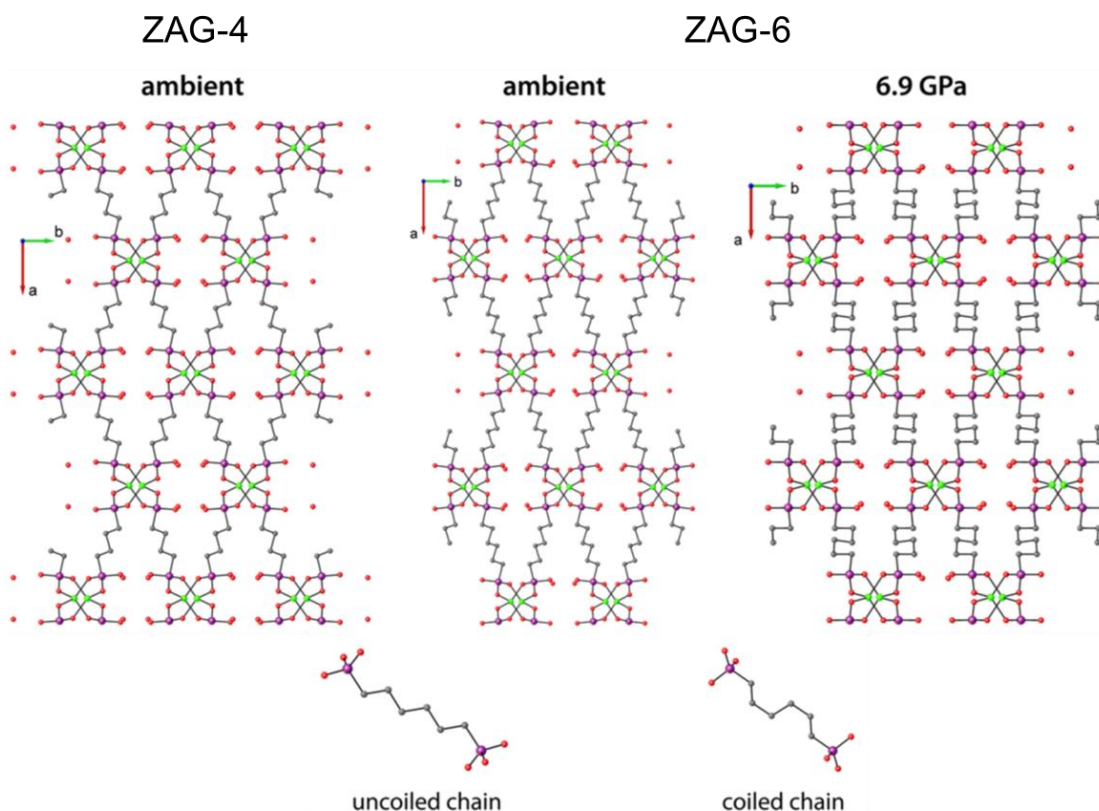
Figure 1.5 The structure of ZAG-4 (left) and ZAG-6 (center) at ambient conditions and 6.9 GPa (right), viewed along the *c* axis, showing the wine rack framework. The bottom panel shows the uncoiled and coiled chains at ambient conditions and higher pressure, respectively.[64]

1.2.3.3 Chemical reactions

Besides the pressure-induced phase transitions, recent researches have shown that chemical reactions could be achieved in some MOFs when high pressure is applied to the framework, resulting in bond formations,[63, 114, 123] breakage[66, 70, 120] and rearrangement.[63, 122] The pressure-induced chemical reactions are very rarely found in MOFs and yet much desirable in the field of material science, with only handful of examples reported up to now. Take ZAG-4 and ZAG-6 as the first example, Ortiz *et al.* illustrated a pressure-induced proton jump between the phosphonate group on the ligand and the included water molecule at about 3 GPa, leading to negative linear compressibility of the frameworks in the pressure range of 2-3 GPa as we discussed above.[64-65]

The second example is erbium-formate MOF ([tmenH$_2$][Er(HCOO)$_4$]$_2$),[63] in which a reversible bond rearrangement is observed upon application of high pressure. Upon compression to 0.6 GPa, the framework exhibits a first-order phase transition, where the chelating formate groups bound to the Er^{3+} ions convert to bridging μ^2-ligands connecting neighboring Er^{3+} ions before and after the phase transition, gives rise to a transformation from a 6-connecting net to an 8-connecting net, as illustrated in Figure 1.6a.[63]
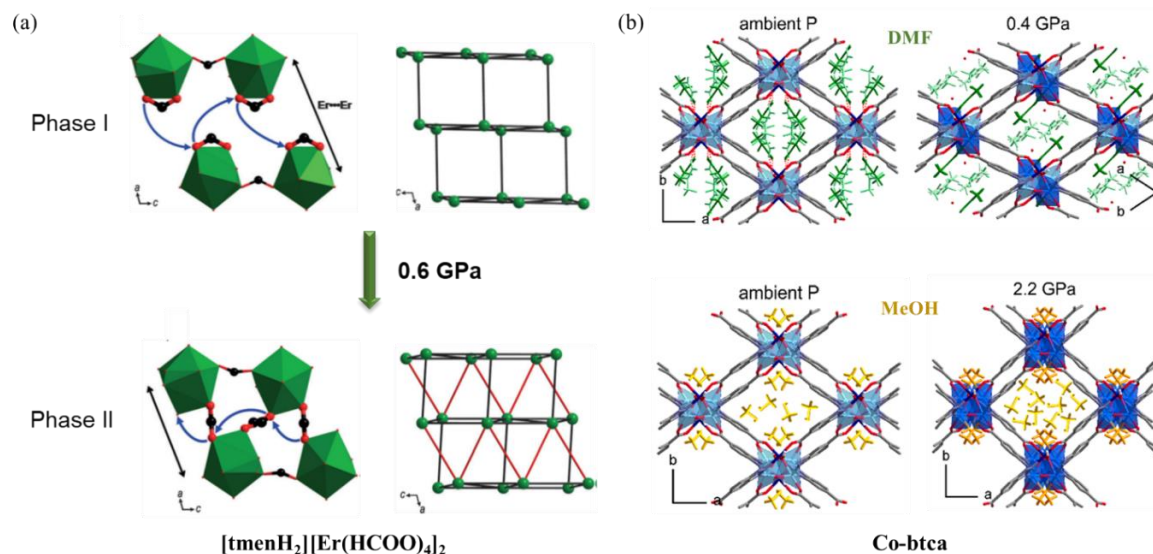
Figure 1.6 (a) Pressure-induced bond rearrangement in [tmenH$_2$][Er(HCOO)$_4$]$_2$ at 0.6 GPa. Black struts represent Er-(HCOO)-Er links that lie approximately within the *b c* plane; red struts show the new linkages that are formed as the framework structure converts from phase I into II. (b) Packing of Co-BTCA as a function of pressure using DMF (upper panel) and methanol (lower panel) as PTMs.[63, 123]

The third example is a reversible nucleophilic addition in Co-BTCA (BTCA = benzotriazolide-5-carboxylato), in which high pressure promotes the coordination of guest methanol molecules to the unsaturated Co centers, and further forms the Co-O$_{MeOH}$ bonds, as shown in Figure 1.6b.[123] This is caused by the sharply reduced Co$\cdots$O$_{MeOH}$ distance under high pressure. The first and second nucleophilic addition reactions are observed at 0.3 GPa and 2.2 GPa respectively, after which the coordination number of the initially unsaturated Co increases from 5 to 6. Consequently, such addition reaction further leads to a (super)filling of the framework channels, in which the unit cell volume smoothly

increases during compression, reaches a maximum expansion of +3% at 0.9 GPa. The similar effects are also observed when substituting MeOH with DMF.[123]

The fourth one is a bond breakage in UiO-66, where the collapse of the pores in UiO-66 forced the breakage of Zr-O bonds between the bridging terephthalates to the $Zr_6O_4(OH)_4$ clusters, as probed by IR spectroscopy and confirmed by extended X-ray absorption fine structure (EXAFS).[70] The mechanical energy adsorbed upon this bond breakage is measured to be about 70 times greater than that of MIL-53(M), in which the MIL-53 framework undergoes a reversible elastic deformation. These observations have shown that UiO-66 possesses great potential for adsorption and dissipation of mechanical shock.[70, 120]

All four cases of very rare pressure-induced chemical reactions demonstrate how deep the field of pressure response of MOFs could go, and how these unanticipated phenomena may lead to a variety of applications in different areas: ZAGs and erbium-formate could be used as pressure sensors or switches;[64-65] UiO-66 may have the potential application as mechanical shock absorbent;[70] Co-BTCA can be exploited even for catalytic purposes.[123]

Table 1.2 A summary of selected high-pressure studies on metal-organic frameworks

Materials	Characterization Methods[a]	Pressure range[b]	Structural changes at HP	Ref
MIL-53(Al)	Synchrotron PXRD	6 GPa	Phase transition: from 0 to 3 GPa NLC: at above 6 GPa	68
MIL-53(Cr)	*in situ* PXRD	400 MPa	Phase transition at 55 MPa (lp to np)	84
NH$_2$-MIL-53(Al)	Synchrotron PXRD	11 GPa	Phase transition: 0 up to 2 GPa (lp to np); Amorphization: 2 to 11 GPa.	68
CB-MOF (Co$_2$(4,4′-bpy)$_3$(NO$_3$)$_4$·xH$_2$O)	*In-situ* Raman, ADXRD	11 GPa	Isostructural phase transition: 6 GPa	76
MIL-47(V)	PXRD, Raman	340.1 MPa	Pore closed at 137 MPa	78
[TPrA][Cd(dca)$_3$]	PXRD, EPR[c], Raman, IR	6 GPa	Phase transition: 0.3 to 0.4 GPa	86
DMAMnF	PXRD, IR and Raman	20 GPa	Phase transition at 3.4 GPa-6 GPa; Amorphization: beyond 7 GPa	89
AceMn ([CH$_3$C(NH$_2$)$_2$][Mn(HCOO)$_3$])	Raman	10.3 GPa	Phase transitions: 0.7 and 1.4 GPa; above 5.3 GPa	95
ZIF-4	Synchrotron PXRD	6.5 GPa	Amorphization: 5.01-6.5 GPa; Pore closure: 0.075 GPa	94
MOF-5	*ab initio*, Bader charge analysis	4 GPa	Amorphization: 3.2 GPa	92

Table 1.2 Continued

Materials	Characterization Methods[a]	Pressure range[b]	Structural changes at HP	Ref
ZAG-4, ZAG-6	SC-XRD, Quantum chemical calculations	7.32, 10 GPa	NLC: 2.81 and 3 GPa	64
$Ag_3[Co(CN)]_6$	High-pressure NPD	7.65 GPa	Phase transition: 0.19 GPa Linear expansion: up to 7.65 GPa	81
$Zn[Au(CN)_2]_2$	SC-XRD, Raman	14.2 GPa	NLC in pressure range of 0-2.2 GPa	80
ZIF-8	Synchrotron PXRD	1.2 GPa	**Activated framework:** Amorphization started at 0.34 GPa **Guest loaded:** gate-opening at various pressures (discuss later)	74
UiO-66	IR, EXAFS, XANES	1.9 GPa	Zr-O(COO) bond breakage at 0.8 GPa	70
CdSDB, PbSDB	Synchrotron PXRD, IR and Raman	10, 13 GPa	Amorphization: 3.44 GPa (CdSDB) 2.97 GPa (PbSDB); reversible up to 13 GPa	116
MIL-68(In)	GCMC[d], IR and Raman	9.3 GPa	Irreversible for the activated framework; reversible for DMF loaded framework	115
α-$Mg_3(HCOO)_6$	IR and Raman	12.55 GPa	**Activated framework**: phase transition at above 2 GPa **DMF/benzene loaded:** no structural transition	69
NiAsp-I[e] ($[Ni(L–Asp)(H_2O)_2]\cdot H_2O$-I)	*in situ* PXRD	6.07 GPa	Phase transition between 0.58 GPa and 1.26 GPa	72

Table 1.2 Continued

Materials	Characterization Methods[a]	Pressure range[b]	Structural changes at HP	Ref
$Co_2Bdc_2Dabco \cdot 4DMF \cdot H_2O$	Synchrotron SCXRD, Synchrotron PXRD	3.5 GPa	Single crystals change color from blue to purple at 0.7 GPa	96
EtAMn $(CH_3CH_2NH_3^+, EtA^+)$	IR and Raman	7.1 GPa	Two phase transitions at 3.7-4.0 GPa, and 5.6-6.0 GPa	97
MHyMn $([CH_3NH_2NH_2][Mn(HCOO)_3])$	SC XRD, pyroelectric measurements, Raman and IR	8.2 GPa	Phase transition between 4.8 and 5.5 GPa	98
Lithium L-tartrate	Synchrotron PXRD	5.5 GPa	NLC at around 2.0 GPa	99
ImMg $([HIm][Mg(HCOO)_3]$, $HIm^+ =$ imidazolium cation)	Single Crystal XRD, pyroelectric measurements, Raman and IR	11.4 GPa	Two phase transitions at about 3 and 7 GPa, structural is well preserved up to 11.4 GPa	98

[a] All studies were carried out at room temperature unless stated otherwise.

[b] The pressure ranges from ambient pressure to the given value.

[c] electron paramagnetic resonance

[d] Grand canonical Monte Carlo

Table 1.2 summarized the recent researches on the structural behaviors of MOFs at high pressures. Overall, the above three pressure effects of MOFs discussed in *1.2.3.1-1.2.3.3* conclude the three outcomes that MOFs could have in response to compression: (1) When applying high external pressure to flexible or soft porous frameworks, the local structure of the frameworks are likely to maintain, accompanied by the decrease of the internal free volume and densification of the material, for instance, ZIF-4 and ZIF-8;[67, 74, 83] (2) in less compressible frameworks, pressure may induce more substantial structural changes that give rise to phase transformations, as in MIL-53;[22, 68, 84, 100] (3) in more rigid frameworks, application of external pressure may cause bond breakage at the rigid site in the structure,[66, 70] as in UiO-66.[70] The pressure responses of MOFs that fall into the first two categories may or may not be reversible upon releasing the pressure, however, the bond breakage in the third case is generally expected to be irreversible.

1.2.3.4 High pressure guest storage

In the high pressure field, the guest adsorption and storage under high pressure is one of the research areas that has drawn much attention in the past decade.[12, 73, 82, 106, 108, 113-117, 119, 121, 123, 130-131] In these studies, MOFs or porous molecular frameworks are usually loaded with small solvent molecules, such as DMF,[123] methanol,[113] ethanol,[111, 113] H_2O,[113] allowing the diffusion of these guest molecules into the pores of the frameworks. The correlations between the flexibility of the frameworks and the adsorption of guests within their pores have been investigated and observed through various characterization methods including powder[116] and single crystal X-ray diffraction,[106, 111, 114, 121, 123] vibrational spectroscopy,[115-117] BET,[66, 70] GCMC,[94, 121] and other calculation and simulation techniques.[92, 119] In many cases, the high-pressure guest insertion goes hand in hand with phase transitions of the framework, where the beginning or the completion of the guest insertion often triggers substantial structural changes and potentially forms a new crystalline phase.[108, 111-114, 123] As illustrated in Table 1.3, there are a plenty of guest-responsive MOFs reported so far, including a few very fascinating phenomena: gating effects in layered or interdigitated frameworks[50, 73, 94, 111]; breathing effects in wine-rack topology MOFs such as the MIL-53[68] and ZAG families[64]; continuous unit cell expansion upon adsorbing solvent molecules in Co-BTCA[123] and MIL-88[132], so forth.

The most representative framework is ZIF-8, which incorporates most of the major high-pressure effects and shows surprising potential in industrial applications as a physical adsorbent for CO_2. As we mentioned in the previous section, the initial high-pressure study on ZIF-8 showed that without guest molecules, the framework undergoes an irreversible amorphization upon a minor compression to 0.34 GPa.[67, 74] Later on, Hu *et al.* confirmed that the chemical connectivity of the framework remains intact after this amorphization,[67] although the pore volume and surface area have been compromised.[66] Continuous study demonstrated that pressure can force the hydrostatic pressure medium to enter the cage of ZIF-8, resulting in an increasing volume of both the cage and the unit cell. More guest molecules could be inserted into the cage upon further compression until the single-crystal-to-single-crystal phase transition is achieved at 1.47 GPa.[111] In the high-pressure phase of ZIF-8, the framework exhibits larger free pore volume and BET surface area compared to that of the ambient pressure phase.[111] Later that year, this group of researchers unveiled the mechanism behind such improvement of the accessible pore volume, as shown in Figure 1.7a,[111] the formation of this high-pressure phase is driven by the rotation of imidazole rings on the 6-member ring (6MR) and 4-member ring (4MR) apertures on the framework, which frees up extra space in the cages.[111] Such phenomenon is also known as gate opening effect, and has been further confirmed by many studies using various methods, including *in situ* inelastic neutron scattering (INS),[79] single crystal X-ray diffraction (SCXRD),[82, 111, 121] grand canonical Monte Carlo simulations (GCMC),[121] as well as computational modelling.[79, 82, 119] Such gating effect is further proved to be attainable using other mediums at various pressures, depending on the size of the guest molecules,[113] as illustrated in Figure 1.7b. Till now, ZIF-8 has been examined on a wide range of small guest molecules, mostly gases (i.e. N_2, CO_2, CH_4, H_2O), to investigate its performance for gas storage and separation under a variety of conditions. For example, Hu *et al.* have demonstrated that fluid state CO_2 can be inserted into the cages of ZIF-8 at the pressure as low as 0.47 GPa, enhanced CO_2-framework interactions and therefore better adsorption properties are achieved upon elevating the pressure. Similar gating effects that involve the reorientation and rotation of the ligands also widely exist in other MOFs, such as ZnAtzOx(H_2O), ZIF-65,[94, 121] ZIF-90,[121] Co(BDP)·2DEF,[133] [Cu(dhbc)$_2$(4,4′-bipy)][134] and so on. These effects

can be stimulated by various factors, whereas the most commonly observed ones are temperature and pressure.
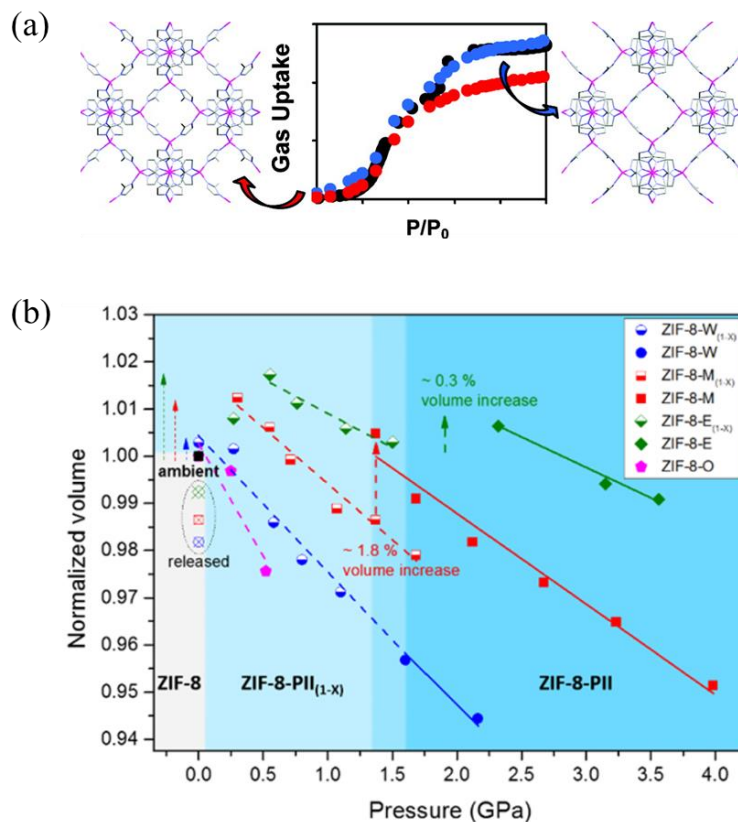
Figure 1.7 (a) Pressure-induced gate opening effect in ZIF-8, leading to increased N_2 uptake. (b) Pressure-dependent changes of the normalized unit cell volume of ZIF-8 in water (W), methanol (M), ethanol (E), and silicone oil PTM (O), highlighting the volume increase at 0.6, 1.4, and 2.3 GPa in water, methanol and ethanol, respectively.[82, 113]

All these studies above have shown a promising future of utilizing high pressure as an efficient approach to modify the pore volume, size, shape, increase the accessible surface area of MOFs, therefore better adsorption properties for the target guest molecules, such as CH_4, CO_2, C_2H_4, H_2O, O_2, etc. It is hoped that these pressure-tuned structures could bring new insight into developing new frameworks in the future, which could potentially be beneficial in the field of the pre- and post-combustion CO_2 captures.[34, 38, 41]

Table 1.3 Summary of selected high-pressure studies on guest-loaded metal-organic frameworks

Materials	Guest molecules	Pressure range (GPa)[a]	Characterization Methods[b]	Pressure effects at HP	Ref
Co-BTCA	DMF	3.6	HP SC-XRD, PXRD, HP PXRD	Pressure-induced nonoxidative nucleophilic addition at 2.2 GPa	123
	MeOH	2.2		Pressure-induced nonoxidative nucleophilic addition at 0.4 GPa	123
MIL-47(V)	H_2O	3	Synchrotron PXRD	Reversible replacement of the TPA by H_2O at 1 GPa	114
	MeOH	3		Irreversible replacement of the TPA by MeOH at 0.3 GPa	114
Sc_2BDC_3	MeOH	2.3	HP SC-XRD, GCMC	Total no. of MeOH molecules per unit cell increased to a maximum of 42 at 1.6 GPa	112
	Hydrocarbon molecules	0.8	Gas adsorption isotherms, HP SC-XRD, DFT	'Oversized' C5-C8 alkane molecules can be squeezed into small-pore Sc_2BDC_3 at 0.8 GPa,	108
Cu-BTC	MeOH, EtOH and water mixture (MEW)	5	Synchrotron HP SC-XRD	Unit cell volume and Cu-O bond contract at 0-3.9 GPa; high pressure squeezes the solvent out at 0.39-5.0 GPa	109
[NH4][Fe(HCOO)3] (**AFeF**)	Ne	10	HP NPD[c], Synchrotron HP SC-XRD	Closed pore of **AFeF** becomes accessible for neon at 1.48 GPa; Ne*x***AFeF** maintains structural stability up to 6.8 GPa	128

Table 1.3 Continued

Materials	Guest molecules	Pressure range (GPa)[a]	Characterization Methods[b]	Pressure effects at HP	Ref
ZIF-8	MeOH and EtOH mixture	1.47	Synchrotron SC-XRD Synchrotron PXRD	Gate opening effect observed at 1.47 GPa	111
	MeOH	4.0		Gate opening effect 1.4 GPa	113
	EtOH	3.6	Synchrotron PXRD Synchrotron PXRD	Intermediate phase at 0.3 GPa; 1st HP phase at 0.6-1.5 GPa; 2nd HP phase at 2.3-3.6 GPa	113
	H_2O	2.2		Volume contraction up to 2.2 GPa	113
	CH_4	1.4	HP SC-XRD	Gate opening effect at 0.7 GPa	119
	N_2	3.25	HP SC-XRD	Gate opening effect at 1.33 GPa	119
	CO_2	2.65	HP IR	Pressure-enhanced CO_2 storage	117
MIL-68(In)	CO_2	10	GCMC, HP-IR, Raman	Hexagonal pores adsorb CO_2 at 0.35 GPa; triangular pores adsorb CO_2 at 1.5 GPa	115
CdSDB	CO_2	4.66	Synchrotron PXRD, HP IR and Raman	Pressure-enhanced CO_2 storage	116
PbSDB	CO_2	4.28		New CO_2 site: 0.29 GPa	116

[a] The pressure ranges from ambient pressure to the given value.

[b] All studies were done at room temperature unless stated otherwise.

[c] Neutron powder diffraction

1.3 Outline and motivations

1.3.1 The objectives of this thesis

Using solid porous materials for CO_2 captures features many advantages over the currently used aqueous amine alternatives, including energy consumption and equipment damage. As a class of porous materials with tunable structures and functionalities, MOFs are well-suited as potential CO_2 absorbents. Moreover, the application of high pressure on MOFs can induce structural modifications on MOFs, and therefore facilitate the CO_2-framework interactions. Hence, it is beneficial to investigate the properties of different MOF materials and their interactions with CO_2 as well as other gases under high external pressure.

This thesis will focus on using PXRD and vibrational spectroscopy to examine the high-pressure responses and gas adsorption proprieties of previously reported frameworks. It has brought to our attention that the V-shaped SDB linker in SDB-based MOFs provides a "π-pocket", which interestingly interacts with the adsorbed CO_2 molecules. In *Chapter 3*, our objective is to comparatively study the structural responses to external compression, and unveil the possible the guest-host interactions between CO_2 and the different PbSDB and CdSDB frameworks.

SIFSIX-3-Zn, a reported ultra-microporous framework, is known to have unusually high adsorption selectivity for CO_2 over gases such as H_2, N_2 and CH_4, although the lack of open metal site. In *Chapter 4,* our goal is to understand the CO_2 adsorption mechanism in SIFSIX-3-Zn at high pressure, and whether pressure would play an important role in enhancing the CO_2-framework interactions.

It has been reported that the fluid CO_2 undergoes a phase change to solid at around 0.6 GPa and room temperature,[135] which severely shortens our scope in exploring the CO_2 adsorption in MOFs under higher pressures, as solid CO_2 is immobile, and it requires CO_2 to be in a fluid state for effective diffusion under pressure. Therefore, in *Chapter 5*, we aim at investigating whether more CO_2 molecules could be inserted into the cages of ZIF-8 and UiO-66 by simultaneously applying both high pressure and temperature. The hypothesis is

that high pressure could facilitate further CO_2 insertion once the solid CO_2 is turned into fluid by high temperature.

The poor stability of most MOFs in the presence of water has always been a major restriction on their applications in post-combustion CO_2 capture, as the gas sources are constantly saturated with water vapor (i.e. 5-7% by volume in flue gas).[136] As an ultra-microporous framework, ZnAtzOx[50] not only exhibits strong CO_2 adsorption sites, but also shows outstanding water durability. In *Chapter 6*, we are interested in examining the CO_2 and water co-adsorption in ZnAtzOx, aiming at understanding how CO_2 and water interact with the framework; to spot the potential guest-guest interactions, and ultimately disclose the impact that water has on CO_2 adsorption in ZnAtzOx under high pressures.

It is hoped that our work could provide guidance to understand the structural properties of MOFs and how they relate to the better CO_2 adsorption performance at high pressures. This information would also bring new insight into the design and development of desirable frameworks or porous materials for CO_2 capture.

1.3.2 The selections of MOFs

Previous studies have discovered many MOFs that possess excellent properties for CO_2 adsorption under near ambient conditions. Among all these promising candidates, we selected the most representative MOFs to the best of our knowledge, taking both material properties and experiential difficulties into account. The following are the principles that we consider when choosing MOFs for this thesis.

Firstly, all objects should have a reasonable CO_2 uptake under near ambient conditions. The prerequisites for MOFs to adsorb CO_2 mainly rely on their structure properties (i.e. channel sizes) and ligand functionalities (i.e. -NH_2, carboxylate, phenyl group, etc.).[41] We are expecting high pressure to work as a facilitator in terms of improving CO_2 adsorption performance in MOFs, however, it is unlikely to tune a MOF that initially does not adsorb CO_2 at all, to one of the promising candidates for CO_2 storage using high pressure.

Secondly, the objects require high CO_2/N_2 selectivity. In all projects of this thesis, the CO_2 loading or sample preparation was operated under N_2 abundant environments (i.e.

cryogenic loading, N_2 filled glovebox). If N_2 could rapidly replace the adsorbed CO_2 molecules in the pores, then it would create major difficulties in performing the experiments. For example, as the MOF with the lowest CO_2/N_2 selectivity among our projects,[137-142] UiO-66 features the selectivity of 16/1 in the ternary mixture.[142]

Furthermore, the objects should not be extremely sensitive to water. In *Chapter 3* and *Chapter 5*, the cryogenic loading method was used to condense CO_2 to the sample chamber of DAC, in which the exposure of the MOFs to the open air is inevitable. Therefore, it is important for the object MOFs to remain physically and chemically stable under the humidity level of the atmosphere, in order to be examined under our experimental conditions. Besides, from the industrial application point of view, water vapor widely exists with the content of 5-7% by volume.[136] Since the complete removal of water from the gas sources is not practical (i.e. pre- and post-combustion), it is critical for MOFs have relatively good water durability. In principle, we would avoid choosing MOFs such as MOF-74,[143] Cu-BTC,[144] MOF-5,[145] and MIL-53,[146] which instantly adsorb water molecules from the air and cause major structural changes.

Lastly, it is of our interest to investigate a wide variety of MOFs that possess completely different structures and topologies, and not just limited by a certain type of framework. From MOF with SOD cages[147] to MOF features 1D channels,[139] we are aiming to see how high-pressure would affect these frameworks similarly and differently, in regard to their structural and guest adsorptions properties.

1.4 References

1.   Yaghi, O. M.; Li, H., Hydrothermal Synthesis of a Metal-Organic Framework Containing Large Rectangular Channels. *J Am Chem Soc* **1995,** *117* (41), 10401-10402.

2.   Furukawa, H.; Cordova, K. E.; O'Keeffe, M.; Yaghi, O. M., The chemistry and applications of metal-organic frameworks. *Science* **2013,** *341* (6149), 1230444.

3.   Zhou, H. C.; Long, J. R.; Yaghi, O. M., Introduction to metal-organic frameworks. *Chem Rev* **2012,** *112* (2), 673-4.

4.   DeCoste, J. B.; Peterson, G. W., Metal-organic frameworks for air purification of toxic chemicals. *Chem Rev* **2014,** *114* (11), 5695-727.

5.   Sumida, K.; Rogow, D. L.; Mason, J. A.; McDonald, T. M.; Bloch, E. D.; Herm, Z. R.; Bae, T. H.; Long, J. R., Carbon dioxide capture in metal-organic frameworks. *Chem Rev* **2012,** *112* (2), 724-81.

6.   Bae, Y. S.; Snurr, R. Q., Development and evaluation of porous materials for carbon dioxide separation and capture. *Angew Chem Int Ed Engl* **2011,** *50* (49), 11586-96.

7.   Meek, S. T.; Greathouse, J. A.; Allendorf, M. D., Metal-organic frameworks: a rapidly growing class of versatile nanoporous materials. *Adv Mater* **2011,** *23* (2), 249-67.

8.   Eddaoudi, M.; Kim, J.; Rosi, N.; Vodak, D.; Wachter, J.; O'Keeffe, M.; Yaghi, O. M., Systematic design of pore size and functionality in isoreticular MOFs and their application in methane storage. *Science* **2002,** *295* (5554), 469-472.

9.   Yaghi, O. M.; O'Keeffe, M.; Ockwig, N. W.; Chae, H. K.; Eddaoudi, M.; Kim, J., Reticular synthesis and the design of new materials. *Nature* **2003,** *423* (6941), 705-714.

10.   Chen, Z.; Hanna, S. L.; Redfern, L. R.; Alezi, D.; Islamoglu, T.; Farha, O. K., Reticular chemistry in the rational synthesis of functional zirconium cluster-based MOFs. *Coord Chem* **2019,** *386*, 32-49.

11.   Lu, J.; Mondal, A.; Moulton, B.; Zaworotko, M. J., Polygons and Faceted Polyhedra and Nanoporous Networks. *Angew Chem* **2001,** *40* (11), 2113-2116.

12.   Xie, L.; Liu, S.; Gao, C.; Cao, R.; Cao, J.; Sun, C.; Su, Z., Mixed-valence iron(II, III) trimesates with open frameworks modulated by solvents. *Inorg Chem* **2007,** *46* (19), 7782-8.

13.   Kramer, M.; Schwarz, U.; Kaskel, S., Synthesis and properties of the metal-organic framework $Mo_3(BTC)_2$ (TUDMOF-1). *J Mater Chem* **2006,** *16* (23), 2245.

14.   Murray, L. J.; Dinca, M.; Yano, J.; Chavan, S.; Bordiga, S.; Brown, C. M.; Long, J. R., Highly-selective and reversible O_2 binding in Cr_3(1,3,5-benzenetricarboxylate)$_2$. *J Am Chem Soc* **2010,** *132* (23), 7856-7.

15.   Kozachuk, O.; Yusenko, K.; Noei, H.; Wang, Y.; Walleck, S.; Glaser, T.; Fischer, R. A., Solvothermal growth of a ruthenium metal-organic framework featuring HKUST-1 structure type as thin films on oxide surfaces. *Chem Commun (Camb)* **2011,** *47* (30), 8509-11.

16.   Rosi, N. L.; Kim, J.; Eddaoudi, M.; Chen, B.; O'Keeffe, M.; Yaghi, O. M., Rod packings and metal-organic frameworks constructed from rod-shaped secondary building units. *J Am Chem Soc* **2005,** *127* (5), 1504-18.

17.   Zhou, W.; Wu, H.; Yildirim, T., Enhanced H_2 adsorption in isostructural metal-organic frameworks with open metal sites: strong dependence of the binding strength on metal ions. *J Am Chem Soc* **2008,** *130* (46), 15268-9.

18.   Farha, O. K.; Eryazici, I.; Jeong, N. C.; Hauser, B. G.; Wilmer, C. E.; Sarjeant, A. A.; Snurr, R. Q.; Nguyen, S. T.; Yazaydin, A. O.; Hupp, J. T., Metal-organic framework materials with ultrahigh surface areas: is the sky the limit? *J Am Chem Soc* **2012,** *134* (36), 15016-21.

19.   Honicke, I. M.; Senkovska, I.; Bon, V.; Baburin, I. A.; Bonisch, N.; Raschke, S.; Evans, J. D.; Kaskel, S., Balancing Mechanical Stability and Ultrahigh Porosity in Crystalline Framework Materials. *Angew Chem Int Ed Engl* **2018,** *57* (42), 13780-13783.

20.   Moghadam, P. Z.; Li, A.; Wiggin, S. B.; Tao, A.; Maloney, A. G. P.; Wood, P. A.; Ward, S. C.; Fairen-Jimenez, D., Development of a Cambridge Structural Database Subset: A Collection of Metal-Organic Frameworks for Past, Present, and Future. *Chem Mater* **2017,** *29* (7), 2618-2625.

21.   Chui, S. S. Y.; Lo, S. M. F.; Charmant, J. P. H.; Orpen, A. G.; Williams, I. D., A Chemically Functionalizable Nanoporous Material [$Cu_3(TMA)_2(H_2O)_3$]n. *Science* **1999,** *283* (5405), 1148-1150.

22.   Serre, C.; Millange, F.; Thouvenot, C.; Noguès, M.; Marsolier, G.; Louër, D.; Férey, G., Very Large Breathing Effect in the First Nanoporous Chromium(III)-Based Solids: MIL-53 or $Cr^{III}(OH)\cdot\{O_2C-C_6H_4-CO_2\}\cdot\{HO_2C-C_6H_4-CO_2H\}x\cdot H_2Oy$. *J Am Chem Soc* **2002,** *124* (45), 13519-13526.

23.   Morris, W.; Stevens, C. J.; Taylor, R. E.; Dybowski, C.; Yaghi, O. M.; Garcia-Garibay, M. A., NMR and X-ray Study Revealing the Rigidity of Zeolitic Imidazolate Frameworks. *J Phys Chem C* **2012,** *116* (24), 13307-13312.

24.   Stock, N.; Biswas, S., Synthesis of metal-organic frameworks (MOFs): routes to various MOF topologies, morphologies, and composites. *Chem Rev* **2012,** *112* (2), 933-69.

25.   Klinowski, J.; Paz, F. A.; Silva, P.; Rocha, J., Microwave-assisted synthesis of metal-organic frameworks. *Dalton Trans* **2011,** *40* (2), 321-30.

26.   Campagnol, N.; Van Assche, T.; Boudewijns, T.; Denayer, J.; Binnemans, K.; De Vos, D.; Fransaer, J., High pressure, high temperature electrochemical synthesis of metal–organic frameworks: films of MIL-100 (Fe) and HKUST-1 in different morphologies. *J Mater Chem A* **2013,** *1* (19), 5827.

27.   Klimakow, M.; Klobes, P.; Thünemann, A. F.; Rademann, K.; Emmerling, F., Mechanochemical Synthesis of Metal−Organic Frameworks: A Fast and Facile Approach toward Quantitative Yields and High Specific Surface Areas. *Chem Mater* **2010,** *22* (18), 5216-5221.

28.   Li, J.-R.; Ma, Y.; McCarthy, M. C.; Sculley, J.; Yu, J.; Jeong, H.-K.; Balbuena, P. B.; Zhou, H.-C., Carbon dioxide capture-related gas adsorption and separation in metal-organic frameworks. *Coord Chem* **2011,** *255* (15-16), 1791-1823.

29.   Monastersky, R., Global carbon dioxide levels near worrisome milestone. *Nature* **2013,** *497* (7447), 13-14.

30.   IPCC, Carbon Dioxide Capture and Storage: A Special Report of Working Group III of the Intergovernmental Panel on Climate Change. *Cambridge, United Kingdom and New York, NY, USA* **2005**.

31.   IPCC, Climate Change 2014: Mitigation of Climate Change. Contribution of Working Group III to the Fifth Assessment Report of the Intergovernmental Panel on Climate Change. *Cambridge University Press: Cambridge, U.K. and New York* **2014**.

32.   Goeppert, A.; Czaun, M.; Surya Prakash, G. K.; Olah, G. A., Air as the renewable carbon source of the future: an overview of CO_2 capture from the atmosphere. *Energy Environ Sci* **2012,** *5* (7), 7833-7853.

33.   Pires, J. C. M.; Martins, F. G.; Alvim-Ferraz, M. C. M.; Simões, M., Recent developments on carbon capture and storage: An overview. *Chem Eng Res Des* **2011,** *89* (9), 1446-1460.

34.   Sanz-Perez, E. S.; Murdock, C. R.; Didas, S. A.; Jones, C. W., Direct Capture of CO2 from Ambient Air. *Chem Rev* **2016,** *116* (19), 11840-11876.

35.   Rochelle, G. T., Amine scrubbing for CO_2 capture. *Science* **2009,** *325* (5948), 1652-1654.

36.   Shakerian, F.; Kim, K.-H.; Szulejko, J. E.; Park, J.-W., A comparative review between amines and ammonia as sorptive media for post-combustion CO_2 capture. *Appl Energy* **2015,** *148*, 10-22.

37.   Knudsen, J. N.; Jensen, J. N.; Vilhelmsen, P.-J.; Biede, O., Experience with CO_2 capture from coal flue gas in pilot-scale: Testing of different amine solvents. *Energy Procedia* **2009,** *1* (1), 783-790.

38.   Kumar, A.; Madden, D. G.; Lusi, M.; Chen, K. J.; Daniels, E. A.; Curtin, T.; Perry, J. J. t.; Zaworotko, M. J., Direct Air Capture of CO_2 by Physisorbent Materials. *Angew Chem Int Ed Engl* **2015,** *54* (48), 14372-7.

39.   Ben-Mansour, R.; Habib, M. A.; Bamidele, O. E.; Basha, M.; Qasem, N. A. A.; Peedikakkal, A.; Laoui, T.; Ali, M., Carbon capture by physical adsorption: Materials, experimental investigations and numerical modeling and simulations – A review. *Appl Energy* **2016,** *161*, 225-255.

40.   Mason, J. A.; Sumida, K.; Herm, Z. R.; Krishna, R.; Long, J. R., Evaluating metal–organic frameworks for post-combustion carbon dioxide capture via temperature swing adsorption. *Energy Environ Sci* **2011,** *4* (8), 3030.

41.   Ye, S.; Jiang, X.; Ruan, L.-W.; Liu, B.; Wang, Y.-M.; Zhu, J.-F.; Qiu, L.-G., Post-combustion CO_2 capture with the HKUST-1 and MIL-101(Cr) metal–organic frameworks: Adsorption, separation and regeneration investigations. *Micropor Mesopor Mat* **2013,** *179*, 191-197.

42.   Farha, O. K.; Yazaydin, A. O.; Eryazici, I.; Malliakas, C. D.; Hauser, B. G.; Kanatzidis, M. G.; Nguyen, S. T.; Snurr, R. Q.; Hupp, J. T., De novo synthesis of a metal-organic framework material featuring ultrahigh surface area and gas storage capacities. *Nat Chem* **2010,** *2* (11), 944-8.

43.   Yazaydın, A. Ö.; Snurr, R. Q.; Park, T.-H.; Koh, K.; Liu, J.; LeVan, M. D.; Benin, A. I.; Jakubczak, P.; Lanuza, M.; Galloway, D. B.; Low, J. J.; Willis, R. R., Screening of Metal−Organic Frameworks for Carbon Dioxide Capture from Flue Gas Using a Combined Experimental and Modeling Approach. *J Am Chem Soc* **2009,** *131* (51), 18198-18199.

44.   Arstad, B.; Fjellvåg, H.; Kongshaug, K. O.; Swang, O.; Blom, R., Amine functionalised metal organic frameworks (MOFs) as adsorbents for carbon dioxide. *Adsorption* **2008,** *14* (6), 755-762.

45.   Llewellyn, P. L.; Bourrelly, S.; Serre, C.; Filinchuk, Y.; Ferey, G., How hydration drastically improves adsorption selectivity for CO_2 over CH_4 in the flexible chromium terephthalate MIL-53. *Angew Chem Int Ed Engl* **2006,** *45* (46), 7751-4.

46.   Chowdhury, P.; Bikkina, C.; Gumma, S., Gas Adsorption Properties of the Chromium-Based Metal Organic Framework MIL-101. *J Phys Chem C* **2009,** *113* (16), 6616-6621.

47.   Wiersum, A. D.; Soubeyrand-Lenoir, E.; Yang, Q.; Moulin, B.; Guillerm, V.; Yahia, M. B.; Bourrelly, S.; Vimont, A.; Miller, S.; Vagner, C.; Daturi, M.; Clet, G.; Serre, C.;

Maurin, G.; Llewellyn, P. L., An evaluation of UiO-66 for gas-based applications. *Chem Asian J* **2011,** *6* (12), 3270-80.

48.   Shekhah, O.; Belmabkhout, Y.; Chen, Z.; Guillerm, V.; Cairns, A.; Adil, K.; Eddaoudi, M., Made-to-order metal-organic frameworks for trace carbon dioxide removal and air capture. *Nat Commun* **2014,** *5*, 4228.

49.   Aprea, P.; Caputo, D.; Gargiulo, N.; Iucolano, F.; Pepe, F., Modeling Carbon Dioxide Adsorption on Microporous Substrates: Comparison between Cu-BTC Metal−Organic Framework and 13X Zeolitic Molecular Sieve. *J Chem Eng Data* **2010,** *55* (9), 3655-3661.

50.   Banerjee, A.; Nandi, S.; Nasa, P.; Vaidhyanathan, R., Enhancing the carbon capture capacities of a rigid ultra-microporous MOF through gate-opening at low CO_2 pressures assisted by swiveling oxalate pillars. *Chem Commun (Camb)* **2016,** *52* (9), 1851-4.

51.   Walsh, J. P. S.; Freedman, D. E., High-Pressure Synthesis: A New Frontier in the Search for Next-Generation Intermetallic Compounds. *Acc Chem Res* **2018,** *51* (6), 1315-1323.

52.   Lattimer, J.; Prakash, M., Neutron star observations: Prognosis for equation of state constraints. *Phys Rep* **2007,** *442* (1-6), 109-165.

53.   Hemley, R. J., Effects of High Pressure on Molecules. *Annu Rev Phys* **2000,** *51*, 763-800.

54.   Shen, G.; Mao, H. K., High-pressure studies with x-rays using diamond anvil cells. *Rep Prog Phys* **2017,** *80* (1), 016101.

55.   Grochala, W.; Hoffmann, R.; Feng, J.; Ashcroft, N. W., The chemical imagination at work in very tight places. *Angew Chem Int Ed Engl* **2007,** *46* (20), 3620-42.

56.   Hemley, R. J.; Ashcroft, N. W., The Revealing Role of Pressure in the Condensed Matter Sciences. *Physics Today* **1998,** *51* (8), 26-32.

57.　　Schettino, V.; Bini, R., Constraining molecules at the closest approach: chemistry at high pressure. *Chem Soc Rev* **2007,** *36* (6), 869-80.

58.　　Schettino, V.; Bini, R., Molecules under extreme conditions: Chemical reactions at high pressure. *Phys Chem Chem Phys* **2003,** *5* (10), 1951.

59.　　McMillan, P. F., Chemistry at high pressure. *Chem Soc Rev* **2006,** *35* (10), 855-7.

60.　　Zhang, L.; Wang, Y.; Lv, J.; Ma, Y., Materials discovery at high pressures. *Nat Rev Mater* **2017,** *2* (4).

61.　　Kuno, K.; Matsuoka, T.; Nakagawa, T.; Hirao, N.; Ohishi, Y.; Shimizu, K.; Takahama, K.; Ohta, K.; Sakata, M.; Nakamoto, Y.; Kume, T.; Sasaki, S., Heating of Li in hydrogen: possible synthesis of LiHx. *High Pressure Res* **2015,** *35* (1), 16-21.

62.　　Struzhkin, V. V.; Kim, D. Y.; Stavrou, E.; Muramatsu, T.; Mao, H. K.; Pickard, C. J.; Needs, R. J.; Prakapenka, V. B.; Goncharov, A. F., Synthesis of sodium polyhydrides at high pressures. *Nat Commun* **2016,** *7*, 12267.

63.　　Spencer, E. C.; Kiran, M. S.; Li, W.; Ramamurty, U.; Ross, N. L.; Cheetham, A. K., Pressure-induced bond rearrangement and reversible phase transformation in a metal-organic framework. *Angew Chem Int Ed Engl* **2014,** *53* (22), 5583-6.

64.　　Ortiz, A. U.; Boutin, A.; Gagnon, K. J.; Clearfield, A.; Coudert, F. X., Remarkable pressure responses of metal-organic frameworks: proton transfer and linker coiling in zinc alkyl gates. *J Am Chem Soc* **2014,** *136* (32), 11540-5.

65.　　Gagnon, K. J.; Beavers, C. M.; Clearfield, A., MOFs under pressure: the reversible compression of a single crystal. *J Am Chem Soc* **2013,** *135* (4), 1252-5.

66.　　Su, Z.; Miao, Y. R.; Mao, S. M.; Zhang, G. H.; Dillon, S.; Miller, J. T.; Suslick, K. S., Compression-induced deformation of individual metal-organic framework microcrystals. *J Am Chem Soc* **2015,** *137* (5), 1750-3.

67.   Hu, Y.; Kazemian, H.; Rohani, S.; Huang, Y.; Song, Y., In situ high pressure study of ZIF-8 by FTIR spectroscopy. *Chem Commun (Camb)* **2011,** *47* (47), 12694-6.

68.   Serra-Crespo, P.; Dikhtiarenko, A.; Stavitski, E.; Juan-Alcaniz, J.; Kapteijn, F.; Coudert, F. X.; Gascon, J., Experimental Evidence of Negative Linear Compressibility in the MIL-53 Metal-Organic Framework Family. *CrystEngComm* **2015,** *17* (2), 276-280.

69.   Mao, H.; Xu, J.; Hu, Y.; Huang, Y.; Song, Y., The effect of high external pressure on the structure and stability of MOF α-$Mg_3(HCOO)_6$ probed by in situ Raman and FT-IR spectroscopy. *J Mater Chem A* **2015,** *3* (22), 11976-11984.

70.   Su, Z.; Miao, Y. R.; Zhang, G.; Miller, J. T.; Suslick, K. S., Bond breakage under pressure in a metal organic framework. *Chem Sci* **2017,** *8* (12), 8004-8011.

71.   Zeng, Z.; Tan, J. C., AFM Nanoindentation To Quantify Mechanical Properties of Nano- and Micron-Sized Crystals of a Metal-Organic Framework Material. *ACS Appl Mater Interfaces* **2017,** *9* (45), 39839-39854.

72.   Gould, J. A.; Rosseinsky, M. J.; Warren, J. E.; Moggach, S., The effect of pressure on a nickel aspartate framework. *Z Kristallogr Cryst Mater* **2014,** *229* (2), 123-128.

73.   Craig, G. A.; Larpent, P.; Kusaka, S.; Matsuda, R.; Kitagawa, S.; Furukawa, S., Switchable gate-opening effect in metal-organic polyhedra assemblies through solution processing. *Chem Sci* **2018,** *9* (31), 6463-6469.

74.   Chapman, K. W.; Halder, G. J.; Chupas, P. J., Pressure-induced amorphization and porosity modification in a metal-organic framework. *J Am Chem Soc* **2009,** *131* (48), 17546-7.

75.   Serra-Crespo, P.; Stavitski, E.; Kapteijn, F.; Gascon, J., High compressibility of a flexible metal–organic framework. *RSC Adv* **2012,** *2* (12), 5051.

76.   Zhou, M.; Wang, K.; Men, Z.; Sun, C.; Li, Z.; Liu, B.; Zou, G.; Zou, B., Pressure-induced isostructural phase transition of a metal–organic framework $Co_2(4,4'$-$bpy)_3(NO_3)_4 \cdot xH_2O$. *CrystEngComm* **2014,** *16* (20), 4084-4087.

77.   Ortiz, A. U.; Boutin, A.; Coudert, F. X., Prediction of flexibility of metal-organic frameworks CAU-13 and NOTT-300 by first principles molecular simulations. *Chem Commun (Camb)* **2014,** *50* (44), 5867-70.

78.   Yot, P. G.; Ma, Q.; Haines, J.; Yang, Q.; Ghoufi, A.; Devic, T.; Serre, C.; Dmitriev, V.; Férey, G.; Zhong, C.; Maurin, G., Large breathing of the MOF MIL-47(V^{IV}) under mechanical pressure: a joint experimental–modelling exploration. *Chem Sci* **2012,** *3* (4), 1100.

79.   Casco, M. E.; Cheng, Y. Q.; Daemen, L. L.; Fairen-Jimenez, D.; Ramos-Fernandez, E. V.; Ramirez-Cuesta, A. J.; Silvestre-Albero, J., Gate-opening effect in ZIF-8: the first experimental proof using inelastic neutron scattering. *Chem Commun (Camb)* **2016,** *52* (18), 3639-42.

80.   Cairns, A. B.; Catafesta, J.; Levelut, C.; Rouquette, J.; van der Lee, A.; Peters, L.; Thompson, A. L.; Dmitriev, V.; Haines, J.; Goodwin, A. L., Giant negative linear compressibility in zinc dicyanoaurate. *Nat Mater* **2013,** *12* (3), 212-6.

81.   Goodwin, A. L.; Keen, D. A.; Tucker, M. G., Large negative linear compressibility of Ag3[Co(CN)6]. *Proc Natl Acad Sci U S A* **2008,** *105* (48), 18708-18713.

82.   Fairen-Jimenez, D.; Moggach, S. A.; Wharmby, M. T.; Wright, P. A.; Parsons, S.; Duren, T., Opening the gate: framework flexibility in ZIF-8 explored by experiments and simulations. *J Am Chem Soc* **2011,** *133* (23), 8900-2.

83.   Bennett, T. D.; Simoncic, P.; Moggach, S. A.; Gozzo, F.; Macchi, P.; Keen, D. A.; Tan, J. C.; Cheetham, A. K., Reversible pressure-induced amorphization of a zeolitic imidazolate framework (ZIF-4). *Chem Commun (Camb)* **2011,** *47* (28), 7983-5.

84.   Neimark, A. V.; Coudert, F. X.; Triguero, C.; Boutin, A.; Fuchs, A. H.; Beurroies, I.; Denoyel, R., Structural transitions in MIL-53 (Cr): view from outside and inside. *Langmuir* **2011,** *27* (8), 4734-41.

85.   Colmenero, F.; Cobos, J.; Timon, V., Negative linear compressibility in uranyl squarate monohydrate. *J Phys Condens Matter* **2019,** *31* (17), 175701.

86.	Mączka, M.; Ptak, M.; Gągor, A.; Sieradzki, A.; Peksa, P.; Usevicius, G.; Simenas, M.; Leite, F. F.; Paraguassu, W., Temperature- and pressure-dependent studies of a highly flexible and compressible perovskite-like cadmium dicyanamide framework templated with protonated tetrapropylamine. *J Mater Chem C* **2019,** *7* (8), 2408-2420.

87.	Ptak, M.; Zarychta, B.; Stefanska, D.; Ciupa, A.; Paraguassu, W., Novel bimetallic MOF phosphors with an imidazolium cation: structure, phonons, high- pressure phase transitions and optical response. *Dalton Trans* **2018,** *48* (1), 242-252.

88.	Adhikari, P.; Li, N.; Rulis, P.; Ching, W. Y., Deformation behavior of an amorphous zeolitic imidazolate framework - from a supersoft material to a complex organometallic alloy. *Phys Chem Chem Phys* **2018,** *20* (46), 29001-29011.

89.	Chitnis, A. V.; Bhatt, H.; Maczka, M.; Deo, M. N.; Garg, N., Remarkable resilience of the formate cage in a multiferroic metal organic framework material: dimethyl ammonium manganese formate (DMAMnF). *Dalton Trans* **2018,** *47* (37), 12993-13005.

90.	Ptak, M.; Stefanska, D.; Gagor, A.; Svane, K. L.; Walsh, A.; Paraguassu, W., Heterometallic perovskite-type metal-organic framework with an ammonium cation: structure, phonons, and optical response of $[NH_4]Na_{0.5}Cr_xAl_{0.5-x}(HCOO)_3$ (x = 0, 0.025 and 0.5). *Phys Chem Chem Phys* **2018,** *20* (34), 22284-22295.

91.	Navarro-Sanchez, J.; Mullor-Ruiz, I.; Popescu, C.; Santamaria-Perez, D.; Segura, A.; Errandonea, D.; Gonzalez-Platas, J.; Marti-Gastaldo, C., Peptide metal-organic frameworks under pressure: flexible linkers for cooperative compression. *Dalton Trans* **2018,** *47* (31), 10654-10659.

92.	Erkartal, M.; Durandurdu, M., Pressure-Induced Amorphization of MOF-5: A First Principles Study. *ChemistrySelect* **2018,** *3* (28), 8056-8063.

93.	Collings, I. E.; Bykov, M.; Bykova, E.; Hanfland, M.; van Smaalen, S.; Dubrovinsky, L.; Dubrovinskaia, N., Disorder–order transitions in the perovskite metal–organic frameworks $[(CH_3)_2NH_2][M(HCOO)_3]$ at high pressure. *CrystEngComm* **2018,** *20* (25), 3512-3521.

94.   Henke, S.; Wharmby, M. T.; Kieslich, G.; Hante, I.; Schneemann, A.; Wu, Y.; Daisenberger, D.; Cheetham, A. K., Pore closure in zeolitic imidazolate frameworks under mechanical pressure. *Chem Sci* **2018,** *9* (6), 1654-1660.

95.   Mączka, M.; da Silva, T. A.; Paraguassu, W., Raman-scattering studies of pressure-induced phase transitions in perovskite-like acetamidninium manganese formate. *J Raman Spectrosc* **2018,** *49* (2), 312-316.

96.   Andrzejewski, M.; Casati, N.; Katrusiak, A., Reversible pressure pre-amorphization of a piezochromic metal-organic framework. *Dalton Trans* **2017,** *46* (43), 14795-14803.

97.   Ciupa, A.; Ptak, M.; Mączka, M.; da Silva Filho, J. G.; Freire, P. T. C., Vibrational investigation of pressure- and temperature-induced phase transitions in metal formates templated by ethylammonium ions. *J Raman Spectrosc* **2017,** *48* (7), 972-982.

98.   Mączka, M.; Gągor, A.; Ptak, M.; Paraguassu, W.; da Silva, T. A.; Sieradzki, A.; Pikul, A., Phase Transitions and Coexistence of Magnetic and Electric Orders in the Methylhydrazinium Metal Formate Frameworks. *Chem Mater* **2017,** *29* (5), 2264-2275.

99.   Yeung, H. H.; Kilmurray, R.; Hobday, C. L.; McKellar, S. C.; Cheetham, A. K.; Allan, D. R.; Moggach, S. A., Hidden negative linear compressibility in lithium l-tartrate. *Phys Chem Chem Phys* **2017,** *19* (5), 3544-3549.

100.   Yot, P. G.; Yang, K.; Guillerm, V.; Ragon, F.; Dmitriev, V.; Parisiades, P.; Elkaïm, E.; Devic, T.; Horcajada, P.; Serre, C.; Stock, N.; Mowat, J. P. S.; Wright, P. A.; Férey, G.; Maurin, G., Impact of the Metal Centre and Functionalization on the Mechanical Behaviour of MIL-53 Metal-Organic Frameworks. *Eur J Inorg Chem* **2016,** *2016* (27), 4424-4429.

101.   Sciortino, N. F.; Ragon, F.; Zenere, K. A.; Southon, P. D.; Halder, G. J.; Chapman, K. W.; Pineiro-Lopez, L.; Real, J. A.; Kepert, C. J.; Neville, S. M., Exploiting Pressure To Induce a "Guest-Blocked" Spin Transition in a Framework Material. *Inorg Chem* **2016,** *55* (20), 10490-10498.

102.   Magos-Palasyuk, E.; Fijalkowski, K. J.; Palasyuk, T., Chemically driven negative linear compressibility in sodium amidoborane, Na(NH$_2$BH$_3$). *Sci Rep* **2016,** *6*, 28745.

103.   Maczka, M.; Marinho Costa, N. L.; Gagor, A.; Paraguassu, W.; Sieradzki, A.; Hanuza, J., Structural, thermal, dielectric and phonon properties of perovskite-like imidazolium magnesium formate. *Phys Chem Chem Phys* **2016,** *18* (20), 13993-4000.

104.   Yot, P. G.; Yang, K.; Ragon, F.; Dmitriev, V.; Devic, T.; Horcajada, P.; Serre, C.; Maurin, G., Exploration of the mechanical behavior of metal organic frameworks UiO-66(Zr) and MIL-125(Ti) and their NH$_2$ functionalized versions. *Dalton Trans* **2016,** *45* (10), 4283-8.

105.   Monteagudo-Olivan, R.; Paseta, L.; Potier, G.; López-Ram-de-Viu, P.; Coronas, J., Solvent-Free Encapsulation at High Pressure with Carboxylate-Based MOFs. *Eur J Inorg Chem* **2019,** *2019* (1), 29-36.

106.   Radhakrishnan, D.; Narayana, C., Guest dependent Brillouin and Raman scattering studies of zeolitic imidazolate framework-8 (ZIF-8) under external pressure. *J Chem Phys* **2016,** *144* (13), 134704.

107.   Lobanov, S. S.; Daly, J. A.; Goncharov, A. F.; Chan, X.; Ghose, S. K.; Zhong, H.; Ehm, L.; Kim, T.; Parise, J. B., Iodine in Metal-Organic Frameworks at High Pressure. *J Phys Chem A* **2018,** *122* (29), 6109-6117.

108.   McKellar, S. C.; Sotelo, J.; Greenaway, A.; Mowat, J. P. S.; Kvam, O.; Morrison, C. A.; Wright, P. A.; Moggach, S. A., Pore Shape Modification of a Microporous Metal-Organic Framework Using High Pressure Accessing a New Phase with Oversized Guest Molecules. *Chem Mater* **2016,** *28* (2), 466-473.

109.   Graham, A. J.; Tan, J. C.; Allan, D. R.; Moggach, S. A., The effect of pressure on Cu-btc: framework compression vs. guest inclusion. *Chem Commun (Camb)* **2012,** *48* (10), 1535-7.

110.   Graham, A. J.; Allan, D. R.; Muszkiewicz, A.; Morrison, C. A.; Moggach, S. A., The Effect of High Pressure on MOF-5: Guest-Induced Modification of Pore Size and Content at High Pressure. *Angew Chem Int Ed Engl* **2011,** *50* (47), 11138-11141.

111.   Moggach, S. A.; Bennett, T. D.; Cheetham, A. K., The effect of pressure on ZIF-8: increasing pore size with pressure and the formation of a high-pressure phase at 1.47 GPa. *Angew Chem Int Ed Engl* **2009,** *48* (38), 7087-9.

112.   Graham, A. J.; Banu, A. M.; Duren, T.; Greenaway, A.; McKellar, S. C.; Mowat, J. P.; Ward, K.; Wright, P. A.; Moggach, S. A., Stabilization of scandium terephthalate MOFs against reversible amorphization and structural phase transition by guest uptake at extreme pressure. *J Am Chem Soc* **2014,** *136* (24), 8606-13.

113.   Im, J.; Yim, N.; Kim, J.; Vogt, T.; Lee, Y., High-Pressure Chemistry of a Zeolitic Imidazolate Framework Compound in the Presence of Different Fluids. *J Am Chem Soc* **2016,** *138* (36), 11477-80.

114.   Im, J.; Seoung, D.; Hwang, G. C.; Jun, J. W.; Jhung, S. H.; Kao, C.-C.; Vogt, T.; Lee, Y., Pressure-Dependent Structural and Chemical Changes in a Metal–Organic Framework with One-Dimensional Pore Structure. *Chem Mater* **2016,** *28* (15), 5336-5341.

115.   Hu, Y.; Lin, B.; He, P.; Li, Y.; Huang, Y.; Song, Y., Probing the Structural Stability of and Enhanced CO_2 Storage in MOF MIL-68(In) under High Pressures by FTIR Spectroscopy. *Chem Eur J* **2015,** *21* (51), 18739-48.

116.   Jiang, S.; Hu, Y.; Chen, S.; Huang, Y.; Song, Y., Elucidation of the Structural Origins and Contrasting Guest-Host Interactions in CO_2-Loaded CdSDB and PbSDB Metal-Organic Frameworks at High Pressures. *Chem Eur J* **2018,** *24* (72), 19280-19288.

117.   Hu, Y.; Liu, Z.; Xu, J.; Huang, Y.; Song, Y., Evidence of pressure enhanced CO_2 storage in ZIF-8 probed by FTIR spectroscopy. *J Am Chem Soc* **2013,** *135* (25), 9287-90.

118.   Lee, Y.; Liu, D.; Seoung, D.; Liu, Z.; Kao, C. C.; Vogt, T., Pressure- and heat-induced insertion of CO_2 into an auxetic small-pore zeolite. *J Am Chem Soc* **2011,** *133* (6), 1674-7.

119. Hobday, C. L.; Woodall, C. H.; Lennox, M. J.; Frost, M.; Kamenev, K.; Duren, T.; Morrison, C. A.; Moggach, S. A., Understanding the adsorption process in ZIF-8 using high pressure crystallography and computational modelling. *Nat Commun* **2018,** *9* (1), 1429.

120. Miao, Y. R.; Su, Z.; Suslick, K. S., Energy Storage during Compression of Metal-Organic Frameworks. *J Am Chem Soc* **2017,** *139* (13), 4667-4670.

121. Hobday, C. L.; Bennett, T. D.; Fairen-Jimenez, D.; Graham, A. J.; Morrison, C. A.; Allan, D. R.; Duren, T.; Moggach, S. A., Tuning the Swing Effect by Chemical Functionalization of Zeolitic Imidazolate Frameworks. *J Am Chem Soc* **2018,** *140* (1), 382-387.

122. Spencer, E. C.; Angel, R. J.; Ross, N. L.; Hanson, B. E.; Howard, J. A., Pressure-induced cooperative bond rearrangement in a zinc imidazolate framework: a high-pressure single-crystal X-ray diffraction study. *J Am Chem Soc* **2009,** *131* (11), 4022-6.

123. Lanza, A.; Germann, L. S.; Fisch, M.; Casati, N.; Macchi, P., Solid-State Reversible Nucleophilic Addition in a Highly Flexible MOF. *J Am Chem Soc* **2015,** *137* (40), 13072-8.

124. Tan, J. C.; Bennett, T. D.; Cheetham, A. K., Chemical structure, network topology, and porosity effects on the mechanical properties of Zeolitic Imidazolate Frameworks. *Proc Natl Acad Sci U S A* **2010,** *107* (22), 9938-43.

125. Coudert, F.-X., Responsive Metal-Organic Frameworks and Framework Materials: Under Pressure, Taking the Heat, in the Spotlight, with Friends. *Chem Mater* **2015,** *27* (6), 1905-1916.

126. Cairns, A. B.; Goodwin, A. L., Negative linear compressibility. *Phys Chem Chem Phys* **2015,** *17* (32), 20449-65.

127. Collings, I. E.; Manna, R. S.; Tsirlin, A. A.; Bykov, M.; Bykova, E.; Hanfland, M.; Gegenwart, P.; van Smaalen, S.; Dubrovinsky, L.; Dubrovinskaia, N., Pressure dependence

of spin canting in ammonium metal formate antiferromagnets. *Phys Chem Chem Phys* **2018,** *20* (37), 24465-24476.

128.   Collings, I. E.; Bykov, M.; Bykova, E.; Tucker, M. G.; Petitgirard, S.; Hanfland, M.; Glazyrin, K.; van Smaalen, S.; Goodwin, A. L.; Dubrovinsky, L.; Dubrovinskaia, N., Structural distortions in the high-pressure polar phases of ammonium metal formates. *CrystEngComm* **2016,** *18* (46), 8849-8857.

129.   Maczka, M.; Kadlubanski, P.; Freire, P. T.; Macalik, B.; Paraguassu, W.; Hermanowicz, K.; Hanuza, J., Temperature- and pressure-induced phase transitions in the metal formate framework of [ND$_4$][Zn(DCOO)$_3$] and [NH$_4$][Zn(HCOO)$_3$]. *Inorg Chem* **2014,** *53* (18), 9615-24.

130.   Chapman, K. W.; Sava, D. F.; Halder, G. J.; Chupas, P. J.; Nenoff, T. M., Trapping guests within a nanoporous metal-organic framework through pressure-induced amorphization. *J Am Chem Soc* **2011,** *133* (46), 18583-5.

131.   Santoro, M.; Gorelli, F.; Haines, J.; Cambon, O.; Levelut, C.; Garbarino, G., Silicon carbonate phase formed from carbon dioxide and silica under pressure. *Proc Natl Acad Sci U S A* **2011,** *108* (19), 7689-92.

132.   Zhang, J.-P.; Zhou, H.-L.; Zhou, D.-D.; Liao, P.-Q.; Chen, X.-M., Controlling flexibility of metal–organic frameworks. *Natl Sci Rev* **2018,** *5* (6), 907-919.

133.   Choi, H. J.; Dinca, M.; Long, J. R., Broadly hysteretic H$_2$ adsorption in the microporous metal-organic framework Co(1,4-benzenedipyrazolate). *J Am Chem Soc* **2008,** *130* (25), 7848-50.

134.   Li, L.; Krishna, R.; Wang, Y.; Yang, J.; Wang, X.; Li, J., Exploiting the gate opening effect in a flexible MOF for selective adsorption of propyne from C1/C2/C3 hydrocarbons. *J Mater Chem A* **2016,** *4* (3), 751-755.

135.   Hirai, H.; Komatsu, K.; Honda, M.; Kawamura, T.; Yamamoto, Y.; Yagi, T., Phase changes of CO$_2$ hydrate under high pressure and low temperature. *J Chem Phys* **2010,** *133* (12), 124511.

136.   Tan, K.; Nijem, N.; Gao, Y.; Zuluaga, S.; Li, J.; Thonhauser, T.; Chabal, Y. J., Water interactions in metal organic frameworks. *CrystEngComm* **2015,** *17* (2), 247-260.

137.   Plonka, A. M.; Banerjee, D.; Woerner, W. R.; Zhang, Z.; Li, J.; Parise, J. B., Effect of ligand geometry on selective gas-adsorption: the case of a microporous cadmium metal organic framework with a V-shaped linker. *Chem Commun (Camb)* **2013,** *49* (63), 7055-7.

138.   Lin, J.-D.; Wu, S.-T.; Li, Z.-H.; Du, S.-W., A series of novel Pb(ii) or Pb(ii)/M(ii) (M = Ca and Sr) hybrid inorganic–organic frameworks based on polycarboxylic acids with diverse Pb–O–M (M = Pb, Ca and Sr) inorganic connectivities. *CrystEngComm* **2010,** *12* (12), 4252.

139.   Nugent, P.; Belmabkhout, Y.; Burd, S. D.; Cairns, A. J.; Luebke, R.; Forrest, K.; Pham, T.; Ma, S.; Space, B.; Wojtas, L.; Eddaoudi, M.; Zaworotko, M. J., Porous materials with optimal adsorption thermodynamics and kinetics for CO_2 separation. *Nature* **2013,** *495* (7439), 80-4.

140.   Vaidhyanathan, R.; Iremonger, S. S.; Dawson, K. W.; Shimizu, G. K., An amine-functionalized metal organic framework for preferential CO_2 adsorption at low pressures. *Chem Commun (Camb)* **2009,** (35), 5230-2.

141.   Chokbunpiam, T.; Fritzsche, S.; Chmelik, C.; Caro, J.; Janke, W.; Hannongbua, S., Gate Opening, Diffusion, and Adsorption of CO_2 and N_2 Mixtures in ZIF-8. *J Phys Chem C* **2016,** *120* (41), 23458-23468.

142.   Maurya, M.; Singh, J. K., Effect of Ionic Liquid Impregnation in Highly Water-Stable Metal–Organic Frameworks, Covalent Organic Frameworks, and Carbon-Based Adsorbents for Post-combustion Flue Gas Treatment. *Energ Fuel* **2019,** *33* (4), 3421-3428.

143.   Kizzie, A. C.; Wong-Foy, A. G.; Matzger, A. J., Effect of humidity on the performance of microporous coordination polymers as adsorbents for CO_2 capture. *Langmuir* **2011,** *27* (10), 6368-73.

144.   Castillo, J. M.; Vlugt, T. J. H.; Calero, S., Understanding Water Adsorption in Cu−BTC Metal−Organic Frameworks. *J Phys Chem C* **2008,** *112* (41), 15934-15939.

145.   Huang, L.; Wang, H. L.; Chen, J.; Wang, Z.; Sun, J.; Zhao, D.; Yan, Y., Synthesis, morphology control, and properties of porous metal-organic coordination polymers. *Micropor Mesopor Mat* **2003,** *58* (2), 105-114.

146.   Giovine, R.; Volkringer, C.; Trebosc, J.; Amoureux, J. P.; Loiseau, T.; Lafon, O.; Pourpoint, F., NMR crystallography to probe the breathing effect of the MIL-53(Al) metal-organic framework using solid-state NMR measurements of ^{13}C-^{27}Al distances. *Acta Crystallogr C Struct Chem* **2017,** *73* (Pt 3), 176-183.

147.   Phan, A.; Doonan, C. J.; Uribe-Romo, F. J.; Knobler, C. B.; O'Keeffe, M.; Yaghi, O. M., Synthesis, structure, and carbon dioxide capture properties of zeolitic imidazolate frameworks. *Acc Chem Res* **2010,** *43* (1), 58-67.

Chapter 2

2 Experimental

2.1 Material preparation

Crystalline MOFs can be synthesized through numerous methods,[1] including solvothermal, microwave-assisted,[2] electrochemical,[3] and mechanochemical routes.[4] Among all these methods, solvothermal synthesis is the most extensively used methods because of its advantages, including: (1) high purity of the final product; (2) energy efficient as it requires low temperature; (3) an eco-friendly process because of closed system conditions; (4) crystal size and morphology of the product can be easily controlled by modifying the conditions.[5]

The solvothermal method is analogous to the hydrothermal method, where the organic solvents are being used in the procedure instead of water. During solvothermal synthesis, the reaction takes place in a closed vessel under self-generated pressure and a temperature above the normal boiling point of the solvent. Such high pressure and temperature conditions efficiently increase the solubility of the solid reactant in the solvent and accelerate the reactions between solid species.

In this thesis, all samples are synthesized solvothermally base on literature reported method.[6-11] A typical solvothermal synthesis of MOFs is performed as follows: The solid reagents and solvent are measured accurately using an analytical balance and graduated cylinders, the mixture is added to a Teflon inlet and mixed by a magnetic stirrer. This inlet then sealed in a stainless-steel autoclave and heated in a lab oven to the designated temperature for a fixed period of time, as shown in Figure 2.1. The final products are collected through filtration or centrifugation depending on the morphology. The purity and crystallinity of the materials are then checked and confirmed by powder X-ray diffraction (PXRD). In most cases, the as-prepared samples contain solvent molecules in their cages or channels. For these MOFs to exhibit permanent porosity, these solvent molecules are

typically removed with the assist of heat under dynamic vacuum. This process is known as "activation". Depending on the affinity of the solvent molecules to the framework, as well as the thermal stability of the material, the activation conditions for different MOFs may vary. Table 2.1 highlights the synthesize and activation conditions for MOFs that are studied in this thesis. The materials used in Chapter 3 (i.e. PbSDB and CdSDB) were synthesized and provided by Dr. Shoushun Chen (Prof. Yining Huang's group, the Department of Chemistry).

Figure 2.1 Photos of the lab oven and the autoclave for synthesis.

Table 2.1 Solvothermal conditions for synthesizing MOF materials studied in this thesis.

Compound	Agent name and Quantity	Temp (°C)	Reaction times (h)	Post treatment	Activation conditions
CdSDB	Cd(NO$_3$)$_2$·4H$_2$O (1 mmol) 4,4'-sulfonyldibenzoic acid (4,4'-SDB) (1 mmol) Ethanol (15 mL)	180	48	Separated by filtration and washed with distilled water	200 °C 12 hrs
PbSDB	Pb(NO$_3$)$_2$ (0.5 mmol) 4,4'-SDB (1 mmol) DMF and methanol mixture (10 mL, v/v=1:1)	160	48	Separated by filtration and washed with distilled water	180 °C 12 hrs
SIFSIX-3-Zn	ZnSiF$_6$·H$_2$O (3 mmol, in 10 mL methanol) Pyrazine (6 mmol, in 10 mL methanol)	Room temp	72	Separated by filtration and washed with methanol	50-100 °C 24 hrs
ZIF-8	Zn(OAc)$_2$·2H$_2$O (0.5 mmol) 2-methylimidazole (5 mmol) H$_2$O (2.0 mL)	120	24	Separated by filtration and washed with distilled water	150-200 °C 24 hrs
UiO-66	Zirconium chloride (ZrCl$_4$, 0.25 mmol) 1,4-benzenedicarboxylate (H$_2$BDC, 0.25 mmol) DMF (300 mmol)	120	24	Collected by centrifugation and washed with distilled water	150 °C 24 hrs
ZnAtzOx(H$_2$O)	3-amino-1,2,4-triazole (5 mmol) Oxalic acid (1 mmol) Zinc carbonate basic (Zn$_5$(CO$_3$)$_2$(OH)$_6$, 1 mmol) H$_2$O and butanol mixture (6 mL, v/v=1:1)	180	48	Separated by filtration and washed with distilled water	150 °C 12 hrs

2.2 High pressure apparatus

2.2.1 Diamond anvil cells (DAC)

The available techniques to achieve ultrahigh-pressures have been developed and modified in the past 60 years.[12] Many advanced devices that are capable of generating high static pressures are designed, such as diamond anvil cells (DAC) and large-volume apparatuses. The large-volume apparatuses could be further divided into simple squeezer, piston-cylinder, belt apparatus, and multi-anvil devices.[13-14] Among all these high-pressure apparatuses, DAC is considered the state-of-art because it has one significant advantage over all the other devices: Diamond. Diamond is not only the hardest known material, but also exhibits excellent properties, such as high thermal conductivity, which adds the temperature factor to the equation; and being an electrical insulator, which enables the *in-situ* measurements of material electroconductivity under high pressure. Most importantly, diamonds are highly transparent to most ranges of electromagnetic radiation, from infrared all the way to hard X-ray, providing opportunities for a wide variety of *in-situ* characterizations, including vibrational spectroscopies, ultraviolet-visible spectroscopy, neutron scattering, and X-ray diffraction, etc.,[15] which could not otherwise be available through the other high-pressure apparatuses.

The principle of the DAC setup is straightforward:[16] a pair of opposing single-crystal diamond anvils with the same culet size are equipped in a cell. These diamonds are specially cut in a way that provides them an extremely small circular facet, which could range from 50 to 700 μm. Such a small contact area results in extremely high pressures with only modest force applied. A piece of pre-indented gasket with a hole drilled in the center is compressed between the diamond anvils, the purpose of which is to produce an encapsulated chamber that secures the sample and the pressure transmitting medium in place. The typical gaskets are made of stainless steel, while other materials such as rhenium and tungsten, may be required when dealing with higher pressures. The diameter of the sample chamber is normally a half to one-third of the diamond culet, to provide sufficient mechanical support for the diamond tips under high pressure. The diamonds are mounted on two supporting tungsten carbide seats, which are aligned and fixed onto the piston and

cylinder sides of the cell. The applied pressure is adjustable by tightening or loosening the screws that are embedded in the pistons, as shown in Figure 2.2.[17] The range of pressure that a DAC could generate is determined by the size of the diamond facets.
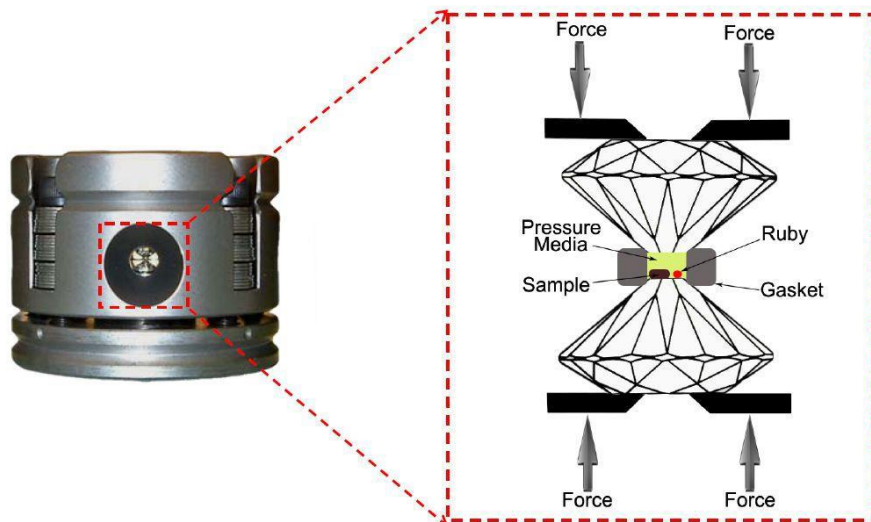
Figure 2.2 A picture of a DAC and the configuration of enlarged diamond anvils.[17]

Typically, diamonds are classified into two types based on the level and type of their chemical impurities. The major difference between these two types of diamonds is the level of their nitrogen impurity content. Nitrogen impurities take up more than 0.1% in type I diamonds, whereas type II contains a wide range of impurities at the parts per million level. Despite that type II diamonds are more expensive, the application of these diamonds is necessary for some spectroscopic measurements, such as infrared and ultraviolet. This is because type II diamonds do not show adsorption bands from nitrogen impurities in these spectral regions. In terms of Raman studies, both type I and II diamonds exhibit a strong first-order Raman line at 1334 cm^{-1}, therefore, type I diamonds are usually sufficient, as the nitrogen impurities are not a concern.

2.2.2 Pressure calibration

In terms of determining the local pressure in the DAC sample chamber, the most commonly used technique is the fluorescence method.[18] The predecessor of this approach can be traced back to 1968 when the shift of an optical absorption band in nickel dimethylglyoxime was used to calibrate pressure.[19] It was later replaced by ruby due to the

more insensitive fluorescence signal.[20-21] The ruby fluorescence method for pressure measurements has grown its popularity since then because of its speed and ease of application, the pressures can be determined within a fraction of minute.

The chemical composition of the ruby is Cr^{3+} doped α-Al_2O_3, in which a chromium ion replaces an occasional aluminum atom. The ruby material that is suitable for pressure calibration contains approximately 3000 to 5500 ppm Cr^{3+} to achieve the satisfactory fluorescence intensity. These ruby calibrants are typically in the shape of grains or chips with the size in the magnitude of 10 μm. When excited by a laser, Cr^{3+} ions emit two luminescent peaks R1 and R2, both are narrow and exhibit a pronounced red-shift with increasing pressure, as shown in Figure 2.3.[17] The relation between the local hydrostatic pressure and the frequency shift of ruby R-line emission is described in Equation 2.1,[20]

$$P = \frac{1904}{B}\left[\left(1 + \frac{\Delta\lambda}{694.24}\right)^B - 1\right]$$

Equation 2.1

where P is the local pressure in GPa, $\Delta\lambda$ is the wavelength shift of R_1 peak in nm, B=7.665 under quasi-hydrostatic conditions, and B=5 for non-hydrostatic conditions. This method features a precision of $\pm$0.05 GPa and can maintain its accuracy up to 80 GPa.[20]
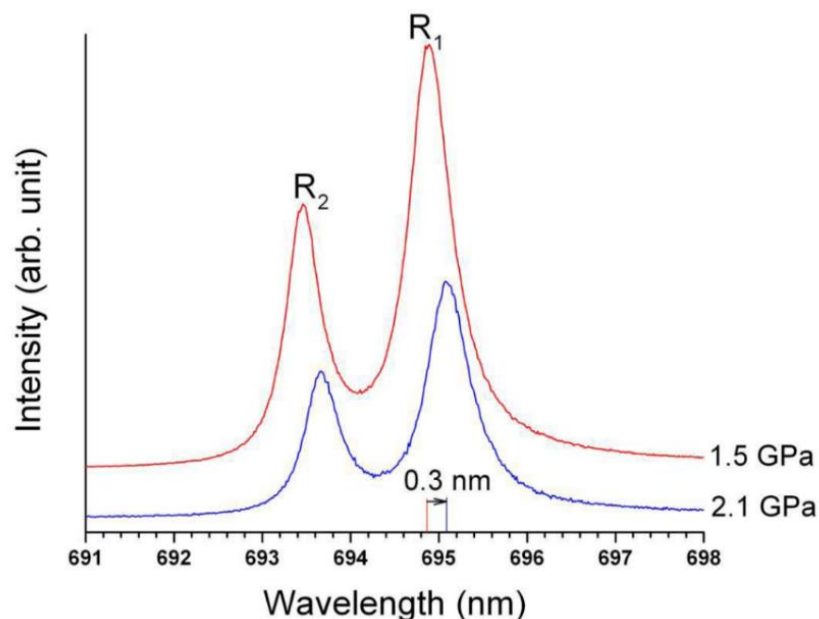
Figure 2.3 Ruby R1 and R2 luminescence measured at 1.5 GPa (red) and 2.1 GPa (blue) under room temperature.[17]

2.2.3 Pressure transmitting medium

Hydrostatic pressure is a thermodynamic parameter, where no pressure gradient is present at any given point of the sample during compression. The experimental results obtained under such conditions are believed to be a better representation of material properties and are more comparable to the theoretical results, as the unevenly distributed pressure under non-hydrostatic environment may induce distorted observations throughout the sample. Therefore, in most cases, the hydrostatic conditions are required for high pressure experiments. To produce hydrostatic environments in DAC, the simplest way is to introduce a compressible fluid to the sample chamber, namely, pressure transmitting medium (PTM). For porous materials specifically, the pressure transmitting mediums can be further classified into two types, penetrating PTM and non-penetrating PTM. The molecular size of the penetrating PTMs is typically smaller than the pore size of the host materials, thus can migrate into the pores and support the framework from the inside at high pressures, while providing hydrostatic conditions in the sample chamber.

A well-suited PTM should accommodate several requirements, including low thermal conductivity, low shear strength, and the ability to maintain the hydrostatic conditions to pressure as high as possible. The highest pressure for the most commonly used PTMs to maintain hydrostatic conditions are illustrated in Table 2.2. Accordingly, the selection of PTM is determined by the highest pressure in the experiment, as well as the chemical and physical sensitivity of the material to the PTM. In this thesis, no PTM was used for SIFSIX-3-Zn and $ZnAtzOx(H_2O)$ to rule out the possible host-guest interactions from other sources. In *Chapter 3* and *Chapter 5*, where the cryogenic CO_2 loading was performed, the fluid CO_2 works as penetrating PTM up to 0.6 GPa. For the synchrotron PXRD measurements, fine-ground CdSDB and PbSDB were loaded along with neon using the gas loading system at GSECARS of APS (Advanced Photon Source).

Table 2.2 The most commonly used PTMs and the highest pressure for them to maintain hydrostatic conditions under room temperature.[22-23]

Pressure Transmitting Medium	P_{max} for Hydrostatic Conditions
Neon	50 GPa
Argon	10 GPa
Helium	40 GPa
Methanol	7 GPa
4:1 Methanol-ethanol	10.5 GPa
16:3:1 Methanol–ethanol–water	14.4 GPa
Silicone oil	20 GPa

2.2.4 Gas loading

In this thesis, two types of gas loading method were used to load CO_2 and other guests (i.e. D_2O) to the framework: cryogenic loading and Schlenk line loading. To carry out cryogenic loading, the objects must not be water sensitive. Figure 2.4 shows the general procedure of the cryogenic CO_2 loading. Firstly, a few grains of ruby and the sample is loaded to the sample chamber, leaving certain space to the CO_2. The piston part of the diamond anvil

cell is secured on the seat and immersed in the liquid nitrogen bath to cool down. When the temperature is lower than the boiling point of CO_2 (i.e. -78.5 °C), the CO_2 gas is introduced to the sample chamber. The condensed CO_2 can be observed on the surface of the gasket and sample after a few seconds through a microscope. Finally, the cell is closed instantly and applied with a minimum pressure of around 0.3 GPa to trap CO_2 in the chamber.

The other way of gas loading is to use the Schlenk line. After the sample is fully activated under the dynamic vacuum, the CO_2 cylinder is then connected to the line. The loading pressure can be monitored by the pressure gauge equipped on the vacuum line. Since the volume of the vacuum line tubing is known, the sample tubes are standardized, therefore, the amount of CO_2 loaded to the framework can be calculated based on the pressure change indicated by the pressure gauge and the volume of the system.

The cryogenic loading is capable of sealing extra CO_2 in the sample chamber, which is necessary for investigating the relationship between pressure and the CO_2 capacity of a MOF. Whereas using the Schlenk line, a better control over the quantity of the loaded CO_2 can be achieved. In the multi-guest experiments, this is the only method available to realize the co-loading with a precise loading ratio (e.g. 1:1 CO_2 to D_2O molar ratio). The entire loading process of this method is in closed systems (i.e. vacuum and N_2 fill glovebox), The purity and quality of the loaded sample are therefore guaranteed.

1. Pre-load sample and ruby
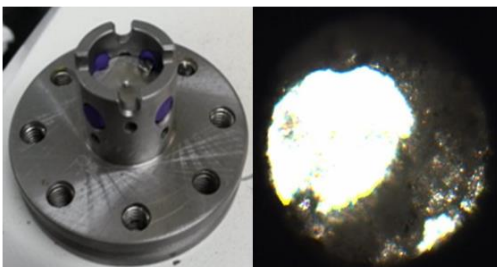
3. Introduce CO_2 gas
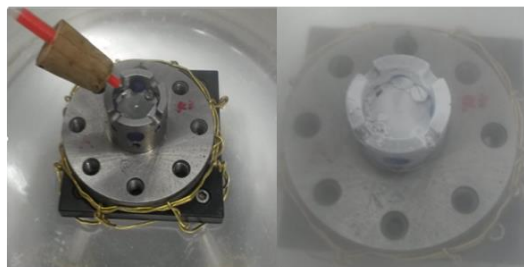
2. Cool down the cell in L-N_2 bath
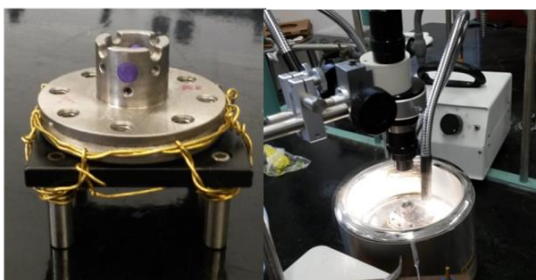
4. Seal the cell
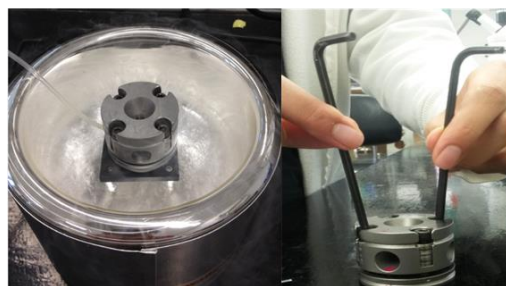
Figure 2.4 The procedures of the cryogenic CO₂ loading.

2.3 In situ high-pressure characterizations

2.3.1 Vibrational spectroscopy

Vibrational spectroscopy is a characterization method for non-destructive measurement of the vibrational energy in a compound. In a chemical sample, each chemical bond has a unique vibrational energy, when the molecule interacts with the light, the energy transferred from the electromagnetic field of the light to the molecule at the vibrational levels can be recorded by vibrational spectroscopy. Such information allows the understanding of the short-range structures, chemical bonding and inter- and intra-molecular interactions, as well as the physical and chemical configurations of the material. Particularly, vibrational spectroscopy is a powerful technique to monitor the pressure effects on chemical bonding and local structures as well as host-guest interactions in high-pressure studies of guest-loaded MOFs, which are investigated in this thesis.

Two of the most common vibrational spectroscopies are infrared (IR) and Raman spectroscopy, which in many circumstances may provide complementary information, as

they follow different selection rules. In IR spectroscopy, an infrared lamp is used to provide electromagnetic radiation between the wavelengths of 700 nm to 1 mm. When a material is exposed to electromagnetic radiation at the right frequency (i.e. when hν = ΔE, as shown in Figure 2.4), the molecule absorbs the radiation at that frequency and vibrates. For a vibrational mode to be IR active, such vibration must induce changes in molecular dipole moment during the vibration. The selection for IR spectroscopy is demonstrated in Equation 2.2, where δμ is the variation of the dipolar moment, δq is the variation of the normal coordinates.

$$\frac{\delta\mu}{\delta q} \neq 0$$

Equation 2.2

Complementary to IR spectroscopy, Raman spectroscopy is another vibrational technique that could be used to characterize the chemical bonding and the molecular structures. In Raman spectroscopy, when a laser beam irradiates on a material, a portion of the photons will be scattered into different directions. The scattered light can be divided into two types, Rayleigh scattering and Raman scattering. The majority of photons undergo an elastic scattering process, also known as Rayleigh scattering, where the scattered photons maintain the same energy (i.e. frequency and wavelength) as the incident photons. Whereas a small fraction of the photons get inelastically scattered and have a different frequency from the incident beam, known as Raman scattering. As demonstrated in Figure 2.5, the Raman scattering is further classified into two types, stokes and anti-stokes scatterings. When the molecule relaxes from the virtual state, if the emitted photons have lower energy than the incident photons, it is Stokes scattering and the material absorbs energy. Contrarily, anti-Stokes scattering happens when a molecule that was initially at its excited state gets further stimulated to the virtual state, then comes back to its ground state, the outcome of which is the molecule loses energy. Given that most molecules are initially in their ground state, Stokes scattering is significantly stronger than anti-Stokes scattering, therefore, Raman spectroscopy mainly measures the Stokes scattering.

The Raman effect is triggered by the interaction between the electron cloud of a molecule and the external electric field of a single wavelength laser. Such interaction can create an induced dipole moment within the molecule based on its polarizability. Therefore, the criteria for a vibration to be Raman active is that the polarizability of the molecule must change when it vibrates. The selection rule for Raman scattering is illustrated in Equation 2.3, where $\delta\alpha$ is the variation of polarizability, δq is the variation of the normal coordinates.

$$\frac{\delta\alpha}{\delta q} \neq 0$$

Equation 2.3

Raman spectroscopy can also be applied to detect the lattice vibrations of crystalline solid-state materials, which are originated from the translational and rotational modes of the ionic or molecular crystals.[24] These modes are usually found at low frequencies (i.e. in the region of 400-10 cm^{-1}) and may provide preliminary information on changes in crystal structures and predict possible phase transitions.
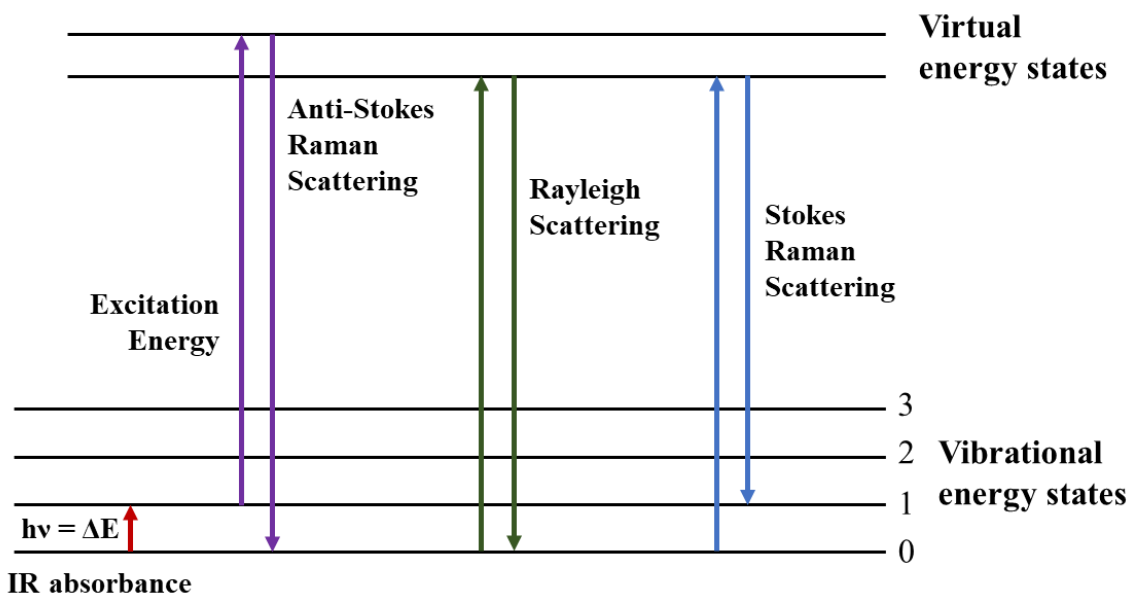
Figure 2.5 Illustration of IR absorption, Rayleigh scattering and Raman scattering process.

2.3.2 *In situ* FTIR spectroscopy system

To carry out *in situ* IR measurements for high pressure studies, a highly customized IR micro-spectroscopy system was assembled in the lab, the schematic diagram of the system is shown in Figure 2.6. A commercially available Fourier transform infrared (FTIR) spectrometer (Model Vertex 80v) and a Globar IR light source constituted the main components of the micro-IR system, which are purchased from Bruker Optics Inc. The sample stage is designed for holding the DAC in place with excellent reproducibility of its vertical and horizontal positions between measurements. A collimated IR beam is directed into a relay box through a KBr window on the spectrometer, it is then focused onto the sample in the DAC using an iris optics and $15\times$ reflective objective lens. The beam size is set to match the size of the sample (i.e. ~150 µm) by a series of iris apertures. By using another identical reflective objective as a condenser, the transmitted IR beam is collected and directed to a wide-band or mid-band mercury cadmium telluride (MCT) detector that records signals in the spectral ranges of 400 to 12000 cm^{-1} and 600 to 12000 cm^{-1}, respectively. The system is operated under a near vacuum condition of pressure less than 5 mbar to avoid interference from ambient CO_2 and H_2O. For calibration purposes, a background spectrum of the diamonds and KBr is collected before each sample measurement. All the IR spectra in this thesis were collected with a resolution of 4 cm^{-1} and 512 scans to ensure the best quality of the data.
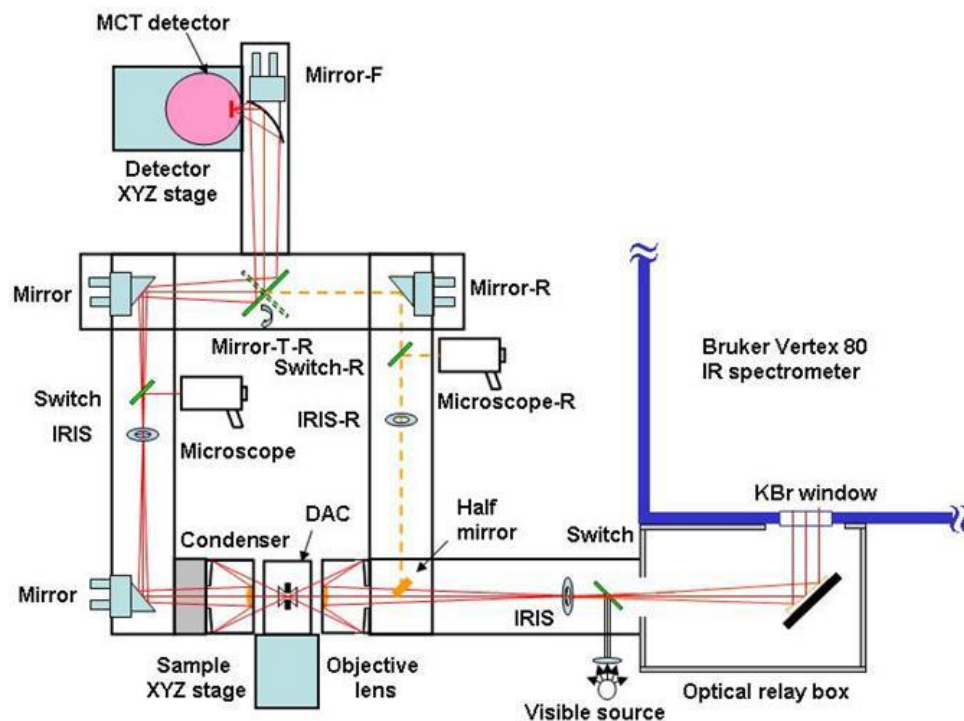
Figure 2.6 The schematic diagram of the IR micro-spectroscopy system.[25]

2.3.3 *In situ* micro-Raman spectroscopy system

Similar to the IR system, the Raman micro-spectroscopy system is also customized and built in our lab for all room-temperature Raman measurements. The schematic of this system is illustrated in Figure 2.7. The laser beam is focused on the sample in the DAC, which is placed on the sample stage and well-aligned with the aid of the microscope. The beam size of the laser is adjusted to < 5 μm and focused on the sample by a 20× objective. The Raman signals are detected with backscattering geometry by the same objective lens. A pair of notch filters are used to block the Rayleigh lines. Solid-state lasers with different wavelengths of 532 nm and 635 nm were used depending on the properties of the samples (i.e. signal to background ratio). Similarly, the choice of the grating is also sample specific, both 1200 lines/mm and 300 lines/mm are used in this thesis to obtain the optimal signals. The spectrum is collected by a CCD detector (charge-coupled device), which is cooled down to the operating temperature of -120 °C by liquid nitrogen. A WinSpec software is installed on the computer to control the collection of the spectrum, the accumulation time

is adjusted to achieve the best resolution. Prior to all measurements, the calibration of the system is carried out using the standard neon lines with a resolution of ± 1 cm^{-1}.
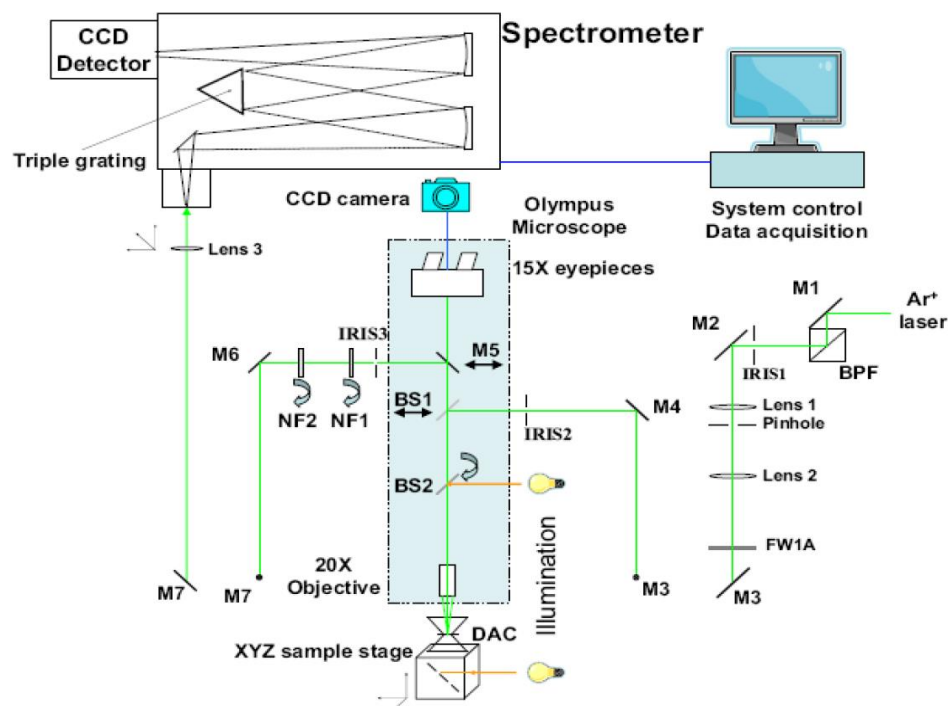
Figure 2.7 The schematic diagram of the Raman micro-spectroscopy system.[17]

2.3.4 Synchrotron X-ray diffraction

X-ray diffraction (XRD) is one of the most important non-destructive tools to analyze a wide range of matter, including powders and crystals. When irradiating X-ray to a crystalline material, the crystalline structure causes the incident X-rays to diffract into many specific directions, by analyzing the angles and intensities of the diffracted beams, the structural information of the material such as chemical bonding, atom positions, as well as crystal structures, can be obtained. The principle of XRD is described by Bragg's law, as shown in Equation 2.4, where λ is the wavelength of the X-ray beam, θ is the scattering angle, d_{hkl} is the spacing of the lattice planes with the Miller indices h, k, l.

$$n\lambda = 2d_{hkl}\sin\theta \qquad\qquad \text{Equation 2.4}$$

XRD is an effective technique for determining the atomic and molecular structure of crystalline material. However, given the small sample size and the limited opening angle of the DACs, intense X-ray beams with high energy and small beam size are necessary for *in situ* high pressure XRD measurements, which is only accessible by synchrotron radiation (SR). Typically, the brightness of the X-ray beam from SR is 10^4 to 10^{12} times greater than that of the conventional X-ray source produced in labs. Furthermore, the highly collimated SR beam with a tiny opening angle results in a small beam size in the magnitude of tens of microns, which makes the measurements of a small amount of sample possible. Besides, the high tunability of the SR allows the researchers to optimize the wavelength of the X-ray beam and acquire the most satisfactory data. Hence, owing to its high brilliance, finely tunable wavelength and beam size,[26] synchrotron X-ray diffraction is so far the most desirable method to investigate the structural behaviors of crystalline materials under high pressure.

The PXRD data in Chapter 3 were at beam-line 16BM at Advanced Photon Source (APS), Argonne National Laboratory (ANL). The initial XRD patterns were recorded as Debye-Scherrer rings by a 2D MARCCD detector, then integrated by the Fit2D program into 1D powder patterns. Figure 2.8 shows the 2D image and the converted 1D diffraction pattern of the calibrant CeO_2 as an example. The cell parameters were further refined using UnitCell software. The setup of the beam-line 16BM is shown in Figure 2.9.
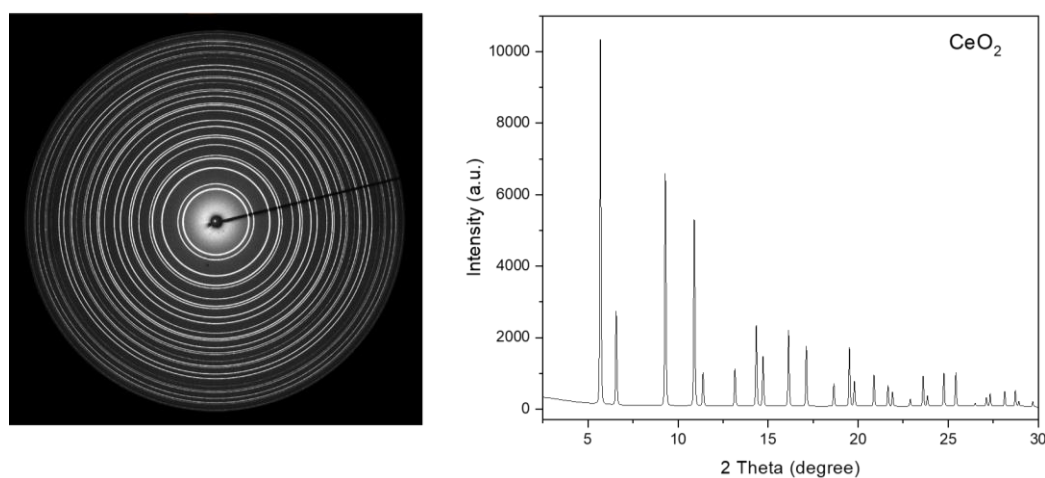
Figure 2.8 2D Debye-Scherrer ring and converted 1D patterns of CeO₂ were collected at Sector 16 BM, APS ($\lambda = 0.3396$ Å).
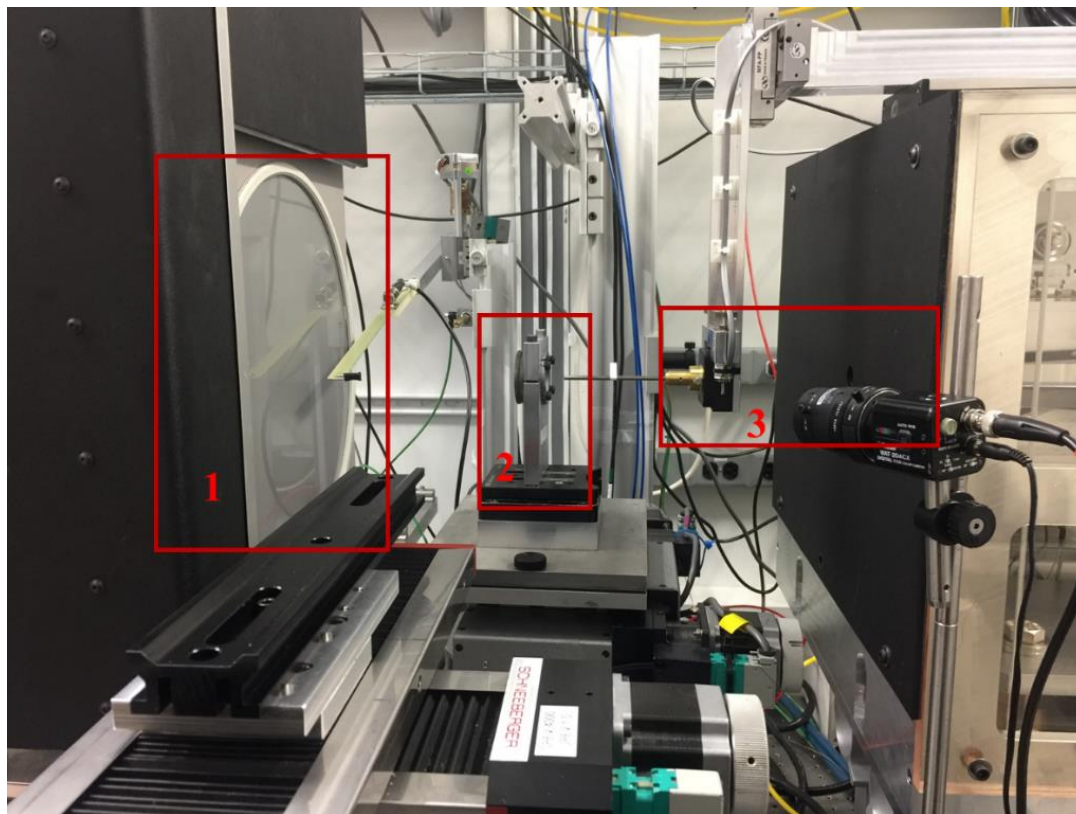
Figure 2.9 The experimental setup of sector 16BM at APS, ANL. The detector, sample stage and X-ray beam are labeled in the figure as 1, 2 and 3, respectively.

2.4 References

1.   Stock, N.; Biswas, S., Synthesis of metal-organic frameworks (MOFs): routes to various MOF topologies, morphologies, and composites. *Chem Rev* **2012,** *112* (2), 933-69.

2.   Klinowski, J.; Paz, F. A.; Silva, P.; Rocha, J., Microwave-assisted synthesis of metal-organic frameworks. *Dalton Trans* **2011,** *40* (2), 321-30.

3.   Campagnol, N.; Van Assche, T.; Boudewijns, T.; Denayer, J.; Binnemans, K.; De Vos, D.; Fransaer, J., High pressure, high temperature electrochemical synthesis of metal-organic frameworks: films of MIL-100 (Fe) and HKUST-1 in different morphologies. *J Mater Chem A* **2013,** *1* (19), 5827.

4.   Klimakow, M.; Klobes, P.; Thünemann, A. F.; Rademann, K.; Emmerling, F., Mechanochemical Synthesis of Metal−Organic Frameworks: A Fast and Facile Approach

toward Quantitative Yields and High Specific Surface Areas. *Chem Mater* **2010,** *22* (18), 5216-5221.

5. Jensen, K. M.; Tyrsted, C.; Bremholm, M.; Iversen, B. B., In situ studies of solvothermal synthesis of energy materials. *ChemSusChem* **2014,** *7* (6), 1594-611.

6. Lin, J.-D.; Wu, S.-T.; Li, Z.-H.; Du, S.-W., A series of novel Pb(ii) or Pb(ii)/M(ii) (M = Ca and Sr) hybrid inorganic-organic frameworks based on polycarboxylic acids with diverse Pb–O–M (M = Pb, Ca and Sr) inorganic connectivities. *CrystEngComm* **2010,** *12* (12), 4252.

7. Plonka, A. M.; Banerjee, D.; Woerner, W. R.; Zhang, Z.; Li, J.; Parise, J. B., Effect of ligand geometry on selective gas-adsorption: the case of a microporous cadmium metal-organic framework with a V-shaped linker. *Chem Commun (Camb)* **2013,** *49* (63), 7055-7.

8. Nugent, P.; Belmabkhout, Y.; Burd, S. D.; Cairns, A. J.; Luebke, R.; Forrest, K.; Pham, T.; Ma, S.; Space, B.; Wojtas, L.; Eddaoudi, M.; Zaworotko, M. J., Porous materials with optimal adsorption thermodynamics and kinetics for CO_2 separation. *Nature* **2013,** *495* (7439), 80-4.

9. Phan, A.; Doonan, C. J.; Uribe-Romo, F. J.; Knobler, C. B.; O'Keeffe, M.; Yaghi, O. M., Synthesis, structure, and carbon dioxide capture properties of zeolitic imidazolate frameworks. *Acc Chem Res* **2010,** *43* (1), 58-67.

10. Guillerm, V.; Gross, S.; Serre, C.; Devic, T.; Bauer, M.; Ferey, G., A zirconium methacrylate oxocluster as precursor for the low-temperature synthesis of porous zirconium(IV) dicarboxylates. *Chem Commun (Camb)* **2010,** *46* (5), 767-9.

11. Vaidhyanathan, R.; Iremonger, S. S.; Dawson, K. W.; Shimizu, G. K., An amine-functionalized metal-organic framework for preferential CO_2 adsorption at low pressures. *Chem Commun (Camb)* **2009,** (35), 5230-2.

12. Dewaele, A.; Loubeyre, P.; Occelli, F.; Marie, O.; Mezouar, M., Toroidal diamond anvil cell for detailed measurements under extreme static pressures. *Nat Commun* **2018,** *9* (1), 2913.

13.   Liebermann, R. C., Multi-anvil, high pressure apparatus: a half-century of development and progress. *High Pressure Res* **2011,** *31* (4), 493-532.

14.   Miletich, R.; Allan, D. R.; Kuhs, W. F., High-Pressure Single-Crystal Techniques. *Rev Mineral Geochem* **2000,** *41* (1), 445-519.

15.   Walker, J., Optical absorption and luminescence in diamond. *Rep Prog Phys* **1979,** *42*, 1605-1659.

16.   Schettino, V.; Bini, R., Constraining molecules at the closest approach: chemistry at high pressure. *Chem Soc Rev* **2007,** *36* (6), 869-80.

17.   Dong, Z., High-pressure study of molecular solids and 1D nanostructures by vibrational spectroscopy and synchrotron x-ray diffraction. *Thesis and Dissertation* **2012**.

18.   Mao, H. K.; Bell, P. M.; Shaner, J. W.; Steinberg, D. J., Specific volume measurements of Cu, Mo, Pd, and Ag and calibration of the rubyR1fluorescence pressure gauge from 0.06 to 1 Mbar. *J Appl Phys* **1978,** *49* (6), 3276-3283.

19.   Davies, H. W., Calibration of the nickel dimethylglyoxime spectral shift at pressures. *J Res Nat Stand* **1967,** *72A*, 149-153.

20.   Mao, H. K.; Xu, J.; Bell, P. M., Calibration of the ruby pressure gauge to 800 kbar under quasi-hydrostatic conditions. *J Geophys Res* **1986,** *91* (B5), 4673.

21.   Syassen, K., Ruby under pressure. *High Pressure Res* **2008,** *28* (2), 75-126.

22.   Klotz, S.; Chervin, J. C.; Munsch, P.; Le Marchand, G., Hydrostatic limits of 11 pressure transmitting media. *J Phys D* **2009,** *42* (7), 075413.

23.   Angel, R. J.; Bujak, M.; Zhao, J.; Gatta, G. D.; Jacobsen, S. D., Effective hydrostatic limits of pressure media for high-pressure crystallographic studies. *J Appl Crystallogr* **2007,** *40* (1), 26-32.

24.   Loudon, R., Theory of Stimulated Raman Scattering from Lattice Vibrations. *Proc Phys Soc* **1963,** *82* (3), 393-400.

25.   Dong, Z.; Song, Y., Transformations of Cold-Compressed Multiwalled Boron Nitride Nanotubes Probed by Infrared Spectroscopy. *J Phys Chem C* **2010,** *114* (4), 1782-1788.

26.   Hemley, R. J.; Mao, H. K.; Struzhkin, V. V., Synchrotron radiation and high pressure: new light on materials under extreme conditions. *J Synchrotron Radiat* **2005,** *12* (Pt 2), 135-54.

Chapter 3

3 Elucidation of the Structural Origins and Contrasting Guest-host Interactions in CO_2 Adsorbed CdSDB and PbSDB MOFs at High Pressures

3.1 Introduction

Metal-organic frameworks (MOFs) are an emerging class of crystalline materials constructed by bridging metal-containing units with organic linkers to create open frameworks with permanent porosity.[1] Due to the high thermal stability, enormous surface area and finely tuneable chemical functionality, MOFs have wide applications in gas separation,[2] catalysis,[3] drug delivery,[4] chemical sensors,[5] and especially gas storage.[6-8] Recently, the SDB (SDB = 4,4′-sulfonyldibenzoate) based MOFs have attracted much attention because of their high CO_2 selectivity over other gas molecules. Moreover, the SDB based MOFs are also known to have relatively large pores and to be stable to humidity,[9, 10] which making the MOFs in SDB family excellent candidates for CO_2 storage applications. For instance, PbSDB was the first reported porous SDB-based MOF,[11] compared to many other Pb-based MOFs that are nonporous.[12] Later on, several SDB-based MOFs with different metal centres have been reported (e.g., Ni, Ca, Zn, Pb, Sr and Na). Among these SDB-based MOFs, CdSDB has been shown to have an excellent CO_2/N_2 selectivity compared to the other MOFs in SDB family.[9] In particular, the CO_2 adsorption mechanisms of PbSDB and CdSDB frameworks have just been investigated recently using solid state nuclear magnetic resonance (SSNMR) spectroscopy at ambient pressure and low temperatures.[13]

Even though PbSDB, and CdSDB are built from the same V-shape organic ligand (SDB), however, different metal centres result in different coordination environments, thus featuring different topologies, shapes of channels, and pore sizes. In the PbSDB framework, the Pb ion is seven-coordinated to oxygen atoms, one of which is from a sulfonyl group while the others are from six different SDB^{2-} anions (Figure 3.1a).[11] Such coordination results in the formation of linear channels (Figure 3.1b) with an average size of 7.4 Å × 7.5 Å in PbSDB framework. In contrast, the Cd metal centre in CdSDB framework is six-

coordinated by bonding to five carboxylate oxygens and one sulfonyl oxygen, forming a quasi-isotropic octahedron (Figure 3.1c). This coordination leads to the formation of a one-dimensional sinusoidal chain in a three-dimensional framework with relatively larger pore size of 8.8 Å × 8.5 Å (Figure 3.1c and d). At ambient conditions, PbSDB crystalizes into an orthorhombic lattice (space group Pnma, a = 5.9527(3) Å, b = 13.0441(6) Å, c = 19.5781(10) Å),[14] whereas the CdSDB belongs to a monoclinic space group of C2/c space group with the unit cell parameters a = 13.3382(4) Å, b = 21.4986(7) Å, c = 10.1527(6) Å and β = 90°.[9]

The differences in the structure and topology of these SDB based MOFs can be correlated to their corresponding CO_2 adsorption behaviours. Moreover, external conditions that induce structural variations may substantially influence the guest-host interactions, leading to a totally different CO_2 adsorption capacity. For instance, application of high external pressure has been demonstrated to be one of the most promising techniques in terms of improving the CO_2 storage capacities in MOFs.[15-18] In particular, the MOF may respond to extreme external constraint by significantly changing the framework topology,[15, 18-28] the pore size,[29, 30] the pore shape, and thus the adsorption properties.[31-36] Furthermore, we have demonstrated that the CO_2 storage capacity can be substantially enhanced at high pressures as a result of pressure-regulated CO_2 insertion into the framework for several MOFs. For instance, using in situ FTIR spectroscopy, Hu *et al*. demonstrated that CO_2 storage capacity in the ZIF-8 frameworks is significantly improved at high loading pressures.[16] More interestingly, we found high external pressure can preferentially tune the CO_2 adsorption behaviour in MOFs with heterogeneous topology such as in MIL-68 and α-$Mg_3(HCOO)_6$.[17,18] Despite the extensive investigations of SDB based MOFs at near ambient conditions, the high-pressure structures and CO_2 adsorption behaviour have remained unknown. Given the large porosity and excellent potential of CO_2 adsorption of PbSDB and CdSDB, it would be of fundamental interest to examine the structural responses to external compression and corresponding guest-host interactions between CO_2 and the different framework environment comparatively.
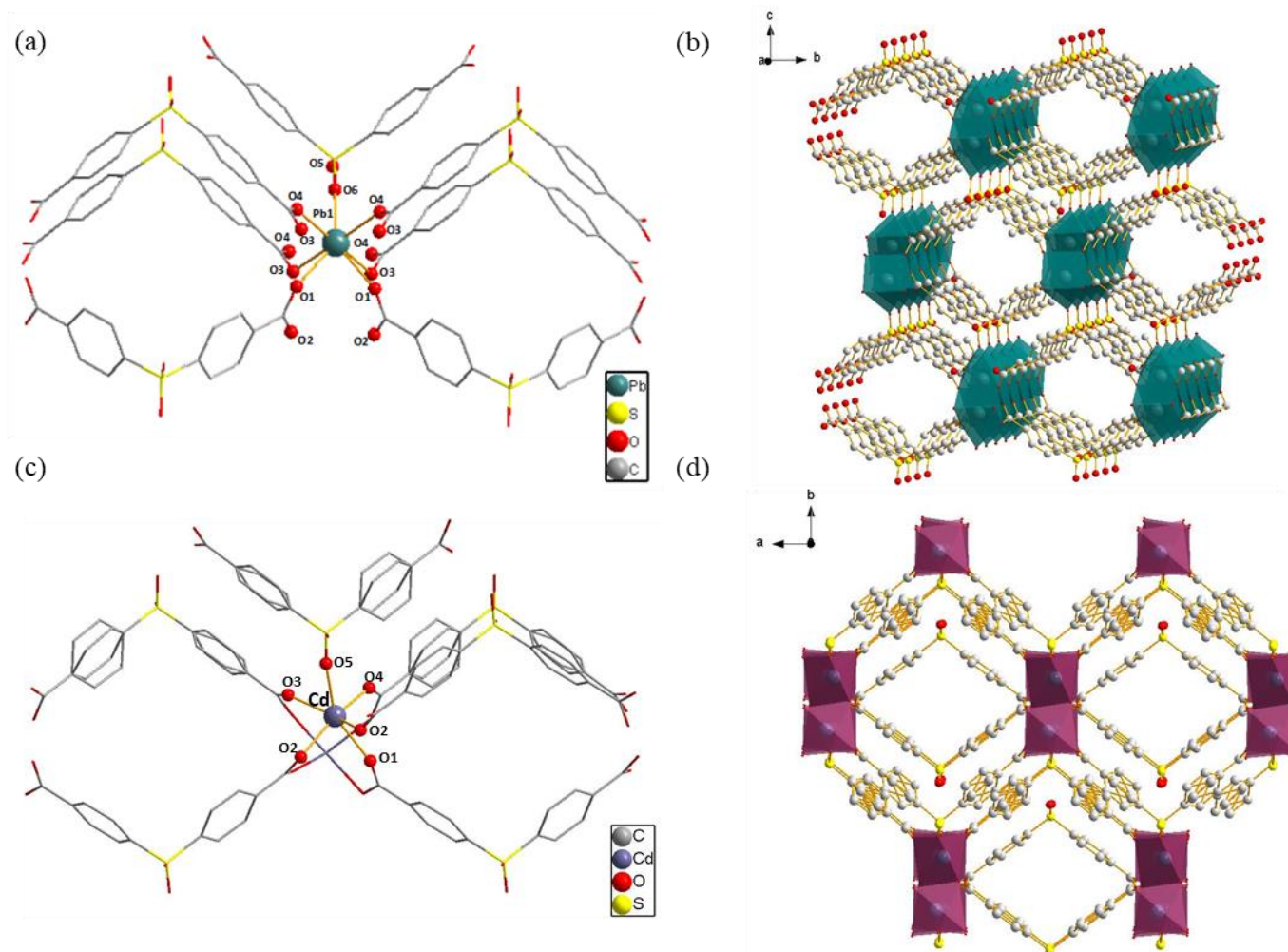
Figure 3.1 (a) Local coordination environment of Pb in PbSDB. (b) Polyhedral view of the 3D microporous framework of PbSDB along the *a*-axis, showing the linear channels. (c) Local coordination environment of Cd in CdSDB. (d) Polyhedral view of the structure of activated CdSDB along *c* axis, showing the 1D sinusoidal chain.

In this work, using in situ Raman and FTIR spectroscopy as well as synchrotron powder X-ray diffraction (XRD), we first investigated the structural stabilities and possible phase transitions of activated PdSDB and CdSDB frameworks at high pressures, followed by a comparative examination of the guest-host interactions in CO_2 loaded PbSDB and CdSDB frameworks. We discovered strongly contrasting pressure-induced modifications in structures and crystallinity, and especially prominent differences in CO_2 adsorption behaviour in two different, but related SDB frameworks, which can be correlated with their different structural and topology origins. We observed pressure-regulated CO_2 populations between different sites for the first time. Our findings greatly enhanced the understanding of guest-host interactions of CO_2 loaded framework by elucidating the structural origins and thus fundamentally contribute to the development of CO_2 storage applications in SDB based and other MOFs.

3.2 Experimental

The PbSDB and CdSDB were synthesized under solvothermal conditions using Teflon lined stainless steel Parr autoclaves according to the literature.[9, 12] The starting materials of $PbNO_3$, $Cd(NO_3)_2 \cdot 4H_2O$ (98%), $LiNO_3$, 4,4'-sulfonyldibenzoic acid (4,4'-SDB), ethanol (95%) were purchased from Sigma-Aldrich and used as is without further purification. For synthesis of PbSDB, 0.5 mmol $Pb(NO_3)_2$ and 1 mmol 4,4'-sulfonyldibenzoic acid were placed in a Teflon-lined stainless-steel autoclave with 10 mL of mixed solvent of DMF (N, N-dimethylformamide) and methanol (v/v = 1: 1) in the presence of $LiNO_3$. The mixture was heated to 433 K for 4 hours and kept at this temperature for 2 days. The reaction system was cooled slowly to room temperature over another two days. For the synthesis of CdSDB, a mixture of 1 mmol $Cd(NO_3)_2 \cdot 4H_2O$ (0.310 g) and 1 mmol 4,4'-SDB (0.296 g) was dissolved in 12 mL ethanol and stirred for 2 hours to achieve homogeneity. The resultant solution was heated at 453 K for 4 days. For both systems, colourless needle-shaped crystals were recovered, washed thoroughly with MeOH three times, and dried in air at room temperature. Disordered solvent molecules are found to be present within the channels of as made PbSDB and CdSDB frameworks after synthesis, which can be readily removed upon activation by heating to 453 K and 473 K in vacuum, respectively. Remarkably, none of the activated PbSDB or CdSDB frameworks reabsorb water when

exposed to air. The identities and phase purities of the samples were confirmed using powder X-ray diffraction (XRD).

Two sets of symmetric diamond anvil cells (DAC) were used to achieve a static high pressure in the lab. For Raman and synchrotron XRD measurements, a DAC equipped with two type-I diamonds with a 600 μm culet size was being used, while a pair of type-II diamonds with the same culet size was used for IR measurements. All the gaskets used in high-pressure experiments were made of stainless steel, and were pre-indented to ~50 μm thick. The sample chambers were 200-210 μm in diameter. A few ruby chips were loaded into the sample chamber as the pressure calibrant. The pressure inside the sample chamber was then measured according to the well-established ruby fluorescent method. In high-pressure studies of empty frameworks, the pure samples were loaded into the DAC without any fluid pressure-transmitting medium (PTM) for Raman and IR measurements to rule out the possible guest-host interactions. In order to obtain unsaturated IR spectra, the samples were packed with solid KBr for IR measurements. For Synchrotron XRD experiments, the neon gas was used as a penetrating PTM, loaded by the gas loading system at the GSECARS beamline of Advanced Photon Source (APS) at Argonne National Laboratory (ANL).

To study the CO_2 adsorption in MOFs under high pressure, the activated PbSDB or CdSDB samples and a few ruby chips were firstly loaded into the sample chamber of the DAC, then the piston side of the DAC was cooled down in a cryogenic bath of liquid nitrogen. An electronic thermometer was used to monitor the temperature of the DAC piston. When the temperature was below the melting point of dry ice (< -78.5 °C), gaseous CO_2 was then introduced into the sample chamber, extra dry ice powder was used to completely fill the piston. Then, the DAC was sealed with a minimal possible pressure (~ 0.5 GPa). After the DAC was warmed up to room temperature, the internal pressure was measured by the ruby fluorescence.

The Raman measurements were carried out with a customized Raman micro-spectroscopy system. Two types of lasers with different wavelengths of 532 and 781 nm were used as the excitation sources. The lasers were focused to < 5 μm on the sample by a 20× Mitutoyo

objective. The scattered light was dispersed using an imaging spectrograph equipped with an 1800 lines/mm grating achieving a 0.1 cm^{-1} resolution. The system was calibrated by neon lines with an uncertainty of $\pm$ 1 cm^{-1}.

A customized IR micro-spectroscopy system was used for IR measurements. A commercial Fourier transform infrared (FTIR) spectrometer from Bruker Optics Inc. equipped with a Globar IR light source constituted the main component of the micro-IR system, which was operated under a vacuum of <5 mbar such that absorption by H_2O and CO_2 was efficiently removed. The size of the IR beam was set to be identical to the entire sample size (e.g., ~150 μm) by a series of iris apertures. The transmitted IR beam was collected using another identical reflective objective as the condenser and was directed to a mid-band mercury cadmium telluride (MCT) detector equipped with a ZnSe window that allows measurements in the spectral range of 400-12000 cm^{-1}. All measurements were undertaken in transmission mode with a resolution of 4 cm^{-1} and 512 scans were applied for each spectrum measurement achieving an excellent signal-to-noise ratio. To collect the absorbance, the absorption of diamond anvils with KBr was used as background for each sample.

The PXRD patterns were collected by the synchrotron facilities at beamline Sector-20ID and 16BM (for PbSDB and CdSDB, respectively) of APS at ANL. The incident X-ray wavelength is 0.4769 Å at Sector 20 ID with a beam size of 5 μm (H) x 5 μm (V) focused at the centre of the sample. The diffraction data for PbSDB were collected by a MARCCD detector with an exposure time from 30 s to 90 s depending on the data qualities, the 2D Debye-Scherrer diffraction patterns were then integrated into 1D patterns by Dioptas030 program for further analysis. The in situ high pressure XRD measurements for CdSDB were carried out at Sector 16 BM, APS. The diffraction data were collected using an exposure time of 600 s and recorded on a MAR345 detector. The integrations were done using Fit2D program.

3.3 Results and discussion

3.3.1 Structural stability of activated frameworks

Upon activation of CdSDB and PbSDB, we characterized both frameworks at ambient conditions using Raman spectroscopy and mid-IR absorption spectroscopy with the corresponding spectra depicted in Fig 3.2 as the starting point. Our results are in excellent agreement with those reported by Plonka *et al.*[10] In the Raman spectrum, specifically, Raman modes below 400 cm^{-1} can be assigned as lattice vibrations, indicating a high degree of crystallinity, consistent with XRD measurements. The metal-ligand stretching mode which is expected at around 300-400 cm^{-1},[37] is observed in the Raman spectrum at 357 cm^{-1}, but beyond the mid-IR range in our measurement. Above 500 cm^{-1}, all the Raman and IR active modes are associated with the internal vibrations of SDB ligands with detailed assignments provided in Table 3.1. Among these vibrations, of particular interests are the sulfonyl stretching vibrations (ν(OSO)) at around 1300 cm^{-1} and the symmetric and asymmetric carbonyl stretching mode at ~ 1400 cm^{-1} (ν_s(OCO)) and ~ 1600 cm^{-1} (ν_{as}(OCO)), respectively, as the metal-ligand interactions under compression maybe sensitively reflected by these modes. In addition, the ring in-plane (1000-1200 cm^{-1}) and out-of-plane (500-900 cm^{-1}) bending modes may provide fingerprint response of SDB ligands to external compression.
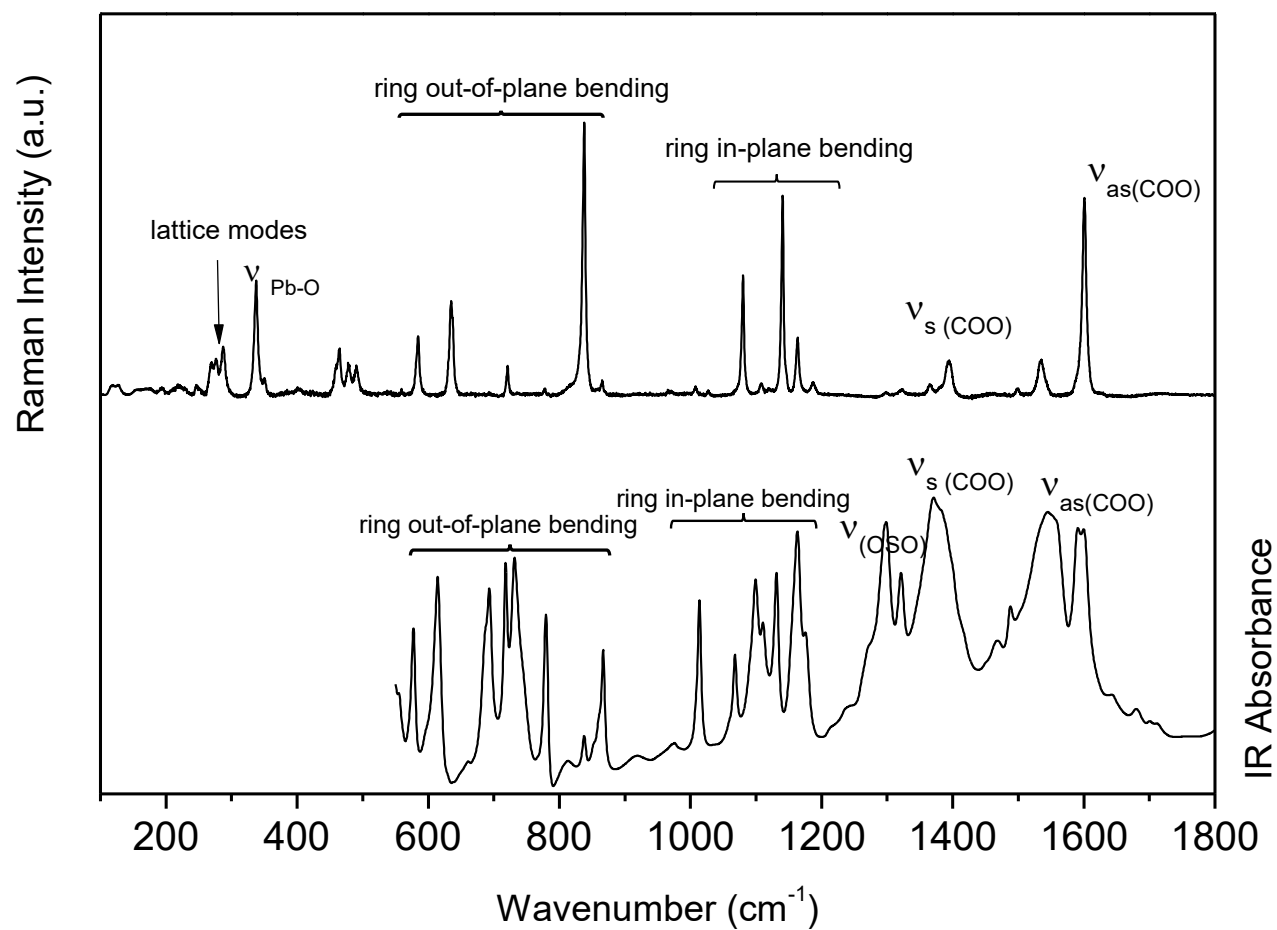
Figure 3.2 IR (bottom) and Raman (top) spectra of activated PbSDB at ambient pressure in the spectral region of 100-1800 cm⁻¹.

Table 3.1 Assignment of the characteristic IR mode of PbSDB and CdSBD.

IR modes	Frequencies (cm^{-1})	
	PbSDB	CdSDB
Ring out-of-plane bending	560-900	540-890
Ring in-plane bending	990-1190	995-1200
ν(OSO)	1298 and 1321	1293 and 1332
ν_s(COO)	1375	1369 and 1401
ν_{as}(COO)	1547 and 1595	1567, 1598 and 1616
ν(C-H)	3040, 3064 and 3093	3042, 3058 and 3072

Upon compression of PbSDB to less than 1 GPa, most of the lattice modes diminished with only the Pb-O stretching mode at 357 cm^{-1} observable, but significantly broadened (Fig 3.3a). This observation suggests that the framework undergoes a structural transition to a highly disordered or amorphous phase. Upon further compression to higher pressures (e.g., 13.44 GPa), the Pb-O stretching mode becomes extremely broad, which is indicative of the total amorphization. The corresponding mid-IR spectra of the framework show a similar trend of pressure-induced structural disorder as characterized by the continuous broadening of most of the IR modes, especially the OSO and OCO stretching modes (Fig 3.3b). Upon decompression, the backward structural changes were observed. However, the Raman spectrum of the recovered material does not completely resemble the one collected before compression. In particular, other than the broadened primary lattice modes, all other modes are substantially suppressed, indicating pressure-induced irreversible modifications of the crystallinity of the framework. The IR spectrum of the recovered material (Fig 3.3b), however, is consistent with that collected before compression, indicating the framework structures, especially the major bonding connectivity, are intact upon compression despite the change in crystallinity.
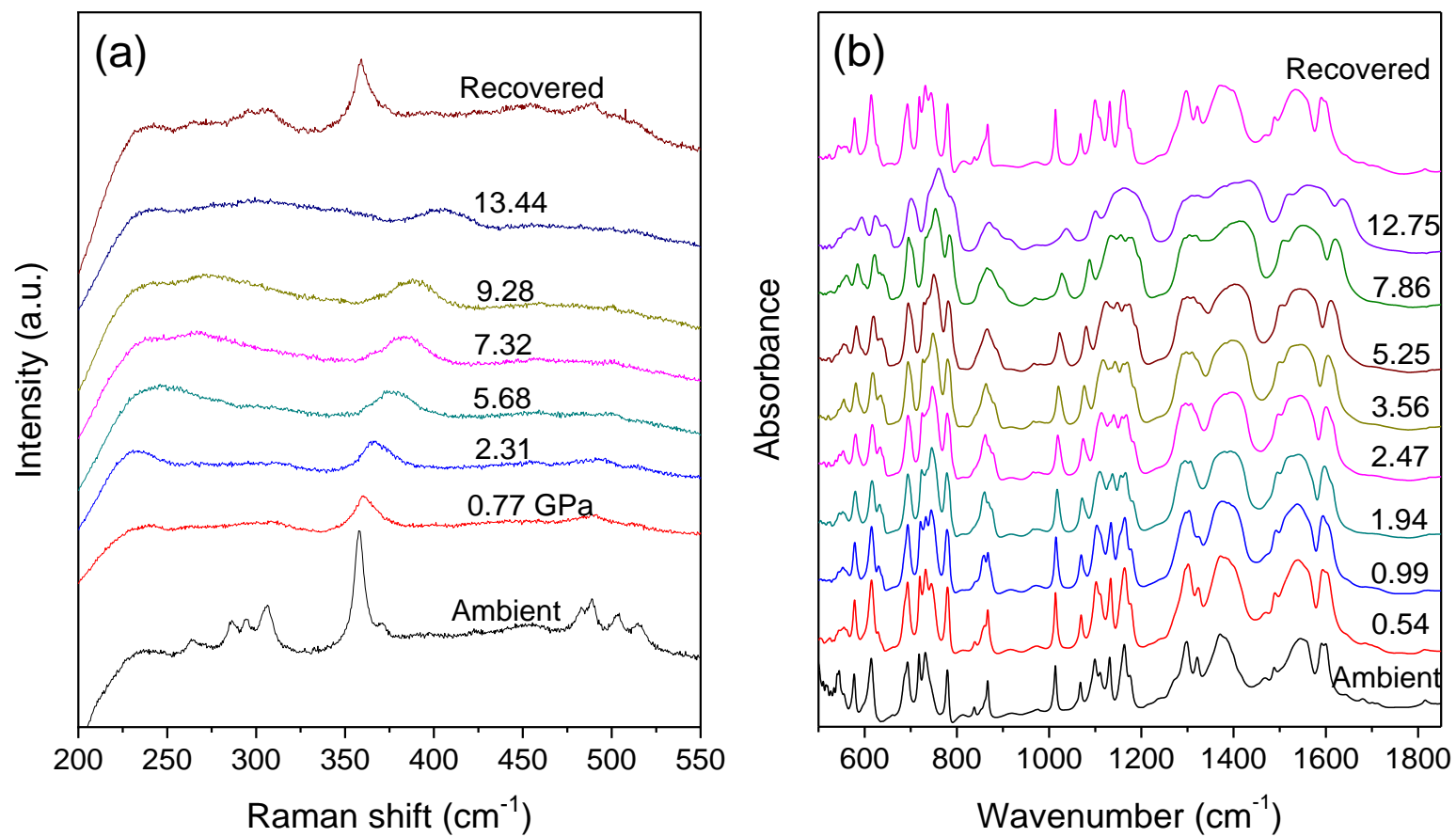
Figure 3.3 Raman (a) and IR (b) spectra of PbSDB at selected pressures upon compression and recovery.

To confirm the pressure-induced crystal and structural change in the PbSDB framework, we performed in situ synchrotron powder X-ray diffraction measurements with representative patterns depicted in Fig 3.6a. As can be seen, the PbSDB at ambient conditions exhibits excellent crystallinity characterized by sharp reflections which can be perfectly indexed with Pnma structure. Upon compression, all reflections become broadened with decreasing intensity indicating the reduced crystallinity of the material. At 6.03 GPa, only an extremely broad reflection at 4.12° was observed, indicating the total amorphization of the materials. These observations are consistent with the Raman and IR measurements. Upon decompression, the reverse transformation from amorphous to crystalline material was observed. However, the recovered material exhibited broadened reflections compared to the pattern of the uncompressed sample, indicating irreversible pressure modification of crystallinity of the framework, again consistent with the Raman results.

We further comparatively studied the structural stability of the CdSDB framework using IR absorption spectroscopy (Fig 3.4) and synchrotron powder XRD measurement (Fig 3.5). The high fluorescent background of the activated CdSDB sample prohibited us from collecting the Raman spectra. Nonetheless, we observed similar pressure effect on the CdSDB framework, i.e., pressure-induced structural disordering and ultimate amorphization at high pressures. Interestingly, the total amorphization pressure for CdSDB framework as indicated by the diffraction profile is substantially higher than that for PbSDB, which is estimated as close to 12.5 GPa. Furthermore, the diffraction pattern for recovered material shows excellent crystallinity almost comparable to the starting materials. These observations suggest that both PbSDB and CdSDB frameworks are chemically stable upon external compression, but CdSDB is more resilient to structural deformation induced by pressure. This difference can be understood from their structural origins which will be discussed next.

Table 3.2 Unit cell parameters and volume of PbSDB and CdSBD on compression.

Pressure (GPa)	a (Å)	b (Å)	c (Å)	V (Å^3)
PbSDB				
0	5.9527	13.0441	19.5721	1520.2
0.24	5.8946	13.1258	19.3952	1500.6
0.87	5.7983	13.1094	19.0436	1447.5
1.80	5.7982	12.9451	17.2935	1292.3
2.97	5.6615	13.1276	16.5630	1231.0
CdSDB				
0	13.3382	21.4986	10.1527	2900.2
0.97	13.0978	21.1392	10.2475	2820.7
1.42	13.0259	21.1031	10.2430	2798.2
2.26	12.9631	21.0214	10.0915	2734.9
3.34	12.8751	20.9434	10.0985	2704.6
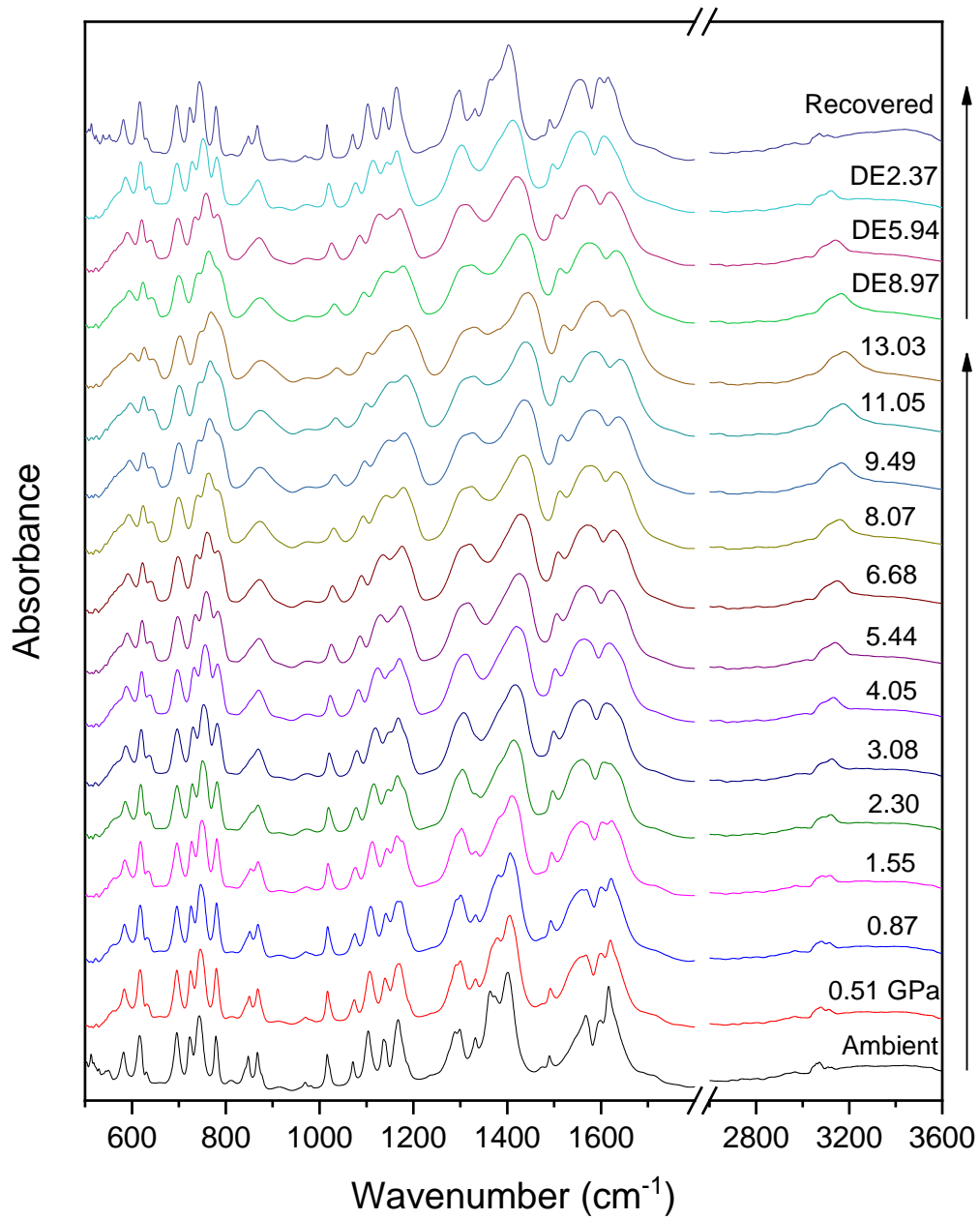
Figure 3.4 Selected IR spectra of activated CdSDB on compression up to the highest pressure of 13.03 GPa and on decompression to ambient pressure.
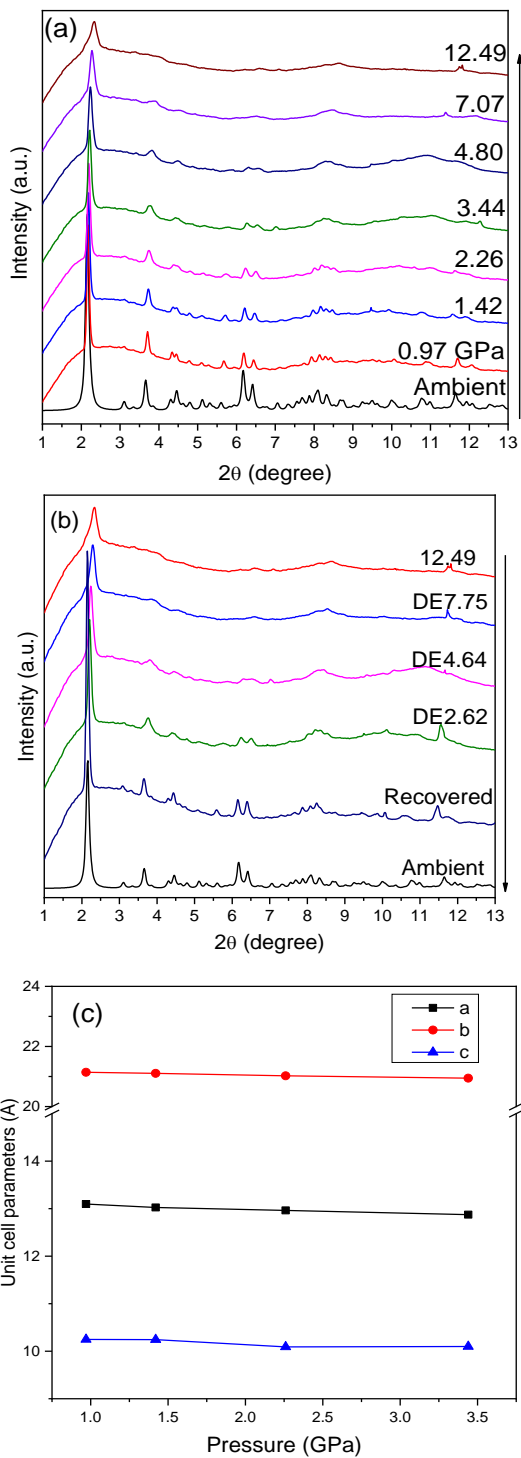
Figure 3.5 Synchrotron XRD spectra of CdSDB upon compression from ambient to 12.49 GPa (a) and recovery (b) in the 2θ region of 3.5-13°. (c) Refined unit cell parameters.
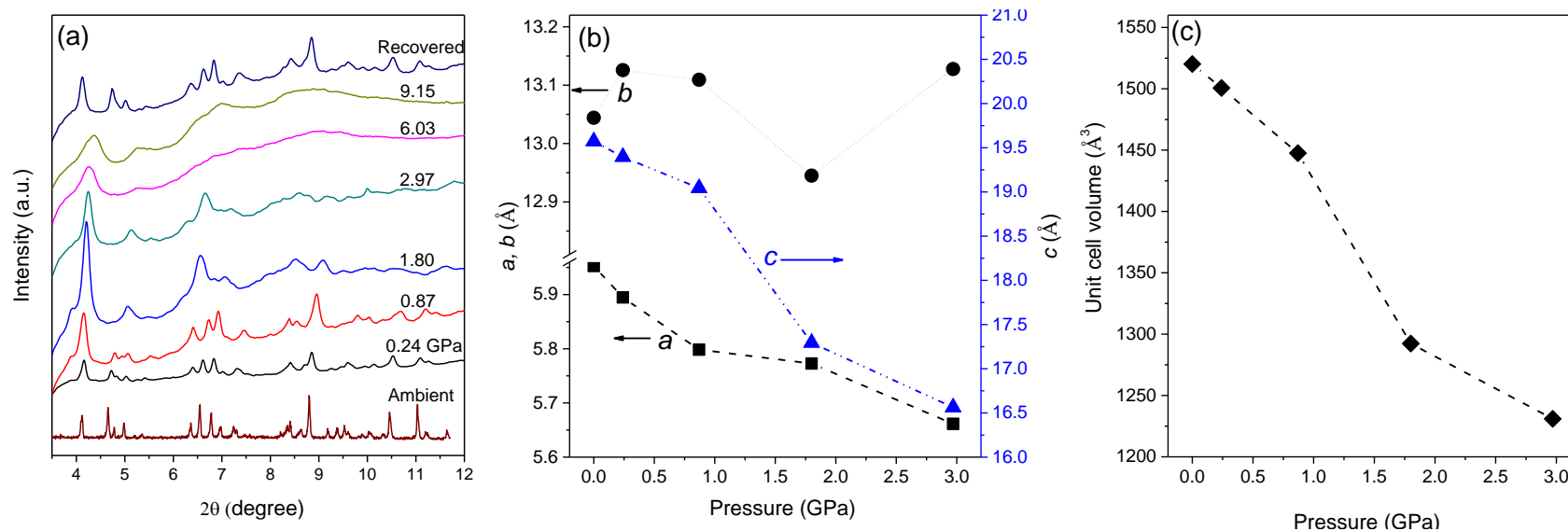
Figure 3.6 (a) Synchrotron powder X-ray diffraction patterns of PbSDB upon compression from ambient to 9.15 GPa and recovery in the 2θ region of 3.5-12°. (b) The refined unit cell parameters of PbSDB framework) as a function of pressure (*a*: black squares; *b*: black circles; and c: blue triangles). (c) The refined unit cell volume of PbSDB as a function of pressure upon compression.

3.3.2 Guest-host interactions in CO_2 loaded CdSDB framework

CdSDB has been reported to have a relatively large surface area (i.e., 100 m^2/g) and moderate porosities, giving an excellent CO_2 adsorption capacity (4.25 wt% at 273 K and 1 atm) under near ambient conditions. We have previously demonstrated that external pressure can substantially enhance the CO_2 intake in MOFs such as ZIF-8. Therefore, it's of particular interest to examine and compare the CO_2 storage capacity of CdSDB at high pressures as well. Fig. 5 shows the typical IR spectra of CdSDB framework loaded with CO_2 at different pressures in the spectral region of 3500-3800 cm^{-1}. Due to the very intense absorption of CO_2 fundamental modes causing spectra saturation, we used this region that correspond to the combination modes (e.g. $\nu_3 + 2\nu_2$ and $\nu_3 + \nu_1$, observed at around 3600 and 3710 cm^{-1}, respectively at 0.50 GPa) to follow the behaviour of the CO_2 as these peaks provide the best resolved and most characteristic features about guest-host interactions between CO_2 and the framework. The splitting of both modes at 0.63 GPa (Fig 3.7a) indicates the insertion of CO_2 into the pores of the CdSDB framework resulting in two different types of CO_2 in the system. The lower frequency modes (3582 and 3690 cm^{-1}) can be assigned as the CO_2 inside the CdSDB channels while the higher frequency modes (3603 and 3712 cm^{-1}) are due to the CO_2 outside the framework as the pressure medium based on the comparison with the observed frequencies of pure CO_2 at similar pressures for these modes (Fig 3.7c).[17, 38] Further compression to 0.87 GPa resulted in more prominent separation of CO_2 in two different environments due to the solid CO_2 formed from liquid-to-solid phase transition residing outside the framework. Continues compression to 2.48 GPa results in no other changes in the adsorption profile with nearly constant relative intensities of the respective mode associated with CO_2 inside and outside framework indicating there is no CO_2 migration in between the two environments as a result of compression. Careful examination of the pressure dependence of the low frequency component of $\nu_3 + 2\nu_2$, however, suggest a redshift of the component till 1.5 GPa above which normal blue shift was observed (Fig. 5c). The redshift is indicative of weakening of the C-O bond in CO_2, as a result of enhanced guest-host interaction due to compression reaching to the strongest at 1.5 GPa.
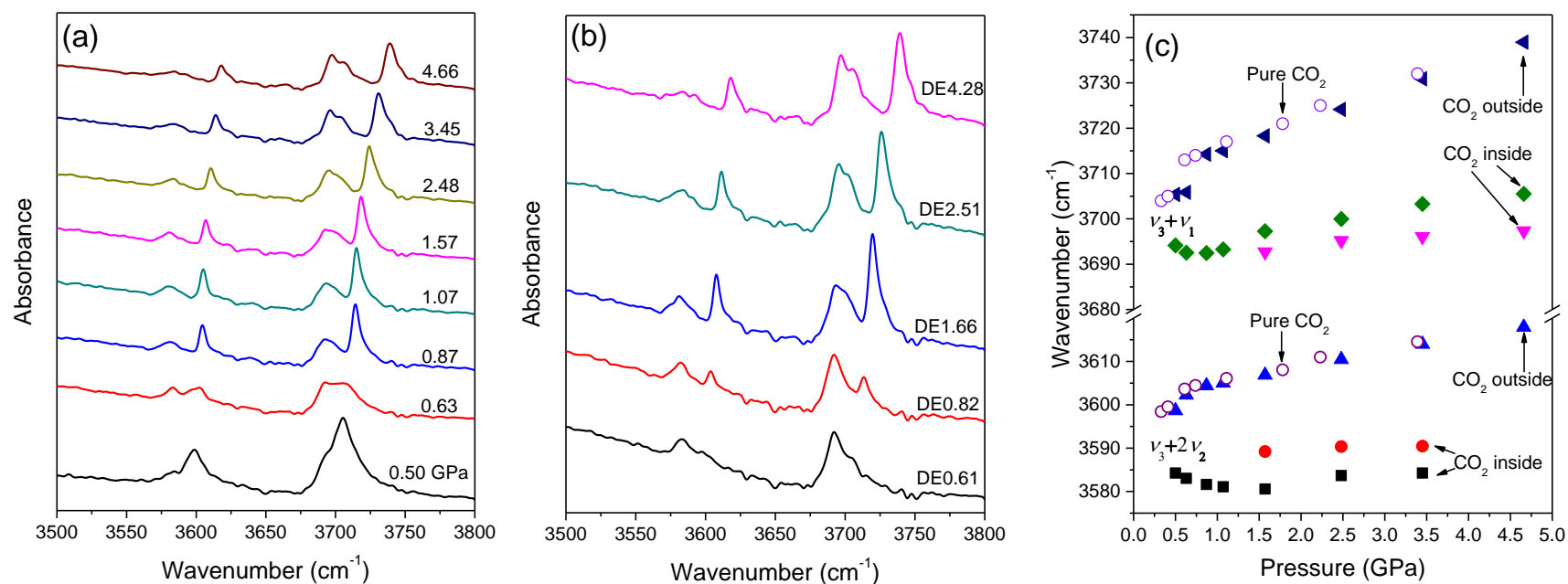
Figure 3.7 IR spectra of CdSDB loaded with CO_2 upon (a) compression from 0.50 to 4.66 GPa and (b) decompression to 0.61 GPa in the spectral region of 3500-3800 cm^{-1}. (c) Pressure dependence of $\nu_3+2\nu_2$ and $\nu_3+\nu_1$ modes of loaded CO_2 in CdSDB.

The most interesting observation is the appearance of a new IR mode as a shoulder for the $v_3 + v_1$ mode of CO_2 inside the framework when compressed to 3.45 GPa (Fig 3.7a). The additional IR absorption suggests the formation of an additional non-equivalent CO_2 adsorption site within the framework due to compression. This new CO_2 adsorption site remains prominent upon further compression to pressures near 5 GPa. Upon decompression, the new CO_2 adsorption remains observable down to 2.5 GPa (Fig 3.7b), below which the IR profile in this region suggests that CO_2 mainly resides on a single adsorption site in the low-pressure region. These observations suggest that high external pressure is responsible for creating and maintaining the new adsorption site, which is highly dependent on the framework structures that are affected by pressures. Overall, the pressure-tuned guest-host interactions between CO_2 and the CdSDB framework are completely reversible with respect to compression and decompression, resulting in neither permanent binding of CO_2 into the framework nor structural change of the framework.

3.3.3 Guest-host interactions in CO_2 loaded PbSDB framework

We also investigated the CO_2 storage capacity and guest-host interaction in the PbSDB system. Fig 3.8 shows the IR spectra of CO_2 loaded PbSDB framework in the combination mode region and the pressure dependence of the two characteristic composition modes. Compared to the IR spectrum of pure liquid CO_2 collected at 0.33 GPa, interestingly, the adsorbed CO_2 at similar loading pressure (e.g., 0.29 GPa) exhibited a distinctively different IR profile in both the band shape and particularly the frequencies that are substantially red-shifted from 3598 and 3704 cm^{-1} to 3581 and 3690 cm^{-1} for $v_3 + 2v_2$ and $v_3 + v_1$, respectively. Moreover, the dominant singlet IR band for adsorbed CO_2 with the extremely low IR intensity associated with CO_2 outside the framework suggests that the CO_2 intake at PbSDB is much more efficient than CdSDB even at low pressures, indicating significantly stronger guest-host interactions in the PbSDB framework than in the CdSDB system. With increasing pressure to 0.59 GPa, the $v_3 + v_1$ mode exhibits an obvious splitting leading to the observation of a higher frequency component at 3694 cm^{-1}. The splitting of this mode is most likely associated the formation of a new, non-equivalent CO_2 adsorption site of the PbSDB framework, similar to the observation of CdSDB framework at 3.45 GPa, although the formation pressure is much lower here. With further compression, strikingly, the

intensity of the new higher-frequency component of $v_3 + v_1$ mode develops rapidly and becomes the dominant mode above 1.68 GPa. At 4.28 GPa, the original low-frequency component of $v_3 + v_1$ mode is completely depleted with only a single sharp symmetrical IR mode observed at 3705 cm^{-1}. This low frequency indicates that all the adsorbed CO_2 is confined in PbSDB framework via the strong guest-host interactions as the $v_3 + v_1$ peak of pure CO_2 at similar pressure (e.g., 4.18 GPa) appears at a much higher frequency of 3732 cm^{-1}.

On decompression, the $v_3 + v_1$ mode of CO_2 adsorbed in the framework maintains a single sharp symmetrical peak until 2 GPa (Fig 3.8b). Starting from 1.68 GPa, the original low-frequency component is resolved, and the intensity is recovered with further decompression. The intensity switch-over between the two components leading to the low frequency component being the dominant mode occurs at 0.91 GPa, a pressure similar to that during compression. Below 0.44 GPa, only the original low-frequency component is observable, indicating the CO_2 mainly resides on a single adsorption site in the PbSDB framework. All these observations suggest that pressure regulated formation and new CO_2 adsorption site is completely reversible.
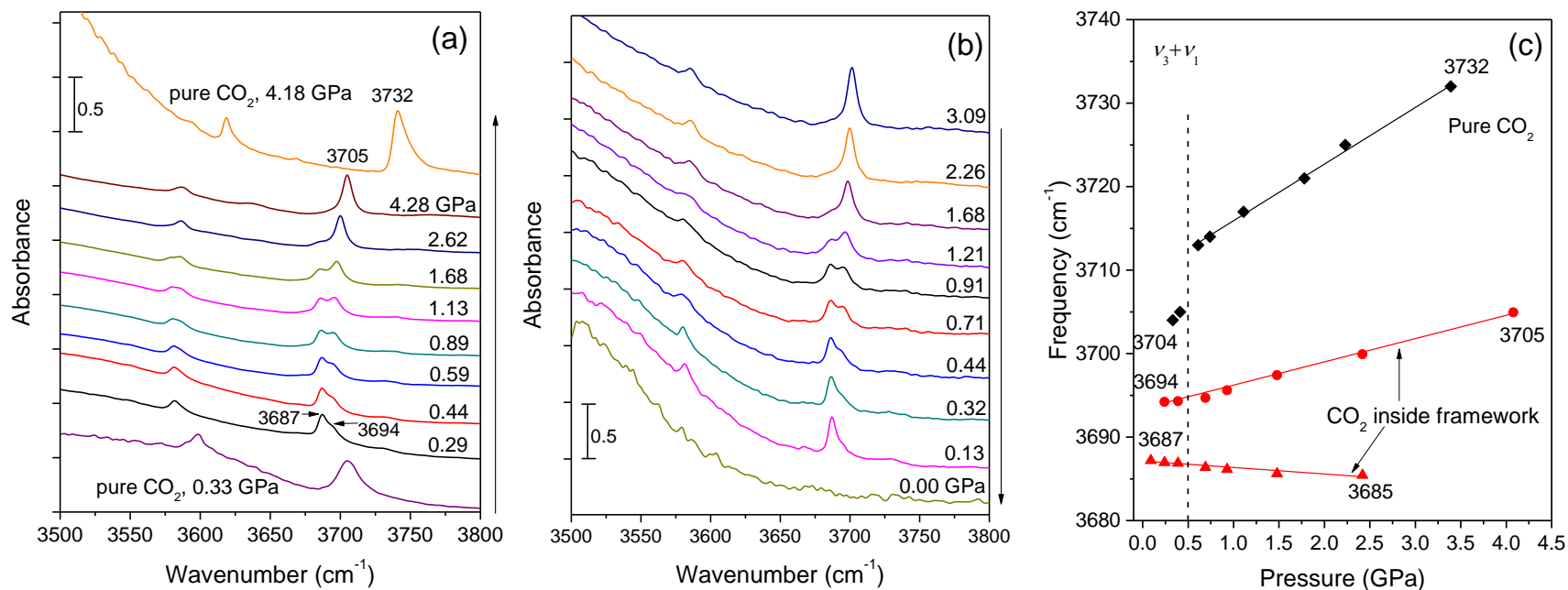
Figure 3.8 IR spectra PbSDB loaded with CO$_2$ upon (a) compression from 0.24 to 4.28 GPa in comparison with that of pure CO$_2$ at representative pressures and (b) decompression to ambient pressure in the spectral region of 3500-3800 cm^{-1}. (c) The pressure dependence of the $v_3 + v_1$ mode of CO$_2$ loaded with PbSDB (red circles and triangles), and that of pure CO$_2$ (black squares).

Table 3.3 Frequencies and pressure dependence (dv/dP) of CO_2 combination modes observed in CdSDB and PbSDB frameworks in comparison with reference values as pure CO_2.

Mode	CdSDB		PbSDB		Pure CO_2	
	Frequency[a] (cm^{-1})	dv/dP (cm^{-1} · GPa^{-1})	Frequency[a] (cm^{-1})	dv/dP (cm^{-1} · GPa^{-1})	Frequency[a] (cm^{-1})	dv/dP (cm^{-1} · GPa^{-1})
$v_3 + 2v_2$	3584	1.96	3581	1.22	3603	3.67
	3589[b]	0.66				
	3599	3.57				
$v_3 + v_1$	3692[b]	1.43	3687	-0.79	3712	6.38
	3694	3.44				
	3705	6.26	3694	2.79		

a. Unless otherwise mentioned, observed and measured at the first point on compression to a pressure close to the pure CO_2 liquid-to-solid phase transition (i.e., ~ 0.5 GPa).

b. Extrapolated to 0.5 GPa based on linear fit.

Interestingly, careful examination of the pressure dependence on the two components of the $v_3 + v_1$ mode reveals that the low frequency component undergoes a redshift while the high frequency component shifts to blue (Fig 3.8c and Table 3.3). Again, this observation is in strong contrast to the CO_2 loaded CdSDB systems and thus the mechanism of pressure regulated adsorption sites could be different in the two systems. First of all, the formation of a new adsorption site at high pressure for CdSDB system is likely the result of removal of degeneracy of equivalent adsorption sites (see following discussion). However, this formation mechanism can be ruled out for the CO_2 loaded PbSDB system in that two components undergo opposite pressure-induced frequency shift, indicating that the two sites are distinctively non-equivalent at the beginning. Moreover, the relative intensity of the two components of the $v_3 + v_1$ mode remains constant upon compression, indicating the binding strength of two sites in PbSDB is independent of compression. In contrast, the intensity variation of the two components of the $v_3 + v_1$ mode in the CO_2 loaded PbSDB

system suggests the CO_2 is migrating from one site to another under the influence of external compression. The depletion of the low frequency component suggests that CO_2 adsorbed on this site is becoming more unstable with weakened C=O bond (as the $\nu_3 + \nu_1$ mode exhibits a redshift) such that the new adsorption site associated with the higher-frequency component is the preferred site at high pressures.

3.3.4 Structural origins of the contrasting compression stabilities of activated frameworks

The Raman, IR and XRD measurements collectively show that although the chemical structures of both frameworks are highly stable upon external compression, the crystallinity of PbSDB is sensitive to compression whereas the pressure modification of the crystallinity of CdSDB completely reversible. These contrasting behaviours can be understood from the starting crystal structure and framework topology of each framework. First of all, the Cd metal centre is six coordinated with oxygen atoms from SDB ligand forming a $[CdO_6]$ octahedron in the CdSDB framework at ambient pressure. Although the six oxygens are non-equivalent (two equivalent with 4 non-equivalent, see Fig 3.1c), the geometry of the octahedron can be considered quasi-isotropic topology with respect to Cd metal centre. As a result, external compression on the framework especially on the CdO_6 octahedron may induce isotropic responses including bond shortening and crystal lattice contraction. A strong evidence of isotropic compression is the smooth evolution of the unit cell parameters with almost identical contraction rate of cell parameters a, b and c (Fig 3.5 and Table 3.2). Moreover, such isotropic topology is also consistent with resilience to external compression which leads to amorphization but only at very high pressures, as well as the complete reversibility of pressure modification of the crystallinity.

In contrast, Pb in the PbSDB framework is coordinated with seven oxygens that are in four symmetry non-equivalent groups (two O1, two O3, two O4 and one O5, see Fig 3.1a), resulting in the formation of an axially truncated nine-faced polyhedron where the axis is defined by the Pb-O5 bond. This seven-coordinated, highly non-symmetrical bonding geometry may respond to isotropic compression in a highly non-isotopically way. Indeed, the XRD analysis suggests that not only the contraction rate of the three cell parameters are drastically different, but *b* axis exhibit a peculiar non-monotonic compression

behaviour with pressure (Fig 3.6b and Table 3.2), although the overall unit cell volume exhibits a normal pressure-induced contraction (Fig 3.4 and Table 3.2). As a result, the $[PbO_7]$ polyhedron is less resilient to external compression that may easily induce structural distortion of the PbO_7 leading to a facile spontaneous amorphization at relatively lower pressures. Such distortion associated with anisotropic responses to external compression may be permanent leading to the irreversible pressure modification of the crystal structures. More importantly, such anisotropic topology of PbSDB framework may profoundly influence the CO_2 adsorption and guest-host interactions which will be discussed next.

3.3.5 Structural origins of the contrasting pressure-tuned CO_2 adsorption sites

The CO_2 adsorption study and guest-host interactions for both CdSDB and PbSDB frameworks at near ambient conditions have been extensively reported.[9, 12, 13] However, the number of CO_2 adsorption sites and the nature of guest-host interactions may be substantially different than at high pressures and can be tuned by external compression efficiently. In particular, low-temperature ^{13}C SSNMR spectroscopic study on CO_2 loaded CdSDB suggests that CO_2 occupies two non-equivalent sites in the CdSDB framework.[13] In addition, single X-ray diffraction on CO_2 loaded CdSDB framework confirmed that the two non-equivalent adsorption sites (labeled as C1A and C1B) are constituted by two different π-pockets from the phenyl-rings of the SDB ligands (Fig 3.9a and 3.9b).[13] As demonstrated by both SSNMR and single crystal XRD studies, the nature of the interaction between CO_2 molecules and both MOF frameworks is that the quadrupole moment of CO_2 interacts with the π-electrons of the two phenyl rings.[13] The prerequisite for π-pocket is that the two phenyl rings in the π-pocket must face to each other, which is met for the first adsorption site in both MOFs (labeled with C1A in Fig 3.9a and 3.9c). In CdSDB, the two rings from two different linkers are also facing each other, and thus form the second CO_2 adsorption site (labeled C1B in Fig 3.9b). In contrast, the single crystal XRD result for PbSDB at ambient pressure has shown that the phenyl rings from two different linkers are almost perpendicular to each other, so that only one effective CO_2 adsorption site can be formed (Fig 3.9c).

Based on the above structural analysis, CdSDB is expected to exhibit two distinctive adsorption sites spectroscopically. At low loading pressures (e.g., < 2.5 GPa) in this experiment, however, only one CO_2 adsorption site was observed as evidenced by the single peak of both $v_3 + 2v_2$ and $v_3 + v_1$ combination modes. This can be interpreted as although the two adsorption sites are crystallographically non-equivalent, the corresponding vibrational frequencies are near degenerate due to the small difference between these two sites. Upon further compression, however, due to the different extent of the guest-host interaction associated with non-equivalent environment of the SDB framework, the degeneracy of the vibrational frequency is removed, resulting in the observation of a higher frequency component associated with the second adsorption site. No further intensity change between the two components suggests the guest-host interactions between the two adsorption sites are equally favoured, consistent with the isotropic compression behaviour of the CdSDB framework discussed above.
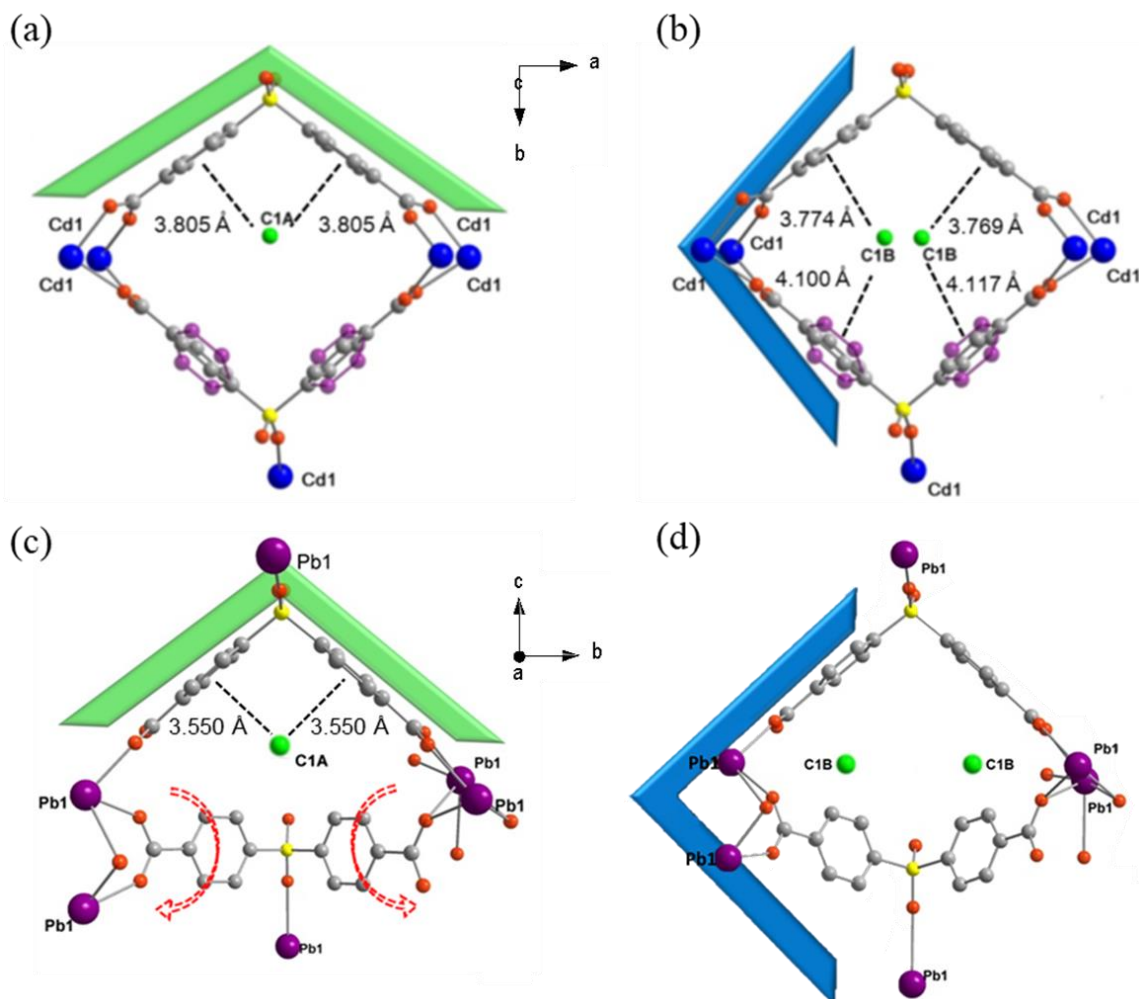
Figure 3.9 Schematics of CO_2 adsorption sites in CdSDB at ambient pressure and low temperature (a) and (b), and at high pressures (b), and in PbSDB at ambient pressure (c) and high pressures (d). The green balls represent CO_2 molecules inside the pores of CdSDB and PbSDB, with the oxygen atoms omitted. The green and blue brackets are showing two different types of π-pockets in the channels. The dash lines symbolize the interactions between CO_2 and the specific adsorption sites of the frameworks.

In contrast, single crystal X-ray diffraction on CO_2 loaded PbSDB frame shows that only one CO_2 adsorption site is possible given the orientations of the SDB ligands in the cavity. This single adsorption site is similarly constituted by a π-pocket from the phenyl rings of the same SDB linker that is 3.550 Å away from the CO_2 centre (Fig 3.9c). The observation of the single component of the $v_3 + v_1$ mode at low loading pressures (e.g., 0.29 GPa) is

consistent with that only one π-pocket is favourable at low pressures. At high pressures, the clear splitting of the $v_3 + v_1$ mode strongly suggests the formation of a new CO_2 adsorption site. Therefore, it is necessary that the phenyl rings involving two SDB linkers undergo a pressure-induced change in their orientations. The fact that the original adsorption site (C1A) remains upon compression indicates that the π-pocket involving the two phenyl rings from the same SDB linker is affected very little by the pressure. Thus, it is highly likely that pressure changes the orientation of the phenyl rings in two adjacent SDB linkers substantially (as illustrated in Fig 3.9c), creating a second π-pocket. As indicated in Fig 3.9d, the rotation along the axis collinear with the C-S and C-COO bonds can change the phenyl orientation. Such rotation results in that the two phenyl rings from the two SDB linkers face to each other, effectively creating a new CO_2 adsorption site (C1B, Fig 3.9d). The pressure-induced ring rotations and pore opening have been reported in ZIF-8 system.[29, 30]

Then the remaining questions is that why the guest-host interactions between CO_2 and the two frameworks are drastically different in that the two adsorption sites in CdSDB is equally favoured at high pressure, whereas the population of CO_2 favours the newly formed adsorption site in PbSDB at high pressures. This again, can be addressed from the anisotropic topology of the PbSDB framework. The XRD analysis shows that *c*-axis is substantially more compressible than the other two, whereas *b*-axis in extremely resistant to compression (Fig 3.6 and Table 3.2). These non-isotropic compression rates necessarily reduce the distances between the two adjacent SDB ligands while elongating the distance between the phenyl rings of the same ligand (Fig 3.9d). As a result, the interaction between the CO_2 and the π-pocket of PbSDB formed by the phenyl rings from the same SDB ligand (depicted as green brackets in Fig 3.9c) is becoming less efficient as a result of compression. At very high pressures (e.g., 4.28 GPa), the structural distortion is so prominent such that the initial π-pocket (green brackets) for Pb is nearly completely inaccessible. In contrast, the π-pocket formed by the phenyl rings from adjacent SDB ligands (blue bracket in Fig 3.9d) becomes the only adsorption site (C1B), while the conservation of the total CO_2 adsorbed in the framework is maintained. In the case of CdSDB, the framework undergoes an isotropic compression, where the a, b and c axes show similar contraction rates upon elevating pressure (See Fig 3.5c and Table 3.2). Therefore, the two different types of π-

pockets in CdSDB remain equally favoured for CO_2 at high pressures. Pressure-induced formation of new CO_2 adsorption sites and the regulation of guest-host interactions between different sites observed in the PbSDB system is unique and unprecedented for any previously studied MOF under high pressures, and thus is of fundamental importance in applications of CO_2 storage in MOFs. Finally, in the future, it would be desirable to conduct in situ synchrotron-based single crystal diffraction measurements of CO_2 loaded SDB frameworks as a function of pressure to gain in-depth understanding of the structure-property relationships and detailed mechanism of guest-host interactions.

3.4 Conclusions

In summary, using Raman spectroscopy, FTIR spectroscopy, synchrotron powder X-ray diffractions, we comparatively investigated the structural stabilities and CO_2 adsorption behaviours of CdSDB and PbSDB MOFs at high pressures up to 13 GPa in situ. Both activated CdSDB and PbSDB frameworks undergo a structural modification to amorphous state but with chemical structures intact. Upon decompression, the structural changes for CdSDB are completely reversible while PbSDB exhibited a reduced crystallinity. The different compression behaviour can be understood from the structural origins pertaining the near isotropic CdSDB coordination vs non-isotropic PbSDB coordination, as strongly corroborated by the pressure dependences of the unit cell parameters of respective frameworks. Although CdSDB is known to possess two CO_2 adsorption sites at ambient pressure, only one spectroscopically degenerate site is observed at low pressures in the CO_2 loaded CdSDB system while the degeneracy is removed at high pressures leading to the observation of the second adsorption site. In contrast, PbSDB has only one CO_2 adsorption site at ambient pressure but exhibits a new adsorption site upon compression. This newly formed adsorption site is structurally and thermodynamically favoured as evidenced by the CO_2 population growth with pressure, which becomes the only populated site at high pressures. The formation of the new CO_2 adsorption site in PbSDB can be understood from pressure-induced structural change associated with symmetry breaking via phenyl-ring rotation. The pressure-tuned CO_2 population variations between the two sites can be attributed to the contrasting, non-isotropic response of the unit cell parameters which leads to the change of the critical distances for the formation and destruction of CO_2 adsorption

sites in the framework. This study demonstrates that pressure can effectively and contrastingly tune the structures and CO_2 adsorption performance of CdSDB and PbSDB MOFs and provide useful insight into the understanding of structural origins for guest-host interactions which are critical for CO_2 storage applications.

3.5 References

1. Furukawa, H.; Cordova, K. E.; O'Keeffe, M.; Yaghi, O. M., The chemistry and applications of metal-organic frameworks. *Science* **2013,** *341* (6149), 1230444.

2. Li, J. R.; Sculley, J.; Zhou, H. C., Metal–Organic Frameworks for Separations. *Chem Rev* **2012**, *112*, 869-932.

3. Ranocchiari, M.; van Bokhoven, J. A., Catalysis by metal–organic frameworks: fundamentals and opportunities. *Phys Chem Chem Phys* **2011**, 13, 6388-6396.

4. Horcajada, P.; Gref, R.; Baati, T.; Allan, P. K.; Maurin, G.; Couvreur, P.; Ferey, G.; Morris, R. E.; Serre, C., Metal–Organic Frameworks in Biomedicine. *Chem Rev* **2012**, *112*, 1232-1268.

5. Kreno, L. E.; Leong, K.; Farha, O. K.; Allendorf, M.; Van Duyne, R. P.; Hupp, J. T., Metal-organic framework materials as chemical sensors. *Chem Rev* **2012**, *112*, 1105-1125.

6. He, Y.; Zhou, W.; Qian G.; Chen, B., Methane storage in metal–organic frameworks. *Chem Soc Rev* **2014**, *43*, 5657-5678.

7. Sumida, K.; Rogow, D. L.; Mason, J. A.; McDonald, T. M.; Bloch, E. D.; Herm, Z. R.; Bae, T. H.; Long, J. R., Carbon Dioxide Capture in Metal–Organic Frameworks. *Chem Rev* **2012**, *112*, 724-781.

8. Suh, M. P.; Park, H. J.; Prasad, T. K.; Lim, D. W., Hydrogen storage in metal-organic frameworks. *Chem Rev* **2012**, *112*, 782-835.

9.   Plonka, A. M.; Banerjee, D.; Woerner, W. R.; Zhang, Z.; Li, J.; Parise, J. B., Effect of ligand geometry on selective gas-adsorption: the case of a microporous cadmium metal organic framework with a V-shaped linker. *Chem Commun (Camb)* **2013**, 49, 7055-7057.

10.   Plonka, A. M.; Banerjee, D.; Woerner, W. R.; Zhang, Z.; Nijem, N.; Chabal, Y. J.; Li, J.; Parise, J. B.Mechanism of Carbon Dioxide Adsorption in a Highly Selective Coordination Network Supported by Direct Structural Evidence. *Angew Chem Int Ed Engl* **2013**, *52*, 1692-1695.

11.   Lin, J.-D.; Wu, S.-T.; Li, Z.-H.; Du, S.-W., A series of novel Pb(ii) or Pb(ii)/M(ii) (M = Ca and Sr) hybrid inorganic–organic frameworks based on polycarboxylic acids with diverse Pb–O–M (M = Pb, Ca and Sr) inorganic connectivities. *CrystEngComm* **2010,** *12* (12), 4252..

12.   Zhang, Y.; Wang, J.; Yan, X.; Liu, X.; Zhou, H.; Yuan, A., Syntheses, structures, thermal stabilities and gas sorption properties of two rod-based microporous lead(II) polycarboxylate coordination frameworks. *Microporous and Mesoporous Materials* **2014**, *184*, 15-20.

13.   Chen, S.; Lucier, B. E. G.; Boyle, P. D.; Huang, Y., Understanding The Fascinating Origins of CO_2 Adsorption and Dynamics in MOFs. *Chem Mater* **2016**, *28*, 5829.

14.   Li, X.-Q.; Zhang, H.-B.; Wu, S.-T.; Lin, J.-D.; Lin, P.; Li, Z.-H.; Du, S.-W., Synthesis, structures and luminescent properties of new Pb(ii)/M(i) (M = K, Rb and Cs) frameworks based on dicarboxylic acids: a novel icosahedral Pb_6-M_6 SBU. *CrystEngComm* **2012**, 14, 936-944.

15.   Hu, Y.; Kazemian, H.; Rohani, S.; Huang, Y.; Song, Y., In situ high pressure study of ZIF-8 by FTIR spectroscopy. *Chem Commun (Camb)* **2011,** *47* (47), 12694-6.

16.   Hu, Y.; Liu, Z.; Xu, J.; Huang, Y.; Song, Y., Evidence of pressure enhanced CO_2 storage in ZIF-8 probed by FTIR spectroscopy. *J Am Chem Soc* **2013,** *135* (25), 9287-90.

17.   Hu, Y.; Lin, B.; He, P.; Li, Y.; Huang, Y.; Song, Y., Probing the Structural Stability of and Enhanced CO_2 Storage in MOF MIL-68(In) under High Pressures by FTIR Spectroscopy. *Chem Eur J* **2015,** *21* (51), 18739-48.

18.   Mao, H.; Xu, J.; Hu, Y.; Huang, Y.; Song, Y., The effect of high external pressure on the structure and stability of MOF α-$Mg_3(HCOO)_6$ probed by in situ Raman and FT-IR spectroscopy. *J Mater Chem* **2015,** *3* (22), 11976-11984.

19.   Spencer, E. C.; Kiran, M. S.; Li, W.; Ramamurty, U.; Ross, N. L.; Cheetham, A. K., Pressure-induced bond rearrangement and reversible phase transformation in a metal-organic framework. *Angew Chem Int Ed Engl* **2014,** *53* (22), 5583-6.

20.   Ortiz, A. U.; Boutin, A.; Gagnon, K. J.; Clearfield, A.; Coudert, F. X., Remarkable pressure responses of metal-organic frameworks: proton transfer and linker coiling in zinc alkyl gates. *J Am Chem Soc* **2014,** *136* (32), 11540-5.

21.   Gagnon, K. J.; Beavers, C. M.; Clearfield, A., MOFs under pressure: the reversible compression of a single crystal. *J Am Chem Soc* **2013,** *135* (4), 1252-5.

22.   Su, Z.; Miao, Y. R.; Mao, S. M.; Zhang, G. H.; Dillon, S.; Miller, J. T.; Suslick, K. S., Compression-induced deformation of individual metal-organic framework microcrystals. *J Am Chem Soc* **2015,** *137* (5), 1750-3.

23.   Serra-Crespo, P.; Dikhtiarenko, A.; Stavitski, E.; Juan-Alcaniz, J.; Kapteijn, F.; Coudert, F. X.; Gascon, J., Experimental Evidence of Negative Linear Compressibility in the MIL-53 Metal-Organic Framework Family. *CrystEngComm* **2015,** *17* (2), 276-280.

24.   Karena W. Chapman, G. J. H., and Peter J. Chupas, Pressure-Induced Amorphization and Porosity Modification in a Metal-Organic Framework. *J Am Chem Soc* **2009,** *131*, 17546-17547.

25.   Serra-Crespo, P.; Stavitski, E.; Kapteijn, F.; Gascon, J., High compressibility of a flexible metal–organic framework. *RSC Adv* **2012,** *2* (12), 5051.

26. Zhou, M.; Wang, K.; Men, Z.; Sun, C.; Li, Z.; Liu, B.; Zou, G.; Zou, B., Pressure-induced isostructural phase transition of a metal-organic framework $Co_2(4,4'$-bpy$)_3$(NO$_3)_4 \cdot x$H$_2$O. *CrystEngComm* **2014,** *16* (20), 4084-4087.

27. Yot, P. G.; Ma, Q.; Haines, J.; Yang, Q.; Ghoufi, A.; Devic, T.; Serre, C.; Dmitriev, V.; Férey, G.; Zhong, C.; Maurin, G., Large breathing of the MOF MIL-47(V^{IV}) under mechanical pressure: a joint experimental–modelling exploration. *Chem Sci* **2012,** *3* (4), 1100.

28. Hobday, C. L.; Marshall, R. J.; Murphie, C. F.; Sotelo, J.; Richards, T.; Allan, D. R.; Duren, T.; Coudert, F. X.; Forgan, R. S.; Morrison, C. A.; Moggach, S. A.; Bennett, T. D., A Computational and Experimental Approach Linking Disorder, High-Pressure Behavior, and Mechanical Properties in UiO Frameworks. *Angew Chem Int Ed Engl* **2016,** *55* (7), 2401-5.

29. Moggach, S. A.; Bennett, T. D.; Cheetham, A. K., The effect of pressure on ZIF-8: increasing pore size with pressure and the formation of a high-pressure phase at 1.47 GPa. *Angew Chem Int Ed Engl* **2009,** *48* (38), 7087-9.

30. Fairen-Jimenez, D.; Moggach, S. A.; Wharmby, M. T.; Wright, P. A.; Parsons, S.; Duren, T., Opening the gate: framework flexibility in ZIF-8 explored by experiments and simulations. *J Am Chem Soc* **2011,** *133* (23), 8900-2.

31. Santoro, M.; Gorelli, F.; Haines, J.; Cambon, O.; Levelut, C.; Garbarino, G., Silicon carbonate phase formed from carbon dioxide and silica under pressure. *Proc Natl Acad Sci U S A* **2011,** *108* (19), 7689-92.

32. Lee, Y.; Liu, D.; Seoung, D.; Liu, Z.; Kao, C. C.; Vogt, T., Pressure- and heat-induced insertion of CO_2 into an auxetic small-pore zeolite. *J Am Chem Soc* **2011,** *133* (6), 1674-7.

33. Graham, A. J.; Allan, D. R.; Muszkiewicz, A.; Morrison, C. A.; Moggach, S. A., The Effect of High Pressure on MOF-5: Guest-Induced Modification of Pore Size

and Content at High Pressure. *Angew Chem Int Ed Engl* **2011,** *50* (47), 11138-11141.

34.   Chapman, K. W.; Sava, D. F.; Halder, G. J.; Chupas, P. J.; Nenoff, T. M., Trapping Guests within a Nanoporous Metal–Organic Framework through Pressure-Induced Amorphization. *J Am Chem Soc* **2011**, *133*, 18583-18585.

35.   Graham, A. J.; Tan, J. C.; Allan, D. R.; Moggach, S. A., The effect of pressure on Cu-btc: framework compression vs. guest inclusion. *Chem Commun (Camb)* **2012,** *48* (10), 1535-7.

36.   Bennett, T. D.; Sotelo, J.; Tan, J.-C.; Moggach, S. A., Mechanical properties of zeolitic metal–organic frameworks: mechanically flexible topologies and stabilization against structural collapse. *CrystEngComm*, **2015**, *17*, 286-289.

37.   Balachander, L.; Ramadevudu, G.; Shareefuddin, M.; Sayanna, R.; Venudhar, Y. C., *ScienceAsia*, **2013**, *39*, 278.

38.   Aoki, K.; Yamawaki, H.; Sakashita, M., Phase study of solid CO_2 to 20 GPa by infrared-absorption spectroscopy. *Phys Rev B Condens Matter* **1993,** *48* (13), 9231-9234.

Chapter 4

4 Discovering the Structural Evolutions of SIFSIX-3-Zn and CO_2-Framework Interactions under Extreme Pressure by In situ Vibrational Spectroscopy

4.1 Introduction

Hybrid ultramicroporous materials (HUMs) are a growing class of metal-organic frameworks (MOFs) investigated for their gas adsorption applications. These materials are made up of metal ions or clusters acting as nodes, which are made into three-dimensional frameworks through a combination of organic and inorganic linkers. SIFSIX materials are a typical example of this kind of framework.[1] SiF_6^{2-} pillars give the materials their name, connecting two-dimensional metal-organic sheets into a porous three-dimensional structure. New combinations of organic and inorganic linkers with different sizes and functionalities have been used to generate structures with particularly unusual and effective gas adsorption properties. Previously investigated HUM materials include SIFSIX materials,[2-3] TIFSIX and SNIFSIX materials,[4-5] MOOFOUR and CROFOUR materials[6], NbOFFIVE materials[7] and AlFFIVE materials.[8] SIFSIX materials are among the most widely studied; numerous SIFSIX frameworks exist consisting of different metal center and organic-linker combinations. These materials are of particular interest due to their highly selective CO_2 adsorption behaviour.[3-5] For instance, at 1 bar of pressure, the selectivity for CO_2 was calculated to be 1818 against N_2, 231 against CH_4, and over 1800 against H_2.[2] These calculated selectivities, particularly the selectivity against N_2 adsorption, are extremely high compared to Mg-MOF-74,[9] which has a selectivity of 800 against N_2, and Zeolite 13X,[10] which has a selectivity of 420 against N_2.
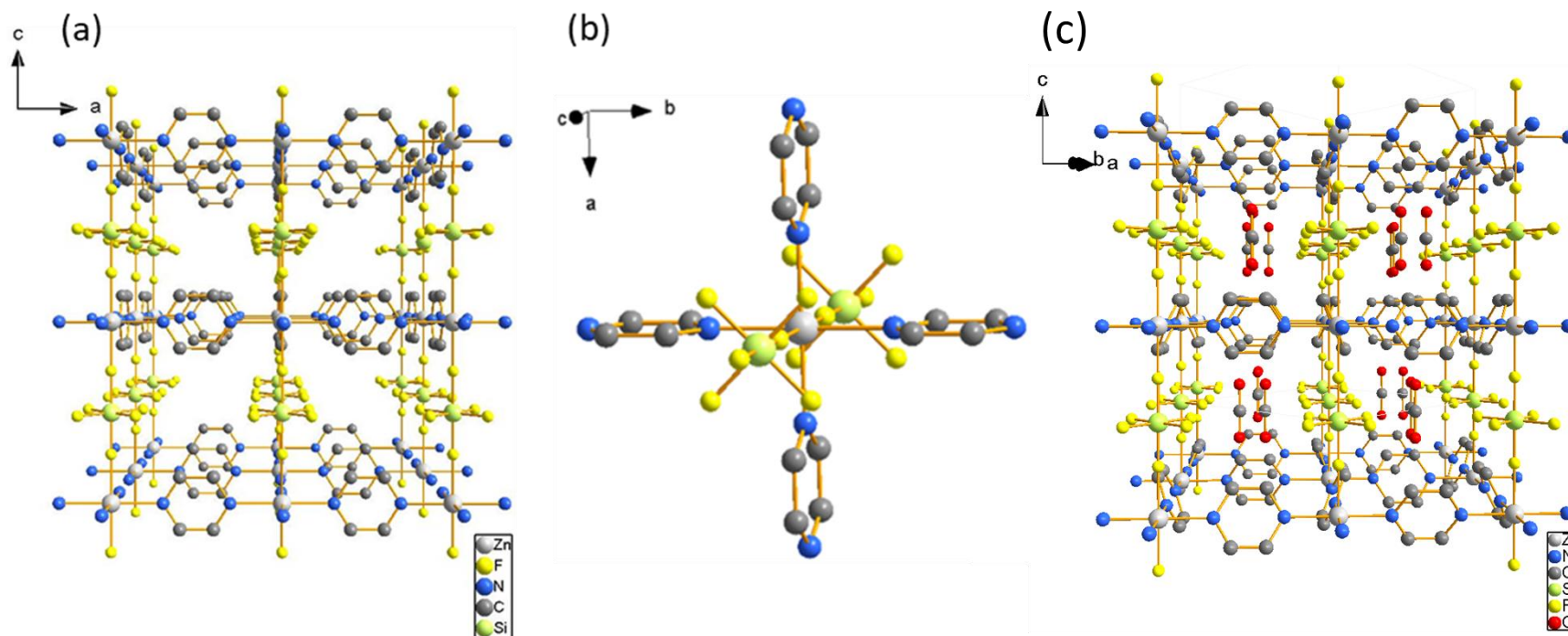
Figure 4.1 (a) View of the 3D ultra-microporous framework of SIFSIX-3-Zn along the b-axis, showing the linear 1D channels. (b) View of the coordination environment of Zn in SIFSIX-3-Zn. (c) The framework structure of CO_2 loaded SIFSIX-3-Zn at 110 K and ambient pressure, highlighting the CO_2 adsorption site in the channel.[11]

The highly selective CO_2 adsorption behavior of SIFSIX-3-Zn is believed to be associated with the crystal structure (Figure 4.1a). The SIFSIX-3-Zn crystalizes into the tetragonal lattice with a space group of P4/mmm. The CO_2 occupies one-dimensional channels running along the length of the framework's *c*-axis. These channels measure 3.84 Å across diagonally (Figure 4.1a), similar in size to the 3.30 Å kinetic diameter of CO_2.[12] Fluorine atoms extend from the corners into these channels out from the SiF_6^{2-} pillars. The channels are connected by small windows measuring 2 Å diagonally, along the *a* and *b*-axes. Computational studies and Raman spectroscopy studies suggest the narrow channels promote strong interactions between the electronegative fluorine atoms in the channel and the electropositive carbon atom on the CO_2 molecule.[13-16] The CO_2 molecule is oriented along the direction of the channel, allowing for stronger carbon-fluorine interactions. This orientation allows for a single CO_2 molecule to occupy each unit cell. This maximum CO_2 uptake remains unchanged at pressures as high as 25.0 atm and temperatures as high as 338 K.[14]

All these CO_2 adsorption properties of SIFSIX-3-Zn including high selectivity towards CO_2 and the strong CO_2-framework interaction can be correlated to the unique framework structure and topology. Furthermore, external conditions such as low temperature and high pressure can effectively alter the structure of MOFs, which further leads to significant changes in CO_2 adsorption behaviors. In particular, it has been demonstrated that by applying high external pressure to MOFs, the physical and chemical properties of the frameworks including pore size[17-19] and shape, topology[20-29], as well as guest-host interactions. For instance, our previous works suggest that high pressure not only can substantially improve the CO_2 storage capacity of ZIF-8,[30] but also generate new CO_2 binding sites in SDB-based MOFs.[31] Our other studies on MOFs with heterogeneous topologies showed that high pressure could potentially tune the CO_2 adsorption prosperities in MIL-68(In)[30] and α-$Mg_3(COO)_6$.[20] Although SIFSIX-3-Zn has been intensively studied at near ambient conditions, the structural stability of the framework as well as gas adsorption properties under high external pressure remain unknown. Given the distinctive ultra microporous structure of SIFSIX-3-Zn framework and its excellent CO_2 adsorption behaviors, exploring how its structure responses to high external pressure and

understanding the guest-host interaction between CO_2 and the framework would be of particular interest.

In this study, the physical and chemical stability of SIFSIX-3-Zn material under high pressure was first examined by in situ mid-IR and Raman spectroscopy, which provides direct information on chemical bonding, local structure, and thus the nature of guest-host interactions. We further demonstrate a substantially enhanced structural stability of SIFSIX-3-Zn framework with CO_2 loaded in the channels, and closer proximity of the framework to the CO_2 molecules at high pressures. Our findings provide a full picture of CO_2-framework interactions under high pressure by illuminating the structural origins and thus bring new insights into the development of CO_2 storage applications in SIFSIX series MOFs as well as other ultra microporous materials.

4.2 Experimental

SIFSIX-3-Zn was synthesized solvothermally using previously published procedures[32] as follows: a 10 mL solution of pyrazine (6 mmol, Alfa Aesar, 98%) was prepared and diffused into a 10 mL solution of hexafluorosilicate hydrate (3 mmol, Sigma-Aldrich, 99%) in methanol. The mixture was let stand at room temperature for 3 days, after which yellow crystals were harvested by decanting the excess methanol and dried in a conventional lab oven at 90 for 3 to 5 hours. As described in the literature, the as-made SIFSIX-3-Zn materials were washed with DMF and solvent exchanged in methanol for 3 days prior to activation and CO_2 loading, the stock methanol was replaced each day. The identity and purity of the final products were tested and confirmed by Powder X-ray diffraction. For sample activation as well as CO_2 gas loading, a Schlenk line was used. The bottom of an L-shaped glass tube was firstly filled with sample, a piece of glass wool was then placed at the neck of the glass tube to secure the sample in place. The samples were desolvated under a dynamic vacuum at 70-80 °C for 24 hours, followed by introducing a known amount of CO_2 onto the vacuum line. Meanwhile, the bottom of the L-shaped tube was immersed in liquid nitrogen to condense CO_2. The glass tube was then flame sealed off from the vacuum line for further operation.

To achieve in-situ high pressure conditions, two diamond anvil cells equipped with type I and type II diamonds with a culet size of 600 µm were used for Raman and IR measurements respectively. The sample chambers with approx. 60-70 µm in thickness and 30-40 µm and 250 µm in diameter were prepared on pre-intended stainless-steel gaskets for Raman and IR measurements. The glass tubes with activated and CO_2 loaded samples sealed inside were opened in a Nitrogen-filled MBraun LAB Master 130 glovebox with O_2 content below 5 ppm and H_2O content below 1 ppm. Both activated samples and CO_2 loaded samples were loaded into the DACs without any pressure transmitting medium or KBr to eliminate possible guest-host interactions that might be induced by mediums, and also to ensure that all our results from different characterization methods are comparable. A few ruby chips were pre-loaded to the sample chambers for pressure calibrations.[33] Owing to the ultra-micro pores of the framework, the strong attraction of the frame to CO_2, as well as the high CO_2 to N_2 adsorption selectivity of this material, the CO_2 molecules remained in the pores during this process. Highly customized IR and Raman micro-spectroscopy systems dedicated to in-situ high pressure experiments were used in this study, with details described in our previous publications.[34]

4.3 Results and discussion

4.3.1 Structural stability of SIFSIX-3-Zn material

Raman and mid-IR spectra of SIFSIX-3-Zn at ambient conditions are depicted in Figure 4.2. In the mid-IR range (400 cm^{-1}-4000 cm^{-1}), most of the absorption bands are associated with the internal vibrations of the organic ligand, which in this case, the vibrations of the pyrazine ring. The bands from 1020 cm^{-1} to 1130 cm^{-1} and from 1120 cm^{-1} to 1200 cm^{-1}, as well as the strong peak located at 1438 cm^{-1} could be assigned ring stretching. The C-H vibrations including C-H out-of-plane bending, C-H in-plane bending and C-H stretching, are observed as single peaks at 844 cm^{-1}, 1438 cm^{-1} and a set of bands in the frequency range of 2800 cm^{-1} to 3160 cm^{-1}, respectively.[35] All these bands above are associated with vibrations of pyrazine ligands and can potentially provide useful information on modification on the rings under external pressure. The bands at 608 cm^{-1} and 787 cm^{-1} are assigned to Si-F stretching.[36] In the local structure of SIFSIX-3-Zn, the SiF_6^{2-} clusters play the role of 'pillar', connecting layers of pyrazine sheets into the 3D

framework. With two of the Fluorine atoms coordinately bonded to Zn atom, the vibrational modes of SiF_6^{2-} may reflect the connectivity of the metal-ligand chemical bonding, and even the decomposition of the framework under pressure. Similarly, all the bands at above 400 cm^{-1} in the Raman spectrum are derived from the vibrations of pyrazine rings and SiF_6^{2-} pillars, with the detailed assignment provided in Table 4.1. In Raman spectra, the unreacted ligand ZnSiF$_6$ displays a single band for the Si-F stretching[36], whereas in SIFSIX-3-Zn framework, the Si-F stretching mode exhibits a doublet at 669 and 694 cm^{-1}. These two peaks are assigned to the Si-F bonds with the F atoms coordinated to Zn (labeled as $\nu_{Si-F(-Zn)}$ in below), and the equatorial Si-F bonds (labeled as ν_{Si-F} in below), respectively (Table 4.1).
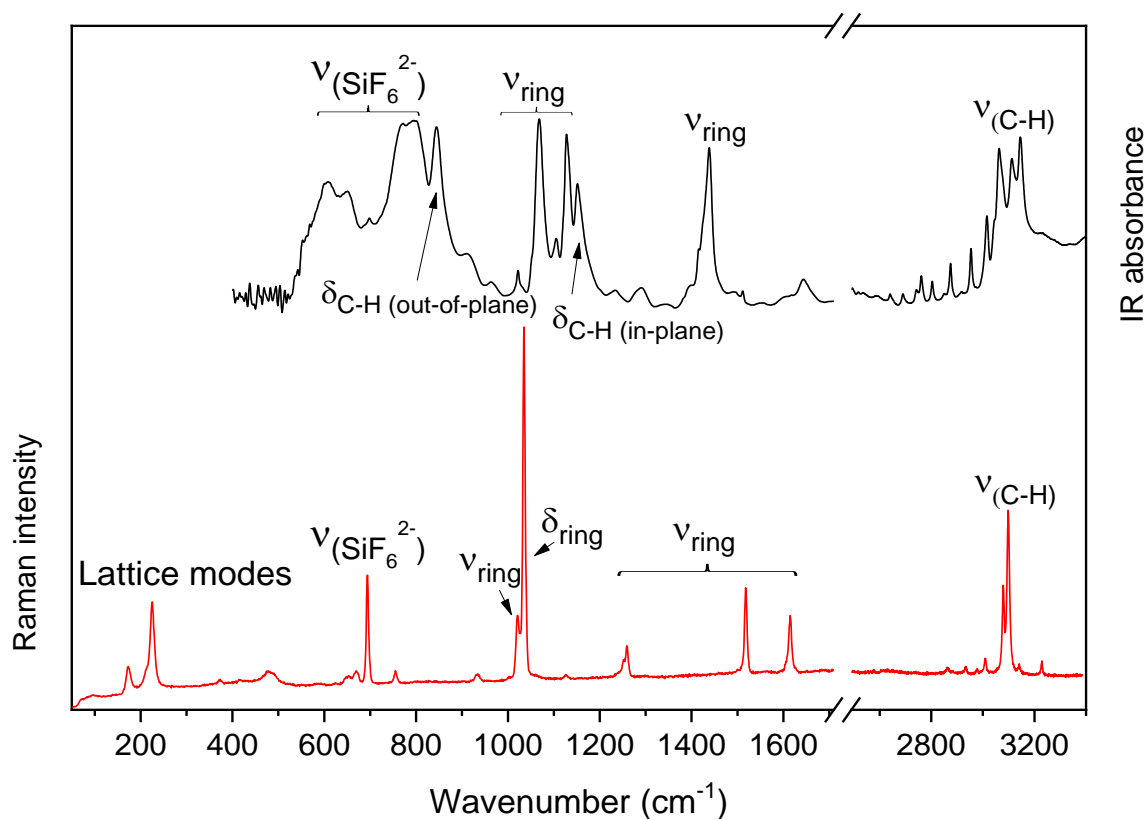
Figure 4.2 IR (top) and Raman (bottom) spectra of activated SIFSIX-3-Zn at ambient pressure in the frequency region of 100-3400 cm^{-1}, the break from 1800 to 2500 cm^{-1} is to omit the IR absorption of diamond.

Table 4.1 IR and Raman bands assignments of activated SIFSIX-3-Zn.

IR Frequency[a] (cm^{-1})	Assignment	Raman Frequency[b] (cm^{-1})	Assignment
608, 647	Si-F bending	173, 225	Lattice modes
787	Si-F stretching	669	Si-F stretching
844	C-H out-of-plane bending	694	Si-F(-Zn) stretching
1022, 1068, 1105, 1127, 1438	Ring stretching	1021, 1259, 1518, 1615	Ring stretching
1151	C-H in-plane bending	1035	Ring bending
2600-3200	C-H stretching	2800-3250	C-H stretching

a. Observed and measured at the first point on compression to a lowest possible pressure (i.e., 0.11 GPa).

b. Observed and measured under ambient conditions.

Upon initial compression to 0.85 GPa, a slight loss of intensity on the lattice modes (Figure 4.3a) and SiF$_6^{2-}$ stretching mode on mid-IR (Figure 4.4), indicating a mild degree of reduction in crystallinity. Further compression to 1.96 GPa, results in a significant band broadening and merging in the lattice region, as well as the SiF$_6^{2-}$ stretching region on IR spectrum under the similar pressure of 2.05 GPa. In particular, the C-H stretching mode on both Raman (at 2.88 GPa) and IR (at 2.65 GPa) exhibits a substantial flattening along with a striking blue-shift (Figure 4.3b). Upon decompression, the spectra of the recovered sample do not resemble that of the initial one in the lattice region (Figure 4.3a) and the C-H stretching (Figure 4.4), indicating that the pressure-induced structural change is permanent, and is mostly associated with the disordering of the pyrazine rings. Nonetheless, most of the Raman modes still exist upon recovery, suggesting that the chemical connectivity of the framework survived from compression up to 5.64 GPa without breaking down completely.
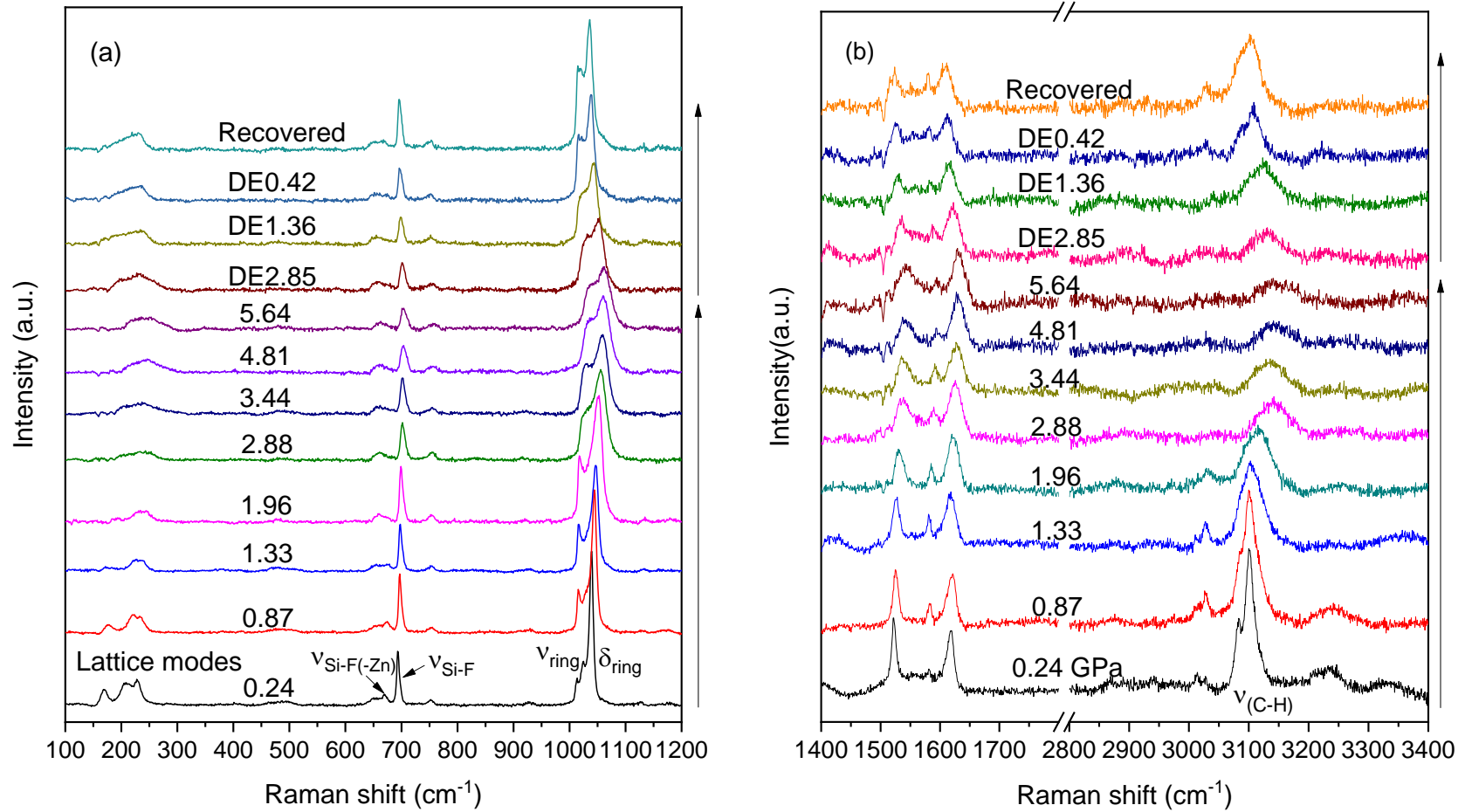
Figure 4.3 Selected Raman spectra of activated SIFSIX-3-Zn upon compression and decompression in the spectral region of 50-1200 cm^{-1} (a) and 1400-3400cm^{-1}.
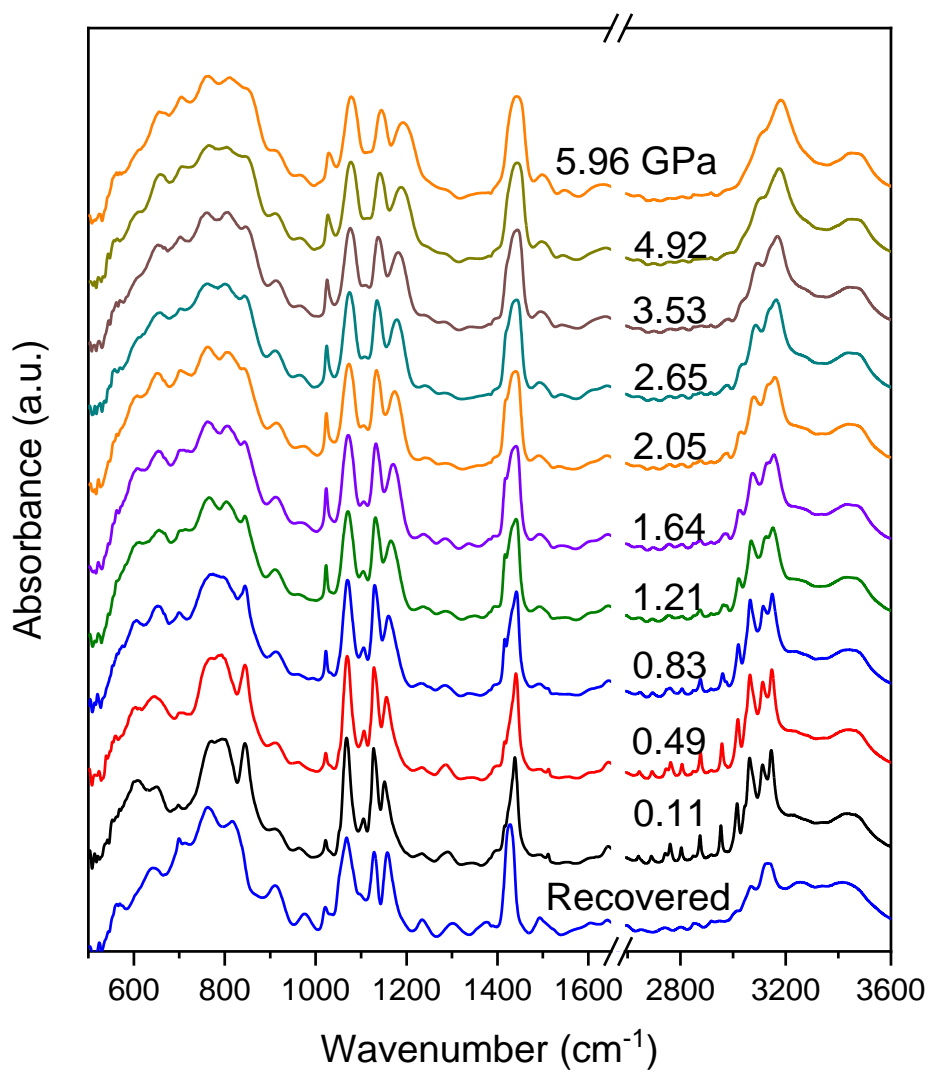
Figure 4.4 Selected mid-IR spectra of activated SIFSIX-3-Zn collected in the pressure range from ambient to 5.96 GPa.

The pressure dependence ($d\nu/dP$, cm^{-1}/GPa) of selected Raman and IR modes was studied by plotting the vibrational frequencies as a function of pressure. In this work, the pressure dependences of ring stretching and C-H in-plane bending modes of pyrazine ring, as well as two of the Si-F stretching modes of the SiF_6^{2-} pillars were monitored (Figure 4.5a and Table 4.2). A discontinuity was observed at around 2 GPa on the curves. In the pressure range from ambient to 2 GPa, the ring stretching mode exhibit a relatively large pressure coefficient on both Raman and IR, whereas the Si-F(-Zn) undergoes a minor blueshift, suggesting that the pyrazine is more sensitive to pressure, while the SiF_6^{2-} pillars are rigid. At 2 GPa and above, the pressure coefficient of ring stretching mode increases while that of the C-H bending mode decreases dramatically. Moreover, the sharply decreased pressure dependence of the Si-F(-Zn) stretching mode suggests that the SiF_6^{2-} pillars are more rigid under higher pressures. Whereas the equatorial fluorine atoms on the SiF_6^{2-} pillars extend from the corners into the channels, and therefore not much affected by external pressure (Figure 4.1b). Consequently, the pressure dependence of this Si-F stretching mode remains extremely small (0.42 cm^{-1}/GPa) and unchanged in the entire compression region, indicating that the pores of the SIFSIX-3-Zn remain intact up to about 6 GPa.
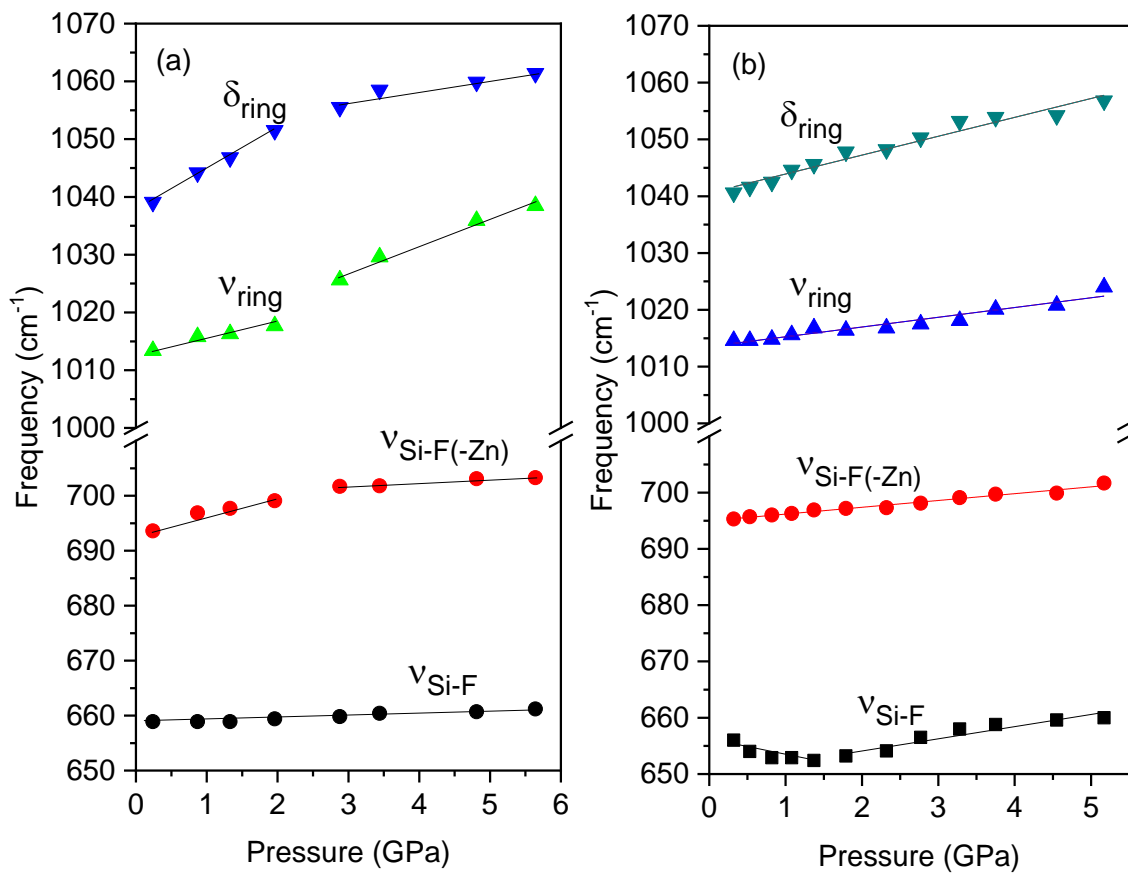
Figure 4.5 Pressure dependence (dv/dP) of selected Raman modes of empty SIFSIX-3-Zn (a) and CO$_2$ loaded SIFSIX-3-Zn (b).

Table 4.2 Pressure dependences [dv/dP (cm^{-1}·GPa^{-1})] of selected Raman bands of empty SIFSIX-3-Zn and CO$_2$ loaded SIFSIX-3-Zn on compression.

Empty SIFSIX-3-Zn			
Raman Modes	Frequency[a] (cm^{-1})	dv/dP (cm^{-1}·GPa^{-1})	
		0.24-1.96 GPa	2.88-5.67 GPa
ν(Si-F)	658	0.42	
ν(Si-F-Zn)	694	3.20	0.58
ν(ring)	1013	2.56	4.67
δ(ring)	1039	7.21	2.14
CO$_2$ loaded SIFSIX-3-Zn			
Raman Modes	Frequency[a] (cm^{-1})	dv/dP (cm^{-1}·GPa^{-1})	
		0.32-1.37 GPa	1.79-5.17 GPa
ν(Si-F)	656	-3.06	2.10
ν(Si-F-Zn)	695	1.49	
ν(ring)	1015	1.72	
δ(ring)	1041	3.32	

a. Observed and measured at the first point on compression to a lowest possible pressure (i.e., ~ 0.3 GPa).

4.3.2 Guest-host interactions of CO_2 loaded SIFSIX-3-Zn framework
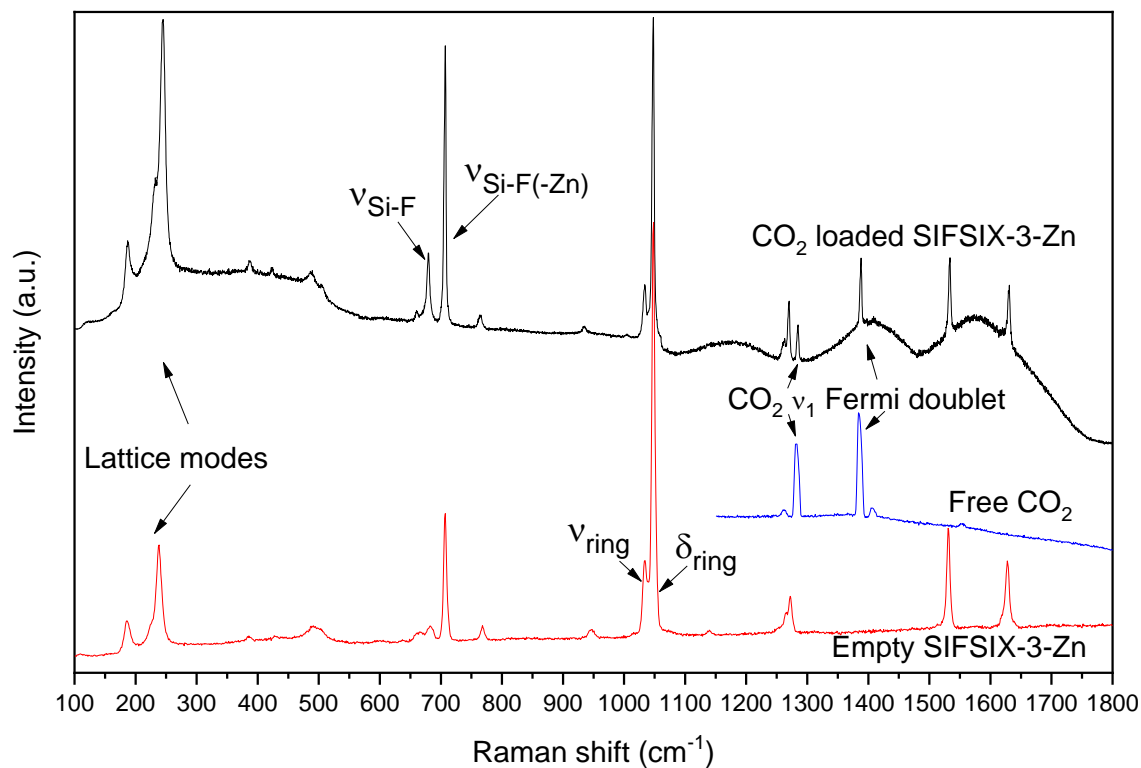
Figure 4.6 Raman spectra of activated SIFSIX-3-Zn (red), CO₂ loaded SIFSIX-3-Zn (black), and free CO₂ under ambient pressure (blue).

Raman spectra of the empty, CO_2 loaded SIFSIX-3-Zn, as well as the free CO_2 gas, are depicted in Figure 4.6. The CO_2 symmetric stretching mode ν_1 at 1284 cm^{-1} and 1388 cm^{-1} on Raman spectrum and the CO_2 asymmetric stretching mode ν_3 at 2341 cm^{-1} as well as the CO_2 combination modes $\nu_3 + 2\nu_2$ and $\nu_3 + \nu_1$ at 3592 cm^{-1} and 3696 cm^{-1} in mid-IR spectrum are observed as expected. The intensity of the Si-F stretching mode (at 665 cm^{-1}) on Raman spectrum increased significantly after the CO_2 was loaded into the sample, similarly, a saturation of the Si-F stretching band on IR spectrum was also observed, both observations suggest a strong interaction between CO_2 molecules and the equatorial fluorine atoms on the SiF_6^{2-} pillar. Other major changes in the IR spectra (Figure 4.7) such as the splitting of the C-H bending and stretching modes may indicate rotations of the pyrazine ring induced by CO_2 molecules (Figure 4.8).
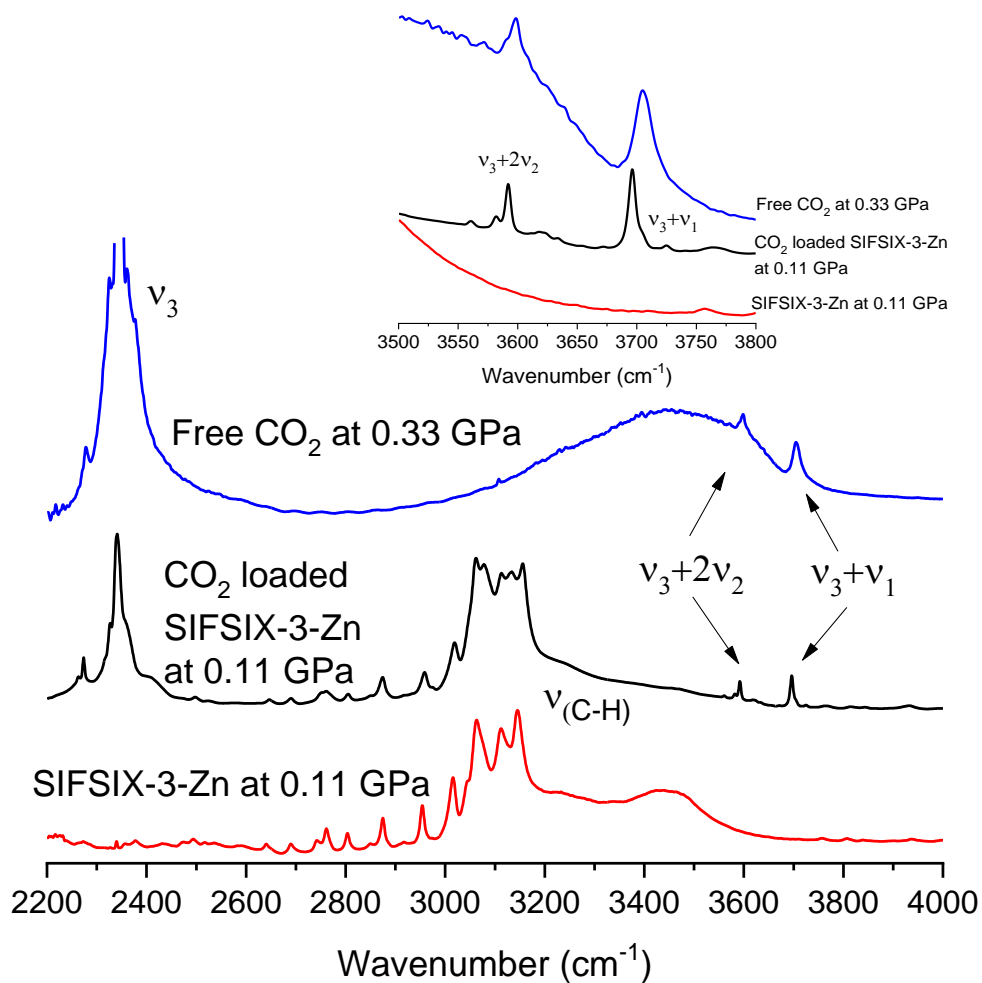
Figure 4.7 IR spectra of activated SIFSIX-3-Zn (red), CO$_2$ loaded SIFSIX-3-Zn (black), and free CO$_2$ under 0.33 GPa (blue). The inlet shows the spectral region of 3500 cm^{-1} to 3800 cm^{-1}, highlighting the CO$_2$ combination modes $\nu_3+2\nu_2$ and $\nu_3+\nu_1$ in the samples.
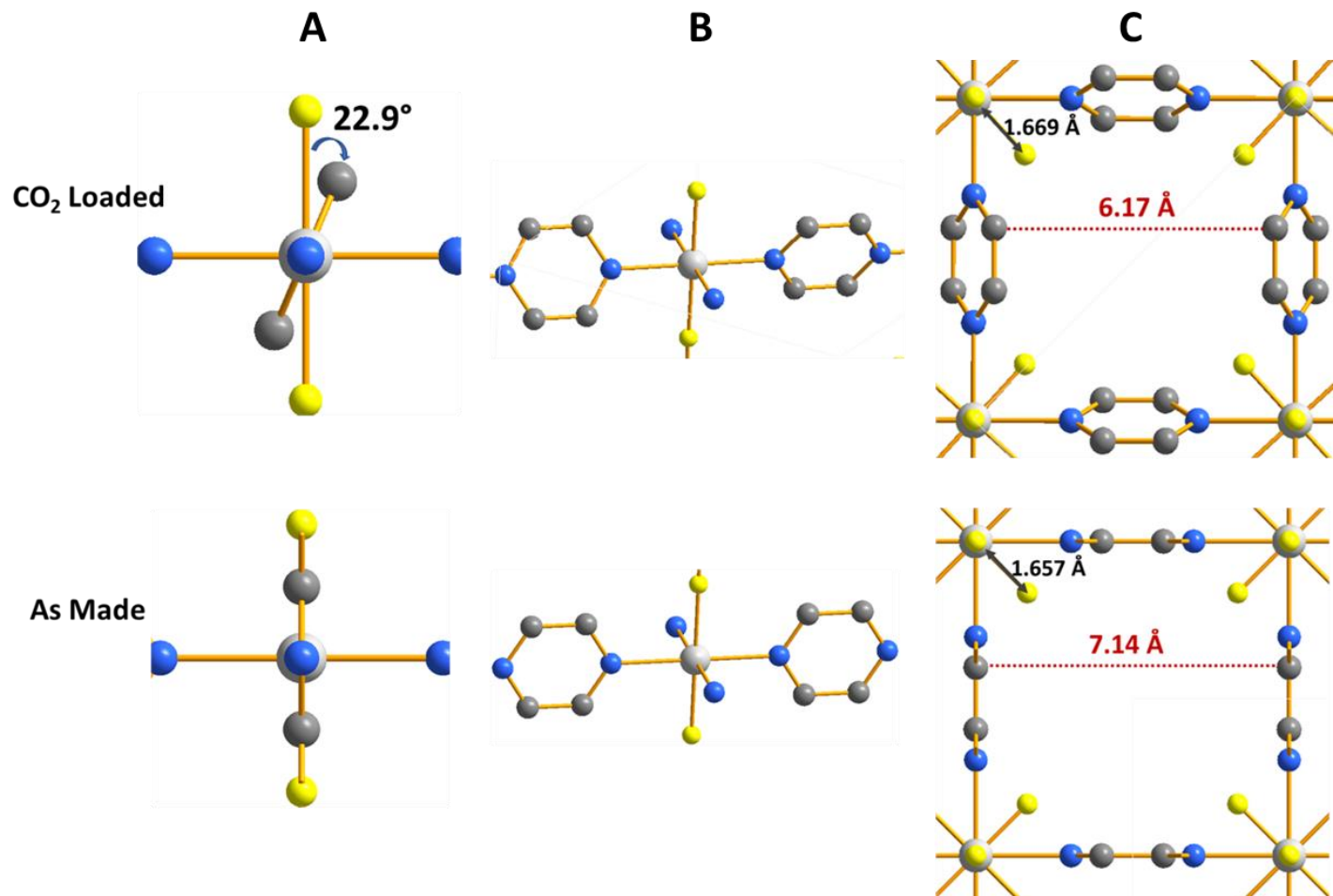
Figure 4.8 The 22.9 ° tilting of the pyrazine rings in the CO₂ loaded framework is depicted as viewed along different directions, in contrast with the parallel rings of the as-made framework (A) (B). Adjacent pyrazine rings are tilted in opposing directions (C). The slanting brings the framework protons closer to the guest CO₂ molecule, enhancing guest-framework interactions.[4, 11]

Raman spectra of CO_2 loaded SIFSIX-3-Zn were collected as a function of pressure from near ambient pressure to 5.17 GPa (Figure 4.9). Unfortunately, the CO_2 symmetric stretching mode at 1284 cm^{-1} and 1388 cm^{-1} in the Raman spectrum was blocked by intense scattering of the diamond at around 1340 cm^{-1}, nonetheless, the other modes still provide characteristic information on the changes of the framework under external high pressure with CO_2 being in the channels. Upon compression all the way to 5.17 GPa, all the changes in the Raman spectra are gradual, suggesting that there is no phase transition under this pressure region. It is worth noting that the intensity of the Si-F stretching mode increases steadily during compression, indicating an enhanced interaction between CO_2 and the equatorial fluorine atoms. The Si-F(-Zn), however, only shows a slight loss of intensity with a minor degree of band broadening. Additionally, the broadening of the lattice modes (0-300 cm^{-1}) was initially observed at 3.28 GPa, which are then further flattened upon compression. These observations suggest a marginal structural disorder of the SIFSIX-3-Zn framework. Upon releasing the pressure, all the pressure-induced changes on Raman and IR spectra were observed in a reverse sequence. The Raman spectrum of the recovered sample has shown similar profiles as the ambient one (Figure 4.9), indicating the structural modifications on CO_2 loaded SIFSIX-3-Zn induced by high external pressure are mostly reversible.
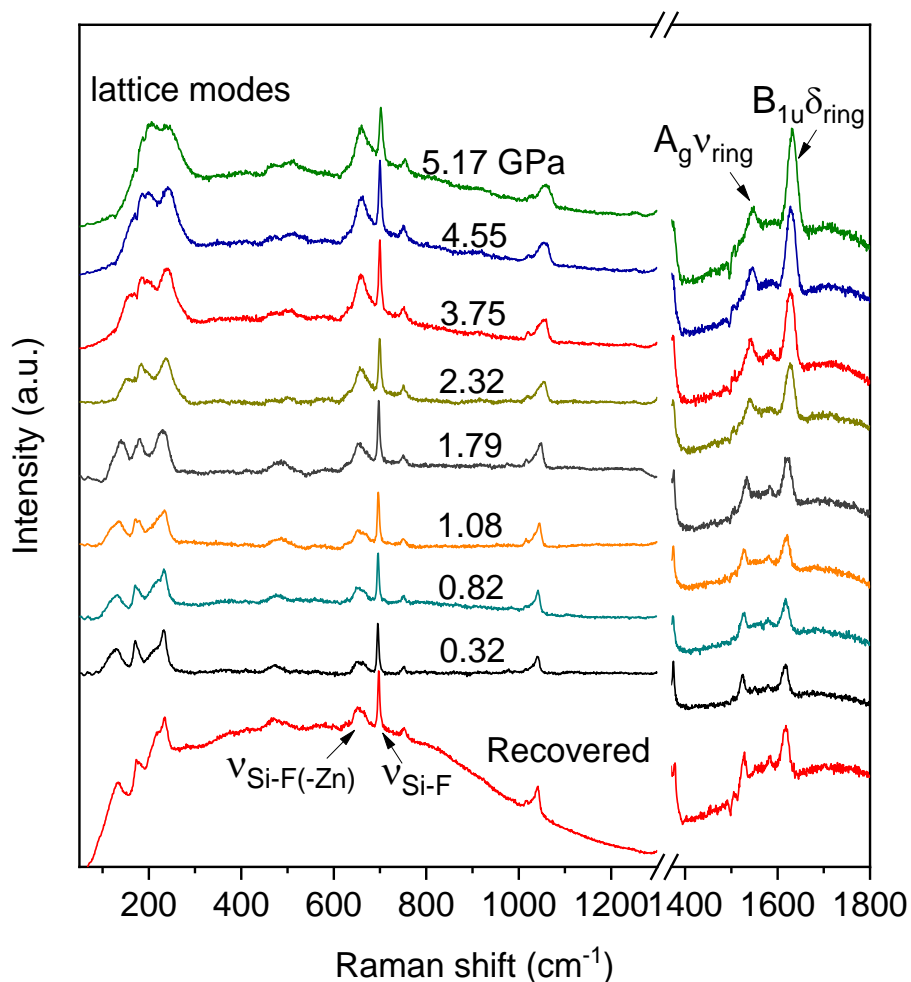
Figure 4.9 Selected Raman spectra of CO₂ loaded SIFSIX-3-Zn upon compression and recovery in the pressure range from ambient to 5.17 GPa.

The pressure dependences of selected vibrational modes of CO_2 loaded SIFSIX-3-Zn were further examined (Figure 4.5b and Table 4.2). The pressure coefficients of these modes are relatively small, compared to that of the empty framework, indicating that the structure is generally under less stress with the CO_2 being in the channels. Interestingly, the Si-F stretching mode has shown a soft behavior ($d\nu/dP$ = -3.06 cm^{-1}/GPa) at below 2 GPa, which typically suggests the weakening of the Si-F bond. As reported by previous studies, CO_2 molecules in the SIFSIX-3-Zn interact strongly with Fluorine atoms on the SiF_6^{2-} pillars even under ambient pressure.[32] Hence, such large pressure dependence (-3.06 cm^{-1}/GPa) of the Si-F stretching mode most likely originates from the enhanced carbon-fluorine attraction upon compression, which weakens the Si-F bonding. The strongest interaction

CO_2-framework interaction was achieved at 1.37 GPa, where the frequency of Si-F(-Zn) stretching mode reaches the lowest. When the pressure is above 2 GPa, the Si-F(-Zn) stretching mode exhibited a regular pressure-induced blue shift same as all the other Raman modes, attributed to the bond stiffening at higher pressures.

Apparently, the structural stability of the SIFSIX-3-Zn framework has been much improved when loaded with CO_2. On Raman spectra, the empty SIFSIX-3-Zn framework started to disorder at a very low pressure of 1.33 GPa, while the decrease of crystallinity of the material was initially present at 3.28 GPa in CO_2 loaded framework. Moreover, the empty framework exhibits a possible phase transition to a less ordered structure at 1.96 GPa, whereas the CO_2 loaded SIFSIX-3-Zn experiences no phase change upon compression. Furthermore, the recovered empty SIFSIX-3-Zn no longer resemble the profile of the initial spectra of both IR and Raman (Figure 4.3 and 4.4), suggesting an irreversible structural amorphization of the framework. In contrast, the CO_2 loaded framework exhibit excellent reversibility in the similar pressure range from ambient to 5 GPa, as both IR and Raman spectra of the recovered sample show little observable difference compared to the initial ones (Figure 4.9 and 4.10).

The mid-IR spectra show a clear profile of pyrazine ring stretching modes (Figure 4.10), CO_2 asymmetric stretching mode v_3 (Figure 4.11 c and d), as well as the CO_2 combination modes (Figure 4.11a and b). The spectra empty SIFSIX-3-Zn framework and pure CO_2 at similar pressures are included in the same figure as a comparison. Upon compression, the splitting of the CO_2 combination mode $v_3 + 2v_2$ was observed (at 3582 and 3592 cm^{-1}) under a moderate pressure of 0.28 GPa. At this point, it is apparent that there are two possible CO_2 binding sites in the channels of SIFSIX-3-Zn at high pressures.

Since the fundamental modes are naturally more intense than combination modes, the changes on fundamental mode v_3 induced by O=C=O bond distortion are more apparent than that of $v_3 + v_1$. As shown in Figure 4.11c, the v_3 mode features a major band at 2341 cm^{-1} as expected, with an observable shoulder at a higher frequency, indicating the second binding site. Upon elevating the pressure, more CO_2 goes to this site, evidenced by a change in the relative intensity between the $v_3 + 2v_2$ doublet, and an enhanced shoulder at v_3. At

very high pressure of 3.30 GPa, the high-frequency component and the low-frequency component of the ν_3 mode are merging in to a much broader band, yet still characterizes as two peaks, indicating that the physical/chemical environments of adsorbed CO_2 molecules at site 1 and 2 are very similar, resulting in singlet at $\nu_3 + 2\nu_2$ mode.
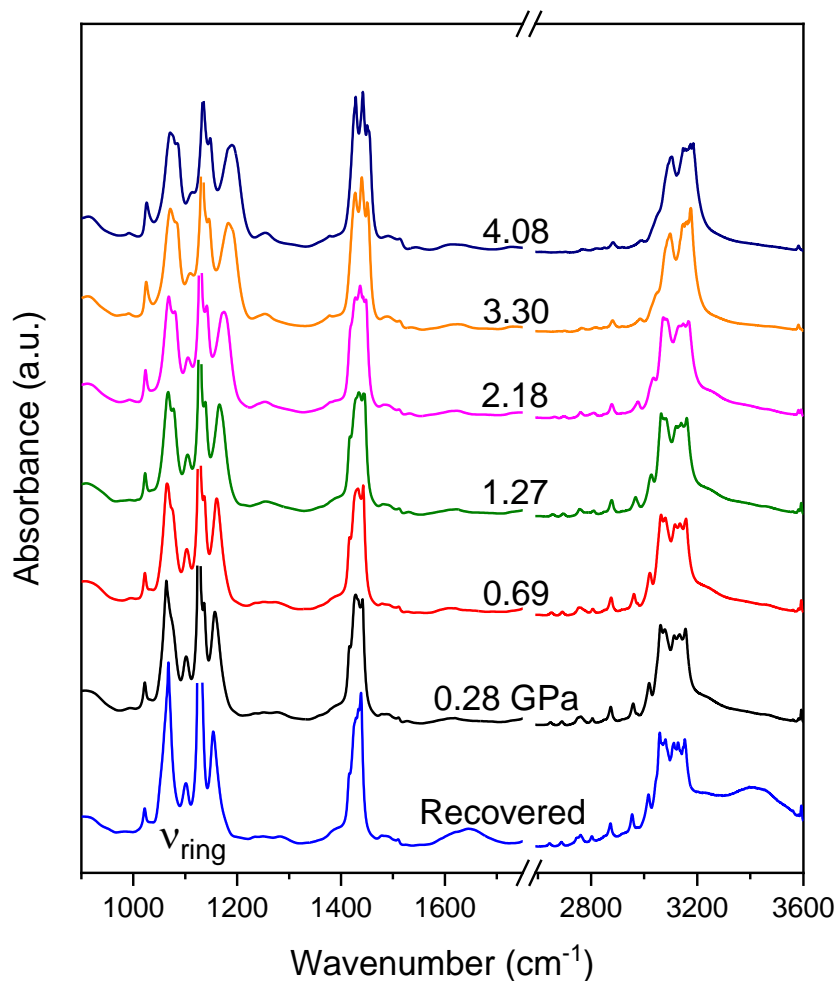
Figure 4.10 Selected mid-IR spectra of activated SIFSIX-3-Zn collected in the pressure range from ambient to 4.08 GPa.
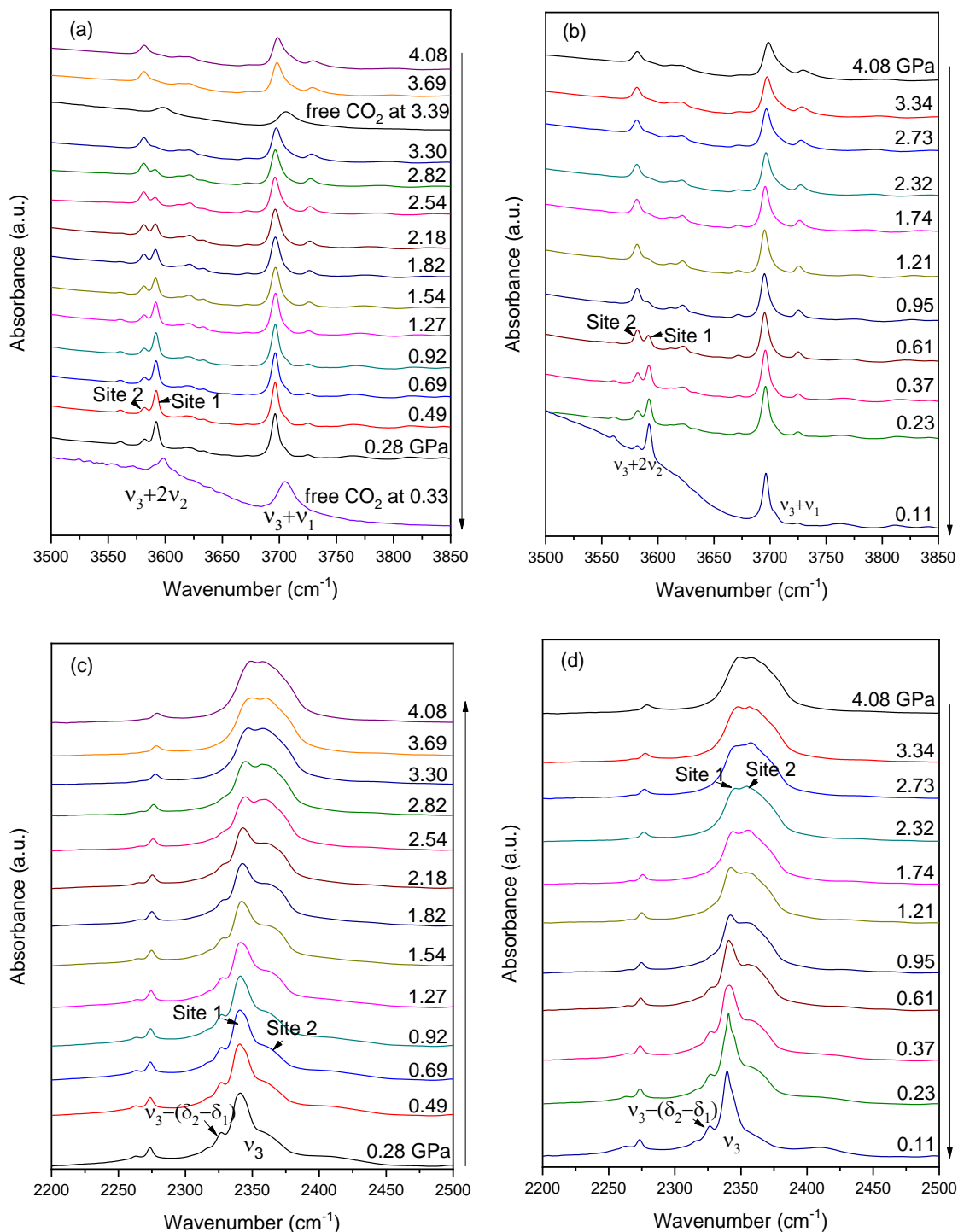
Figure 4.11 IR spectra of $\nu_3+2\nu_2$, $\nu_3+\nu_1$ (a) and ν_3 (c) modes of adsorbed CO_2 in SIFSIX-3-Zn on compression from 0.33 to 4.08 GPa and decompression (b)(d) to 0.11 GPa in the frequency region of 2200-2500 cm^{-1} and 3500-3800 cm^{-1}. IR spectra of pure CO_2 at 0.33 GPa and 3.39 GPa are plotted in (a) as comparisons.

4.3.3 Structural origins of the pressure effect on tuning CO_2 binding sites in SIFSIX-3-Zn material

Our previous single-crystal XRD analysis on CO_2 loaded SIFSIX-3-Zn under ambient pressure and 110 K has shown that the CO_2 molecules feature 2 symmetry-equivalent positions, instead of being adsorbed in the center of the channel (Figure 4.12a and c). The orientation of the adsorbed CO_2 molecules is found to be parallel to the framework channels. Structurally, by including CO_2 molecules in the channels, the space group of the framework structure changes from P4/mmm to I4/mcm. With the presence of CO_2, the framework is slightly contracted compared to the previously reported structure of the empty SIFSIX-3-Zn at 100 K. This contraction can be attributed to a shrinking of the Zn-F-Si and Zn-N bonds by 0.015 Å and 0.018 Å along the *c*-axis and the *a*-axis, respectively, as well as a contraction of the pyrazine ring diameter by 0.015 Å. The Si-F equatorial bonds, however, are observed to be elongated from 1.657 Å to 1.669 Å (Figure 4.8c). This elongation results in the weakening of the Si-F bond, which is due to the enhanced dipolar interaction between the fluorine atoms with the adsorbed CO_2 molecule in the channel. Furthermore, the pyrazine rings are found to be tilted and formed an angle of 22.9° with respect to the c-axis, whereas the adjacent pyrazine rings within the same unit cell are reported to be coplanar to each other in the empty SIFSIX-3-Zn framework at 293 K (Figure 4.8a). This rotation of the pyrazine rings brings the framework protons closer to the adsorbed CO_2 molecule in the channel. These overall modifications on SIFSIX-3-Zn framework upon loading CO_2 to the channels lead to a stronger CO_2-framework interaction.
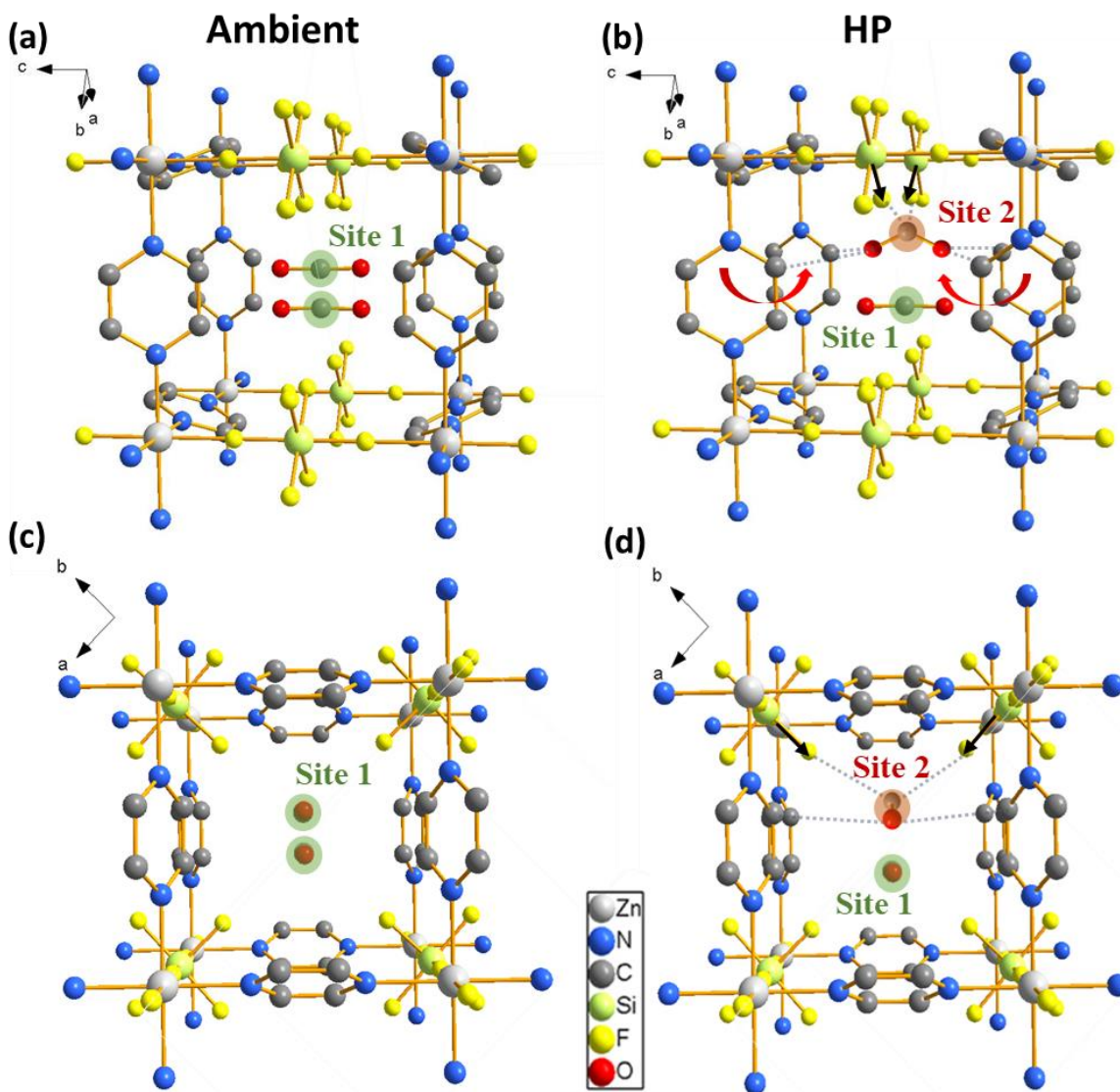
Figure 4.12 Schematics of CO₂ adsorption sites in SIFSIX-3-Zn at (a)(c) ambient pressure; (b)(d) high pressures, along two facets of the channels, respectively. Green dots correspond to site 1 observed under ambient pressure and 110 K, red dots represent site 2 formed under high pressure. The dash lines are showing the interactions between CO₂ and the specific components of the framework. Red arrows in (b) indicate the rotation direction of the pyrazine rings, the black arrows in (b) and (d) are showing the elongation of the Si-F bond at high pressures.[11]

Upon applying high external pressure to the CO_2 loaded SIFSIX-3-Zn framework, most of the above changes at 110 K and ambient pressure further enhanced. The pyrazine rings continue tilting into the channels up to 2.65 GPa, consistent with an extremely large pressure coefficient of the C-H bending mode (11.70 cm^{-1}/GPa^{-1}), which then dramatically dropped to 5.63 cm^{-1}/GPa^{-1} (Figure 4.13a). Interestingly, the higher frequency component of the CO_2 $\nu_3 + 2\nu_2$ doublet is observed to be red-shifting consistently from ambient pressure and disappears at the same pressure of 2.65 GPa (Figure 4.13b), indicating further weakening of the the O=C=O bonds, which is owing to the enhanced dipolar interaction between CO_2 carbon and fluorine atoms on the pillars. This discontinuity of the pressure dependence of the CO_2 $\nu_3 + 2\nu_2$ doublet at 3 GPa suggests the closest affinity between framework and site 2 CO_2, after which both $\nu_3 + 2\nu_2$ and $\nu_3 + \nu_1$ display blueshifts, corresponding to pressure-induced C=O bond stiffening.

From all these observations above, the new CO_2 binding site induced by high pressure likely adopts V-shaped CO_2 molecules, with the carbons attracted to the F atoms on the pillar while the O atoms pulled by H atoms on the pyrazine rings (Figure 4.12b and d). At ambient pressure and 110 K, O=C=O bond angle of adsorbed CO_2 is measured to be 178.1°. Such CO_2 molecule distortion induced by strong guest-host interaction has been previously observed in other MOFs as well.[37] At high pressures, the formation of site 2 involves further tilting of the pyrazine rings to a higher degree with respect to the c-axis (Figure 4.12b), a further elongation of the Si-F bonds toward the center of the channel. All these structural changes bring the functional groups closer to CO_2, which gives rise to stronger interactions at high pressures, resulting in a larger torsion angle of the CO_2 molecule at site 2. Moreover, site 1 and site 2 co-exist in the channels in the entire pressure region from ambient to 4.08 GPa, suggests that the high-pressure has induced non-isotropic responses of the framework, which leads two distinct environments for CO_2 adsorption.
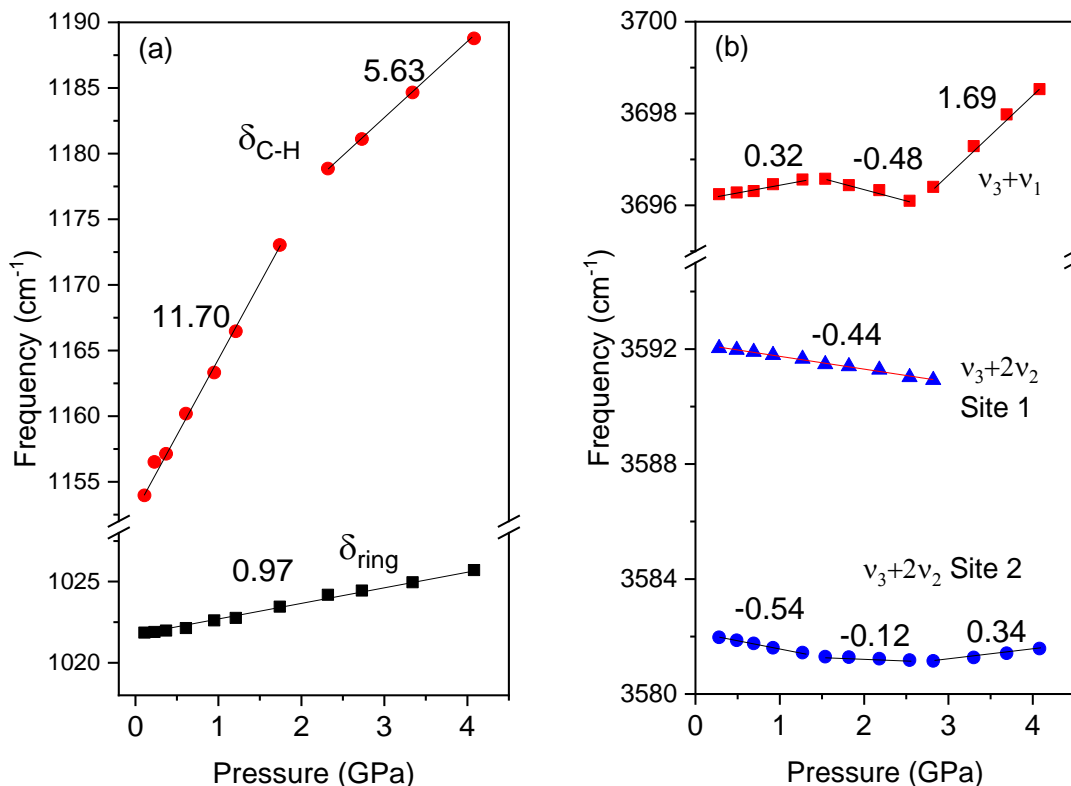
Figure 4.13 IR frequencies of δ(ring) and δ(C-H) modes of CO₂ loaded SIFSIX-3-Zn (a) as a function of pressure; (b) IR frequencies of νs(O=C=O), ν₃+2ν₂ and ν₃+ν₁ of adsorbed CO₂ in SIFSIX-3-Zn as a function of pressure. The pressure coefficients are labeled on each line.

4.4 Conclusions

Overall, combined results from *in situ* high pressure mid-IR and Raman experiments provide a full picture of the evolution of the crystallinity, framework structure, as well as the behavior of CO_2 within the SIFSIX-3-Zn channels under external pressure. The empty SIFSIX-3-Zn shows flexibility along Zn-pyrazine sheets, while it is rigid along SiF_6^{2-} pillars. A crystalline-to-crystalline phase transition is predicted at 2 GPa. Though the empty SIFSIX-3-Zn undergoes a partially irreversible compression, the pores remain intact along the process. In contrast, the compression of CO_2 loaded SIFSIX-3-Zn is found to be completely recoverable. The adsorbed CO_2 features 2 nonequivalent binding sites in the channels under high pressures. The structural origins of the formation of the new binding site are unveiled, the driving force for forming the second is the enhanced interaction

between fluorine SiF_6^{2-} pillars and the CO_2 carbon, as well as the proximity of pyrazine carbons to the CO_2 oxygen under high pressure. Our study has also demonstrated that high pressure facilitates the rotation of the pyrazine rings and the elongation of the Si-F bonds, and thus regulates the distortion of the CO_2 molecules. Finally, this work demonstrates that pressure can effectively tune the structural properties and CO_2 adsorption performance of SIFSIX-3-Zn and fundamentally contribute to the understanding of structural origins for CO_2-framework interactions in the SIFSIX series MOFs as well as ultra-microporous materials which are critical for their CO_2 storage applications.

4.5 References

1. Subramanian, S.; Zaworotko, M. J., Porous Solids by Design:[Zn(4,4'-bpy)2(SiF_6)_n· _x_DMF, a Single Framework Octahedral Coordination Polymer with Large Square Channels. *Angew Chem Int Ed Engl* **1995,** *34* (19), 2127-2129.

2. Nugent, P.; Belmabkhout, Y.; Burd, S. D.; Cairns, A. J.; Luebke, R.; Forrest, K.; Pham, T.; Ma, S.; Space, B.; Wojtas, L.; Eddaoudi, M.; Zaworotko, M. J., Porous materials with optimal adsorption thermodynamics and kinetics for CO_2 separation. *Nature* **2013,** *495* (7439), 80-84.

3. Uemura, K.; Maeda, A.; Maji, T. K.; Kanoo, P.; Kita, H., Syntheses, Crystal Structures and Adsorption Properties of Ultramicroporous Coordination Polymers Constructed from Hexafluorosilicate Ions and Pyrazine. *Eur J Inorg Chem* **2009,** (16), 2329-2337.

4. Nugent, P. S.; Rhodus, V. L.; Pham, T.; Forrest, K.; Wojtas, L.; Space, B.; Zaworotko, M. J., A Robust Molecular Porous Material with High CO_2 Uptake and Selectivity. *J Am Chem Soc* **2013,** *135* (30), 10950-10953.

5. Kumar, A.; Hua, C.; Madden, D. G.; O'Nolan, D.; Chen, K. J.; Keane, L. A. J.; Perry, J. J.; Zaworotko, M. J., Hybrid ultramicroporous materials (HUMs) with enhanced stability and trace carbon capture performance. *Chem Comm* **2017,** *53* (44), 5946-5949.

6.   Mohamed, M. H.; Elsaidi, S. K.; Wojtas, L.; Pham, T.; Forrest, K. A.; Tudor, B.; Space, B.; Zaworotko, M. J., Highly Selective CO_2 Uptake in Uninodal 6-Connected "mmo" Nets Based upon MO_4^{2-} (M = Cr, Mo) Pillars. *J Am Chem Soc* **2012,** *134* (48), 19556-19559.

7.   Bhatt, P. M.; Belmabkhout, Y.; Cadiau, A.; Adil, K.; Shekhah, O.; Shkurenko, A.; Barbour, L. J.; Eddaoudi, M., A Fine-Tuned Fluorinated MOF Addresses the Needs for Trace CO_2 Removal and Air Capture Using Physisorption. *J Am Chem Soc* **2016,** *138* (29), 9301-9307.

8.   Cadiau, A.; Belmabkhout, Y.; Adil, K.; Bhatt, P. M.; Pillai, R. S.; Shkurenko, A.; Martineau-Corcos, C.; Maurin, G.; Eddaoudi, M., Hydrolytically stable fluorinated metal-organic frameworks for energy-efficient dehydration. *Science* **2017,** *356* (6339), 731-735.

9.   Caskey, S. R.; Wong-Foy, A. G.; Matzger, A. J., Dramatic tuning of carbon dioxide uptake via metal substitution in a coordination polymer with cylindrical pores. *J Am Chem Soc* **2008,** *130* (33), 10870.

10.   Cavenati, S.; Grande, C. A.; Rodrigues, A. E., Adsorption equilibrium of methane, carbon dioxide, and nitrogen on zeolite 13X at high pressures. *J Chem Eng Data* **2004,** *49* (4), 1095-1101.

11.   Desveaux, B. E.; Wong, Y. T. A.; Lucier, B. E. G.; Terskikh, V. V.; Boyle, P. D.; Jiang, S.; Huang, Y., CO_2 Behavior in a Highly Selective Ultramicroporous Framework: Insights from Single-Crystal X-ray Diffraction and Solid-State Nuclear Magnetic Resonance Spectroscopy. *J Phys Chem C* **2019,** *123* (29), 17798-17807.

12.   D'Alessandro, D. M.; Smit, B.; Long, J. R., Carbon Dioxide Capture: Prospects for New Materials. *Angew Chem Int Ed Engl* **2010,** *49* (35), 6058-6082.

13.   Kanoo, P.; Reddy, S. K.; Kumari, G.; Haldar, R.; Narayana, C.; Balasubramanian, S.; Maji, T. K., Unusual room temperature CO_2 uptake in a fluoro-functionalized MOF: insight from Raman spectroscopy and theoretical studies. *Chem Comm* **2012,** *48* (68), 8487-8489.

14.   Forrest, K. A.; Pham, T.; Hogan, A.; McLaughlin, K.; Tudor, B.; Nugent, P.; Burd, S. D.; Mullen, A.; Cioce, C. R.; Wojtas, L.; Zaworotko, M. J.; Space, B., Computational Studies of CO_2 Sorption and Separation in an Ultramicroporous Metal-Organic Material. *J Phys Chem C* **2013,** *117* (34), 17687-17698.

15.   Pham, T.; Forrest, K. A.; McLaughlin, K.; Tudor, B.; Nugent, P.; Hogan, A.; Mullen, A.; Cioce, C. R.; Zaworotko, M. J.; Space, B., Theoretical Investigations of CO_2 and H_2 Sorption in an Interpenetrated Square-Pillared Metal-Organic Material. *J Phys Chem C* **2013,** *117* (19), 9970-9982.

16.   Ziaee, A.; Chovan, D.; Lusi, M.; Perry, J. J.; Zaworotko, M. J.; Tofail, S. A. M., Theoretical Optimization of Pore Size and Chemistry in SIFSIX-3-M Hybrid Ultramicroporous Materials. *Cryst Growth Des* **2016,** *16* (7), 3890-3897.

17.   Moggach, S. A.; Bennett, T. D.; Cheetham, A. K., The effect of pressure on ZIF-8: increasing pore size with pressure and the formation of a high-pressure phase at 1.47 GPa. *Angew Chem Int Ed Engl* **2009,** *48* (38), 7087-9.

18.   Fairen-Jimenez, D.; Moggach, S. A.; Wharmby, M. T.; Wright, P. A.; Parsons, S.; Duren, T., Opening the gate: framework flexibility in ZIF-8 explored by experiments and simulations. *J Am Chem Soc* **2011,** *133* (23), 8900-2.

19.   Claire L. Hobday, T. D. B., David Fairen-Jimenez , Alexander J. Graham, Carole A. Morrison, David R. Allan, Tina Düren , and Stephen A. Moggach, Tuning the Swing Effect by Chemical Functionalization of Zeolitic Imidazolate Frameworks. *J Am Chem Soc* **2018,** *140* (1), 382–387.

20.   Mao, H.; Xu, J.; Hu, Y.; Huang, Y.; Song, Y., The effect of high external pressure on the structure and stability of MOF α-$Mg_3(HCOO)_6$ probed by in situ Raman and FT-IR spectroscopy. *J Mater Chem A* **2015,** *3* (22), 11976-11984.

21.   Spencer, E. C.; Kiran, M. S.; Li, W.; Ramamurty, U.; Ross, N. L.; Cheetham, A. K., Pressure-induced bond rearrangement and reversible phase transformation in a metal-organic framework. *Angew Chem Int Ed Engl* **2014,** *53* (22), 5583-6.

22.   Ortiz, A. U.; Boutin, A.; Gagnon, K. J.; Clearfield, A.; Coudert, F. X., Remarkable pressure responses of metal-organic frameworks: proton transfer and linker coiling in zinc alkyl gates. *J Am Chem Soc* **2014,** *136* (32), 11540-5.

23.   Gagnon, K. J.; Beavers, C. M.; Clearfield, A., MOFs under pressure: the reversible compression of a single crystal. *J Am Chem Soc* **2013,** *135* (4), 1252-5.

24.   Serra-Crespo, P.; Dikhtiarenko, A.; Stavitski, E.; Juan-Alcaniz, J.; Kapteijn, F.; Coudert, F. X.; Gascon, J., Experimental Evidence of Negative Linear Compressibility in the MIL-53 Metal-Organic Framework Family. *CrystEngComm* **2015,** *17* (2), 276-280.

25.   Karena W. Chapman, G. J. H., and Peter J. Chupas, Pressure-Induced Amorphization and Porosity Modification in a Metal-Organic Framework. *J Am Chem Soc* **2009,** *131*, 17546-17547.

26.   Serra-Crespo, P.; Stavitski, E.; Kapteijn, F.; Gascon, J., High compressibility of a flexible metal-organic framework. *RSC Adv* **2012,** *2* (12), 5051.

27.   Zhou, M.; Wang, K.; Men, Z.; Sun, C.; Li, Z.; Liu, B.; Zou, G.; Zou, B., Pressure-induced isostructural phase transition of a metal-organic framework $Co_2(4,4'-bpy)_3(NO_3)_4 \cdot xH_2O$. *CrystEngComm* **2014,** *16* (20), 4084-4087.

28.   Yot, P. G.; Ma, Q.; Haines, J.; Yang, Q.; Ghoufi, A.; Devic, T.; Serre, C.; Dmitriev, V.; Férey, G.; Zhong, C.; Maurin, G., Large breathing of the MOF MIL-47(VIV) under mechanical pressure: a joint experimental–modelling exploration. *Chem Sci* **2012,** *3* (4), 1100.

29.   Hobday, C. L.; Marshall, R. J.; Murphie, C. F.; Sotelo, J.; Richards, T.; Allan, D. R.; Duren, T.; Coudert, F. X.; Forgan, R. S.; Morrison, C. A.; Moggach, S. A.; Bennett, T. D., A Computational and Experimental Approach Linking Disorder, High-Pressure Behavior, and Mechanical Properties in UiO Frameworks. *Angew Chem Int Ed Engl* **2016,** *55* (7), 2401-5.

30.   Hu, Y.; Lin, B.; He, P.; Li, Y.; Huang, Y.; Song, Y., Probing the Structural Stability of and Enhanced CO_2 Storage in MOF MIL-68(In) under High Pressures by FTIR Spectroscopy. *Chem Eur J* **2015,** *21* (51), 18739-48.

31.   Jiang, S.; Hu, Y.; Chen, S.; Huang, Y.; Song, Y., Elucidation of the Structural Origins and Contrasting Guest-Host Interactions in CO_2-Loaded CdSDB and PbSDB Metal-Organic Frameworks at High Pressures. *Chem Eur J* **2018,** *24* (72), 19280-19288.

32.   Nugent, P.; Belmabkhout, Y.; Burd, S. D.; Cairns, A. J.; Luebke, R.; Forrest, K.; Pham, T.; Ma, S.; Space, B.; Wojtas, L.; Eddaoudi, M.; Zaworotko, M. J., Porous materials with optimal adsorption thermodynamics and kinetics for CO_2 separation. *Nature* **2013,** *495* (7439), 80-4.

33.   Mao, H. K.; Xu, J.; Bell, P. M., Calibration of the ruby pressure gauge to 800 kbar under quasi-hydrostatic conditions. *J Geophys Res* **1986,** *91* (B5), 4673.

34.   Dong, Z.; Yang, S., Transformations of Cold-Compressed Multiwalled Boron Nitride Nanotubes Probed by Infrared Spectroscopy. *J Phys Chem C* **2010,** *114*, 1782–1788.

35.   Joseph, T.; Varghese, H. T.; Panickerc, C. Y.; Viswanathane, K.; Sundaraganesan, N.; Subramanian, N.; Dolezal, M., Vibrational spectroscopic studies and computational study of 6-chloro-N-(4-trifluoromethylphenyl)-pyrazine-2-carboxamide. *Int J Anal* **2012,** *3* (18), 1-11.

36.   R. B. Badachhape, G. H., L. D. McCory, and J. L. Margrave, Infrared Absorption Spectra of Inorganic Solids. IV. Hexafluorosilicates. Raman Spectra of Aqueous SiF_6^{2-}. *Inorg Chem* **1966,** *5* (5), 929–931.

37.   Banerjee, A.; Nandi, S.; Nasa, P.; Vaidhyanathan, R., Enhancing the carbon capture capacities of a rigid ultra-microporous MOF through gate-opening at low CO_2 pressures assisted by swiveling oxalate pillars. *Chem Commun (Camb)* **2016,** *52* (9), 1851-4.

Chapter 5

5 Monitoring the Synergetic Effect of High Pressure and Temperature on Enhancing CO$_2$ Adsorptive Capacity of ZIF-8 and UiO-66 by *In-Situ* FTIR Spectroscopy

5.1 Introduction

The sharply rising concentration of atmospheric carbon dioxide is one of the major concerns with respect to the global warming effect. Currently, the most commonly used method for CO$_2$ capture is chemical absorption by alkanolamine aqueous solutions. However, these solution-based chemical absorbents carry many main drawbacks such as low energy efficiency and huge loss during solvent evaporation and degradation. Alternatively, solid physisorbent materials including activated carbons, zeolites and ZIFs (zeolitic imidazolate frameworks), as well as MOFs (metal-organic frameworks), which have lower heat capacities and require lower regeneration energy, have attracted an increasing amount of research. Among these solid adsorption materials, the most promising candidates are ZIFs and MOFs due to their extremely high surface area and porosity, relatively large pore size, high chemical and structure stability, as well as high tunability.[1-4] All these properties give ZIFs and MOFs great potential to achieve optimal CO$_2$ capture and storage performance. In the large ZIF family, ZIF-8 [Zn(MeIm)$_2$, MeIm = 2-methylimidazolate] is one of the few noble ZIFs whose structural properties and gas adsorption performance (i.e. CH$_4$, N$_2$, H$_2$O and CO$_2$) have been intensively studied in the past decade, both under ambient conditions, low temperatures as well as high external pressures by experimental and computational methods.[5-10] For industrial applications, the exposure of the sorbents to harsh environments, such as heat, pressure, and strong basic or acidic chemical conditions, are inevitable.[11] Therefore, materials with long-term structural and chemical stability are requisite. As the charge of the metal center in a MOF plays an important role in increasing the stability of the framework, zirconium(IV)-based MOFs in general, exhibit excellent stability.[12] For the same reason, we have also chosen for this study is UiO-66 [Zr$_6$O$_4$(OH)$_4$(BDC)$_6$, BDC = benzene-1,4-dicarboxylate], which has shown high stability under humidity, can also sustain temperatures higher than 375 °C.[13-

[15] The adsorption of CO_2 and other gases (CH_4, H_2, etc.) in UiO-66(Zr) has been extensively explored,[16-19] and the material is commercially available.

The local structure of ZIF-8 is constructed by tetrahedrally connecting a zinc metal center to four individual methylimidazolate ligands, as illustrated in Figure 5.1. It possesses a sodalite (SOD) topology with a cage diameter of 11.6 Å and a cage aperture of 3.4 Å, formed by 4 membered rings and 6 membered rings.[3] UiO-66 is built from octahedral $Zr_6O_4(OH)_4$ metal clusters and 12 terephthalate bridging units, coordinated through the carboxylate groups on the linkers (Figure 5.1c-f).[13] Each Zr(IV) is connected to four other Zr(IV) by bridging μ_3-O or μ_3-OH groups, to form a Zr_6-octahedron with a Zr$\cdots$Zr distance of 3.513 Å. The assembled UiO-66 features three distinct types of Zr-O bonds: the Zr-$O_{(COO^-)}$, the Zr-$O_{\mu_3\text{-}O}$ and Zr-$O_{\mu_3\text{-}OH}$. Consequently, such unique connection between the $Zr_6O_4(OH)_4(BDC)_6$ clusters and the bridging terephthalate ligands give rise to the formation of two micropores of cages in the 3D framework of UiO-66: the larger octahedral cavities are 11 Å in diamter, and the smaller tetrahedral cavities are 8 Å in diamater.[20]

A significant amount of research effort has been paid to modifying and optimizing the CO_2 adsorption performance in ZIF-8 through chemical and post-synthetic methods. For instance, by the inclusion of the ionic liquid into the cages, the CO_2/CH_4 and CO_2/N_2 separation performances of ZIF-8 has been greatly enhanced. Similarly, base on the skeleton of UiO-66, a series of MOFs that possess the same topologies but different functionalities and pore sizes have been synthesized (i.e. UiO-68, UiO-66-NH_2). The isoretular synthesized UiO-66-NH_2 shows a superior CO_2 adsorption performance in both adsorption capacity and selectivity compared to that of the pristine UiO-66, which is owing to the strong interaction between CO_2 and the NH_2 functional group. Moreover, by incorporating graphene oxide (GO) to the framework, researches found that the CO_2 capacity and CO_2/N_2 selectivity of UiO-66 and UiO-66-NH_2 can be further improved. Besides all these synthetic and post-synthetic ways to improve the performance of MOFs, high pressure has been previously proven to be another promising method to efficiently modify the structural properties of MOFs. Previous studies have demonstrated that high pressure can tune the channel size and shape, accessible pore volume and surface area in MOFs. Consequently, these pressure-induced modifications on the framework will affect

the adsorption capacity, selectivity, and access to the binding sites, which eventually leads to better adsorption performance. Hu *et al* have demonstrated pressure-enhanced CO_2 storage in ZIF-8. Stronger CO_2-framework interactions regulated by pressure are probed using FTIR spectroscopy. However, all our previous high pressure studies were carried out at room temperature, where CO_2 solidified at a moderate pressure of 0.6-0.7 GPa. This phase change of CO_2 severely limits the further insertion of CO_2 into the cavities of MOFs since the solid CO_2 is less dynamic and immobile. Meanwhile, numerous of studies have illustrated that introducing small guest molecules to ZIF-8 framework (i.e. H_2O, methanol, CH_4, and CO_2) as PTMs can not only enhance the stability of the framework substantially to ~4 GPa, but also induce a unit cell expansion under various pressures.[21-24] Base on these observations, it is expected that introducing CO_2 molecules to ZIF-8 may also expand the unit cell volume and further improve the CO_2 adsorptive capacity, if fluid phase CO_2 could be achieved by elevating the temperature under higher pressures (i.e. above 0.6 GPa).

Contrary to the large number of high pressure studies on ZIF-8, our knowledge on the guest adsorption behaviors of UiO-66 under high pressure, on the other hand, is very limited. Despite the intensive investigations on the sorption and separation performance of various gas in UiO-66 and its analogs at near ambient conditions,[12, 16-20] so far, only the mechanical properties of UiO-66 under high pressure have been reported.[25-26] Thus, understanding the CO_2 adsorption behaviors of UiO-66 and the corresponding CO_2-framework interactions under high pressure is an important step toward discovering its best CO_2 storage conditions. Herein, based on the CO_2 phase diagram, we predict that by heating up the DAC system and liquidizing CO_2 under pressures higher than 0.7 GPa, more CO_2 would be forced into the framework. Considering the outstanding CO_2 adsorption performances of ZIF-8 and UiO-66 under ambient conditions, high structural and thermal stability, it is believed that the application of high pressure and high temperature could further bring their CO_2 storage efficiencies to a whole new level. It is also of our fundamental interest to comparatively study the similarities and differences in the CO_2 adsorption behaviors of ZIF-8 and UiO-66 under high pressure and high temperature conditions, and understand how the topological features in MOFs affect their adsorption properties.
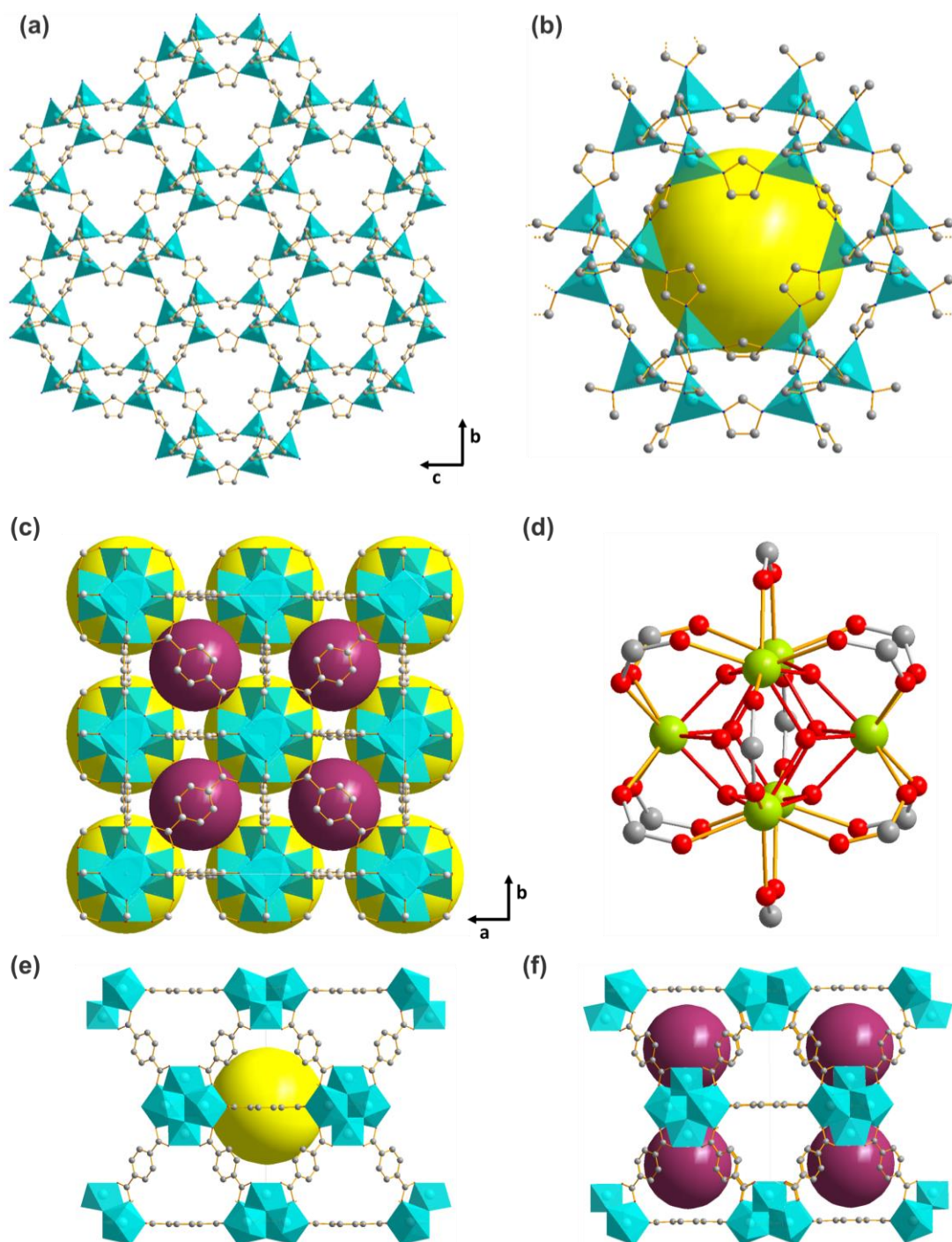
Figure 5.1 (a) Framework topology of ZIF-8 viewing along *a* axis. (b) Structure of the sodalite (SOD) cage in ZIF-8. (c) Framework topology of UiO-66 viewing along *c* axis. (d) The coordination environment of the $Zr_6O_4(OH)_4(O_2C)_{12}$ clusters. The octahedral cage (e) and the tetrahedral cage (f) in the UiO-66 structure. These images have been reproduced from previously reported structures. [19, 27]

5.2 Experimental

ZIF-8 and UiO-66 were synthesized solvothermally following the literature reported method.[19, 27] The identity and purity were checked using PXRD. To carry out in-situ high pressure experiments, a diamond anvil cell equipped with a pair of 600 µm type II diamonds was used for all IR measurements in this work. The sample chamber was prepared on a stainless-steel gasket, with 60-80 µm in thickness and 300 µm in diameter. A few ruby chips were pre-loaded to the sample chamber for pressure calibration. For sample loading, in order to load ZIF-8 along with extra CO_2 outside the framework, the sample chamber was firstly half-filled with activated ZIF-8. The piston side of the DAC was then immersed in a liquid nitrogen bath to cool down. During this process, the sample chamber was cover up with a plastic film to avoid moisture condensing on the sample. When the temperature of the gasket was below the melting point of dry ice (i.e. <-78.5 °C), the plastic film was removed, and the CO_2 gas was introduced into the sample chamber. Upon closing the DAC, an initial pressure of approximately 0.3 GPa was applied to secure the gaseous/liquid CO_2 in the sample chamber for further measurements.

The FTIR spectroscopy is highly customized for *in-situ* measurements under high pressure, with the details described in *Chapter 2*. In this work, to conduct *in-situ* high-pressure and high-temperature conditions simultaneously, the regular DAC stage for room temperature measurements is replaced by a custom-designed heating stage, which is composed of an aluminum stand, a heating holder, and a glass wool board for heat isolation. By placing the DAC onto this stage, a moderate temperature (up to ~500 °C) could be achieved by powering up the resistance heating holder. A temperature controller (omega iSeries) is equipped to control the temperature of the DAC precisely. The temperature is measured by attaching a thermocouple to the back of the piston diamond. The accuracy of the heating system is tested and recorded (as shown in Appendix), which has shown that the system is having a precision of ±2.3 K in the temperature range from 50-80 °C, ±5.0 K from 80 to 200 °C. In addition, the melting temperatures of solid CO_2 we observed are based on the substantial shape and frequency changes of the CO_2 combination modes on the IR spectra, melting temperatures in our works at various pressures are in good consistency with the CO_2 phase diagram reported by Giordano *et al.*[28]

5.3 Result and discussion

5.3.1 Characterization of CO_2 adsorption properties of ZIF-8 under high temperature and high-pressure conditions

The IR spectra of activated ZIF-8 and CO_2 loaded ZIF-8 are shown in Figure 5.2, the peak assignments are labeled below each band. The intense CO_2 fundamental modes ν_1 (O=C=O bending) and ν_3 (O=C=O asymmetric stretching) in the IR spectra of CO_2 loaded ZIF-8 suggest a successful gas loading. At 1.02 GPa and room temperature, CO_2 combination modes each exhibit two components, indicating that the CO_2 molecules in the sample chamber have two distinct environments. As discussed previously, the sharp high-frequency components of each mode are assigned to the free CO_2 in the sample chamber but outside the ZIF-8 framework, which undergoes a gaseous/liquid to solid phase change at about 0.6 GPa. The CO_2 molecules adsorbed in ZIF-8, on the other hand, are located at specific CO_2 binding sites in the cages and correspond to the low-frequency components of the doublets. The significantly enhanced C=N stretching mode at ~1600 cm^{-1} as well as the ring stretching mode between 1400 cm^{-1} and 1500 cm^{-1} indicating a stronger CO_2-framework interaction at high pressure (see Figure 5.2).[29-30]
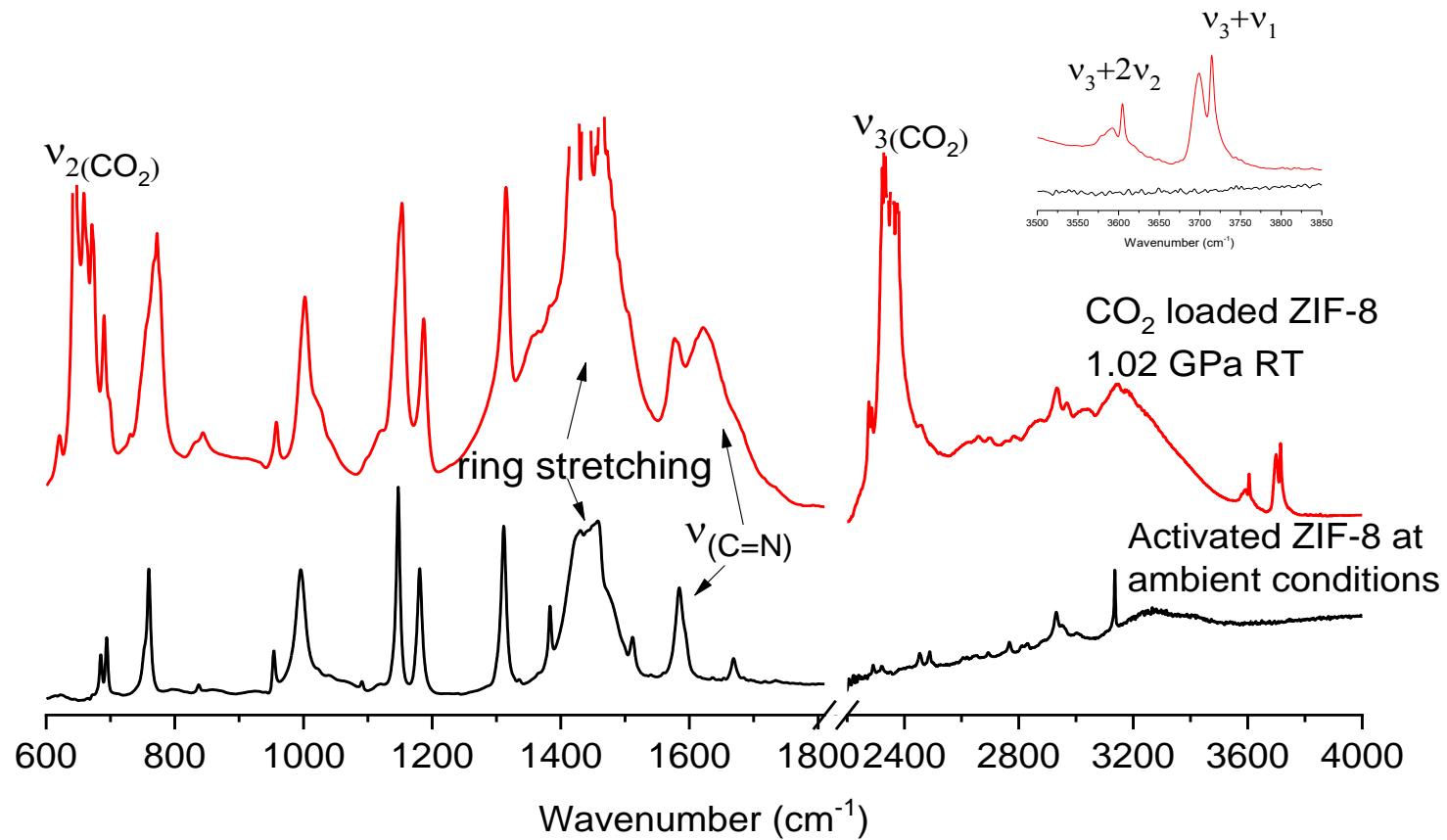
Figure 5.2 Mid-IR spectra of activated ZIF-8 at ambient pressure (black) and CO₂ loaded ZIF-8 at 1.02 GPa (red). The inset shows the comparison between the activated (bottom) and CO₂ loaded ZIF-8 (top) in the spectral region of the CO₂ combination modes.

After the cryogenic CO_2 loading, the FTIR spectra of CO_2 loaded ZIF-8 were collected as a function of temperature at fixed pressures. In all high pressure and high temperature measurements, CO_2 combination modes (i.e. $\nu_3 + 2\nu_2$ and $\nu_3 + \nu_1$, observed at around 3600 and 3710 cm^{-1} respectively) in FTIR spectra are used to follow the behavior of adsorbed CO_2 in MOFs, the host-guest interaction between CO_2 and the framework, as well as the phase change of the CO_2 outside framework. The selected FTIR spectra of CO_2 combination modes collected under 0.83 GPa and at various temperatures are depicted in Figure 5.3a. At 36 °C, both the high-frequency components of $\nu_3 + 2\nu_2$ and $\nu_3 + \nu_1$ bands become less intense while the low-frequency components become broader, suggesting that the solid CO_2 residing outside the framework starts to melt into liquid/gaseous phase at this temperature and pressure with part of it already adsorbed into the cages. Upon further heating, at the temperature of 40 °C, it is apparent that all solid CO_2 that was initially outside the ZIF-8 framework is liquefied, as the high-frequency and low-frequency components of both CO_2 combination modes merged into a singlet. After cooling the DAC system down to room temperature, the higher frequency component of both $\nu_3 + 2\nu_2$ and $\nu_3 + \nu_1$ bands reappear, but become significantly weaker, suggesting that more CO_2 is adsorbed in ZIF-8 cages compared to those before heating, in spite that part of the extra CO_2 transits from liquid phase back to solid phase at the temperatures of 36 °C and below. The quantity of each CO_2 species is determined by peak deconvolution and integration.

The $\nu_3 + \nu_1$ bands in CO_2 loaded ZIF-8 under 0.83 GPa and at various temperatures were deconvoluted and integrated (see Figure 5.4), with the normalized peak areas listed in Table 5.1. After initial CO_2 loading, the peak area of the low-frequency component of $\nu_3 + \nu_1$ was 0.55, it then slightly increased to 0.62 upon heating to 36 °C. At 40 °C, the peak area reached a maximum of 0.78, whereas the rest was attributed to the fluid CO_2 outside the framework (Figure 5.4). The peak area of the adsorbed CO_2 decreased to 0.62 upon cooling down to room temperature. Based on these numbers, we estimated the amount of CO_2 adsorbed in the framework is increased by 11.9% compared to that before heating.
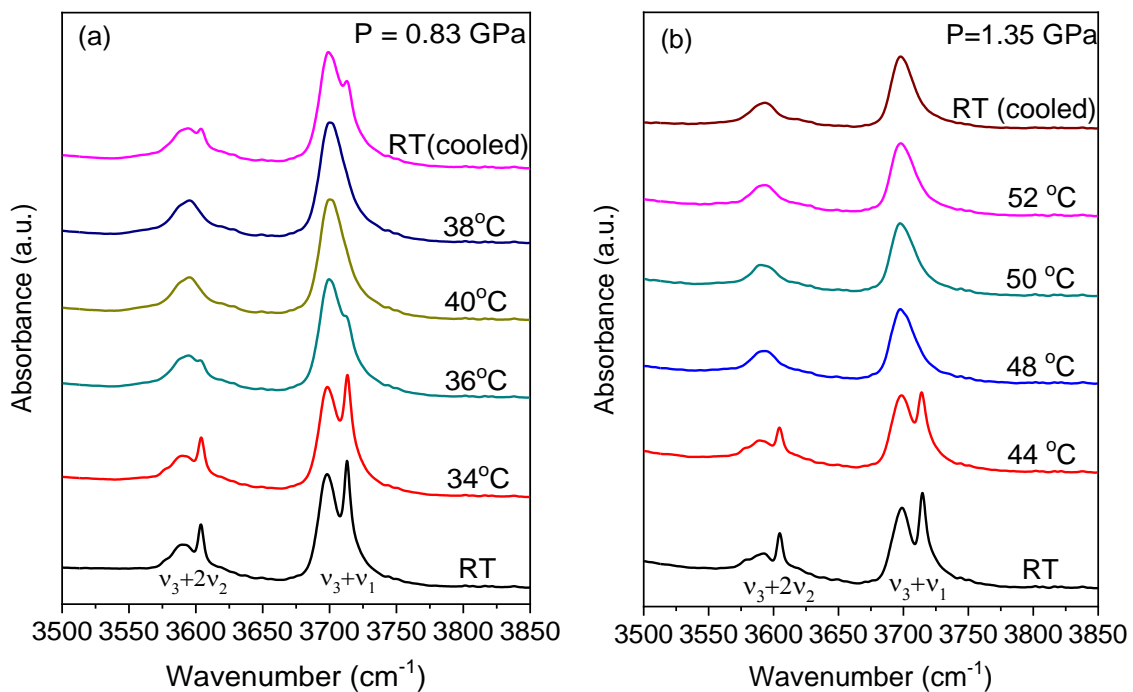
Figure 5.3 Selected mid-IR spectra of CO_2 combination modes under various temperatures in ZIF-8 at 0.83 GPa (a) and 1.35 GPa (b).

To optimize the synergetic effect of high pressure and high temperature on enhancing CO_2 capacity, a few high-temperature cycles with fixed pressures are also performed. Improved CO_2 capacities in ZIF-8 is found when the pressure is at 1.35 GPa. Upon heating up the sample to 44 °C, the melting of solid CO_2 was also observed (Figure 5.3b). At 48 °C and above, all extra CO_2 was melted by heating and diffused into the cages of ZIF-8. Upon cooling the sample down to room temperature, both $\nu_3 + 2\nu_2$ and $\nu_3 + \nu_1$ modes remain as single peaks, suggesting that these extra CO_2 molecules stay in the framework permanently upon cooling the sample down to RT.

The amount of adsorbed CO_2 in ZIF-8 is increased by 84.5% upon heat treatment at 1.35 GPa (Table 5.2). Such a substantial difference in capacity improvement between two runs is intriguing and is thought to be closely related to the framework structure under different pressures and temperatures. Indeed, Hobday *et al.* established a correlation between the pressure and the rotation angle (θ) of the imidazole rings, until the aperture reaches its maximum opening. Such rotation further gives rise to the maximum unit cell volume and

solvent-accessible volume, as illustrated in Figure 5.6.[9, 24] In our case, it is believed that the pressure-induced gate opening of ZIF-8 is not complete at 0.83 GPa, where the rotation of the imidazole rings has not yet reached the maximum of 90°. Therefore, the pressure as low as 0.83 GPa is not sufficient to maximize the CO_2 storage potential in ZIF-8. Whereas at 1.35 GPa, such "gate-opening" is complete, resulting in a significant increase in CO_2 adsorption. After peak deconvolution, an additional CO_2 site is discovered at a higher frequency (Figure 5.5 c-f), which could be assigned to the CO_2 molecules adsorbed in the channels surrounding the central pore. These channels are otherwise blocked by imidazole linkers and not accessible at the ambient pressure, which explains why this new site is not found under 0.83 GPa (Figure 5.4 a-f).[21]

Different from that has been observed above, heating up the DAC system under a much higher pressure of 2.61 GPa, however, has led to a decrease in adsorption capacity. As shown in Figure 5.7, at the highest temperature of 100 °C, the solid free CO_2 residing outside the frame remains solid and unadsorbed, consistent with the phase diagram that the free CO_2 should be solid under such conditions. Moreover, by comparing the series of spectra, there is less CO_2 adsorbed in the framework during the heating and cooling cycle, evidenced by the gradually flatten and weakened low-frequency component of CO_2 combination modes. These observations suggest that the ZIF-8 framework collapsed, and the porosity of the framework might have been partially damaged by exposing the ZIF-8 to harsher conditions (i.e. 2.61 GPa and 100 ℃).
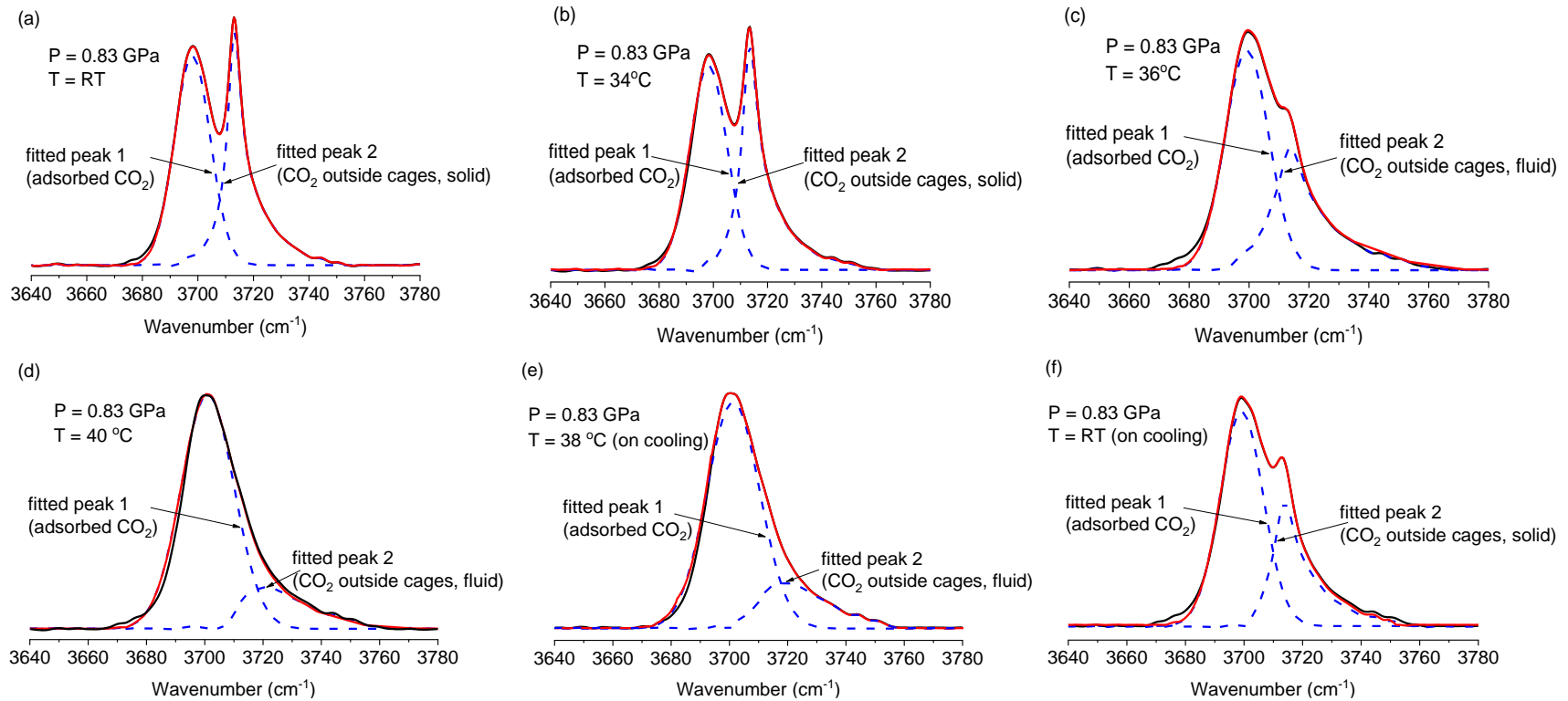
Figure 5.4 (a)-(f) Deconvolution of CO₂ v₃+v₁ mode on the FTIR spectra of CO₂ loaded ZIF-8 at 0.83 GPa and various temperatures. In all figures, the black solid line represents the actual spectrum, the red solid line is the fitted spectrum. The blue dash lines represent different species of CO₂.
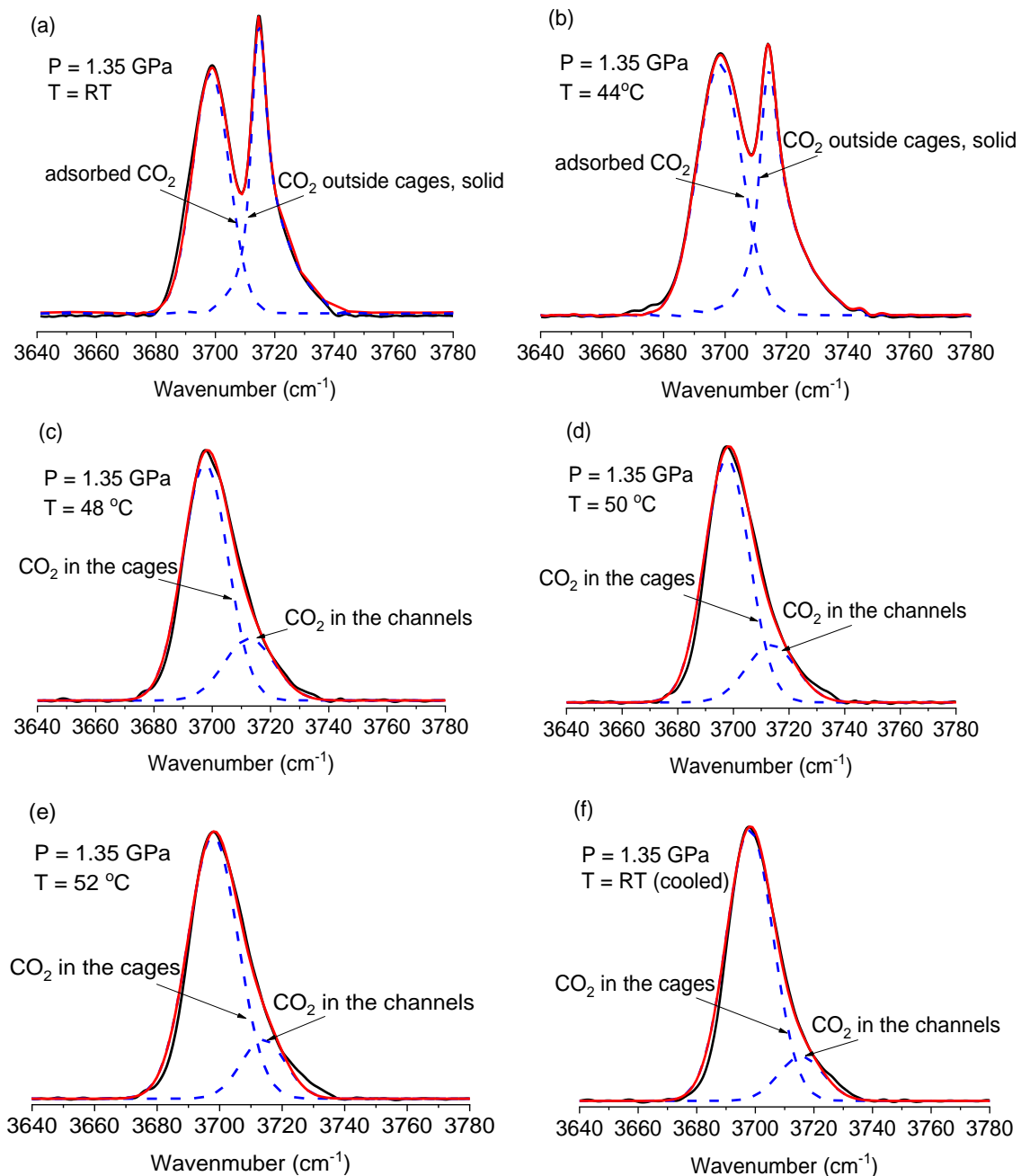
Figure 5.5 (a)-(f) Deconvolution of CO_2 v_3+v_1 mode on the FTIR spectra of CO_2 loaded ZIF-8 at 1.35 GPa and various temperatures. In all figures, the black solid line represents the actual spectrum, the red solid line is the fitted spectrum. The blue dash lines represent different species of CO_2. In figure (c)-(f), the main peak at lower frequency could be assigned as CO_2 molecules adsorbed in the central cage, whereas the higher frequency peak is thought to be attributed to the CO_2 adsorbed in the channels surrounding the central cage.[21]

Table 5.1 Normalized peak area of CO_2 $\nu_3 + \nu_1$ mode at 0.83 GPa and various temperatures in CO_2 loaded ZIF-8.

Temperature		RT	34 °C	36 °C	40 °C	38 °C	RT (cooled)
$\nu_3 + \nu_1$	Peak area of adsorbed CO_2	0.55	0.56	0.62	0.78	0.79	0.62
	Peak area of CO_2 outside framework	0.45	0.44	0.38	0.22	0.21	0.38

Table 5.2 Normalized peak area of CO_2 $\nu_3 + \nu_1$ mode at 1.35 GPa and various temperatures in CO_2 loaded ZIF-8.

Temperature		RT	44 °C	48 °C	50 °C	52 °C	RT (cooled)
$\nu_3 + \nu_1$	Peak area of adsorbed CO_2	0.54	0.58	1.00	1.00	1.00	1.00
	Peak area of CO_2 outside framework	0.46	0.42	-	-	-	-
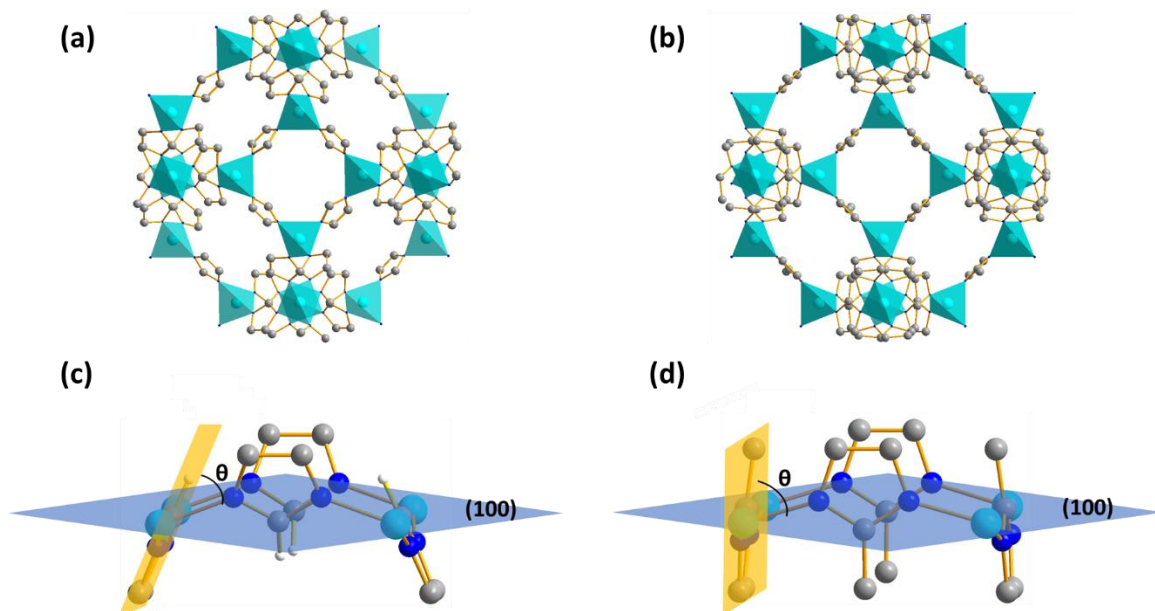
Figure 5.6 Structure of ambient phase ZIF-8 (a) and high-pressure phase ZIF-8 (b), the imidazole linkers rotated by 30° under high pressure compared to the ambient phase structure. The 4 MR window in ZIF-8 structure, showing the opening angle (θ) of 68° in ambient phase (c) and 89° in high pressure phase. These ambient pressure (AP) and high pressure (HP) structure images of ZIF-8 are reproduced from literature.[21]
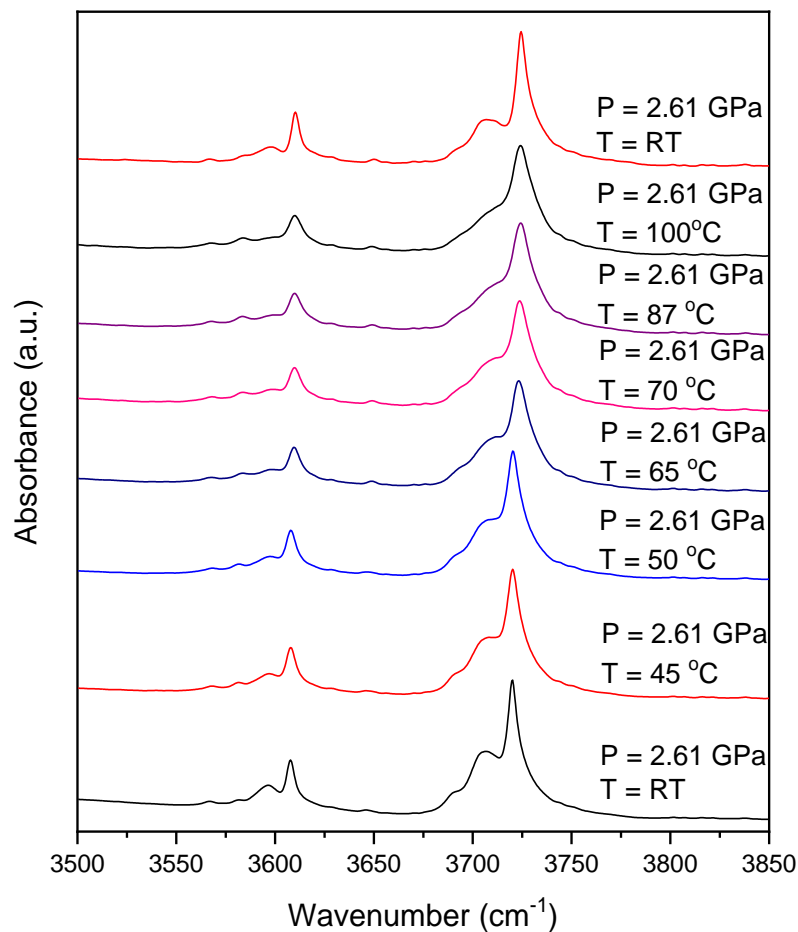
Figure 5.7 Selected mid-IR spectra of CO_2 combination modes in CO_2 loaded ZIF-8 at 2.61 GPa and various temperatures.

5.3.2 The pressure behavior of activated UiO-66 framework

The structural stability and reversibility in response to mechanical pressure are critical to their applications. The first high pressure study on mechanical properties of UiO-66 was reported by Su *et al*. In their study, UiO-66 nanocrystals were compressed by a hydraulic piston pelletizer, its morphology and structural properties were then investigated using SEM, FTIR and XANES after the pressure was released. However, reports have shown that the morphology of material may substantially affect its pressure behaviors.[31-32] Besides, the compression method used in Su's study is only able to detect the irreversible changes induced by high pressures, there are still potentially reversible changes under high pressures that are yet to explore. Therefore, we performed *in situ* high pressure FTIR study

on activated UiO-66 to investigate the structural properties prior to high pressure and high temperature studies on CO_2 adsorption. In the FTIR spectrum of the activated UiO-66 (Figure 5.8), most of the bands in the spectral region (i.e. 600-4000 cm^{-1}) are attributed to the internal vibrations of the BDC ligands in the framework, whereas the Zr-O asymmetric stretching vibration is expected at 546 cm^{-1} and therefore cannot be detected.[33] The broad band at 659 cm^{-1} corresponds to the vibration of the $Zr_6O_4(OH)_4$ hexanuclear cluster.[33] The peaks in the 700-900 cm^{-1} spectral region can be assigned as the out-of-plane C-H bending of the terephthalate, while the bands at around 1000-1200 cm^{-1} are associated with the in-plane C-H bending. In the higher frequency region, the symmetric and asymmetric stretching modes of the terephthalic carboxylate group can be found at around 1400 cm^{-1} and 1500-1630 cm^{-1}, respectively. The band at around 3100 cm^{-1} is attributed to the aromatic C-H stretching. At the highest frequency, a very weak peak observed at 3673 cm^{-1} is assigned to the O-H stretching mode of the μ_3-OH groups (Figure 5.8).[34] Such assignment is confirmed by a deuterium-exchange experiment, in which the D-exchanged UiO-66 no longer exhibits the O-H stretching mode at this frequency (Figure 5.8 inlet).
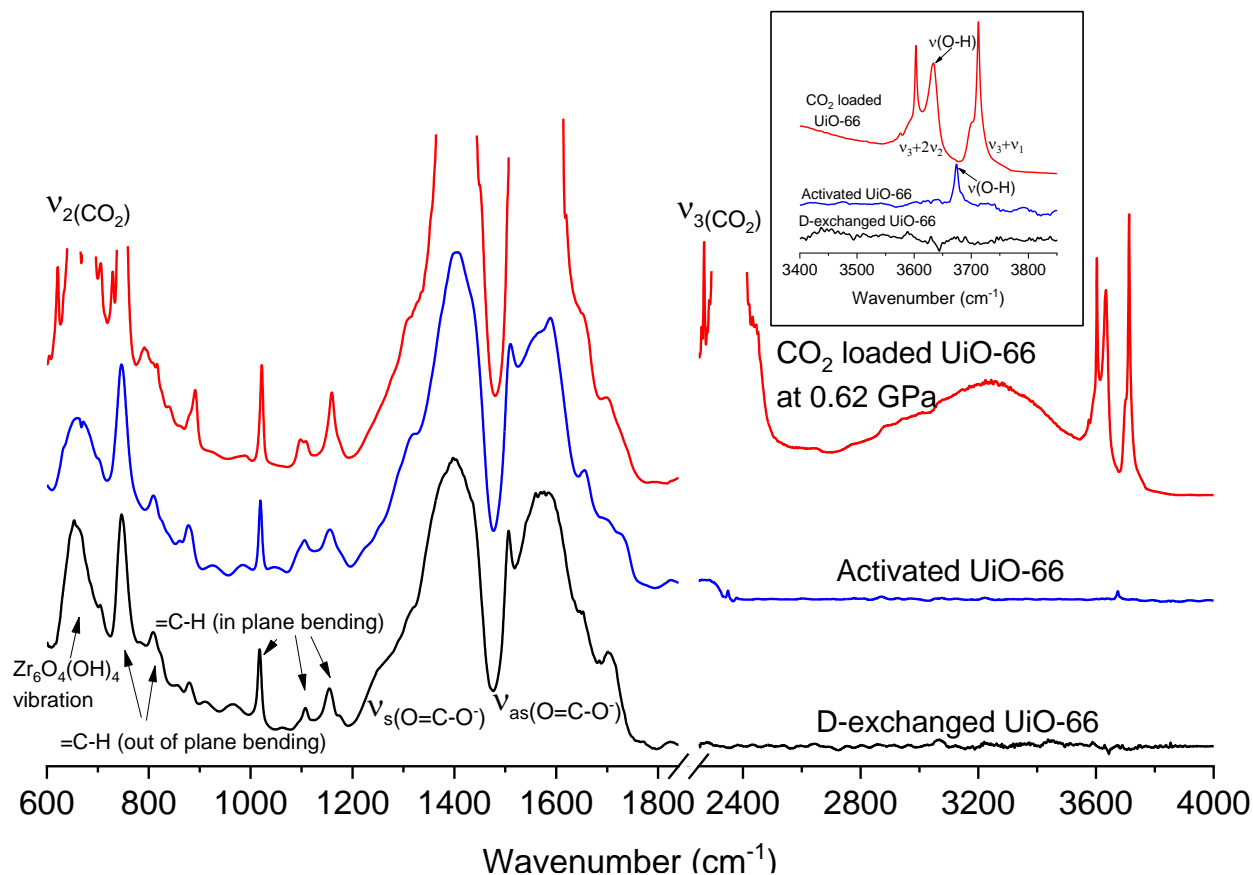
Figure 5.8 Mid-IR spectra of activated (blue) and deuterium-exchanged (black) UiO-66 at ambient pressure, in comparison with CO₂ loaded UiO-66 at 0.62 GPa (red). The inset shows the spectral region of 3400-3850 cm⁻¹, highlighting the CO₂ v_3+2v_2 and v_3+v_1 combination modes in CO₂ loaded UiO-66. The disappearance of the O-H mode in the deuterium-exchanged UiO-66 (blue) confirmed the assignment of this mode.

Upon a slight compression to 0.64 GPa, the band at 1587 cm^{-1} exhibits a significant intensity decrease, while a shoulder band at 1561 cm^{-1} emerges (Figure 5.9a and inlet). These observations are typical signs for the transition of the coordination mode of the carboxylate group from the *syn-syn* bridging to a monodentate mode,[35] as previously reported in Su's study,[25] which indicates that the Zr-O$_{(COO^-)}$ coordination bonds between Zr(IV) metal centers and terephthalic carboxylate groups are partially broken. Such bond breakage was first demonstrated by Su *et al*,[25] in their work, after compressed UiO-66 nanocrystals to 0.8 GPa, a similar *syn-syn* bridging to monodentate coordination mode transition was also observed using FTIR and confirmed by extended X-ray absorption fine structure (EXAFS).[25] The difference in the threshold pressure for the Zr-O$_{(COO^-)}$ bond breakage between their work and this work could be associated with the size and morphology of the sample, where bulk samples were synthesized and used in this study instead of nanocrystals. This size-dependent pressure-induced amorphization has been found in a wide range of materials, such as TiO$_2$, Y$_2$O$_3$ and PbTe.[31-32] Nanoparticles are usually predicted to have a higher transition pressure than their bulk counterparts of the same composition. Aside from what Su *et al.* previously reported, our spectra have shown a decreasing intensity of the other sharp band at 1510 cm^{-1} in the carboxylate asymmetric stretching region, this peak is then completely flattened at the pressure of 5.19 GPa (Figure 5.9a and inlet), suggesting the disorder of the monodentate coordinated Zr-O$_{(COO^-)}$ bond at higher pressures. On decompression, the bond at 1510 cm^{-1} gradually remerges, accompanied by the recovery of other bands such as the C-H in-plane and out-of-plane bending modes, whereas the peak at 1587 cm^{-1} disappeared permanently as anticipated, corresponding to the irreversibility of the Zr-O$_{(COO^-)}$ bond breakage.

Pressure dependence of vibration modes, defined as vibrational frequencies as a function of pressure, is an important parameter to appraise the sensitivity of a vibrational mode in response to external pressure, and gain better understandings of pressure effect on structures and host-guest interactions. The pressure coefficients of selected IR modes of UiO-66 were calculated by linear regression and illustrated in Figure 5.9b. Most IR modes have shown a blueshift in the entire pressure region, this is owing to the reduced bond length induced by high pressure. Among all these modes, the C-H stretching mode at 3064

cm^{-1} exhibits the greatest pressure coefficient of 7.04 cm^{-1}/GPa, whereas the blueshifts of other modes are less than 3.2 cm^{-1}/GPa in magnitude. It is worth noting that the $Zr_6O_4(OH)_4$ cluster vibration display a degree of redshift with -3.36 cm^{-1}/GPa in magnitude, which is consistent with the weakening of the Zr-O$_{(COO^-)}$ under high pressures,[25] before the breakage of the bond occurs. The pressure range for such redshift (i.e. 0.09 to 1.30 GPa) also coincides with that for the Zr-O$_{(COO^-)}$ bond breakage. In fact, the pressure dependence of all IR modes has shown discontinuities in between 1.30 to 1.79 GPa, it is believed that this bond breakage has led to a substantial structural transition.
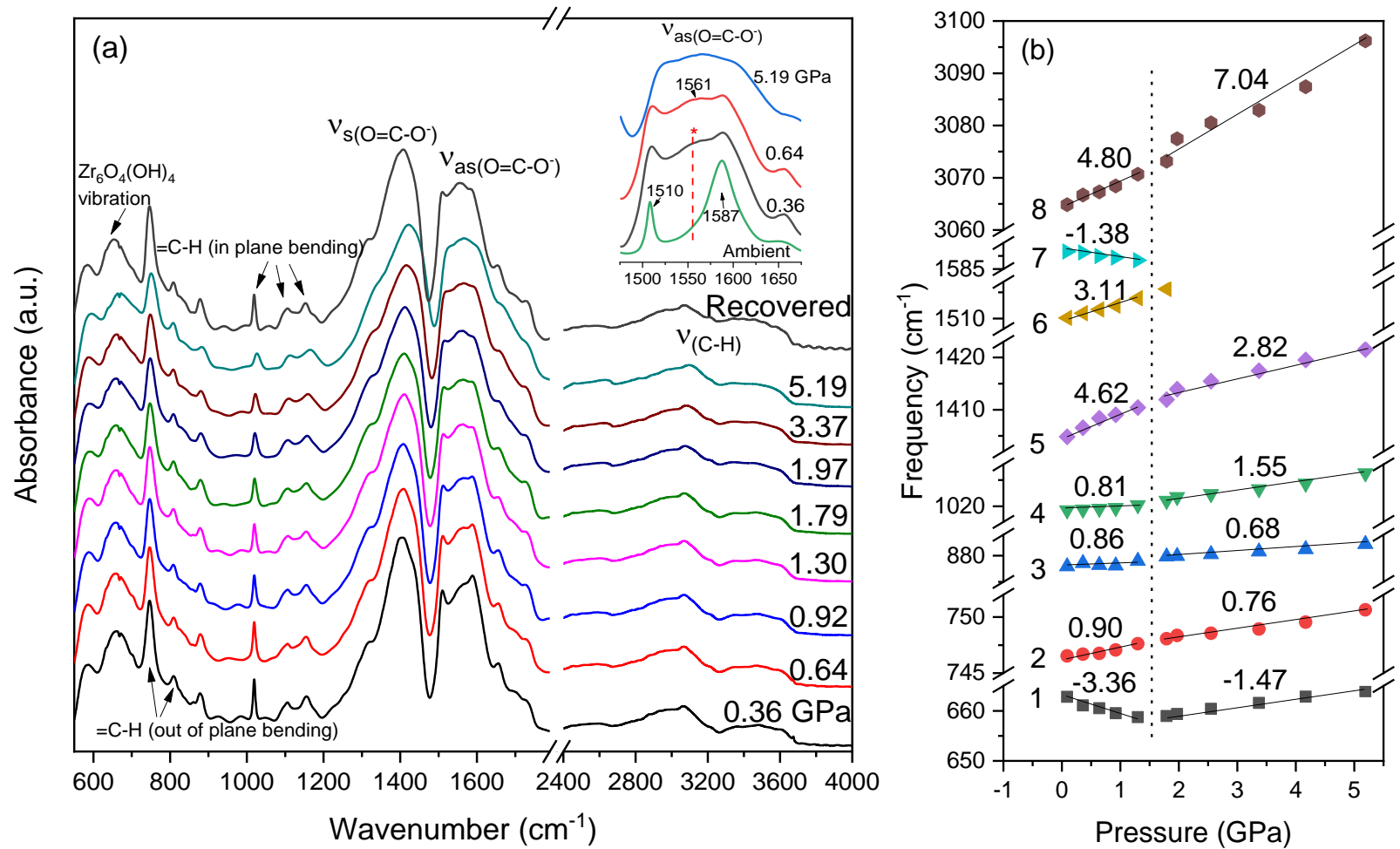
Figure 5.9 (a) Selected FTIR spectra of empty UiO-66 at high pressures. (b) Pressure dependence of selected IR modes. The inlet in (a) shows the zoomed spectral region of the ν_{as}(O=C-O) mode under selected pressures.

5.3.3 The structural behavior of CO_2 loaded UiO-66 and the host-guest interactions at high pressures

The CO_2 loaded UiO-66, however, undergoes a completely different structural evolution compared to that of the empty UiO-66. The FTIR spectra of CO_2 loaded UiO-66 were collected as a function of pressure from ambient to 6.13 GPa at room temperature. At the initial pressure of 0.62 GPa (Figure 5.8), the intense CO_2 ν_3 (O=C=O asymmetric stretching) mode at 2340 cm^{-1} and the relatively weaker CO_2 combination bands ($\nu_3+2\nu_2$ and $\nu_3+\nu_1$) at 3600 and 3800 cm^{-1} confirmed the existence of CO_2 in the sample chamber.[36] It has been previously reported and well-established that the CO_2 combination modes can be used to monitor the insertion of CO_2 into the pores of porous materials, CO_2 behaviors, as well as the host-guest interactions.[5, 37] Given that the ν_3 mode of CO_2 is extremely saturated under our loading conditions, the well-resolved combination mode ($\nu_3+\nu_1$) is chosen for further analysis. In the spectral region from 3500 to 3800 cm^{-1} (Figure 5.10a), $\nu_3+\nu_1$ mode exhibits two components, which typically suggests the co-existence of two different types of CO_2 molecules. Base on the high pressure phase diagram of CO_2, as well as our previous studies, the sharper band at 3603 cm^{-1} and 3712 cm^{-1} are attributed to the CO_2 residing outside the framework as solid.[28, 38-39] Whereas the less intense shoulder band at around 3700 cm^{-1} on the lower frequency end are assigned to the adsorbed CO_2. Upon elevating the pressure, a pressure-induced blueshift is observed for $\nu_3+\nu_1$ doublet, indicating that the O=C=O bond becomes stiffen under pressure. At 0.92 GPa and higher, the O-H stretching mode displays different components, suggesting the OH groups are under multiple different environments. Interestingly, the O-H stretching mode exhibits a moderate redshift, which is typically a result of bond weakening. Such softening behavior is most often associated with enhanced intermolecular interactions, in this case, the interaction between CO_2 molecules and the μ_3-OH groups. Indeed, by carrying out neutron powder diffraction (NPD) measurements and DFT calculations, Chevreau *et al.*[16] proved that the CO_2 molecules located in the tetrahedral cage are orientated with one oxygen atom facing the -OH functional group on the $Zr_6O_4(OH)_4$ cluster, while the other oxygen atom pointing into the cage. The CO_2-OH distance was determined to be 2.40(2) Å, which allows the coulombic interaction between

the electronegative oxygen atom of the CO_2 molecule and the electropositive hydrogen atom from the μ_3-OH group.[16]

On the pressure dependence graph (Figure 5.10b), a mild redshift with the coefficient of -2.17 cm^{-1}/GPa was observed in the pressure region of 0.62-4 GPa, followed by a blueshift under higher pressures (i.e. 4-6.13 GPa), indicating that the external pressure promotes the affinity between CO_2 and μ_3-OH group during compression up to 4 GPa, nevertheless, such interaction becomes repulsive at higher pressures, results in the O-H bond stiffening. In terms of the guest molecules, the pressure coefficient of the $\nu_3+\nu_1$ doublets for the pure solid CO_2 and adsorbed CO_2 are 6.9 and 4.1 $cm^{-1}\cdot GPa^{-1}$, respectively. In principle, the observed pressure dependence ($d\nu/dP$) of the adsorbed CO_2 has contributions from two opposite effects: strong CO_2-framework interactions would cause redshift of the mode, whereas the pressure-induced shortening of the bond length would lead to blueshift. Therefore, a smaller pressure coefficient corresponds to a stronger interaction between the adsorbed CO_2 and the framework. Moreover, according to previous work of in ZIF-8, the pressure coefficient of the same combination mode for the adsorbed CO_2 is 5.26 cm^{-1}/GPa,[5] compared to 4.1 cm^{-1}/GPa for UiO-66, meaning that CO_2 interacts with UiO-66 framework more intensively than it with ZIF-8 under high pressures, which is attributed to the naturally stronger O=C=O···H-O interaction in UiO-66, compared to the π-π stacking interaction between CO_2 and the imidazole ring in ZIF-8.
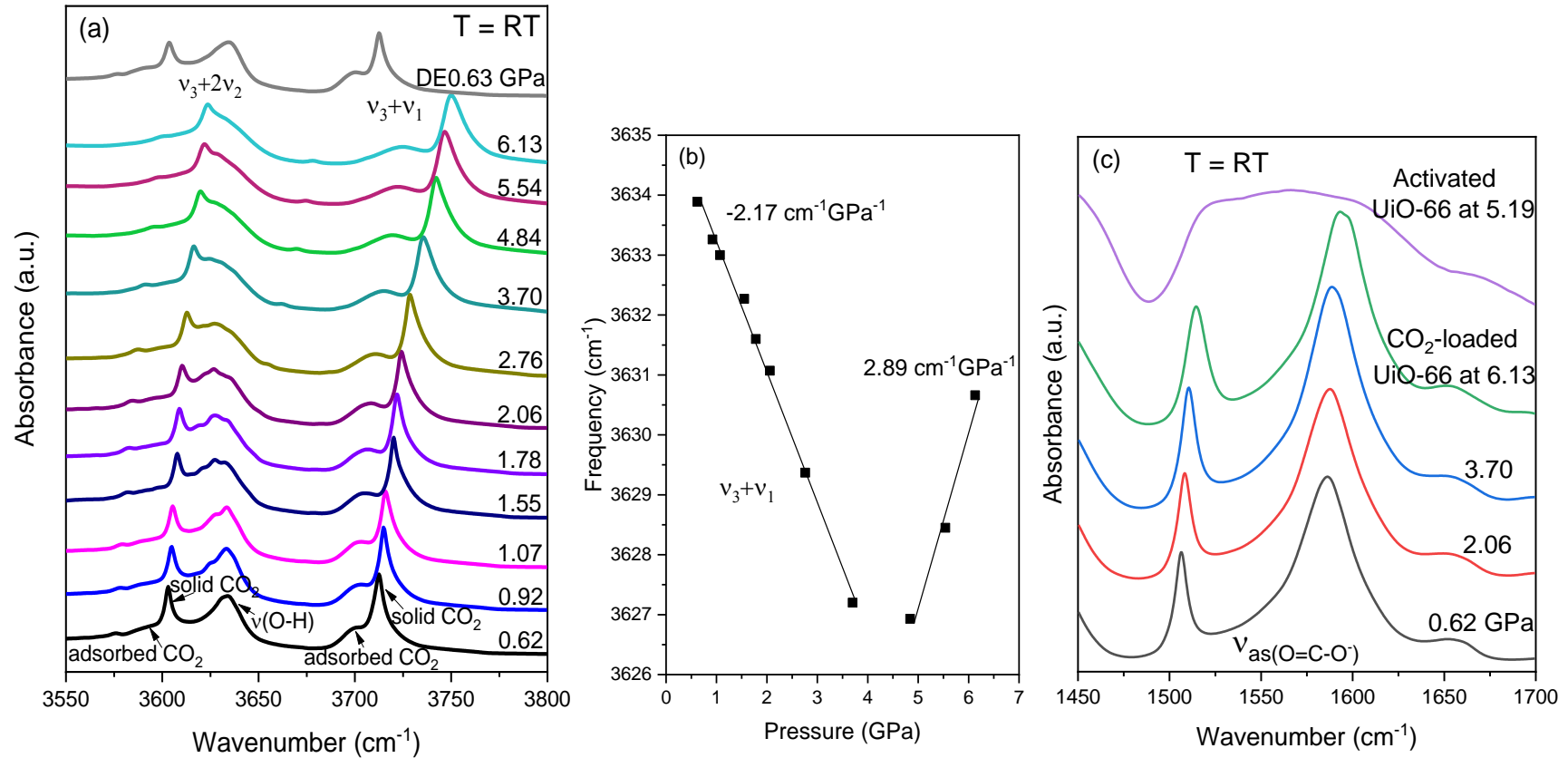
Figure 5.10 (a) FTIR spectra of $\nu_3+2\nu_2$ and $\nu_3+\nu_1$ modes of CO_2 in UiO-66 upon compression and decompression in the spectral region of 3550-3800 cm^{-1}. **(b)** Pressure dependence of $\nu_3+\nu_1$ mode of adsorbed CO_2 in ZIF-8. **(c)** Zoomed in spectral region of 1450-1700 cm^{-1}, showing that the Zr-$O_{(COO^-)}$ bonds in CO_2 loaded UiO-66 remain intact under pressure up to 6.13 GPa. The spectrum of activated UiO-66 under 5.19 GPa is plotted in the figure as a comparison.

Being the guest molecules, CO_2, in turn, affects the structural stability of both UiO-66 and ZIF-8. The structural reversibility of UiO-66 at high pressures is believed to be highly guest-dependent, similar to that has been reported for ZIF-8. As we discussed previously, the compression on empty UiO-66 framework led to a permanent $Zr-O_{(COO^-)}$ bond breakage at around 1 GPa, the pore volume and BET surface dropped rapidly from 0.54 $cm^3 \cdot g^{-1}$ and 1050 $m^2 \cdot g^{-1}$ before compression, to 0.05 $cm^3 \cdot g^{-1}$ and 130 $m^2 \cdot g^{-1}$ after the compression of 1.5 GPa reported by Su *et al.*[25] Whereas the CO_2 loaded UiO-66 survived the highest compression pressure of 6.13 GPa, with the framework structure and porosity remain intact (Figure 5.10a). No sign of coordination mode transition from *syn-syn* bridging to monodentate of the carboxylate group has been observed (Figure 5.10c), suggesting that there is no breakage of the $Zr-O_{(COO^-)}$ bonds in the entire pressure region. In the case of ZIF-8, the empty framework underwent an irreversible amorphization starting from 0.34 GPa,[40] the pore volume of which decreased sharply from 0.66 before compression to 0.24 after the compression to 1.1 GPa,[41] though there is no bond breakage involved in this process. In contrast, the compression on guest-loaded ZIF-8 is proved to be completely reversible by many studies with the usage of various guest molecules, the highest reported pressure for the framework to maintain its properties is 4.0 GPa in the MeOH loaded ZIF-8. Overall, the excellent structural stability of the CO_2 loaded UiO-66 and ZIF-8 fulfilled the fundamental requirements for the further investigation of CO_2 adsorptions in these two frameworks under high temperature and high-pressure conditions.

5.3.4 Characterization of CO_2 adsorption properties of UiO-66 under high temperature and high-pressure conditions

In the high pressure and high temperature work on UiO-66, CO_2 combination mode ($v_3 + v_1$) at around 3710 cm^{-1} in the FTIR spectra is again used to follow the behavior of adsorbed CO_2 and the MOF framework. The FTIR spectra of CO_2 loaded UiO-66 were collected as a function of temperature at 1.32 GPa (Figure 5.11a). Similar to what we observed previously in ZIF-8, upon heating up the sample, the peaks correspond to solid CO_2 (i.e. 3605 cm^{-1} for v_3+2v_2, and 3714 cm^{-1} for v_3+v_1) started to broaden along with a loss in intensity, indicating that the crystalline CO_2 (phase I, space group Pa3) gradually become fluid with increasing temperature. At 47 °C, all solid CO_2 transitioned into fluid CO_2, as

evidenced by the disappearance of the high frequency components of v_3+2v_2 and v_3+v_1 modes. Upon cooling, these two bands reappeared at 40 °C, indicating that the solid CO_2 completed the recrystallization process at 35 °C, as the peak intensities were no longer increasing. When the system is completely cooled down to the room temperature, there is an observable intensity decrease of the solid CO_2 peaks compared to that of the initial temperature.
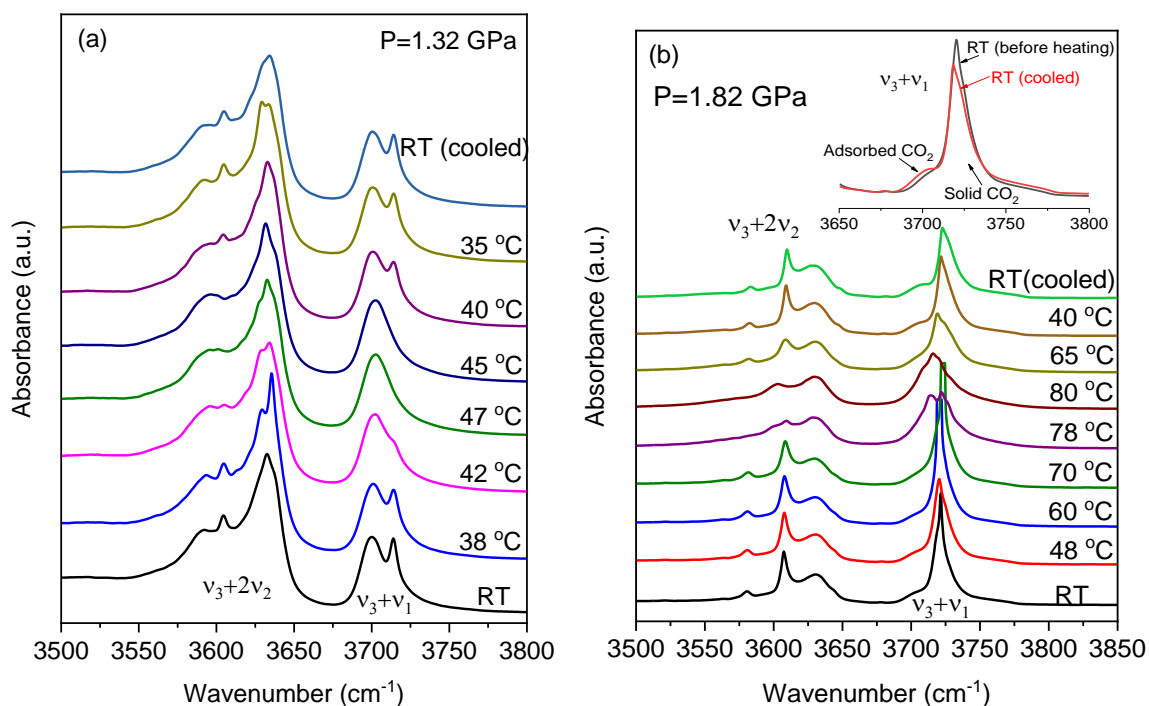
Figure 5.11 Selected mid-IR spectra of CO_2 combination modes under various temperatures and 1.32 GPa (a), 1.82 GPa (b) in UiO-66. The inlet in (b) depicted the zoomed spectral region of the CO_2 v_3+v_1 mode before heating (black) and after cooling (red).

In the high temperature cycle on CO_2 loaded UiO-66 at 1.32 GPa, the $v_3 + v_1$ bands at selected temperatures were deconvoluted and integrated (See Figure 5.12a-c), with the normalized peak areas listed in Table 5.3. After the initial gas loading, the normalized peak area for the solid and adsorbed CO_2 are 0.47 and 0.53, respectively. At the highest temperature of 47 °C, the peak area of the adsorbed CO_2 increased to 0.65 while the quantity of free CO_2 molecules reduced, suggesting that with the aid of high pressure, a

substantial amount of CO_2 was diffused and inserted into the cages of the UiO-66 framework after being liquefied. Upon cooling down to room temperature, the amount of adsorbed CO_2 in UiO-66 is increased by 16.4% compared to that before heating.

To understand what role pressure plays in this synergetic effect on enhancing CO_2 capacity of UiO-66, another high-temperature cycle with the DAC fixed at a higher pressure is also carried out. The FTIR spectra of CO_2 loaded UiO-66 were collected as a function of temperature at 1.82 GPa (Figure 5.11b). Upon elevating the temperature, the initial sign for CO_2 melting is observed at 78 °C, where the solid CO_2 components of both v_3+2v_2 and v_3+v_1 modes became much weaker and broader. At 80 °C, the intensity of the high-frequency component of v_3+v_1 mode further decreased and red-shifted, indicates that the solid CO_2 is partially liquefied (Figure 5.11b). Upon cooling down to room temperature, the intensity of the adsorbed CO_2 component appears to increase, compared to that of the initial sample (Figure 5.11b inlet), suggesting that the CO_2 capacity of UiO-66 has been improved in the run. Due to the amount of the CO_2 loaded to the sample in the run, unfortunately, the high-frequency component of v_3+v_1 mode is saturated under most temperatures, which makes deconvolution of the peaks difficult and less accurate.

Table 5.3 Normalized peak area of CO_2 $v_3 + v_1$ and v_3+2v_2 modes at 1.32 GPa and selected temperatures in CO_2 loaded UiO-66.

Temperature		RT	47 °C	RT (cooled)
v_3+v_1	Peak area of adsorbed CO_2	0.53	0.65	0.62
	Peak area of CO_2 outside framework	0.47	0.35	0.38
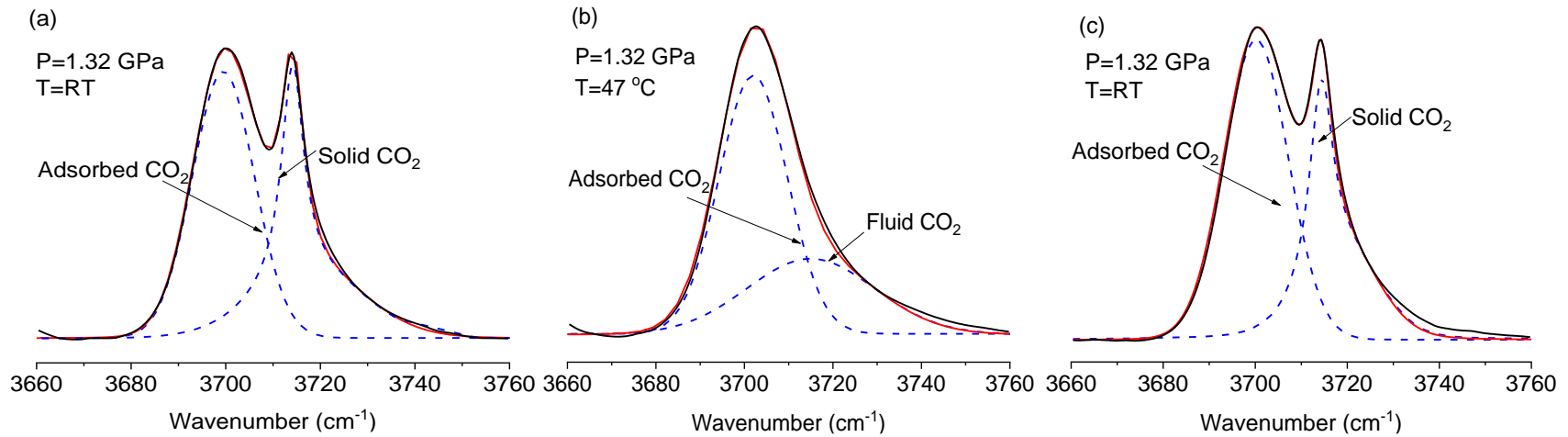
Figure 5.12 Deconvolution of CO₂ $v_3 + v_1$ mode on the FTIR spectra of CO₂ loaded UiO-66 at 1.32 GPa (a)-(c) and CO₂ $v_3 + 2v_2$ mode at 1.82 GPa (d)-(f) and selected temperatures. In all figures, the black solid line represents the actual spectrum, the red solid line is the fitted spectrum. The blue dash lines represent different species of CO₂, and the pink dash line corresponds to O-H stretching mode.

5.3.5 The structural origins of contrasting CO_2 adsorption properties in ZIF-8 and UiO-66 under high temperature and high-pressure conditions

It becomes apparent that the improvement on CO_2 adsorption capacity in ZIF-8 is significantly greater than that of UiO-66 under similar pressures, the root of which can be tracked down to the inherent structural properties of these two frameworks. In ZIF-8, upon melting the extra CO_2, high pressure not only promotes further CO_2 insertion into the cages, most importantly, it triggers the gate-opening effect of the ZIF-8 framework, which involves the rotation and reorientation of the imidazole rings on the 4-membered window on the central pore of ZIF-8 framework.[9] This rotation results in an increase in the size of the 6-membered aperture, and an expansion of the free pore volume from 2497 Å^3 at ambient conditions to 2710 Å^3 at high pressure,[24] thus acquires the ability to accommodate more small guest molecules. It has been illustrated by many other studies that this gate opening effect could be achieved using a few different small molecules such as H_2O, methanol, ethanol, CH_4, O_2, N_2,[24] and the mixture of MeOH and EtOH, at pressures of 2.2 GPa, 0.3 GPa, 0.6 GPa, 1.4 GPa, 2.0 GPa, 3.25 GPa[22] and 1.47 GPa, respectively.[15] For instance, using the methanol and ethanol mixture as PTM, the total number of methanol molecules increased from 12 per unit cell at ambient pressure, to 41 per unit cell at 1.47 GPa.[21] In our case, the gate opening effect of ZIF-8 induced by CO_2 takes place at around 1.35 GPa, meanwhile, heating up the sample under this pressure results in the melting of the extra solid CO_2 into liquid. By such synergetic effect of high pressure and high temperature, more CO_2 molecules get adsorbed into the cages of ZIF-8. The similar heat and pressure-induced CO_2 insertion has also been observed in an auxetic small-pore zeolite but with the requirements of higher pressure (above 1.5 GPa) and higher temperature (over 110 °C).[42] In contrast, the principle behind the capacity improvement in UiO-66 is straightforward: without any gating effect that allows the cage size to increase, high pressure simply plays the role of forcing more fluid CO_2 into the framework to further fill the pores. Moreover, the μ_3-OH group sits in all four corners of the tetrahedral cage, with the H atom pointing into the cage.[16] These μ_3-OH groups form strong O-H$\cdots$O=C=O interaction once exposing to CO_2, which may block the window and prevent the entrance of more CO_2 at higher pressures.

5.4 Conclusions

In summary, using FTIR spectroscopy, our work confirmed that the structural stability of UiO-66 at high pressure is highly guest-dependent, the empty framework displays a permanent $Zr(IV)-O_{COO}$ bond breakage at very low pressures, whereas the CO_2 loaded UiO-66 framework is found to be completely reversible up to 6 GPa, with the chemical connectivity and porosity remain intact. A stronger host-guest interplay between CO_2 and the μ_3-OH group is observed under high pressures. More importantly, we demonstrate that by applying heating the sample at a fixed pressure, the CO_2 storage capacities of both ZIF-8 and UiO-66 are further improved at modest pressures. In ZIF-8, such improvement is more striking at 1.35 GPa due to the pressure-induced gate opening effect of the framework. Whereas in UiO-66, the improvement on the CO_2 capacity is less dramatic due to the lack of such gating effect. In this study, high-temperature and high-pressure display a synergetic effect in facilitating the CO_2 adsorption in ZIF-8 and UiO-66: heating liquefies the extra CO_2 outside the framework, while high pressure promotes the diffusion of the fluid CO_2 into the frameworks. However, our work of applying the heat to the sample under 2.61 GPa results in loss of the framework porosity in ZIF-8 gradually. Therefore, the optimum conditions for CO_2 storage in ZIF-8 is only under moderate pressure and temperature. It is hoped that our work will encourage studies on further modifying the storage conditions for CO_2 in other MOFs and porous materials.

5.5 References

1.   Park, K. S.; Ni, Z.; Côté, A. P.; Choi, J. Y.; Huang, R.; Uribe-Romo, F. J.; Chae, H. K.; O'Keeffe, M.; Yaghi, O. M., Exceptional chemical and thermal stability of zeolitic imidazolate frameworks. *Proc Natl Acad Sci U S A* **2006,** *103* (27), 10186-10191.

2.   Wang, B.; Cote, A. P.; Furukawa, H.; O'Keeffe, M.; Yaghi, O. M., Colossal cages in zeolitic imidazolate frameworks as selective carbon dioxide reservoirs. *Nature* **2008,** *453* (7192), 207-11.

3.   Phan, A.; Doonan, C. J.; Uribe-Romo, F. J.; Knobler, C. B.; O'Keeffe, M.; Yaghi, O. M., Synthesis, Structure, and Carbon Dioxide Capture Properties of Zeolitic Imidazolate Frameworks. *Acc Chem Res* **2010,** *43* (1), 58-67.

4.   Sumida, K.; Rogow, D. L.; Mason, J. A.; McDonald, T. M.; Bloch, E. D.; Herm, Z. R.; Bae, T. H.; Long, J. R., Carbon dioxide capture in metal-organic frameworks. *Chem Rev* **2012,** *112* (2), 724-81.

5.   Hu, Y.; Liu, Z.; Xu, J.; Huang, Y.; Song, Y., Evidence of pressure enhanced CO_2 storage in ZIF-8 probed by FTIR spectroscopy. *J Am Chem Soc* **2013,** *135* (25), 9287-90.

6.   Nune, S. K.; Thallapally, P. K.; Dohnalkova, A.; Wang, C.; Liu, J.; Exarhos, G. J., Synthesis and properties of nano zeolitic imidazolate frameworks. *Chem Commun (Camb)* **2010,** *46* (27), 4878-80.

7.   Fairen-Jimenez, D.; Galvelis, R.; Torrisi, A.; Gellan, A. D.; Wharmby, M. T.; Wright, P. A.; Mellot-Draznieks, C.; Duren, T., Flexibility and swing effect on the adsorption of energy-related gases on ZIF-8: combined experimental and simulation study. *Dalton Trans* **2012,** *41* (35), 10752-62.

8.   Perez-Pellitero, J.; Amrouche, H.; Siperstein, F. R.; Pirngruber, G.; Nieto-Draghi, C.; Chaplais, G.; Simon-Masseron, A.; Bazer-Bachi, D.; Peralta, D.; Bats, N., Adsorption of CO_2, CH_4, and N_2 on zeolitic imidazolate frameworks: experiments and simulations. *Chem Eur J* **2010,** *16* (5), 1560-71.

9.   Fairen-Jimenez, D.; Moggach, S. A.; Wharmby, M. T.; Wright, P. A.; Parsons, S.; Duren, T., Opening the gate: framework flexibility in ZIF-8 explored by experiments and simulations. *J Am Chem Soc* **2011,** *133* (23), 8900-2.

10.   Pantatosaki, E.; Megariotis, G.; Pusch, A.-K.; Chmelik, C.; Stallmach, F.; Papadopoulos, G. K., On the Impact of Sorbent Mobility on the Sorbed Phase Equilibria and Dynamics: A Study of Methane and Carbon Dioxide within the Zeolite Imidazolate Framework-8. *J Phys Chem C* **2011,** *116* (1), 201-207.

11.   Tan, K.; Nijem, N.; Gao, Y.; Zuluaga, S.; Li, J.; Thonhauser, T.; Chabal, Y. J., Water interactions in metal organic frameworks. *CrystEngComm* **2015,** *17* (2), 247-260.

12.   Grissom, T. G.; Driscoll, D. M.; Troya, D.; Sapienza, N. S.; Usov, P. M.; Morris, A. J.; Morris, J. R., Molecular-Level Insight into CO_2 Adsorption on the Zirconium-Based Metal–Organic Framework, UiO-66: A Combined Spectroscopic and Computational Approach. *J Phys Chem C* **2019,** *123* (22), 13731-13738.

13.   Cavka, J. H.; Jakobsen, S.; Olsbye, U.; Guillou, N.; Lamberti, C.; Bordiga, S.; Lillerud, K. P., A new zirconium inorganic building brick forming metal organic frameworks with exceptional stability. *J Am Chem Soc* **2008,** *130* (42), 13850-13851.

14.   Shearer, G. C.; Chavan, S.; Bordiga, S.; Svelle, S.; Olsbye, U.; Lillerud, K. P., Defect Engineering: Tuning the Porosity and Composition of the Metal–Organic Framework UiO-66 via Modulated Synthesis. *Chem Mater* **2016,** *28* (11), 3749-3761.

15.   Peterson, G. W.; DeCoste, J. B.; Glover, T. G.; Huang, Y.; Jasuja, H.; Walton, K. S., Effects of pelletization pressure on the physical and chemical properties. *Microporous and Mesoporous Materials* **2013,** *179* (15), 48-53.

16.   Chevreau, H.; Liang, W.; Kearley, G. J.; Duyker, S. G.; D'Alessandro, D. M.; Peterson, V. K., Concentration-Dependent Binding of CO_2 and CD_4 in UiO-66(Zr). *J Phys Chem C* **2015,** *119* (13), 6980-6987.

17.   Abid, H. R.; Tian, H.; Ang, H.-M.; Tade, M. O.; Buckley, C. E.; Wang, S., Nanosize Zr-metal organic framework (UiO-66) for hydrogen and carbon dioxide storage. *Chem Eng J* **2012,** *187*, 415-420.

18.   Chavan, S.; Vitillo, J. G.; Gianolio, D.; Zavorotynska, O.; Civalleri, B.; Jakobsen, S.; Nilsen, M. H.; Valenzano, L.; Lamberti, C.; Lillerud, K. P.; Bordiga, S., H_2 storage in isostructural UiO-67 and UiO-66 MOFs. *Phys Chem Chem Phys* **2012,** *14* (5), 1614-26.

19.   Zhao, Q.; Yuan, W.; Liang, J.; Li, J., Synthesis and hydrogen storage studies of metal-organic framework UiO-66. *Int J Hydrog Energy* **2013,** *38* (29), 13104-13109.

20.   Yang, Q.; Wiersum, A. D.; Llewellyn, P. L.; Guillerm, V.; Serre, C.; Maurin, G., Functionalizing porous zirconium terephthalate UiO-66(Zr) for natural gas upgrading: a computational exploration. *Chem Commun (Camb)* **2011,** *47* (34), 9603-5.

21.   Moggach, S. A.; Bennett, T. D.; Cheetham, A. K., The effect of pressure on ZIF-8: increasing pore size with pressure and the formation of a high-pressure phase at 1.47 GPa. *Angew Chem Int Ed Engl* **2009,** *48* (38), 7087-9.

22.   Im, J.; Seoung, D.; Hwang, G. C.; Jun, J. W.; Jhung, S. H.; Kao, C.-C.; Vogt, T.; Lee, Y., Pressure-Dependent Structural and Chemical Changes in a Metal-Organic Framework with One-Dimensional Pore Structure. *Chem Mater* **2016,** *28* (15), 5336-5341.

23.   Radhakrishnan, D.; Narayana, C., Guest dependent Brillouin and Raman scattering studies of zeolitic imidazolate framework-8 (ZIF-8) under external pressure. *J Chem Phys* **2016,** *144* (13), 134704.

24.   Hobday, C. L.; Woodall, C. H.; Lennox, M. J.; Frost, M.; Kamenev, K.; Duren, T.; Morrison, C. A.; Moggach, S. A., Understanding the adsorption process in ZIF-8 using high pressure crystallography and computational modelling. *Nat Commun* **2018,** *9* (1), 1429.

25.   Su, Z.; Miao, Y. R.; Zhang, G.; Miller, J. T.; Suslick, K. S., Bond breakage under pressure in a metal-organic framework. *Chem Sci* **2017,** *8* (12), 8004-8011.

26.   Yot, P. G.; Yang, K.; Ragon, F.; Dmitriev, V.; Devic, T.; Horcajada, P.; Serre, C.; Maurin, G., Exploration of the mechanical behavior of metal-organic frameworks UiO-66(Zr) and MIL-125(Ti) and their NH_2 functionalized versions. *Dalton Trans* **2016,** *45* (10), 4283-8.

27.   Shi, Q.; Chen, Z.; Song, Z.; Li, J.; Dong, J., Synthesis of ZIF-8 and ZIF-67 by steam-assisted conversion and an investigation of their tribological behaviors. *Angew Chem Int Ed Engl* **2011,** *50* (3), 672-5.

28.   Giordano, V.; Datchi, F., Molecular carbon dioxide at high pressure and high pressure. *Eur Phys* **2007,** *77*, 46002.

29.   Hu, Y.; Kazemian, H.; Rohani, S.; Huang, Y.; Song, Y., In situ high pressure study of ZIF-8 by FTIR spectroscopy. *Chem Commun (Camb)* **2011,** *47* (47), 12694-6.

30.   Ordoñez, M. J. C.; Balkus, K. J.; Ferraris, J. P.; Musselman, I. H., Molecular sieving realized with ZIF-8/Matrimid® mixed-matrix membranes. *J Membr Sci* **2010,** *361* (1-2), 28-37.

31.   Wang, L.; Yang, W.; Ding, Y.; Ren, Y.; Xiao, S.; Liu, B.; Sinogeikin, S. V.; Meng, Y.; Gosztola, D. J.; Shen, G.; Hemley, R. J.; Mao, W. L.; Mao, H. K., Size-dependent amorphization of nanoscale Y_2O_3 at high pressure. *Phys Rev Lett* **2010,** *105* (9), 095701.

32.   Machon, D.; Melinon, P., Size-dependent pressure-induced amorphization: a thermodynamic panorama. *Phys Chem Chem Phys* **2015,** *17* (2), 903-10.

33.   Van de Voorde, B.; Stassen, I.; Bueken, B.; Vermoortele, F.; De Vos, D.; Ameloot, R.; Tan, J.-C.; Bennett, T. D., Improving the mechanical stability of zirconium-based metal-organic frameworks by incorporation of acidic modulators. *J Mater Chem A* **2015,** *3* (4), 1737-1742.

34.   Shearer, G. C.; Forselv, S.; Chavan, S.; Bordiga, S.; Mathisen, K.; Bjørgen, M.; Svelle, S.; Lillerud, K. P., In Situ Infrared Spectroscopic and Gravimetric Characterisation of the Solvent Removal and Dehydroxylation of the Metal-Organic Frameworks UiO-66 and UiO-67. *Top in Catal* **2013,** *56* (9-10), 770-782.

35.   Zelenak, V.; Vargova, Z.; Gyoryova, K., Correlation of infrared spectra of zinc(II) carboxylates with their structures. *Spectrochim Acta A Mol Biomol Spectrosc* **2007,** *66* (2), 262-72.

36.   Aoki, K.; Yamawaki, H.; Sakashita, M., Phase study of solid CO_2 to 20 GPa by infrared-absorption spectroscopy. *Phys Rev B Condens Matter* **1993,** *48* (13), 9231-9234.

37.   Hu, Y.; Lin, B.; He, P.; Li, Y.; Huang, Y.; Song, Y., Probing the Structural Stability of and Enhanced CO_2 Storage in MOF MIL-68(In) under High Pressures by FTIR Spectroscopy. *Chem Eur J* **2015,** *21* (51), 18739-48.

38.   Jiang, S.; Hu, Y.; Chen, S.; Huang, Y.; Song, Y., Elucidation of the Structural Origins and Contrasting Guest-Host Interactions in CO_2-Loaded CdSDB and PbSDB Metal-Organic Frameworks at High Pressures. *Chem Eur J* **2018,** *24* (72), 19280-19288.

39.   Santoro, M.; Lin, J. F.; Mao, H. K.; Hemley, R. J., In situ high P-T Raman spectroscopy and laser heating of carbon dioxide. *J Chem Phys* **2004,** *121* (6), 2780-7.

40.   Chapman, K. W.; Halder, G. J.; Chupas, P. J., Pressure-Induced Amorphization and Porosity Modification in a Metal-Organic Framework. *J Am Chem Soc* **2009,** *131* (48), 17546-17547.

41.   Su, Z.; Miao, Y. R.; Mao, S. M.; Zhang, G. H.; Dillon, S.; Miller, J. T.; Suslick, K. S., Compression-induced deformation of individual metal-organic framework microcrystals. *J Am Chem Soc* **2015,** *137* (5), 1750-3.

42.   Lee, Y.; Liu, D.; Seoung, D.; Liu, Z.; Kao, C. C.; Vogt, T., Pressure- and heat-induced insertion of CO_2 into an auxetic small-pore zeolite. *J Am Chem Soc* **2011,** *133* (6), 1674-7.

Chapter 6

6 Understanding Carbon Dioxide and Water Adsorptions within the Ultramicroporous ZnAtzOx Framework and the Guest-Host Interactions under High External Pressures

6.1 Introduction

The tailoring of metal-organic frameworks (MOFs) to increase gas adsorption affinities is key for practical applications. The usage of open metal sites is one popular technique for accomplishing this,[1-2] as well as the addition of amine groups to the linkers.[3-5] These additions can be especially impactful within ultra-microporous structures, where subtle changes to the linkers can strongly impact the porosity and guest-host interactions that occur within a given MOF.[6] While the structural dynamics MOFs are known for[7-9] are not generally expected within these ultra-microporous materials, there are known examples of "gate-opening" creating new adsorption sites within such materials. A series of zinc-aminotriazolate-oxalate (ZnAtzOx) structures reported by Banerjee *et al*. is a key example of this phenomenon.[3, 6, 10]

These ZnAtzOx frameworks contain ultra-micropores, amine-functionalized ligands and in some cases a gate-opening mechanism that can increase the CO_2 uptake of the structure. Due to this set of features, a comprehensive understanding of their absorption behavior is warranted. The framework exhibiting a gate-opening mechanism, $ZnAtzOx(H_2O)$, is of particular interest due to the observed 42% increase in CO_2 uptake with respect to the earlier ZnAtzOx frameworks (i.e. ZnAtzOx(MeOH) and ZnAtzOx(EtOH)). This increased uptake is marked by a dramatic adsorbed CO_2 at a P/P0 of 0.2 at 273 K (where P0 is the saturation pressure), with the adsorption isotherm curve being characteristic of a gate-opening mechanism.[10] The effect of this gate-opening increases the maximum occupancy of the unit cell from 1.3 to 2.25 CO_2 molecules. The $ZnAtzOx(H_2O)$ framework is best described as an assembly of zinc-3-amino-1,2,4-triazolate layers that are pillared into a three-dimensional structure by oxalate linkers, with channels running along the a-axis, b-axis, and [0 1 1] axis. This creates ultra-micropores within the framework 4 Å across, as shown in Figure 6.1.
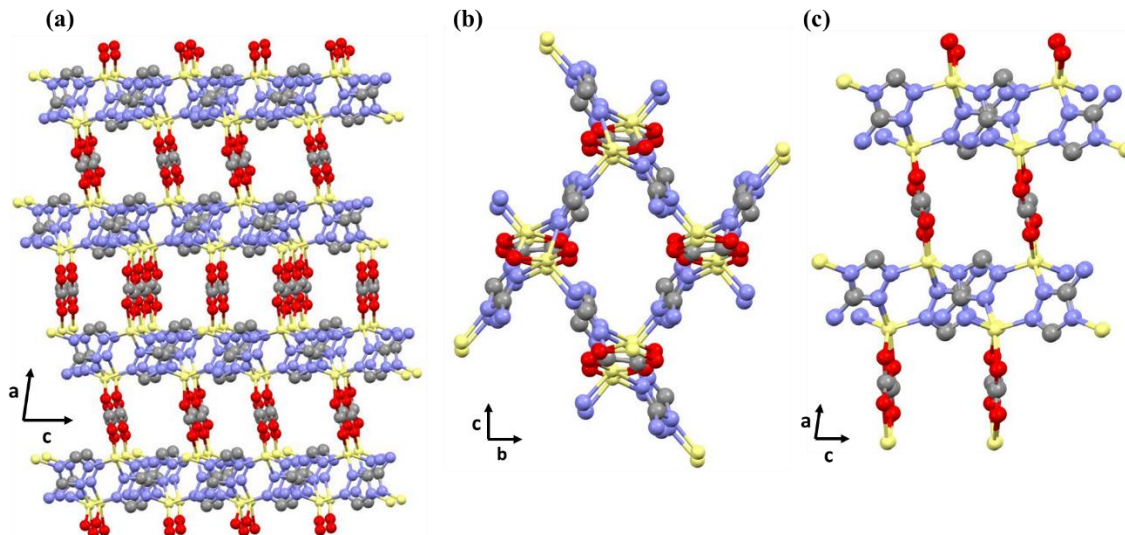
Figure 6.1 Framework topology of ZnAtzOx(H₂O) viewing along b axis (a). Different channels from the perspective that lies along a-axis (b) b-axis (c).[10] In all figures, atoms are colored as: Zn-yellow, C-grey, N-blue, O-red, respectively. Hydrogen atoms are omitted for clarity.

The ZnAtzOx(H₂O) framework was synthesized solvothermally within water, rather than the previous framework synthesized within methanol, causing subtle differences in the buckling and pillaring of the Zn_2Atz_2 layers within the structure, which ultimately leads to the gate opening effect.[3, 6] Besides, such special usage of water as solvent makes ZnAtzOx(H₂O) particularly stable in water vapor or moisture, which is an important trait towards industrial applications. As one of the major applications, MOFs could potentially be used as physical adsorbents for post-combustion capture, in which the gas sources always contain saturated water (5-7% in volume). However, many MOFs that possess excellent CO_2 adsorption properties suffer from their poor structural and chemical stability under humid environments. Thus, with the combination of the amine-functionalized layers and swiveling oxalate pillars for efficient CO_2 adsorption, as well as the remarkable water durability, further research should be put into fully unveil the CO_2 adsorption behavior and the mechanism of the host-guest interactions in ZnAtzOx under moist conditions.

High pressure is well known for its abilities in tuning the structural properties of porous materials, and access to their physical and chemical performances. In spite of the

previously reported intriguing high-pressure phenomena that involve the mechanical and chemical properties of empty MOFs in response to pressure,[11-13] the pressure effects on improving the gas storage in MOFs are thought to be more beneficial to practical applications. In the field of gas adsorption in MOFs, high pressure is found to play an important role in modifying the pore or channel sizes,[14-16] channel shape and opening, surface area and framework geometry.[17-20] As a result, high pressure has great potential in improving the adsorption properties through enhancing the guest-host interactions. For instance, ZIF-8 exhibits a pressure-induced crystalline-to-crystalline phase transition when loaded with pressure-transmitting mediums. This pressure response gives rise to unit cell volume expansion and further guest inclusion with the aids of pressure, such phenomenon is also known as "gate opening effect". Moreover, our previous works on diverse MOFs have demonstrated that the application of high pressure could substantially enhance the CO_2 storage capacity in these MOFs under room temperature, the origins of which are revealed by analyzing the structural evolutions and the guest-host interactions that were probed by vibrational spectroscopies.[21-23] Therefore, it is of great interest to investigate the high-pressure properties of the $ZnAtzOx(H_2O)$ framework itself, as well as its performances for single and multicomponent (i.e. CO_2 and water) adsorption at high pressure. Herein, we performed the *in situ* high pressure examinations on $ZnAtzOx(H_2O)$, CO_2-loaded and water-loaded $ZnAtzOx(H_2O)$ frameworks via Fourier Transformation Inferred spectroscopy. These new findings in our work will enhance the understanding of how the $ZnAtzOx(H_2O)$ framework interacts with CO_2 and water within its channels, as well as the interplay between these two species of guests under high pressure.

6.2 Experimental

$ZnAtzOx(H_2O)$ is synthesized solvothemally according to the previously published method[10] as described: 0.42 grams of 3-amino-1,2,4-triazole (5 mmol Sigma-Aldrich, $\geq$ 95%), 0.09 grams of oxalic acid and 0.12 grams of zinc carbonate basic ($Zn_5(CO_3)_2(OH)_6$) were added to a 3 mL H_2O and 3 mL butanol solvent mixture in a glass vial. The mixture was set to stir for 30 mins using a magnetic stirrer under room temperature. The glass vial was then placed in a 23 mL Teflon-lined autoclave to heat up to 180 °C, colorless crystals were yielded after 2 days. The crystals were washed with distilled water, collected using

vacuum filtration, and dried at 90 °C for 3 hours, after which the identity and purity of the crystals were confirmed by PXRD with Co Kα radiation.

A Schlenk line was used for sample activation, CO_2 loading, D_2O loading, as well as CO_2 and D_2O co-loading. A typical CO_2 and D_2O co-loading is as follows: the sample was firstly activated under a dynamic vacuum line at 150 °C for 12 hours, followed by introducing a calculated amount of CO_2 onto the vacuum line. After CO_2 was loaded, a known amount of D_2O was injected to the bottom of the L-shape tube. The bottom part of the tube was then flame sealed off from the vacuum line. Prior to sample loading, the sealed tube was heated at 90 °C for 2 hours to distribute D_2O evenly through the sample. The sample tube was immersed in liquid N_2 before the sample was transferred to the DAC, ensuring both guests adsorbed in the pore during sample loading.

To create in-situ high pressure, a diamond anvil cell constructed by a pair of opposing type II diamonds with a culet size of 600 µm were used for FTIR experiments. A highly customized IR micro-spectroscopy system designed for in-situ high pressure measurements was used in this study, with the details stated in *Chapter 2*. The sample chambers were prepared on pre-intended stainless-steel gaskets with an approximate thickness of 60-70 µm. The typical diameter of these sample chambers was about one third to a half of the diamond culet size. To rule out any interference from the air, the glass tubes that contain activated or pre-loaded samples (i.e. with CO_2, D_2O, and both CO_2 and D_2O) were opened in a Nitrogen-filled MBraun LAB Master 130 glovebox with O_2 content below 10 ppm and H_2O content below 0.3 ppm. All batches of samples were packed in the DAC along with KBr to keep the IR signals in the dynamic range of the detector, and to ensure that all the results from different high-pressure cycles are comparable. A few ruby chips were loaded to the sample chambers for pressure calibrations.[24]

6.3 Results and discussion

6.3.1 IR spectra of activated and guest-loaded ZnAtzOx(H$_2$O) frameworks

The IR spectra of activated, CO_2 loaded, D_2O loaded, and CO_2 and D_2O co-loaded ZnAtzOx(H_2O), as depicted in Figure 6.2. In the mid-IR region, all the absorption bands

are attributed to the internal vibrations of the organic ligands on the framework, as the vibrations of the metal-ligand bonding (i.e. Zn-N and Zn-O) are expected in the far-IR region. By comparing the framework structure with the corresponding spectra, we are able to assign all the major bands on the spectra, with the assigned modes labeled on the graph and listed in Table 6.1. On the spectrum of the empty ZnAtzOx framework, the bands at 3476 and 3347 cm^{-1} are attributed to N-H asymmetric stretch of the amino group on the 1-2-4-amino-triazole ligand, whereas the N-H bending modes are local at 1663 and l626 cm^{-1}.[25] The triplet at 1107, 1060 and 1017 cm^{-1} are associated with the triazole ring vibration.[25] In terms of oxalate units, the O=C-O asymmetric and symmetric stretching modes are observed as doublets at 1549 and 1517 cm^{-1}, 1294 and 1319 cm^{-1}, respectively.[26] This could be due to the local coordination environment, where the 4 oxygen atoms on the oxalate are not completely structurally equivalent although they are all bonded to the metal center Zn. Base on the measured bond length,[6, 10] it is believed that the peaks at 1549 cm^{-1} and 1319 cm^{-1} are associated with the stretch of the short C-O(-Zn) bond, while the peaks at 1517 cm^{-1} and 1292 cm^{-1} corresponds to the longer C-O(-Zn) bond. The intense single band at 1226 cm^{-1} is believed to be originated from C-O(-Zn) stretching.

D_2O is used to replace H_2O in the *in situ* high pressure experiments on water loaded ZnAtzOx(H_2O), as well as CO_2 and water co-loaded ZnAtzOx(H_2O), to avoid overlapping with the NH_2 asymmetric stretching modes within the similar spectral region. After gas loadings, as shown in Figure 6.2, the peak found at 2336 cm^{-1} is attributed to the asymmetric stretching mode of CO_2, whereas the broad bands observed in the spectral region from 2360 to 2620 cm^{-1} are attributed to D-O-D asymmetric stretch. In addition, it is apparent that after D_2O was introduced to the framework, the N-H asymmetric stretching mode that was initially located at 3476 and 3347 cm^{-1} became much weaker and shifted to a lower frequency, resulted in a weak peak at 3128 cm^{-1} and a broad band from 3200 to 3470 cm^{-1}. Meanwhile, the N-H bending mode exhibits only one band at 1660 cm^{-1} instead of a set of doublets. All these observations are the characteristics of the N-D vibrations.[27] Indeed, it has been previously observed and proven by solid-state NMR experiments that the -NH_2 group on the ZnAtzOx framework undergoes an instant deuterium exchange with the guest D_2O molecules.
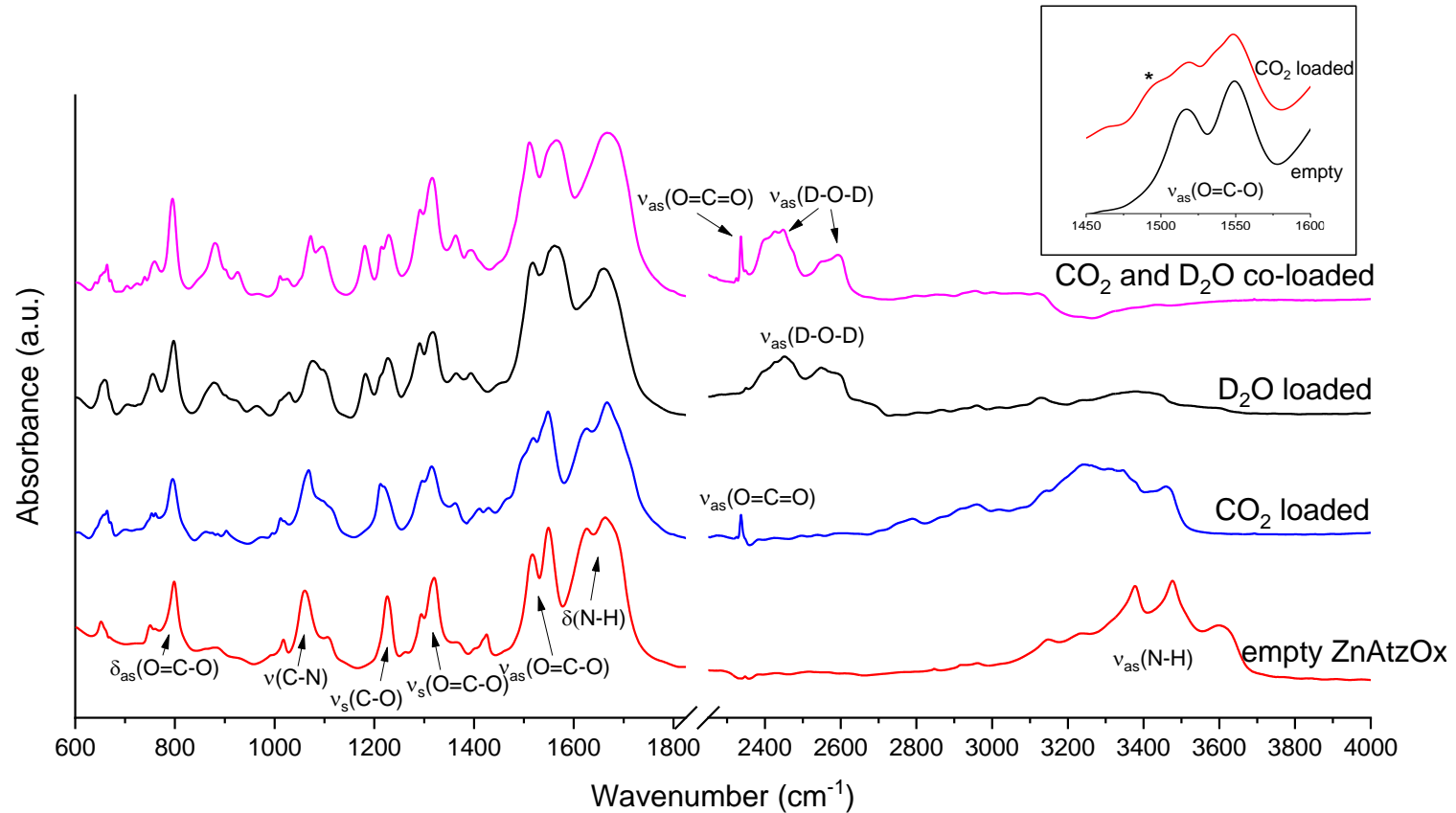
Figure 6.2 FTIR spectra of activated ZnAtzOx (H₂O) at initial pressures (red) CO₂ loaded ZnAtzOx(H₂O) (blue), D₂O loaded ZnAtzOx(H₂O) (black), as well as CO₂ and D₂O co-loaded ZnAtzOx(H₂O) (purple). The inset shows the comparison between the activated (bottom) and CO₂ loaded framework (top) in the spectral region of the ν_{as}(O=C-O) mode. The new peak observed upon CO₂ loading is highlighted by the asterisk.

Table 6.1 IR mode assignments of ZnAtzOx(H₂O) framework vibrations in all four loading conditions.

Peak Assignment	Frequency (cm^{-1})			
	Empty ZnAtzOx[a]	CO₂ Loaded ZnAtzOx[b]	D₂O Loaded ZnAtzOx[c]	CO₂ and D₂O Co-loaded ZnAtzOx[d]
O=C-O bending	750, 798	753, 761, 795	755, 797	759, 795
C-N stretch	1017, 1060, 1107	1011, 1068, 1105	1023, 1077, 1098	1011, 1072, 1096
C-O sym stretch	1226	1212, 1219	1227	1214, 1228
O=C-O sym stretch	1294, 1319	1296, 1314	1290, 1317	1291, 1315
O=C-O asym stretch	1517, 1549	1498, 1518, 1548	1517, 1561	1511, 1564
N-H bending	1626, 1665	1626, 1666	-	-
N-D bending	-	-	1660	1668
N-H stretch	3378, 3476, 3610	3245, 3345, 3458	-	-
N-D stretch	-	-	3129, 3380	-

a. Observed at the lowest possible loading pressure (i.e. 0.27 GPa) and room temperature.

b. Observed and measured at 0.63 GPa and room temperature.

c. Observed and measured at 0.38 GPa and room temperature.

d. Observed and measured in the 1:1 CO₂ to D₂O ratio loading at 0.47 GPa and room temperature.

6.3.2 Structural responses of activated ZnAtzOx(H_2O) at high pressures

In-situ high-pressure IR spectra of activated ZnAtzOx(H_2O) were collected under high pressure up to 3 GPa to examine the pressure responses of the framework, as shown in Figure 6.3. During compression, all IR modes exhibit different degrees of band-merging and broadening, which are typical signs for structural disordering at elevated pressures. The most striking changes are found at the N-H stretch modes (3350-3500 cm^{-1}), where a significant band broadening and enhancing is observed, likely due to a hydrogen bond formation related to the NH$_2$ group. At the highest pressure of 3.13 GPa, the spectrum shows a much flattened and broadened profile, indicating a decrease in crystallinity at high pressure. Upon decompression, all the frequency shifts and peak broadening of the IR modes disappear, suggesting that pressure-induced modifications on the ZnAtzOx(H_2O) framework structure, as well as the formation of the hydrogen bonds, are completely reversible.
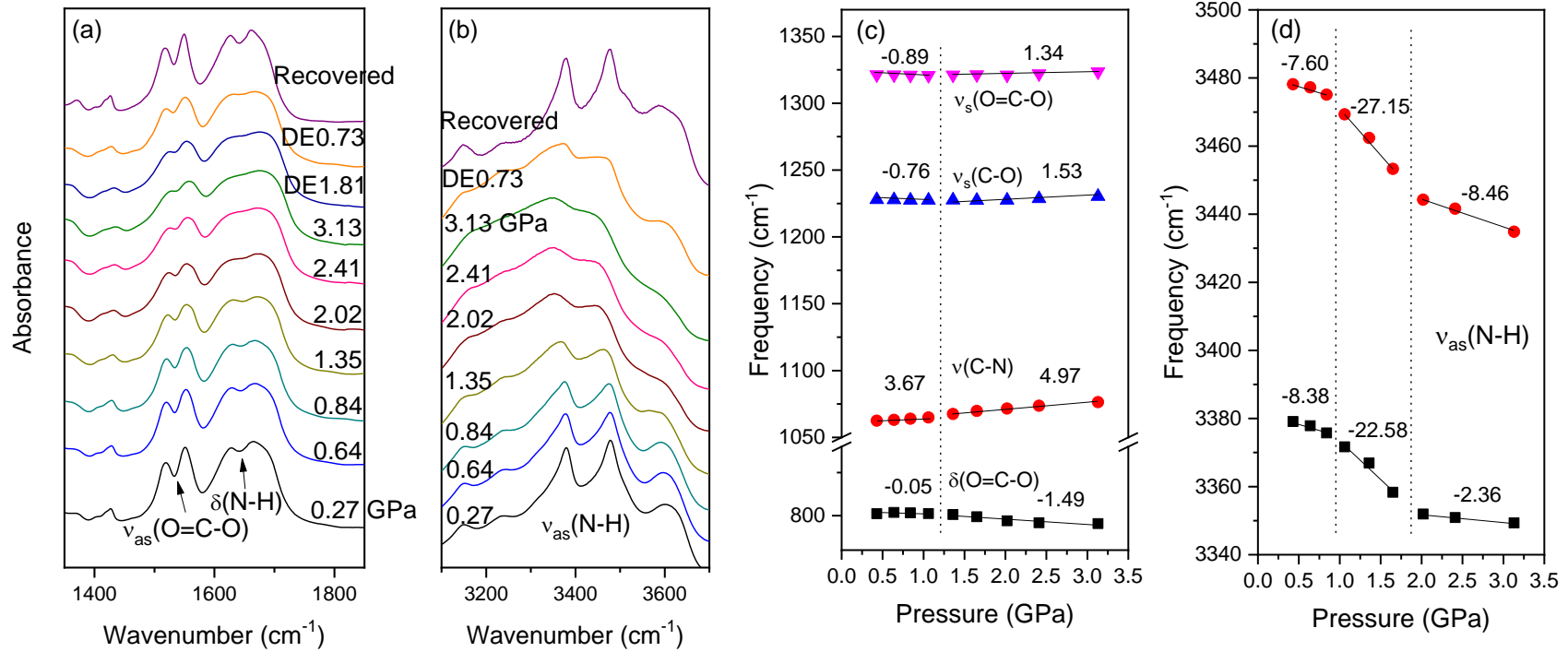
Figure 6.3 FTIR spectra of activated ZnAtzOx(H₂O) at high pressures (a)(b), and pressure dependence (dv/dP, cm⁻¹/GPa) of selected IR modes (c)(d). Dash lines in (c) and (d) represent the pressure points where possible isostructural changes take place upon compression, although lack of phase changes.

Table 6.2 Pressure dependence (dv/dP, cm-1/GPa) of IR modes of activated ZnAtzOx(H₂O) framework on compression.

Modes	Frequency (cm⁻¹)	Pressure region		
		0-1.35 GPa	**1.35-3.13 GPa**	
O=C-O bending	798	-0.05	-1.49	
C-N stretch	1060	3.67	4.97	
C-O sym stretch	1226	-0.76	1.53	
O=C-O sym stretch	1319	-0.89	1.34	
O=C-O asym stretch	1517	3.58		
	1549	3.23	2.10	
N-H bending	1626	2.80	3.59	
	1665	8.78	1.54	
N-H stretch		**0.27-0.84 GPa**	**0.84-1.65 GPa**	**1.65-3.13 GPa**
	3378	-8.23	-22.58	-2.36
	3476	-7.60	-27.15	-8.46

The pressure dependence of selected IR modes of ZnAtzOx is depicted in Figure 6.3, with the pressure coefficients listed in Table 6.2. The pressure dependences of most IR modes of the framework exhibit a blueshift upon compression, which is typically associated with a pressure-induced bond stiffening. The most intriguing observation is the pressure dependences of the N-H stretching mode, where a substantial red-shift is observed upon initial compression to 0.84 GPa. This is due to the N-H bond softening induced by a stronger inter-molecular interaction. In the local structure of ZnAtzOx(H_2O) reported by literature,[10] the amino groups (-NH_2) on each Zn-amino-triazole layer are orientated toward the channel along a-axis (Figure 6.4). This unique orientation brings the -NH_2 groups very close to the oxalate units, and thus creates possibilities for forming hydrogen bonds. The atomic distance between H1 from the amino group and O1 from the adjacent oxalic ligand within the same pore is measured to be 2.965 Å (Figure 6.4), the corresponding N-H$\cdots$O bond angle is 130.25° (labeled as site 1). Another possible site is the interaction between the second H from the same amino group (labeled on the graph as H2), and O2 from the adjacent oxalic ligand located on the opposite side of the pore (labeled as site 2). At this site, the atomic distance and bond angle are measured to be 2.561 Å and 122.60°, respectively. Both site 1 and 2 meet the criteria for hydrogen bond forming,[28] site 1 features a longer distance but a small bonding angle (i.e. closer to 180), whereas site 2 obsesses a shorter distance while a wider bonding angle. Apparently, the formation and enhancement of the hydrogen bond are greatly facilitated upon increasing the external pressure and thus shortening the distance between the O donor and H acceptor. In particular, the pressure coefficients of the N-H stretching modes increase rapidly from 8.23 to 22.58 $cm^{-1} \cdot GPa^{-1}$ in the pressure range of 1-2 GPa, suggesting that the formation of hydrogen bond takes place in this pressure region. Beyond 2 GPa, pressure coefficients drop dramatically yet exhibit redshift, indicating that high pressure continually enhances the N-H$\cdots$C-O hydrogen bonding in higher pressure region up to 3.13 GPa. Consequently, the pressure dependences of O=C-O asymmetric bending and symmetric stretching modes, as well as the C-O symmetric stretching mode also experienced moderate red-shifts in the lower pressure region (i.e. below 1.35 GPa), as this intense van der Waals N-H$\cdots$O-C interactions would weaken the C-O bonding.
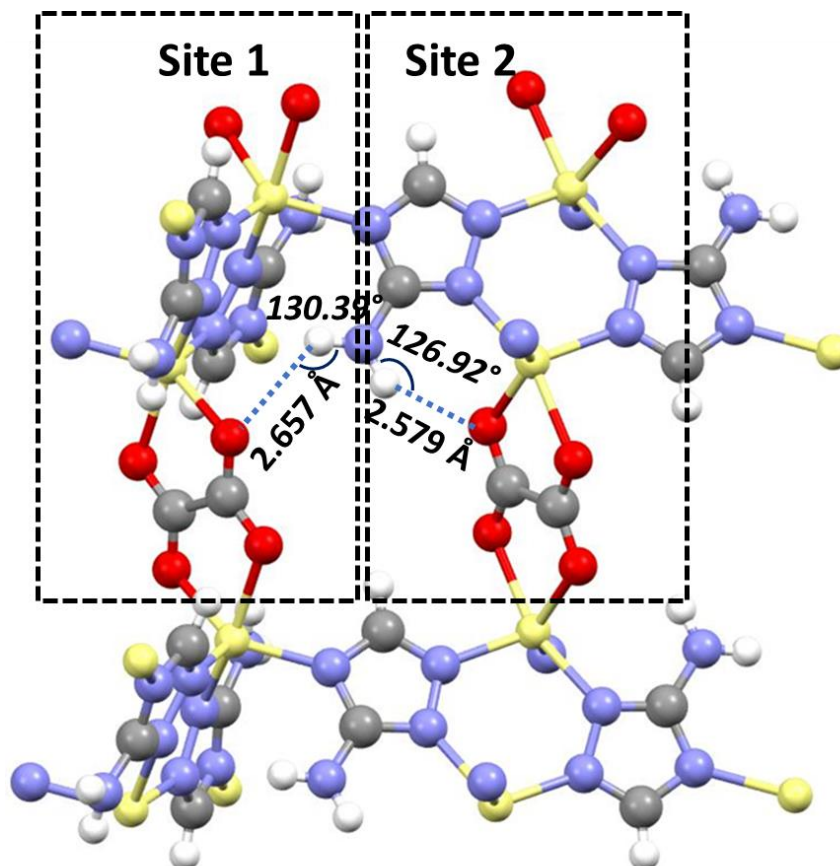
Figure 6.4 Two possible sites for hydrogen bond formation at high pressures within the pore of ZnAtzOx(H$_2$O).[10]

Furthermore, the IR results also demonstrated that the activated ZnAtzOx(H$_2$O) framework exhibits high structural stability up to 3.13 GPa, which is comparable to α-Mg$_3$(HCOO)$_6$ and significantly better than other previously reposted MOFs under high pressure such as ZIF-4, ZIF-8 and UiO-66. Mao *et al* have illustrated that the activated α-Mg$_3$(HCOO)$_6$ framework remains crystalline up to 4 GPa. In contrast, compressing the activated ZIF-8 framework resulted in an irreversible crystalline-to-amorphous phase transition upon initial compression to 0.34 GPa. Similarly, UiO-66 exhibits a permanent bond breakage between the Zr metal center and the oxygen from the bridging carboxylate group at 0.8 GPa.[29] These observations suggest that the structural stability of a MOF framework may closely correlate to its porosity and the connectivity between the metal center and organic ligands. The BET surface area of ZnAtzOx(H$_2$O) is 308 m$^2\cdot$g^{-1},[10] which is slightly higher than 297 m$^2\cdot$g^{-1} of

α-Mg$_3$(HCOO)$_6$,[30] yet much smaller than that of ZIF-8 and UiO-66 (i.e. 1851 m$^2\cdot$g^{-1} and 1580 m$^2\cdot$g^{-1}, respectively). Therefore, it could be understood that the structural stability of ZnAtzOx is slightly lower than that of α-Mg$_3$(HCOO)$_6$, and much higher than that of ZIF-8 and UiO-66. Moreover, the high compressibility of ZnAtzOx(H$_2$O) can be attributed to its special mix-ligand geometry. This high structural stability induced by connecting metal centers to multicomponent from the ligands is also previously found in SDB series MOF, where the metal center Pb, Ca and Cd in their respective frameworks are bonded to both carboxylic oxygens and sulfonyl oxygens on the SDB (1,4-benzenedicarboxylate) ligands. These SDB MOFs are found to be structurally stable up to 10 GPa.[31-33] These unique geometries of metal centers coordinating to bi-functional groups or multiple types of ligands further help stabilize the crystallinity of the framework.

6.3.3 Guest-host interactions in CO_2 loaded ZnAtzOx(H_2O) framework at high pressures
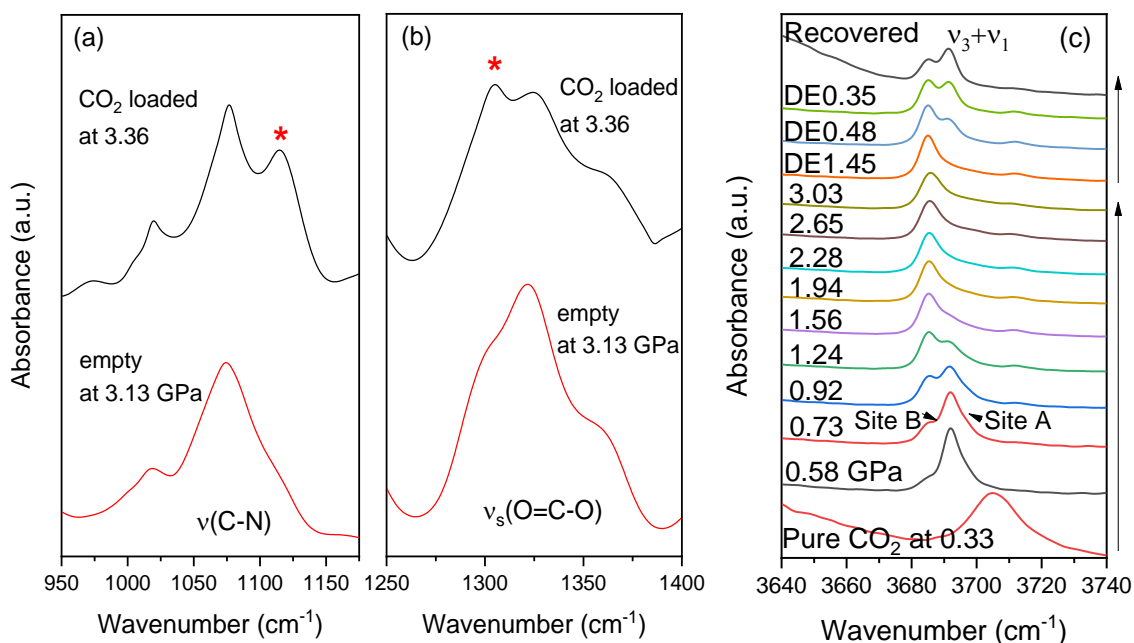
Figure 6.5 Zoomed IR spectral region for the C-N stretching (a) and C-O stretching (b) modes of CO_2 loaded ZnAtzOx(H_2O) (top) and activated ZnAtzOx(H_2O) (bottom). (c) IR spectra of $\nu_3+\nu_1$ combination mode of adsorbed CO_2 in ZnAtzOx(H_2O) upon compression and decompression in the spectral region of 3600-3800 cm^{-1}, two symmetry independent CO_2 sites are labeled on the spectra as site A and B, the spectrum of pure CO_2 at 0.33 GPa is depicted as a comparison.

IR spectra of CO_2 loaded ZnAtzOx(H_2O) were collected as a function of pressure from near ambient pressure to 3.13 GPa (Appendix Figure B1). On the spectral region of the CO_2 combination mode (Figure 6.5c), the CO_2 $\nu_3+\nu_1$ combination mode exhibits a sharp and intense peak at 3692 cm^{-1} with a shoulder-like peak at 3685 cm^{-1}, whereas the free CO_2 only features a signal peak at this mode, which is expected at 3702 cm^{-1} under the similar pressure (i.e. 0.58 GPa)[23] Therefore, it is clear that there are two CO_2 binding sites in the framework, where most CO_2 molecules reside in the major site (label as site A) while only a minor amount of CO_2 sits in the other site (labeled as site B). At the initial pressure of 0.58 GPa, site B is observed at a lower frequency, corresponding to weaker O=C=O bond strength compared to that of site A. Such bond weakening is induced by strong

intermolecularCO$_2$-framework interaction. Therefore, CO$_2$ molecules at site B are believed to interact with the ZnAtzOx(H$_2$O) framework more closely.

Moreover, the O=C-O asymmetric stretch is observed to be a set of triplets instead of the doublet for the empty framework (Figure 6.2 inset). A similar change is found in the O=C-O symmetric stretching as well, where an enhancement of the shoulder-liked peak at 1296 cm^{-1} is observed (Appendix Figure A1). These modifications on carboxylate group related vibrations suggest a CO$_2$-induced structural disorder of the oxalate units, which further establishes a third non-equivalent C-O bond with a unique bond length. Indeed, a striking gate opening effect in ZnAtzOx(H$_2$O) regulated by CO$_2$ loading pressure was reported previously, where the oxalate groups swivel when the external CO$_2$ pressure goes higher than 200 mbar under 273K.[10] Their study showed that without the gate-opening effect, the adsorption isotherm at 303 K only represents the capacity at one CO$_2$ binding site.[10] By lowing the temperature, the gate opening effect could be achieved, which not only drastically increases the accessible pore volume, but also opens up a secondary CO$_2$ binding site. The requirement for this gating effect to occur is the special symmetrical structure of the oxalate groups in ZnAtzOx(H$_2$O) (Figure 6.6), which allows the oxalate units to rotate. Consistently, our IR results suggest that the rotation of the oxalate groups started at the initial pressure of 0.58 GPa, evidenced by the formation of the third symmetry independent C-O bond.
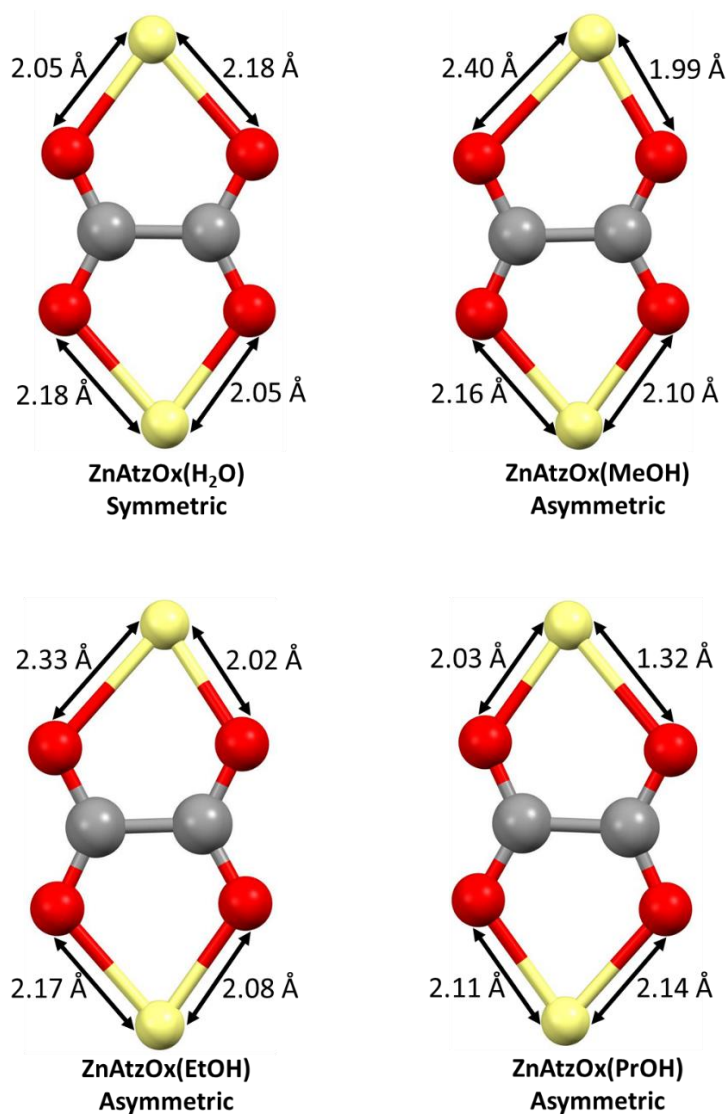
Figure 6.6 Local geometry of zinc-oxalate unit in ZnAtzOx(H_2O), in comparison to other MOFs in the same series (i.e. ZnAtzOx(MeOH), ZnAtzOx(EtOH), ZnAtzOx(PrOH)). It is believed that the symmetrical Zn-O bonds within ZnAtzOx(H_2O) are related to the gating effect with the presence of CO_2, as the oxalate units are easier to rotate.[10]
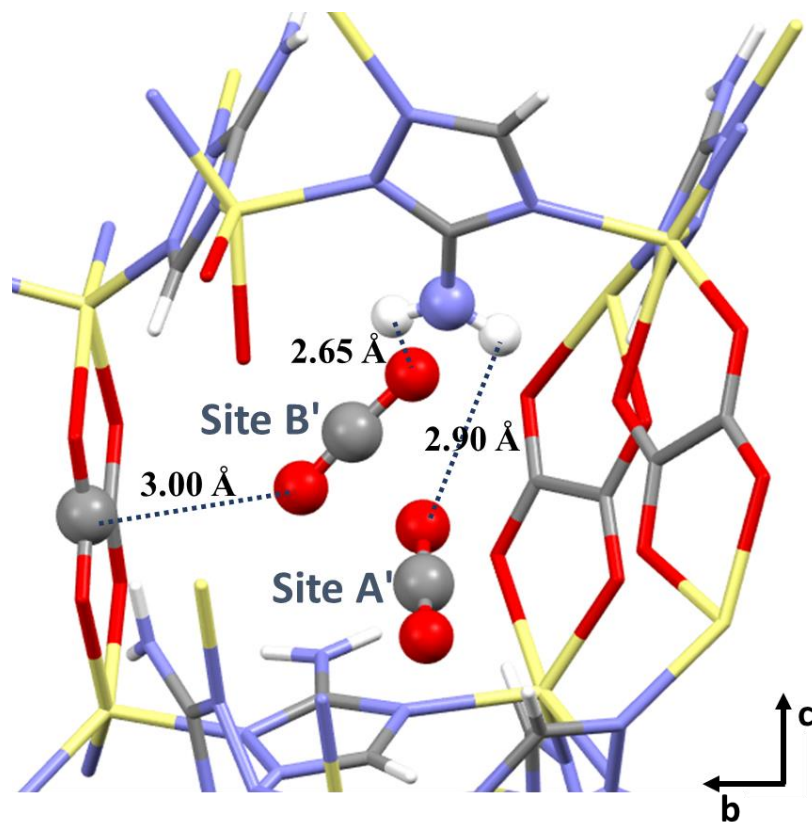
Figure 6.7 The locations of CO_2 binding sites A' and B' in ZnAtzOx(MeOH), the distance between CO_2 and the functional groups are as labeled. The atoms that are not involved in the CO_2-framework interactions in this pore are simplified as sticks for clarity.[3]

It has been reported that the ZnAtzOx(MeOH) framework features two independent CO_2 sites in its channels, herein labeled as site A' and site B' (Figure 6.7). Site A' sits between oxalate units along *b* axis and only interacts with the closest amine through H-bond. Whereas site B' is adjacent to the free amino group and is thought to interact with NH_2 either through N-H···O hydrogen bond or via an interaction between the N lone pair and the C atom of CO_2, which make site B' interaction generally stronger than site A'.[3] Although ZnAtzOx(H_2O) exhibits slightly different crystal structure from ZnAtzOx(MeOH), the nature behind the guest-host interactions between CO_2 and framework are believed to resemble. On the framework vibration region of the spectra, a significant red-shift is observed at the -NH_2 asymmetric stretching region upon introducing CO_2 to the framework (Figure 6.2), which is attributed to an interaction-induced N-H bond weakening. Moreover,

the interaction between CO_2 and oxalate units has also been observed and discussed. Therefore, we suggest that the CO_2 binding sites in $ZnAtzOx(H_2O)$ at 0.58 GPa are located in similar positions as those in ZnAtzOH(MeOH), although the exact distance between CO_2 and the functional groups may slightly differ. Base on the strength of interactions at each site, we could relate site A and B in $ZnAtzOx(H_2O)$ to site A' and B' respectively in $ZnAtzOx(MeOH)$.

Upon elevating the pressure, the most intriguing observation is the change in the intensity ratio of the CO_2 v_3+v_1 doublet, indicating that most CO_2 molecules that were originally adsorbed at site A at lower pressures gradually show similar profile as site B CO_2 molecules until the pressure reached 1.56 GPa. At this pressure, all adsorbed CO_2 molecules exhibit the same types of interactions with the $ZnAtzOx(H_2O)$ framework, as the doublet merged to a single peak. At above 1.56 GPa, these interactions resemble that of site B at ambient condition. In addition, on the pressure dependence curves (Figure 6.8a), the lower frequency component (site A) redshifts until it completely vanishes at 1.56 GPa, suggesting a stronger interaction between site A CO_2 and the framework upon compression.

On the framework, the N-H stretching mode at 3458 cm^{-1} has shown a substantial red-shift with a coefficient of 8.39 cm^{-1}·GPa^{-1} in the entire compression range (Figure 6.8a), suggesting enhanced CO_2-amino interaction through hydrogen bonding. Meanwhile, the O=C-O asymmetric modes exhibit minor degrees of blue shift, the middle triplet at 1518 cm^{-1} features the highest dependence to pressure, implying that this new C-O(-Zn) bonds are more sensitive to pressure, which is consistent with the swiveling of the oxalate units in the gating effect. In addition, the C-N stretch mode observed an intense shoulder at 1100 cm^{-1}, with the intensity of which gradually increasing throughout the entire compression process. This observation suggests a possible pressure-induced interaction between N lone pair electrons with the electrophilic carbon atom of CO_2.[3] A similar enhanced shoulder peak is also seen in the C-O stretching region, indicating a stronger interaction between CO_2 and the oxalate unit at high pressure. The comparison between CO_2 loaded and empty $ZnAtzOx(H_2O)$ under similar pressures in the spectral region of C-N stretching and C-O stretching is depicted in Figure 6.5a and 6.5b.

Upon decompression, as can be seen at CO_2 combination mode $\nu_3+\nu_1$, site A starts to appear at 0.69 GPa and gradually grows stronger with decreasing pressure. Nonetheless, there are still more CO_2 molecules residing at site B upon releasing the pressure, compared to that of the initial pressure. For framework (Appendix Figure A1), the major changes observed under high pressure are not completely recovered. All these observations suggest that the high pressure-induced structural modifications on the CO_2 loaded $ZnAtzOx(H_2O)$ are permanent. Such pressure-modified structure is believed to have a stronger affinity with CO_2 and is likely capable of storing additional CO_2 molecules.
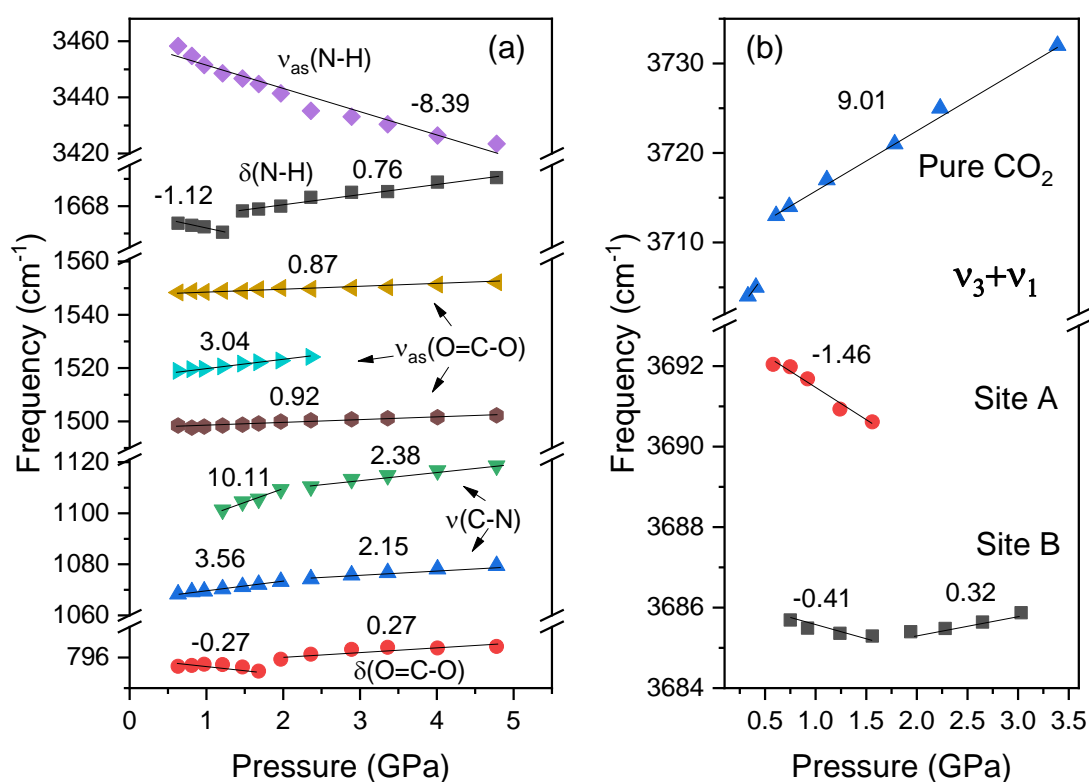

Figure 6.8 Pressure dependences ($d\nu/dP$, cm^{-1}/GPa) of IR modes of CO_2 loaded ZnAtzOx(H$_2$O) in the pressure range from 0.63 GPa to 4.78 GPa. (a) Framework vibrations. (b) Pressure dependence of CO_2 combination mode $\nu_3+\nu_1$. Pure CO_2 from previous work is depicted as comparisons.

6.3.4 Guest-host interactions in D_2O-loaded ZnAtzOx(H_2O) framework at high pressures

At the initial pressure of 0.38 GPa, two broad bands are observed at around 2450 cm^{-1} and 2565 cm^{-1} in the spectral region of v_{as}(D-O), whereas the IR spectrum of pure D_2O exhibits a single band at 2480 cm^{-1}.[34] The splitting of this band upon D_2O loading suggests that there are 2 independent types of D_2O molecules adsorbed in the framework. These 2 types of D_2O correspond 2 non-equivalent D_2O sites in the channel, which is consistent with previously reported Single Crystal XRD data on as-made ZnAtzOx(H_2O) framework. Base on the resolved oxygen positions (Figure 6.9), the distance between H_2O oxygen atom and amine hydrogen is 2.28 Å and the oxygen is 3.25 Å away from the C-H carbon at site I (2.65 Å from C-H hydrogen). At site II, H_2O hydrogen is located 3.13 Å away from the amine hydrogen and is 3.51 Å from C-H carbon (2.58 Å from C-H hydrogen). While the structural environments at both sites are similar, site I shows slightly higher proximity to the groups of interest on the ZnAtzOx(H_2O) framework and therefore more likely to correspond to the band observed at a lower frequency in the D-O asymmetric stretching region.

IR spectra of CO_2 loaded ZnAtzOx(H_2O) were collected as a function of pressure from near ambient pressure to 6.05 GPa. Upon compression, the intensity of the band corresponds to site I gradually enhanced, while the band assigned to site II becomes much weaker. With the total amount of adsorbed D_2O remain constant, it is apparent that more D_2O molecules are migrating to site I upon elevating pressure, as site I features closer affinity to the framework than site II. Moreover, both these bands show a substantial red-shift during compression up to 3.29 GPa, after which these bands only exhibit blue-shifting all the way to the highest pressure of 6.05 GPa (Figure 6.10d and Table 6.3). These above observations implicate that the interaction between adsorbed D_2O achieved the maximum at 3.29 GPa. Additionally, the enhanced broad band observed in the N-D stretching region (3100-3500 cm^{-1}) implies a stronger hydrogen bonding through D-O$\cdots$H-D upon compression. In contrast, there are no major modifications on either O=C-O asymmetric stretching or C-O stretching modes (Figure 6.10a and Table 6.3), meaning that the gating effect has not occurred throughout the entire high-pressure cycle. Therefore, it is apparent

that this effect is not only driven by external conditions (i.e. CO_2 loading pressure, temperature, external high pressure, etc.), but also guest molecule specific.

During decompression, the population of D_2O at site 1 starts to reduce (Figure 6.10b), as more D_2O molecules migrate back to site B with decreasing pressure. Upon recovery, the spectrum of the recovered sample shows identical profile as that of the initial spectrum, suggesting that the compression on both the framework structure and the adsorbed D_2O molecules are completely reversible up to 6 GPa. Overall, D_2O loaded $ZnAtzOx(H_2O)$ framework has shown remarkable structural stability under high pressure, whereas many MOFs could not survive from being exposed to water vapor, let alone if being compressed with loaded water to the gigapascal level. For instance, MOFs that are built up from carboxylate containing ligands such as MOF-5, MOF-74 and HKUST-1 exhibit different degrees of water sensitivities.[35] In these cases, water molecules would essentially displace the ligands and further lead to framework structure failure. The fact that the D_2O loaded $ZnAtzOx(H_2O)$ could remain its crystallinity, chemical connectivity, and most importantly, the porosity for adsorption and storage, provides the foundation for us to carry out further investigations on how CO_2 molecules interact with the framework under high pressure with the presence of water.
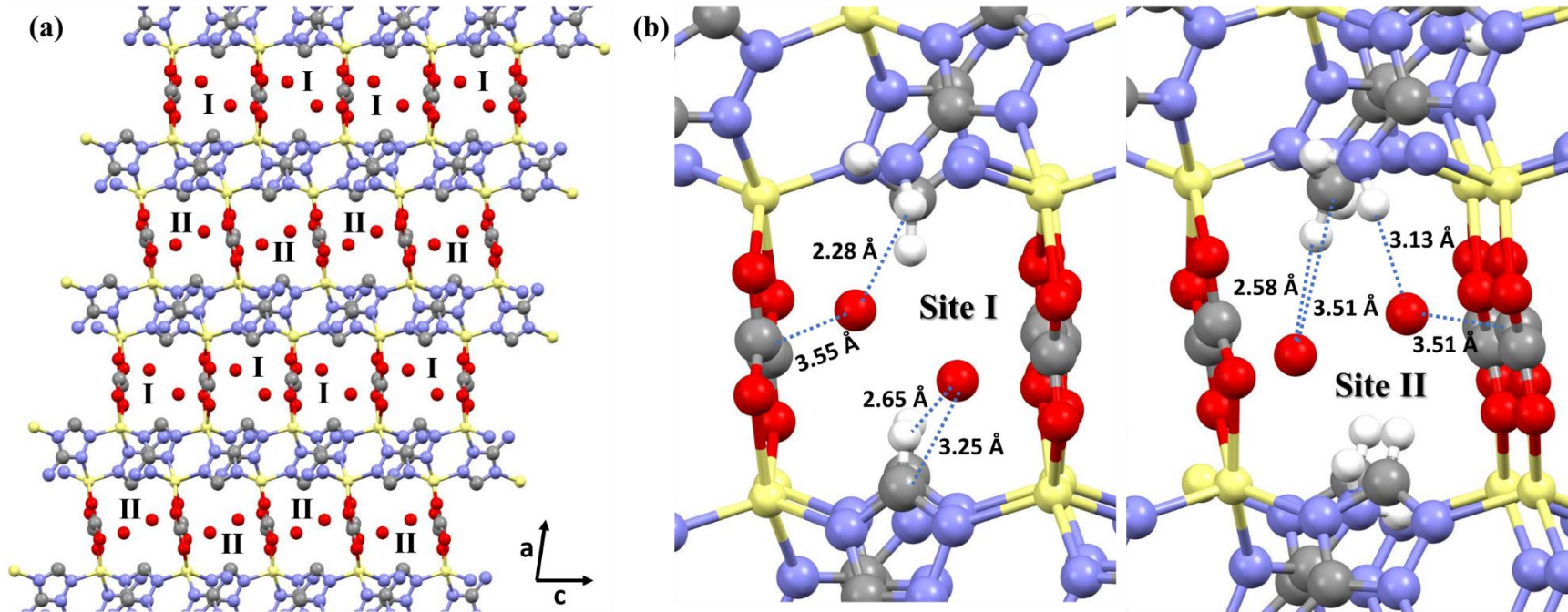
Figure 6.9 (a) The locations of oxygen atoms from water molecules in as-made ZnAtzOx(H_2O) viewing along b-axis. A and B are two non-equivalent H_2O sites reported by literature, the two possible oxygen locations in each pore are symmetry equivalent. (b) The distances between the oxygen atoms and the groups of interest (i.e. NH_2 and oxalate) at each site.[10]
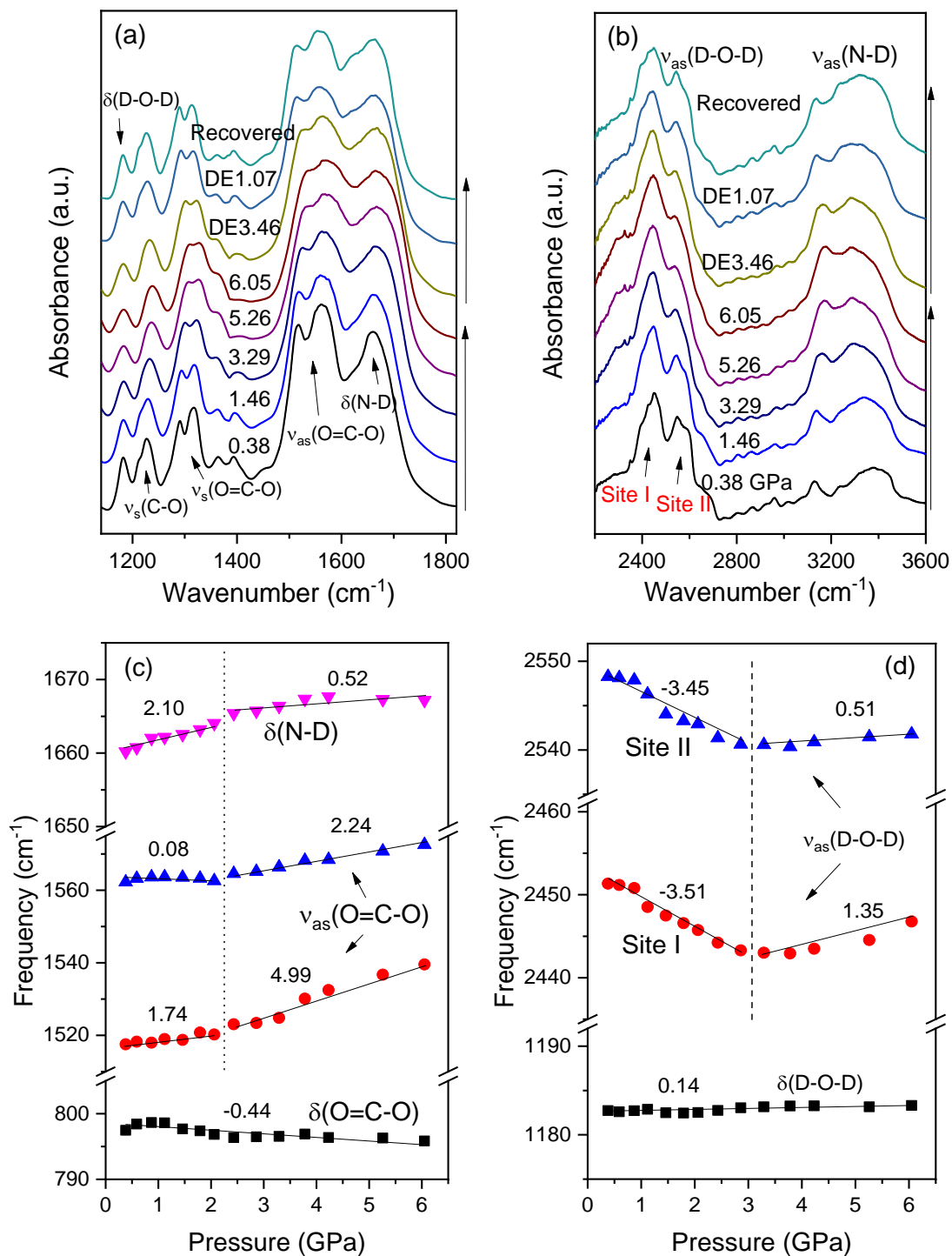
Figure 6.10 FTIR spectra of D₂O loaded ZnAtzOx(H₂O) collected at room temperature and high pressure in the region from 1100-1800 cm⁻¹ (a) and 3000-3600 cm⁻¹ (b). Pressure dependence (dv/dP, cm⁻¹/GPa) of selected framework vibrations (c) and D₂O vibrations (d).

Table 6.3 Pressure dependence (dv/dP, cm^{-1}/GPa) of IR modes of D$_2$O loaded ZnAtzOx(H$_2$O) from 0.38 GPa to 6.05 GPa.

Modes	Frequency (cm^{-1})	Pressure region	
		0.38-2.06 GPa	**2.06-6.05 GPa**
O=C-O bending	797	-0.44	
O=C-O asym stretch	1517	1.74	4.99
	1561	0.08	2.24
N-D bending	1660	2.10	0.52
		0.38-3.29 GPa	**3.29-6.05 GPa**
D-O-D stretch	2451	-3.51	1.35
	2548	-3.45	0.51
D-O-D bending	1183	0.14	

6.3.5 Properties of CO_2 and D_2O co-adsorption in ZnAtzOx(H_2O) at high pressures

The *in situ* IR experiments were performed on CO_2 and D_2O loaded ZnAtzOx(H_2O) with two different CO_2 to D_2O molar ratios to investigate how the loading level affects their adsorption behaviors in the framework under high pressure. IR spectra of CO_2 and D_2O co-loaded ZnAtzOx(H_2O) (1:9 molar ratio) were collected as a function of pressure from near ambient pressure to 8.20 GPa (Appendix Figure A2). After initial sample loading, the appearance of CO_2 v_3 mode at 2337 and 2350 cm^{-1} (labeled as CO_2 site C1 and C2) and D_2O asymmetric stretching mode at 2450 cm^{-1}, 2542 cm^{-1} and 2590 cm^{-1} (labeled as D_2O site D1, D2 and D3) confirm a successful guest loading (Figure 6.11). Upon slight compressions to 0.83 GPa and 1.36 GPa, the relative intensity between two CO_2 bands is switching, meaning that the occupancy of each site is being regulated by the external pressure. Furthermore, it is intriguing to see the third peak at a lower frequency of 2325 cm^{-1} in the same region (Figure 6.11), which indicates the formation of a new non-equivalent CO_2 site (marked as site C3). Indeed, this additional CO_2 site was also detected by SSNMR, when CO_2 was co-loaded to the ZnAtzOx(H_2O) framework along with D_2O under low temperature. Upon further compression, the amount of CO_2 adsorbed at site C1 gets further reduced, whereas site C2 and site C3 peaks become more intense. At a higher pressure of 2.41 GPa, site C1 is no longer observable. In terms of the adsorbed D_2O, it is worth noting that with the presence of CO_2 molecules, D_2O also displays an additional binding site at 2590 cm^{-1} upon initial loading (labeled as D3), compared to the D_2O loaded framework. The formation of the additional adsorption site for both CO_2 and D_2O is likely due to the guest-guest interaction through C=O···D-O hydrogen bonding. Upon compression, the pressure-regulated occupancy changes among three sites are also observed for D_2O, with a larger amount of D_2O adsorbed at site D1 while less at site D2 and D3 accordingly.

The reversibility of the system is examined during decompression (Figure 6.11b), the weakening of CO_2 site C3 is initially observed at 3.84 GPa, it further disappears from the spectrum at 1.11 GPa, indicates that this third CO_2 site only exists under pressure that is higher than 1 GPa under this loading conditions. This is usually associated with the nature

of these frameworks being highly reversible upon increasing and releasing the pressure.[23] At 0.51 GPa, the peak for site 1 starts to appear on the spectrum. Under the same pressure, the intensity of D_2O site D2 and site D3 begin increasing and resolve a clear profile, meaning that the D_2O populations at these two sites start to rise.
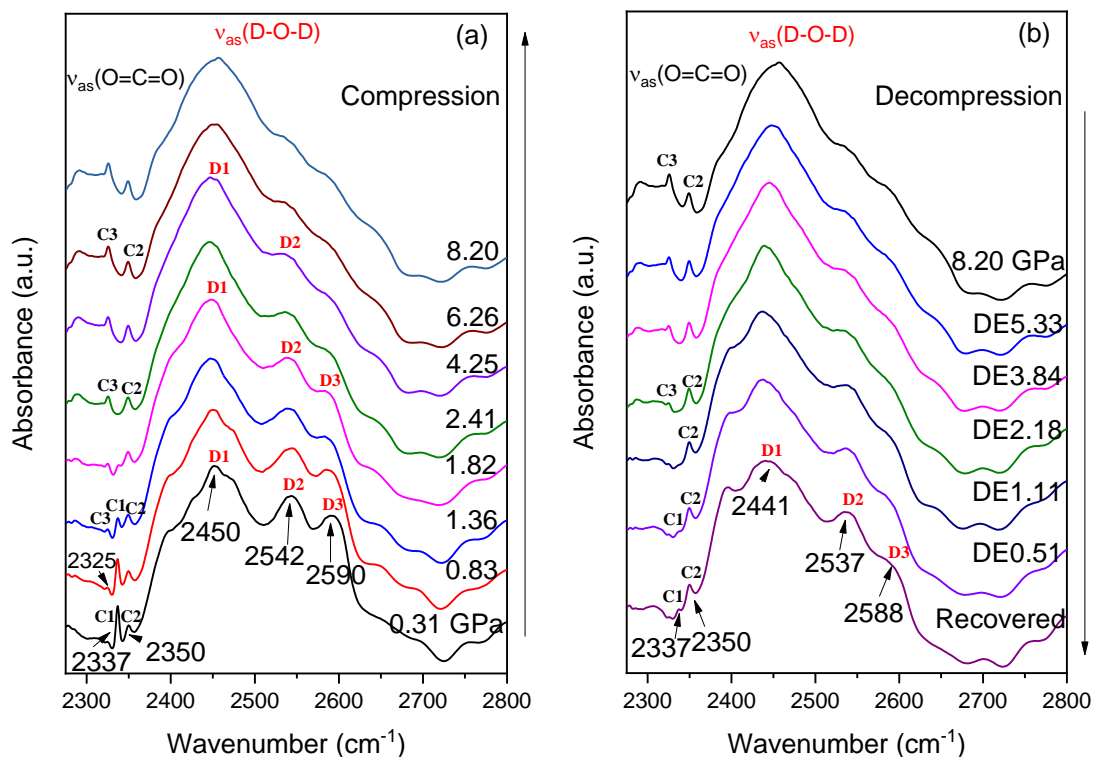

Figure 6.11 Selected FTIR spectra of CO_2 and D_2O co-adsorbed ZnAtzOx(H_2O) on compression (a) and decompression (b) for the 1:9 CO_2 to D_2O molar ratio loading.
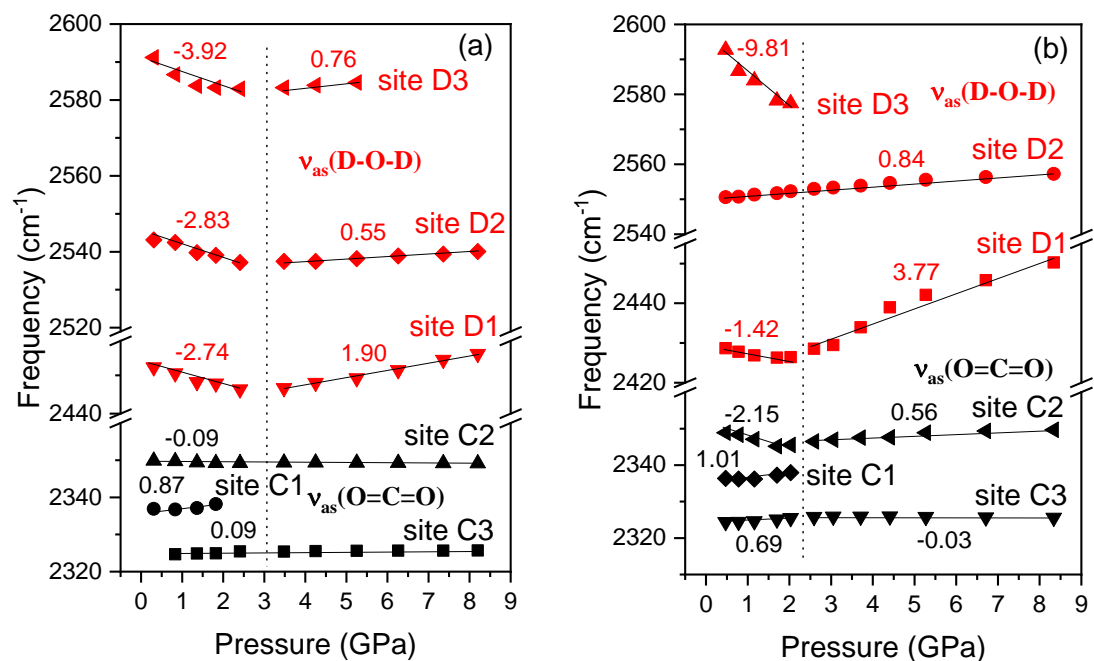
Figure 6.12 Pressure dependence (dv/dP, cm⁻¹/GPa) of CO₂ (black) and D₂O (red) vibrations in 1:9 CO₂ to D₂O molar ratio loading (a), and 1:1 CO₂ to D₂O molar ratio loading (b).

Table 6.4 Comparison of CO_2 and D_2O vibration frequencies in CO_2 and D_2O co-loaded ZnAtzOx(H_2O) before and after compression for two loadings with different CO_2 to D_2O molar ratios.

	Frequency (cm^{-1})					
	CO_2 asym			D_2O asym		
Conditions	1:9 CO_2 to D_2O molar ratio[a]					
Binding sites	Site 1	Site 2	Site 3	Site 1	Site 2	Site 3
Initial pressure[a]	-	2337	2350	2450	2542	2590
Recovered[a]	-	2337	2350	2441	2537	2588
Conditions	1:1 CO_2 to D_2O molar ratio[b]					
Initial pressure[b]	2337	2349	2324	2449	2551	2593
Recovered[b]	2336	2347	-	2445	2554	-

a. Frequencies observed and measured in the 1:9 CO_2 to D_2O ratio loading, at the lowest possible loading pressure (i.e. 0.31 GPa) and room temperature.

b. Frequencies observed and measured in the 1:1 CO_2 to D_2O ratio loading, at the lowest possible loading pressure (i.e. 0.47 GPa) and room temperature.

Pressure dependences for all D_2O adsorption modes exhibit notable red-shift at modest pressures (Figure 6.12a). A turning point is shown on the curves at 3 GPa, after which the modes start blue shifting, indicating the strongest D_2O-framework affinity is obtained at 3 GPa, which is similar to what we have observed in D_2O-loaded framework. For CO_2 adsorptions, all three sites exhibit very small pressure dependence, indicating that the CO_2-framework interaction at each site is not much affected by D_2O at high pressures. After releasing the pressure, both CO_2 site 1 and site 2 are recovered and observed at the same frequencies as before compression (Table 6.4). In contrast, site C2 became the more populated site upon recovery, whereas only a small amount of CO_2 is adsorbed at site C1 (Figure 6.11b). Given that the CO_2-framework interactions at site C2 are less intense, it is apparent that the D_2O molecules have a major influence on the amount of CO_2 to a less favorable and less confined position within the channels under high pressure.

Upon recovery, it appears that more D_2O molecules are residing in site D1 (Figure 6.11b). Since D_2O molecules adsorbed at site D1 feature the closest proximity with the framework, it becomes apparent that pressure has improved the D_2O adsorption by transporting more D_2O molecules to this favorable location. Moreover, all three sites are observed at a lower frequency compared to that of the initial spectrum (Table 6.4), suggesting that the interactions at each site are permanently enhanced under high pressure. Overall, the presence of a minor amount of CO_2 molecules enhanced the D_2O adsorption in the framework.

Table 6.5 Pressure dependence (dv/dP, cm^{-1}/GPa) of CO_2 and D_2O vibrations in ZnAtzOx(H_2O) for two loadings with different CO_2 to D_2O molar ratios.

Binding sites	1:9 ratio			1:1 ratio		
	Frequency[a] (cm^{-1})	Pressure region (GPa)		Frequency[a] (cm^{-1})	Pressure region	
		0-3.48	3.48-8.20		0-2.59	2.59-8.34
Site 1 (CO_2)	2337	0.87	-	2337	1.01	-
Site 2 (CO_2)	2350	-0.09		2349	-2.15	0.56
Site 3 (CO_2)	2325[b]	0.09		2324	0.69	-0.03
Site 1 (D_2O)	2450	-2.74	1.90	2449	-1.42	3.77
Site 2 (D_2O)	2542	-2.83	0.55	2551	0.84	
Site 3 (D_2O)	2590	-3.92	0.76	2593	-9.81	-

a. Unless otherwise motioned, the frequencies of all modes are observed and measured at room temperature, and 0.31 GPa and 0.47 GPa for 1:9 ratio loading and 1:1 ratio loading (i.e. CO_2 to D_2O), respectively.

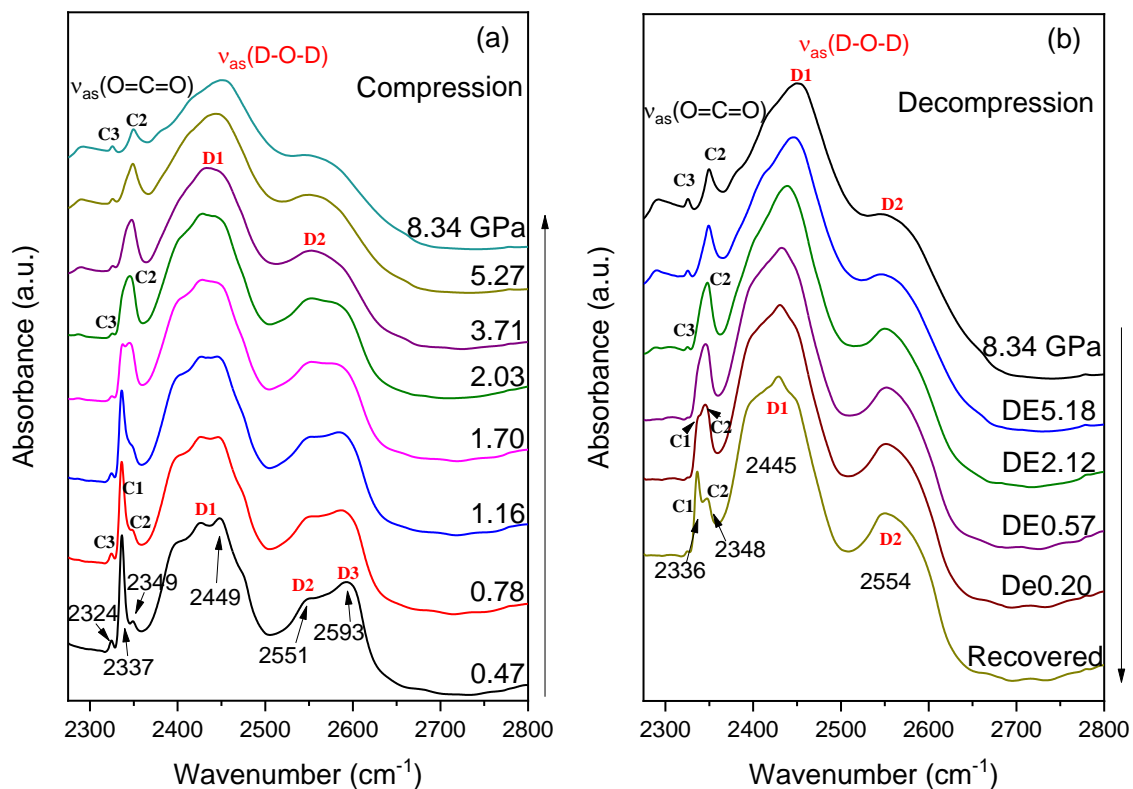b. In the 1:9 CO_2 to D_2O ratio loading, CO_2 site 3 was not observed until compressed to 0.83 GPa.

Figure 6.13 Selected FTIR spectra of CO_2 and D_2O co-adsorbed ZnAtzOx(H_2O) on compression (a) and decompression (b) for the 1:1 CO_2 to D_2O molar ratio loading.

The *in situ* high pressure IR study was then carried on CO_2 and D_2O co-loaded ZnAtzOx(H_2O) with a 1:1 molar ratio (Figure 6.13 and Appendix Figure A3). In this run, all three D_2O sites are observed at a higher frequency upon initial loading, which corresponds to weaker interactions with the framework at each site (Table 6.5). The similar occupancy changes among three D_2O sites is also observed. However, site D2 exhibits a blueshift throughout the entire compression region, compared to the modest redshift in the previous run. Therefore, the pressure is inducing the stiffening of the D-O bond at site D2, instead of promoting the D_2O-framework interactions. Moreover, site D2 is observed at a higher frequency upon releasing the pressure (Figure 6.13), indicating that these D_2O molecules adsorb to a position in the channels with weaker interactions with the framework. At site D1, the redshift is less substantial in the lower pressure region (below 2 GPa), and a more intense blueshift at higher pressures. These observations suggest that D_2O molecules in general exhibit less affinity to the framework at high pressures in this loading.

In contrast, high pressure shows a positive impact on improving CO_2 adsorption, in comparison to the previous loading. First of all, due to the higher loading level of CO_2, site 3 is observed upon initial loading (Figure 6.13a). Both site C2 and C3 are found at slightly lower frequencies compared to the previous trial (Table 6.5), suggesting stronger interactions with the framework at these sites. Secondly, CO_2 site C2 features a notable redshift in the lower pressure region, compared to the little pressure dependence of the same site in the first loading (Figure 6.12b). Furthermore, both site C1 and site C2 are recovered at a low frequency upon releasing the pressure (Table 6.4), suggesting permanently enhanced interactions between CO_2 and the framework at both sites.

Overall, the above two runs established that the $ZnAtzOx(H_2O)$ framework performed differently with different CO_2 to D_2O loading ratios under high pressure. Due to the overlapping between CO_2 sites and D_2O sites, it is believed that the CO_2 and D_2O adsorptions within the framework are of a competitive nature. Inevitably, the presence of D_2O does have negative effects on CO_2 storage under high pressure when the content of D_2O is dominant. However, upon increasing the CO_2 content to 50% in the second trial, the negative impact of D_2O on CO_2 adsorption is found to be less significant and improves the CO_2-framework affinity upon compression and recovery. CO_2 develops stronger interactions with the system at both site C1 and C2 after releasing the pressure, compared to that of the initial sample. Such enhanced interactions could be correlated with the guest-guest interaction between CO_2 and D_2O through hydrogen bonding.[36]

6.4 Conclusion

In summary, our study has demonstrated excellent reversibility and structural stability of $ZnAtzOx(H_2O)$ framework under all 4 conditions (i.e. empty, CO_2 loaded, D_2O loaded, and CO_2 D_2O co-loaded frameworks) up to 8 GPa, with chemical connectivity, local structure, as well as the porosity of the framework, remain intact. In the empty $ZnAtzOx(H_2O)$ framework, a reversible pressure-induced and enhanced hydrogen bond are observed in the pressure range from 1 to 3 GPa. The investigation on CO_2 loaded $ZnAtzOx(H_2O)$ under high pressure has shown that the gating effect that requires high CO_2 loading pressure and low temperature can also be achieved by high external pressure, which further leads to great potential in capturing more CO_2. In the D_2O loaded

ZnAtzOx(H_2O), it is of great significance that the framework exhibits prominent stability in the presence of water at high pressures. Moreover, the D_2O molecules are found to interact with the framework more closely under high pressure, where the best CO_2-framework affinity is obtained at 3 GPa. Furthermore, when CO_2 and D_2O are co-existing in the ZnAtzOx(H_2O) framework, both D_2O and CO_2 developed a third binding site at a modest pressure (i.e.~0.5 GPa). For D_2O, the interactions at all three binding sites are enhanced at higher pressures in the presence of CO_2. The pressure dependence analysis has proven that the framework features the closest proximity to both CO_2 and D_2O at around 2-3 GPa depending on the molar ratio between these two components. Overall, its remarkable mechanical and adsorption properties for CO_2 and water make ZnAtzOx(H_2O) a promising candidate for CO_2 capture in moisture environments under high pressure.

6.5 References

1.   Gedrich, K.; Senkovska, I.; Klein, N.; Stoeck, U.; Henschel, A.; Lohe, M. R.; Baburin, I. A.; Mueller, U.; Kaskel, S., A highly porous metal-organic framework with open nickel sites. *Angew Chem Int Ed Engl* **2010,** *49* (45), 8489-92.

2.   Caskey, S. R. W.-F., A. G.; Matzger, A. J., Dramatic tuning of carbon dioxide uptake via metal substitution in a coordination polymer with cylindrical pores. *J Am Chem Soc* **2008,** *130* (33), 10870-10871.

3.   Vaidhyanathan, R. I., S. S.; Shimizu, G. K. H.; Boyd, P. G.; Alavi, S.; Woo, T. K., Direct Observation and Quantification of CO_2 Binding Within an Amine-Functionalized Nanoporous Solid. *Science* **2010,** *330* (6004), 650-653.

4.   Cmarik, G. E.; Kim, M.; Cohen, S. M.; Walton, K. S., Tuning the adsorption properties of UiO-66 via ligand functionalization. *Langmuir* **2012,** *28* (44), 15606-13.

5.   Bae, Y.-S.; Farha, O. K.; Hupp, J. T.; Snurr, R. Q., Enhancement of CO_2/N_2 selectivity in a metal-organic framework by cavity modification. *J Mater Chem* **2009,** *19* (15), 2131.

6.   Vaidhyanathan, R.; Iremonger, S. S.; Dawson, K. W.; Shimizu, G. K., An amine-functionalized metal-organic framework for preferential CO_2 adsorption at low pressures. *Chem Comm* **2009,** (35), 5230-5232.

7.   Zhao, P.; Lampronti, G. I.; Lloyd, G. O.; Wharmby, M. T.; Facq, S.; Cheetham, A. K.; Redfern, S. A., Phase Transitions in Zeolitic Imidazolate Framework 7: The Importance of Framework Flexibility and Guest-Induced Instability. *Chem Mater* **2014,** *26* (5), 1767-1769.

8.   Cheng, Y.; Kajiro, H.; Noguchi, H.; Kondo, A.; Ohba, T.; Hattori, Y.; Kaneko, K.; Kanoh, H., Tuning of gate opening of an elastic layered structure MOF in CO_2 sorption with a trace of alcohol molecules. *Langmuir* **2011,** *27* (11), 6905-9.

9.   Ethiraj, J. B., F.; Vitillo, J. G.; Lomachenko, K. A.; Lamberti, C.; Reinsch, H.; Lillerud, K. P., Solvent‑Driven Gate Opening in MOF‑76‑Ce: Effect on CO_2 Adsorption. *ChemSusChem* **2016,** *9* (7), 713-719.

10.   Banerjee, A.; Nandi, S.; Nasa, P.; Vaidhyanathan, R., Enhancing the carbon capture capacities of a rigid ultra-microporous MOF through gate-opening at low CO_2 pressures assisted by swiveling oxalate pillars. *Chem Commun (Camb)* **2016,** *52* (9), 1851-4.

11.   Hobday, C. L.; Marshall, R. J.; Murphie, C. F.; Sotelo, J.; Richards, T.; Allan, D. R.; Duren, T.; Coudert, F. X.; Forgan, R. S.; Morrison, C. A.; Moggach, S. A.; Bennett, T. D., A Computational and Experimental Approach Linking Disorder, High-Pressure Behavior, and Mechanical Properties in UiO Frameworks. *Angew Chem Int Ed Engl* **2016,** *55* (7), 2401-5.

12.   Gagnon, K. J.; Beavers, C. M.; Clearfield, A., MOFs under pressure: the reversible compression of a single crystal. *J Am Chem Soc* **2013,** *135* (4), 1252-5.

13.   Zhou, M.; Wang, K.; Men, Z.; Sun, C.; Li, Z.; Liu, B.; Zou, G.; Zou, B., Pressure-induced isostructural phase transition of a metal-organic framework $Co_2(4,4'\text{-}bpy)_3(NO_3)_4 \cdot xH_2O$. *CrystEngComm* **2014,** *16* (20), 4084-4087.

14.   Moggach, S. A.; Bennett, T. D.; Cheetham, A. K., The effect of pressure on ZIF-8: increasing pore size with pressure and the formation of a high-pressure phase at 1.47 GPa. *Angew Chem Int Ed Engl* **2009,** *48* (38), 7087-9.

15.   Fairen-Jimenez, D.; Moggach, S. A.; Wharmby, M. T.; Wright, P. A.; Parsons, S.; Duren, T., Opening the gate: framework flexibility in ZIF-8 explored by experiments and simulations. *J Am Chem Soc* **2011,** *133* (23), 8900-2.

16.   Hobday, C. L.; Bennett, T. D.; Fairen-Jimenez, D.; Graham, A. J.; Morrison, C. A.; Allan, D. R.; Düren, T.; Moggach, S. A., Tuning the Swing Effect by Chemical Functionalization of Zeolitic Imidazolate Frameworks. *J Am Chem Soc* **2018,** *140* (1), 382–387.

17.   Mao, H.; Xu, J.; Hu, Y.; Huang, Y.; Song, Y., The effect of high external pressure on the structure and stability of MOF α-$Mg_3(HCOO)_6$ probed by in situ Raman and FT-IR spectroscopy. *J Mater Chem A* **2015,** *3* (22), 11976-11984.

18.   Spencer, E. C.; Kiran, M. S.; Li, W.; Ramamurty, U.; Ross, N. L.; Cheetham, A. K., Pressure-induced bond rearrangement and reversible phase transformation in a metal-organic framework. *Angew Chem Int Ed Engl* **2014,** *53* (22), 5583-6.

19.   Ortiz, A. U.; Boutin, A.; Gagnon, K. J.; Clearfield, A.; Coudert, F. X., Remarkable pressure responses of metal-organic frameworks: proton transfer and linker coiling in zinc alkyl gates. *J Am Chem Soc* **2014,** *136* (32), 11540-5.

20.   Yot, P. G.; Ma, Q.; Haines, J.; Yang, Q.; Ghoufi, A.; Devic, T.; Serre, C.; Dmitriev, V.; Férey, G.; Zhong, C.; Maurin, G., Large breathing of the MOF MIL-47(V^{IV}) under mechanical pressure: a joint experimental–modelling exploration. *Chem Sci* **2012,** *3* (4), 1100.

21.   Hu, Y.; Lin, B.; He, P.; Li, Y.; Huang, Y.; Song, Y., Probing the Structural Stability of and Enhanced CO_2 Storage in MOF MIL-68(In) under High Pressures by FTIR Spectroscopy. *Chem Eur J* **2015,** *21* (51), 18739-48.

22. Hu, Y.; Liu, Z.; Xu, J.; Huang, Y.; Song, Y., Evidence of pressure enhanced CO_2 storage in ZIF-8 probed by FTIR spectroscopy. *J Am Chem Soc* **2013,** *135* (25), 9287-90.

23. Jiang, S.; Hu, Y.; Chen, S.; Huang, Y.; Song, Y., Elucidation of the Structural Origins and Contrasting Guest-Host Interactions in CO_2-Loaded CdSDB and PbSDB Metal-Organic Frameworks at High Pressures. *Chem Eur J* **2018,** *24* (72), 19280-19288.

24. Mao, H. K.; Xu, J.; Bell, P. M., Calibration of the ruby pressure gauge to 800 kbar under quasi-hydrostatic conditions. *J Geophys Res* **1986,** *91* (B5), 4673.

25. Puviarasan, N.; Arjunan, V.; Mohany, S., FT-IR and FT-Raman Studies on 3-Aminophthalhydrazide and N-Aminophthalimide. *Turk J Chem* **2002,** *26*, 323-333.

26. Mancilla, N.; D'Antonio, M. C.; González-Baró, A. C.; Baran, E. J., Vibrational spectra of lead(II) oxalate. *J Raman Spectrosc* **2009,** *40* (12), 2050-2052.

27. Zundel, G.; Lubos, W. D.; Kölkenbeck, K.; Fermi Resonance of Infrared Vibrations in the -NH_2 Groups of Polynucleotides. *Can J Chem* **1971,** *49* (23), 3795-3798.

28. Torshin, I. Y.; Weber, I. T.; Harrison, R. W., Geometric criteria of hydrogen bonds in proteins and identification of `bifurcated' hydrogen bonds. *Protein Eng Des Sel* **2002,** *15* (5), 359–363.

29. Su, Z.; Miao, Y. R.; Zhang, G.; Miller, J. T.; Suslick, K. S., Bond breakage under pressure in a metal organic framework. *Chem Sci* **2017,** *8* (12), 8004-8011.

30. Rood, J. A.; Noll, B. C.; Henderson, K. W., Synthesis, structural characterization, gas sorption and guest-exchange studies of the lightweight, porous metal-organic framework alpha-[$Mg_3(O_2CH)_6$]. *Inorg Chem* **2006,** *45* (14), 5521-8.

31. Yeh, C.-T.; Lin, W.-C.; Lo, S.-H.; Kao, C.-C.; Lin, C.-H.; Yang, C.-C., Microwave synthesis and gas sorption of calcium and strontium metal–organic frameworks with high thermal stability. *CrystEngComm* **2012,** *14* (4), 1219.

32.   Lin, J.-D.; Wu, S.-T.; Li, Z.-H.; Du, S.-W., A series of novel Pb(ii) or Pb(ii)/M(ii) (M = Ca and Sr) hybrid inorganic–organic frameworks based on polycarboxylic acids with diverse Pb–O–M (M = Pb, Ca and Sr) inorganic connectivities. *CrystEngComm* **2010,** *12* (12), 4252.

33.   Plonka, A. M.; Banerjee, D.; Woerner, W. R.; Zhang, Z.; Li, J.; Parise, J. B., Effect of ligand geometry on selective gas-adsorption: the case of a microporous cadmium metal organic framework with a V-shaped linker. *Chem Commun (Camb)* **2013,** *49* (63), 7055-7.

34.   Lappi, S. E.; Smith, B.; Franzen, S., Infrared spectra of $H_2^{16}O$, $H_2^{18}O$ and D_2O in the liquid phase by single-pass attenuated total internal reflection spectroscopy. *Spectrochim Acta A Mol Biomol Spectrosc* **2004,** *60* (11), 2611-9.

35.   Tan, K.; Nijem, N.; Gao, Y.; Zuluaga, S.; Li, J.; Thonhauser, T.; Chabal, Y. J., Water interactions in metal organic frameworks. *CrystEngComm* **2015,** *17* (2), 247-260.

36.   Kaur, S. P.; Ramachandran, C. N., Host–guest and guest–guest interactions in noble gas hydrates. *Mol Phys* **2017,** *116* (1), 54-63.

Chapter 7

7 Summary and future work

7.1 Summary

As a class of porous materials with tunable structures and functionalities, MOFs are well-suited as potential CO_2 absorbents. In this work, in situ high pressure FTIR and Raman, as well as synchrotron XRD experiments were carried out to investigate the structural stability and CO_2 adsorption performance of different MOFs with distinctive topologies and structures. The activated CdSDB, PbSDB, SIFSIX-3-Zn, UiO-66 and $ZnAtzOx(H_2O)$ frameworks exhibit different pressure stabilities, whereas all of them were much improved when loaded with CO_2. Moreover, application of high pressure substantially improved the CO_2 adsorption performances in all the MOFs through different mechanisms: for instance, additional CO_2 binding sites were found in PbSDB, SIFSIX-3-Zn, and ZnAtzOx at high pressures; an increased CO_2 adsorption capacity was found in ZIF-8 and UiO-66 by the synergetic effect of high pressure and high temperature. Overall, our work has shown that pressure plays an important role in facilitating CO_2 adsorption.

Chapter 3 demonstrates that pressure can effectively tune the structures and CO_2 adsorption performance of CdSDB and PbSDB. A fully reversible structural amorphization up to 13 GPa is observed in both CdSDB and PbSDB. Upon CO_2 loading, both frameworks show enhanced CO_2-framework interactions; PbSDB exhibits a new CO_2 adsorption site upon compression, which is structurally and thermodynamically favored at higher pressures, as the CO_2 population at this new site increases with pressure. The formation of this site originates from the pressure-induced structural changes on the PbSDB framework, in which the rotation phenyl-ring creates a second "π-pocket" in the channel to accommodate CO_2 molecules.

Chapter 4 illustrates the pressure-enhanced CO_2-framework interactions in SIFSIX-3-Zn. A new CO_2 binding site that exhibits closer affinity with the framework is found under high pressures. The formation of this new site is due to the rotation of the pyrazine rings

and the elongation of the Si-F bonds. Moreover, it is shown that CO_2 plays an important role in improving the structural stability of the framework under high pressures.

It has been reported that gaseous/fluid CO_2 undergoes a phase change to solid at around 0.6 GPa and room temperature, which severely shortens our scope in exploring the CO_2 adsorption in MOFs under higher pressures, as solid CO_2 is immobile, and it requires CO_2 to be in a fluid state for effective diffusion under pressure. In *Chapter 5*, by simultaneously applying high temperature and pressure to the selected MOF systems, we have demonstrated that high pressure (i.e. above 0.6 GPa) could further facilitate CO_2 insertion into the cages of ZIF-8 and UiO-66 with the assist of high temperature, as characterized using FTIR spectroscopy. The gate opening effect in ZIF-8 was found to be responsible for the dramatic improvement in its CO_2 adsorption capacity.

In *Chapter 6*, the structure evolution of the activated $ZnAtzOx(H_2O)$ framework in response to high pressure, the high pressure effect on both CO_2 and D_2O adsorptions, as well as the CO_2 and D_2O co-adsorption were investigated. The framework has shown remarkable structural stability in the presence of water at high pressures. Moreover, a new binding site is observed for both CO_2 and D_2O in CO_2-D_2O co-adsorbed framework, a competitive relationship between CO_2 and water adsorption under high pressure is established. The CO_2-framework interactions are enhanced when the amount of CO_2 is dominant.

It is hoped that our work could provide guidance to understand the structure-property relations of MOFs and how they affect the CO_2 adsorption performance at high pressures. This information would also bring new insight into the design and development of desirable frameworks or porous materials for CO_2 capture.

7.2 Suggestions for future work

From this work, we gained a general knowledge of pressure effects on different MOFs and their CO_2 adsorption performance at high pressures. Further studies should help answer some remaining questions.

In *Chapter 4*, the *in-situ* synchrotron single crystal XRD data of CO_2 loaded SIFSIX-3-Zn was collected at APS and is currently under process. If these results could be successfully solved, it would help fully unveil the structural behaviors of the framework and track the location of the CO_2 molecules at high pressures, which is complementary to our vibration spectroscopy results.

In *Chapter 5*, a significantly improved CO_2 capacity in ZIF-8 and UiO-66 is induced by the synergetic effect of high pressure and high temperature, probed by in situ FTIR. However, the exact location of these adsorbed CO_2 molecules remains unknown. If high-pressure and high-temperature single crystal XRD experiments could be carried out, not only the exact number and binding sites of CO_2 molecules can be pinpointed, it could also monitor the structural evolution of these frameworks at high pressures. Moreover, not just limited to ZIF-8 and UiO-66 that we worked on, other MOFs with promising CO_2 adsorption properties are also of great interest to investigate using the high-pressure and high-temperature single crystal XRD method. For instance, NH_2-UiO-66, a UiO-66 analog with the -NH_2 functionality that enhances the CO_2 selectivity and guest-host interactions could be a good object. Furthermore, MOFs that feature gate opening effect could be another direction that we could look into in the future, such as MIL-47, Sc_2BDC_3, ZIF-90, etc.

For *Chapter 6*, since it is difficult to use single crystal XRD to solve the location of the hydrogen or deuterium atoms in water, it would be particular interesting and helpful if computational simulations could be performed to investigate the structural changes, as well as the CO_2 and water co-adsorption in $ZnAtzOx(H_2O)$, which could help further confirm the conclusion we drew from the FTIR data. Such method could also be incorporated into our further studies on multi-component adsorption in MOFs under high pressures. The combination of vibration spectroscopy study and the computational simulations would provide us a full picture of the evolution of the structure responses, the behavior of the guest molecules, as well as the guest-host interactions at high pressures.
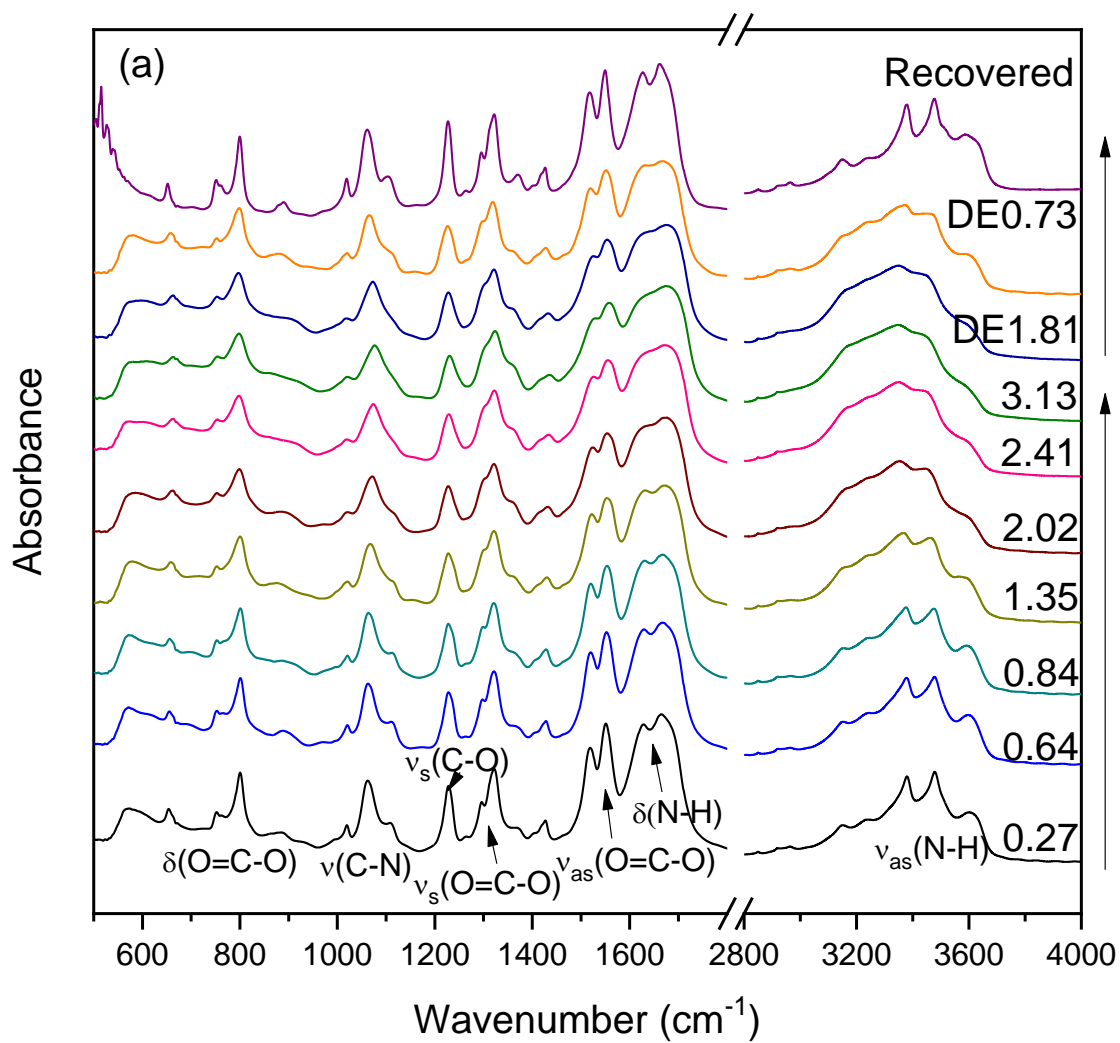
Appendix A Supporting Results of ZnAtzOx(H₂O)

Figure A 1 FTIR spectra of activated ZnAtzOx (H₂O) at high pressures.

Table A 1 Pressure dependence (dv/dP, cm^{-1}/GPa) of framework vibrations in CO$_2$ and D$_2$O co-loaded ZnAtzOx(H$_2$O) for two loadings with different CO$_2$ to D$_2$O molar ratios.

Modes	1:9 ratio[a]			1:1 ratio[b]		
	Frequency (cm^{-1})	Pressure region		Frequency (cm^{-1})	Pressure region	
		0.31-2.41 GPa	2.41-8.20 GPa		0.47-2.03 GPa	2.03-8.34 GPa
O=C-O bending	757	2.00	0.01	759	2.45	0.95
	798	-0.59	0.16	795	-0.46	-0.09
C-N stretch				1011	3.56	1.66
	1011	3.65	1.49	1072	2.56	1.71
	1071	3.16	1.84	1096	7.06	3.72
C-O sym stretch	1226	0.68	2.13	1228	1.09	2.03
O=C-O sym stretch				1291	3.84	2.77
	1318	2.14	1.50	1315	2.10	1.52
O=C-O asym stretch	1520	2.56	2.96	1511	2.26	2.32
	1567	-1.61	1.69	1564	-1.67	1.71
N-D bending	1660	3.81	1.39	1668	0.59	0.86

a. Frequencies and pressure dependences measured in the 1:9 CO$_2$ to D$_2$O ratio loading.

b. Frequencies and pressure dependences measured in the 1:1 CO$_2$ to D$_2$O ratio loading.
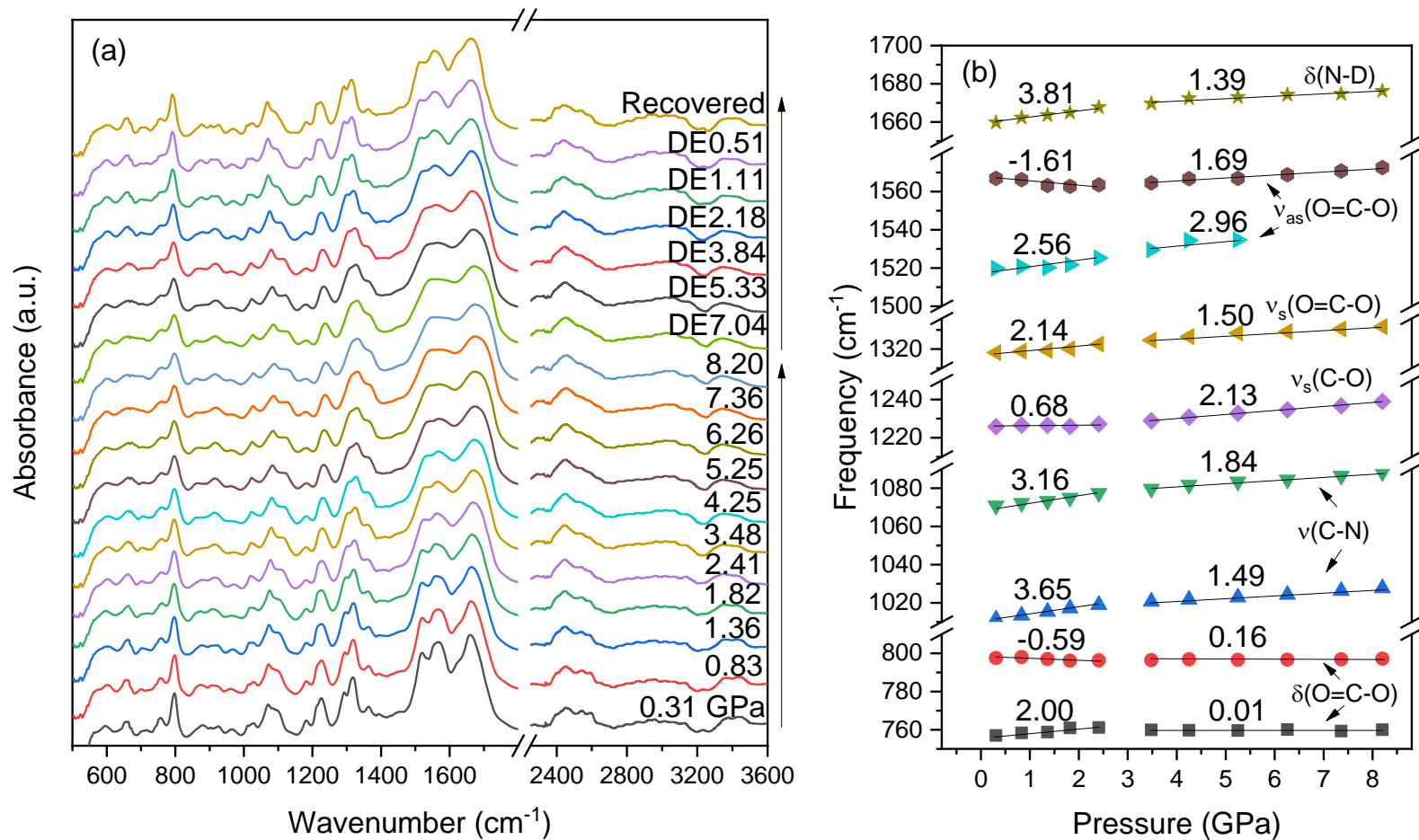
Figure A 2 (a) Selected IR spectra of CO_2 and D_2O co-loaded ZnAtzOx(H_2O) upon compression and decompression in the pressure range from 0.31 GPa to 8.20 GPa in the 1:9 CO_2 to D_2O ratio loading. (b) Pressure dependence of selected framework vibrations of ZnAtzOx(H_2O) on compression.
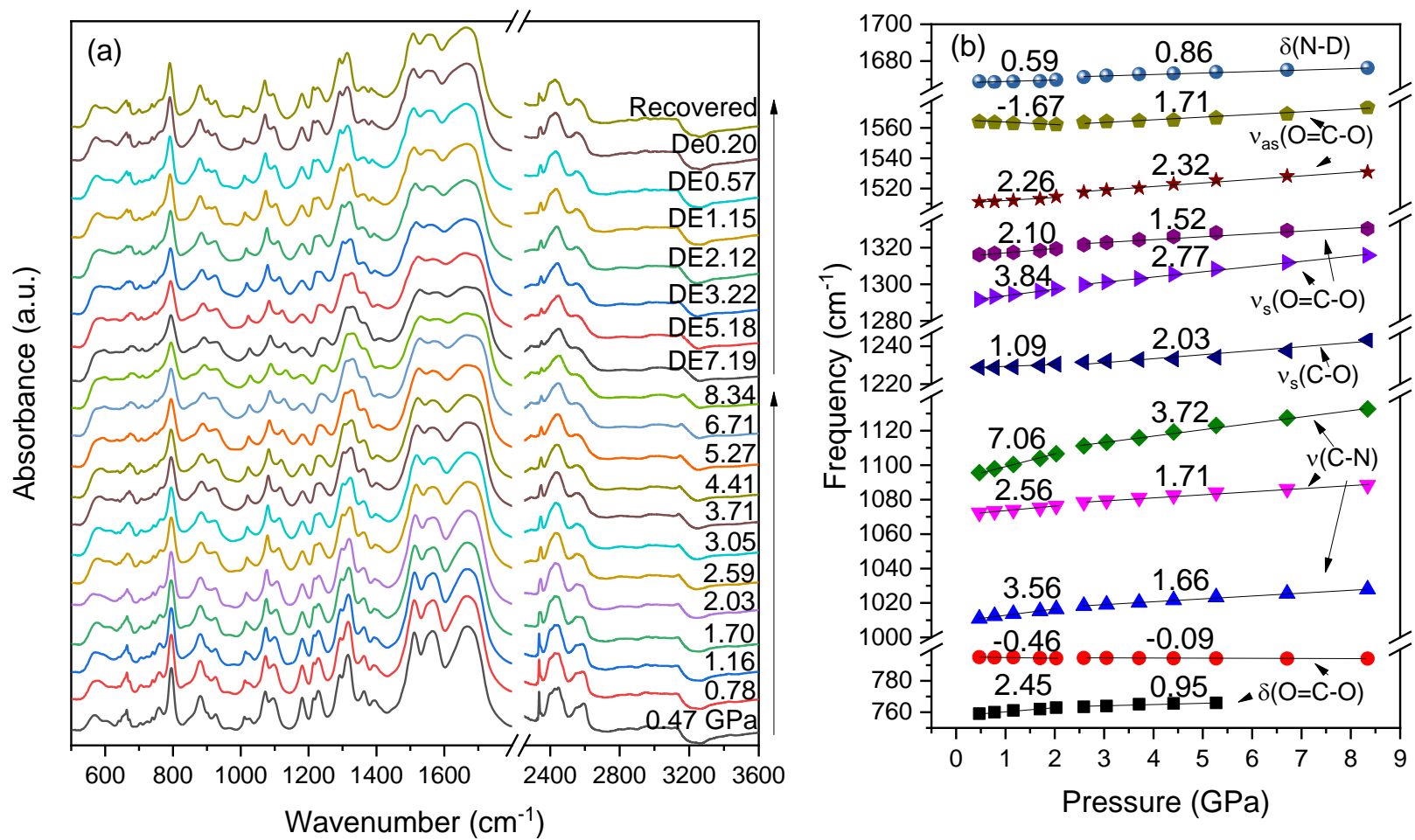
Figure A 3 (a) Selected IR spectra of CO₂ and D₂O co-loaded ZnAtzOx(H₂O) upon compression and decompression in the pressure range from 0.47 GPa to 8.34 GPa in the 1:1 CO₂ to D₂O ratio loading. (b) Pressure dependence of selected framework vibrations of ZnAtzOx(H₂O) on compression.

Appendix B Copyright Permission

Curriculum Vitae

Name:	Shan Jiang
Post-secondary Education and Degrees:	Northeastern University Shenyang, Liaoning, China 2010-2014 B.Sc.
	The University of Western Ontario London, Ontario, Canada 2014-2019 Ph.D. candidate
Honours and Awards:	International Graduate Student Scholarship (UWO) 2014-2019
	Northeastern University Third-class Scholarship 2011-2012
Related Work Experience	Teaching Assistant The University of Western Ontario 2014-2019

Publications:

1. **Jiang, S.**, Hu, Y., Chen, S., Huang, Y., Song, Y. Elucidation of the Structural Origins and Contrasting Guest‑Host Interactions in CO_2-Loaded CdSDB and PbSDB Metal-Organic Frameworks at High Pressures. *Chemistry-A European Journal*, **2018**, *24*(72), 19280-19288.

2. Desveaux, B. E., Wong, Y. A., Lucier, B. E., Terskikh, V. V., Boyle, P. D., **Jiang, S.**, Huang, Y. CO_2 Behavior in a Highly Selective Ultramicroporous Framework: Insights from Single-Crystal X-ray Diffraction and Solid-State Nuclear Magnetic Resonance Spectroscopy. *The Journal of Physical Chemistry C*, **2019**, *123*(29), 17798-17807.

3. Wang, P., Guan, J., Galeschuk, D. T., Yao, Y., He, C. F., **Jiang, S.**, Zhang, S., Liu, Y., Jin, M., Jin, C., Song, Y. Pressure-induced polymorphic, optical, and electronic transitions of formamidinium lead iodide perovskite. *The Journal of Physical Chemistry Letters*, **2017**, *8*(10), 2119-2125.

Presentations:

1. Understanding the Behaviors of Various Adsorbed Gases and Guest-Host Interactions in an Ultramicroporous Metal-Organic Framework under High Pressures; poster presentation, Montreal, CSC **2019**.

2. Monitoring the Synergetic Effect of High Pressure and Temperature on Enhancing CO_2 Adsorptive Capacity of ZIF-8 by In-Situ FTIR Spectroscopy; oral presentation, Waterloo, IDW **2018**.

3. The Structural Stability and CO_2 Storage of SIFSIX-3-Zn under High Pressures probed by Vibrational Spectroscopy; oral presentation, Toronto, CSC **2017**.

4. High Pressure Studies on the Structural Stabilities of MOFs and Their Performances for CO_2 Storage Probed by Vibrational Spectroscopies and Synchrotron Powder X-ray Diffraction; poster presentation, Hamilton, IDW **2016**.

5. *In situ* High Pressure Study of MOF PbSDB and Its Performance for CO_2 Storage by Vibrational Spectroscopy and Synchrotron Powder X-ray Diffraction; poster presentation, Halifax, CSC **2016**.